Imaging at high field is a pain,
but if done right, there is much to gain.
FSE shows more
than we could see before
and has many applications in the brain.

University of Alberta

Advances in Magnetic Resonance Imaging of the Human Brain at 4.7 Tesla

by

Robert Marc Lebel

A thesis submitted to the Faculty of Graduate Studies and Research
in partial fulfillment of the requirements for the degree of

Doctor of Philosophy

Biomedical Engineering

Fall 2010
Edmonton, Alberta

Examining Committee

Dr. Alan H. Wilman, Department of Biomedical Engineering

Dr. Richard B. Thompson, Department of Biomedical Engineering

Dr. Christian Beaulieu, Department of Biomedical Engineering

Dr. W.R. Wayne Martin, Department of Neurology

Dr. Nicola De Zanche, Department of Oncology

Dr. Alex L. MacKay, Department of Physics and Astronomy, University of British Columbia

Abstract

Magnetic resonance imaging is an essential tool for assessing soft tissues. The desire for increased signal-to-noise and improved tissue contrast has spurred development of imaging systems operating at magnetic fields exceeding 3.0 Tesla (T). Unfortunately, traditional imaging methods are of limited utility on these systems. Novel imaging methods are required to exploit the potential of high field systems and enable innovative clinical studies. This thesis presents methodological advances for human brain imaging at 4.7 T. These methods are applied to assess sub-cortical gray matter in multiple sclerosis (MS) patients.

Safety concerns regarding energy deposition in the patient precludes the use of traditional fast spin echo (FSE) imaging at 4.7 T. Reduced and variable refocusing angles were employed to effectively moderate this energy deposition while maintaining high signal levels; an assortment of time-efficient FSE images are presented. Contrast changes were observed at low angles, but images maintained a clinically useful appearance.

Heterogeneous transmit fields hinder the measurement of transverse relaxation times. A post-processing technique was developed to model the salient signal behaviour and enable accurate transverse relaxometry. This method is robust to transmit variations observed at 4.7 T and improves multislice imaging efficiency.

Gradient echo sequences can exploit the magnetic susceptibility difference between tissues to enhance contrast, but are corrupted near air/tissue interfaces. A correction method was developed and employed to reliably produce a multitude of quantitative and qualitative image sets.

Using these techniques, transverse relaxation times and susceptibility field shifts were measured in sub-cortical nuclei of relapsing-remitting MS patients. Abnormalities in the globus pallidus and pulvinar nucleus were observed in all quantitative methods; most other regions differed on one or more measures. Correlations with disease duration were not observed, reaffirming that the disease process commences prior to symptom onset.

The methods presented in this thesis enable efficient qualitative and quantitative imaging at high field strength. Unique challenges, notably patient safety and field variability, were overcome via sequence implementation and data processing. These techniques enable visualization and measurement of unique contrast mechanisms, which reveal insight into neurodegenerative diseases, including widespread sub-cortical gray matter damage in MS.

Table of Contents

List of Tables

List of Figures

List of Symbols and Abbrev.

A_{scale}	Scaling factor in the stimulated echo compensating fit, Page 84
Abbrev.	Abbreviation, Page xiii
b	Local magnetic field perturbation, Page 7
$\vec{B}$	Magnetic field (vector), Page 3
B_0	Static magnetic field, Page 3
B_1	Generic radiofrequency field, Page 4
B_1^-	Receive field, Page 11
B_1^+	Transmit field, Page 11
$B_1^{+\,rel}$	Relative transmit field, Page 84
B_{eff}	Effective magnetic field in the rotating frame of reference, Page 5
BPP	Bloembergen-Purcell-Pound (relaxation theory), Page 9
C	Objective function for non-linear least-squares fitting, Page 85
$\hat{C}$	Cartesian coordinate system (lab frame), Page 3
$\hat{C}'$	Cartesian coordinate system (rotating frame), Page 4
CN	Caudate nucleus, Page 122
CNR	Contrast-to-noise ratio, Page 108
CSF	Cerebrospinal fluid, Page 37
DESPOT1,2	Driven equilibrium single pulse observation of $T_{1,2}$, Page 83
E	Energy, Page 3
EDSS	Extended disability status scale, Page 39
EPG	Extended phase graph, Page 32
ES	Effect size, Page 122

ESP	Inter-echo spacing, Page 28
ETL	Echo train length, Page 28
f_0	Larmor frequency, Page 3
f_A	Fraction of spins in pool “A”, Page 9
f_B	Fraction of spins in pool “B”, Page 9
$f_{coherence}$	Echo scaling factor attributed to spin coherence, Page 46
$f_{relaxation}$	Echo scaling factor attributed to relaxation, Page 46
F	Transverse phase coefficient in the EPG representation, Page 33
F_{LP}	Low-pass frequency filter, Page 20
FOV	Field-of-view, Page 14
FSE	Fast spin echo, Page 2
$\vec{G}$	Magnetic field gradient (vector), Page 11
GM	Gray matter, Page 37
GP	Globus pallidus, Page 122
GRE	Gradient echo, Page 2
H	2D or 3D k-space data, Page 20
HASTE	Half Fourier acquisition single shot turbo spin echo, Page 44
i	Imaginary unit ($i^2 = -1$), Page 4
IC	Internal capsule, Page 122
j	Generic index, Page 7
J	Spectral density function, Page 8
k_B	Boltzmann’s constant, Page 4
$\vec{k}$	Spatial frequency (vector), Page 14
K	Constant in the Bloembergen-Purcell-Pound relaxation model, Page 9
LFS	Local field shift, Page 107
LFSSD	Standard deviation of the local field shift, Page 122
$\vec{M}$	Magnetization (vector), Page 3
M_0	Equilibrium magnetization, Page 3
M_{EX}	Transverse magnetization immediately following excitation, Page 84

$M_{x,y,z}$	Magnetization components, Page 3
$\vec{M}_{\perp}$	Transverse magnetization (vector), Page 4
$\vec{M}_{\parallel}$	Longitudinal magnetization (vector), Page 4
MPRAGE	Magnetization prepared rapid gradient echo, Page 153
MRI	Magnetic resonance imaging, Page 1
MS	Multiple sclerosis, Page 37
n	Generic index, Page 27
n_{eff}	Effective echo number, Page 28
N	Total number of spins, Page 7
N_{PE}	Number of 2D phase encode lines, Page 15
N_{PE2}	Number of 3D phase encode lines, Page 15
N_{RO}	Number of readout points, Page 104
NMR	Nuclear magnetic resonance, Page 2
P_j	Location of the j^{th} multiecho gradient echo peak, Page 104
PC	Percent change, Page 122
ppb	Parts per billion, Page 108
PSF	Point spread function, Page 73
PSS	Pseudosteady state, Page 30
Pul	Pulvinar nucleus, Page 122
Put	Putamen, Page 122
Q	Quality metric for adaptive phase filtering, Page 107
$\vec{r}$	Generic position (vector), Page 10
$\mathbf{R}$	Radiofrequency nutation operator (matrix), Page 5
R	Autocorrelation function, Page 7
R_1	Longitudinal relaxation rate, Page 8
R_2	Transverse relaxation rate, Page 8
R_{2eff}	Effective transverse relaxation rate with low refocusing angles, Page 30
R_{sphere}	Radius of a sphere, Page 29
RARE	Rapid acquisition with refocused echoes, Page 25

RF	Radiofrequency, Page 4
ROI	Region-of-interest, Page 122
RN	Red nucleus, Page 122
S	Signal, Page 10
S_0	Virtual 180 base line signal, Page 72
$S_{envelope}$	Virtual 180 signal envelope, Page 72
S_{prep}	Additional signal for SPSS preparation, Page 72
S_{V180}	Virtual 180 echo train amplitude, Page 72
$S_{x,y,z}^{(\mathrm{sinc})}$	Signal decay from background field gradients, Page 101
$\mathbf{S}$	Precession operator (matrix), Page 6
SAR	Specific absorption rate, Page 29
SD	Standard deviation, Page 107
SN	Substantia nigra, Page 122
SNR	Signal-to-noise ratio, Page 12
SPSS	Static pseudosteady state, Page 30
SWI	Susceptibility weighted imaging, Page 20
t	Generic time variable, Page 4
T	Temperature, Page 4
$\mathbf{T}$	Relaxation operator (matrix), Page 6
T	Tesla (SI unit of magnetic flux density), Page 1
T_1	Longitudinal relaxation time, Page 5
T_2	Irreversible transverse relaxation time, Page 5
T_2'	Reversible transverse relaxation time, Page 20
$T_2^\star$	Net transverse relaxation time, Page 18
TE	Echo time, Page 18
TE_{eff}	Effective echo time, Page 28
Th	Thalamus, Page 122
TR	Repetition time, Page 14
TSE	Turbo spin echo, Page 25

VHF	Very high field (loosely defined as >3.0 T), Page 119
$w_{envelope}$	Width of the virtual 180 signal envelope, Page 72
w_{prep}	Width of SPSS preparation envelope, Page 72
W_E	Spatial thickness of the excitation slice, Page 82
W_R	Spatial thickness of the refocusing slice, Page 82
WM	White matter, Page 37
$\hat{x}, \hat{y}, \hat{z}$	Unit vectors in the laboratory coordinate system, Page 3
$\hat{x}', \hat{y}', \hat{z}'$	Unit vectors in the rotating coordinate system, Page 4
Z	Longitudinal phase coefficient in the EPG representation, Page 33
α	Generic RF pulse angle, Page 5
α_{EX}	Excitation pulse angle, Page 84
$\alpha_{penalty}$	Penalty factor for non-zero local phase in adaptive filtering, Page 107
α_t	Transition pulse angle, Page 64
β	Target standard deviation in adaptive filtering, Page 107
γ	Gyromagnetic ratio, Page 3
δ_j	Spacing between peaks in the multiecho gradient echo tweak, Page 104
$\Delta k_{x,y,z}$	Sampling intervals in k-space, Page 14
$\Delta x, y, z$	Sampling intervals in image space, Page 15
ζ	Virtual 180 amplitude attenuation factor, Page 72
$\xi_{a,b}$	Scale factors for gradient pre- and re-phasing lobes, Page 104
ρ_0	Proton density, Page 4
σ	Noise amplification factor, Page 74
σ_{cond}	Electrical conductivity, Page 29
τ	Generic time interval, Page 18
τ_c	Correlation time, Page 8
τ_α	Radiofrequency pulse duration, Page 5
ϕ_α	Phase angle of a radiofrequency pulse, Page 6
Φ	High pass filtered phase image, Page 20

Φ_{loc}	High pass filtered phase in the local neighbourhood, Page 107
ψ	Generic function, Page 13
Ψ	Generic function, Page 13
ω	Angular frequency, Page 3
ω_0	Larmor angular frequency, Page 3
ω_S	Angular frequency shift from static field heterogeneities, Page 11
$\hbar$	Plank's constant, Page 3

Chapter 1

Introduction

1.1 Thesis Overview

Magnetic resonance imaging (MRI) is a truly mediocre imaging modality. It consistently underperforms in most defining characteristics: its spatial resolution is inferior to that of optical imaging and microscopy; its temporal resolution is typically lower than that of computed tomography and is abysmal relative to ultrasound. It lacks the contrast afforded by nuclear medicine. Its accessibility is limited, patient throughput is low, and contraindications are numerous. Furthermore, the siting and operating costs for high field systems approach the cumulative sum of its alternatives.

Yet, MRI remains a valuable diagnostic and research tool. Its utility stems from this remarkably consistent mediocrity. Or perhaps, from its lack of catastrophic faults. Regardless, it is the sole modality to non-invasively generate high contrast images anywhere in the human body (almost) with acceptable spatial resolution ($\sim$1 mm^3) in a tolerable acquisition time (several minutes), all without any harmful side effects (we hope).

Fundamentally, MRI is an extremely signal-starved modality: intense magnetic fields are required to elicit minute signals, and efficient signal generation, detection, and processing technologies are required. These technologies have evolved rapidly over the last three decades. Notable advances include a steady increase of the static magnetic field strength (currently, clinical systems operate at 3.0 T; preclinical systems are available at 7.0 T), strength and speed of gradient coils (human systems with 60 mT/m and 200 mT/m/ms are available), efficient use of multiple independent receiver elements (modern spectrometers are equipped with 8 to 32 channels), and recently, support for multiple independent transmit elements. These hardware advances are, by causality, pursued by refinements in imaging technique, then by clinical investigation and application. *Currently, a notable lack of imaging techniques can exploit the potential of high field imaging systems.*

This thesis presents methodological advances in human brain imaging at a magnetic field strength of 4.7 T with volume transmit coils and up to four independent receiver elements. Emphasis is placed on implementation, characterization, and application of robust imaging sequences at this challenging field strength. Two sequences are implemented and used: fast spin echo (FSE), a routine clinical imaging sequence that is crippled at high field due to unsafe energy deposition, and multiecho gradient echo (GRE), a less conventional — but extremely useful — pulse sequence. The utility of these sequences is demonstrated for studying abnormalities in the brains of MS patients.

This thesis is compiled in a "mixed" format, a concatenation of published and unpublished research articles bound by introduction and conclusion chapters to provide a sense of coherence. This introductory chapter explains key concepts and motivates the research contained in this thesis; the introductory chapter concludes by clearly defining the objectives of this thesis. Chapter 2 describes qualitative FSE imaging of the human brain with low and variable refocusing angles. Also presented are novel methods for rapidly and efficiently modulating these refocusing angles. Chapter 3 describes an advanced processing method for mapping transverse relaxation times at high field. Chapter 4 digresses from spin echo methods and presents a processing pipeline for extracting multiple datasets from multiecho GRE images. The techniques developed in this thesis are applied to quantification of MRI parameters in sub-cortical gray matter in a cohort of relapsing remitting MS patients. This work is presented in Chapter 5. It is followed by brief concluding remarks in Chapter 6, then, in Appendix A, by descriptions of the new imaging capabilities of the 4.7 T spectrometer as a result of this work. This thesis wraps up with a lighthearted craft section in Appendix B.

1.2 Nuclear Magnetic Resonance

Nuclear magnetic resonance (NMR) involves the manipulation, and subsequent detection, of nuclear spin states via electromagnetic interaction. Information regarding the magnetic environments of an ensemble of nuclei is obtainable, ultimately exposing molecular structures, chemical reaction pathways, and diffusion rates. In this section, the fundamental principles of nuclear magnetic resonance are presented. Only concepts crucial for comprehension of subsequent topics are presented.

1.2.1 Nuclear Spin

The proton, a constituent of all atomic nuclei and the sole hydrogen nucleon, is a spin 1/2 particle and possesses a nuclear magnetic dipole moment. When placed in a magnetic field[1], $\vec{B} = [0\ 0\ B_0]^T$, its dipole moment possesses two discrete projection states along the $\hat{z}$ axis. These states correspond to spins aligned with, or against, the magnetic field; spins in these states differ in energy by

$$E = \gamma \hbar B_0, \tag{1.1}$$

where $\hbar$ is the reduced Plank's constant and $\gamma/2\pi = 42.576$ MHz/T is the proton's gyromagnetic ratio. State transitions are mediated by emission or absorption of a photon with energy proportional to its angular frequency, ω:

$$E = \hbar \omega. \tag{1.2}$$

The photon's energy is, by necessity, equivalent to the energy gap between states, Eq. 1.1, yielding a linear relationship between angular frequency (or conventional frequency, f_0), and applied magnetic field,

$$\omega_0 = \gamma B_0 \tag{1.3a}$$

$$f_0 = \frac{\gamma}{2\pi} B_0. \tag{1.3b}$$

Electromagnetic fields at this frequency, termed the Larmor frequency, are employed in NMR to probe the magnetic environment of the nucleus. This is arguably the most important — yet splendidly compact! — equation of NMR: every nuclear magnetic resonance experiment, including imaging, is derived from this relationship. It would not be altogether fallacious to immediately conclude this thesis with a brief remark that all methodological advancements are tractable extensions of this equation. End of story. Let's go pop a bottle of Dom.

1.2.2 Magnetization

The volume average of a statistical ensemble of spins behaves as a classical magnetization vector, $\vec{M} = [M_x\ M_y\ M_z]^T$. It is energetically favourable (by an amount $\gamma \hbar B_0$) for spins to align with $\vec{B}$. At thermal equilibrium, the Boltzmann distribution dictates a small net spin excess exists collinear with the field; the equilibrium magnetization is approximated[2] by [1]

$$\vec{M} = M_0 \hat{z} = \frac{\rho_0 \gamma^2 \hbar^2}{4 k_B T} B_0 \hat{z}, \tag{1.4}$$

---

[1] We define a right-handed Cartesian coordinate system $\hat{C} = [\hat{x}\ \hat{y}\ \hat{z}]^T$ based on the application of this external field.

[2] This formulation applies to spin 1/2 systems and is a linearization for small B_0. It applies to all plausible NMR field strengths.

where k_B is Boltzmann's constant, T is temperature, and ρ_0 is the volume density of spins.

1.2.3 Equations of Motion

Equation 1.4 describes a time-independent equilibrium magnetization oriented parallel to the applied magnetic field. If perturbed, magnetization evolves in a magnificent and graceful manner.

Using the concepts that (1) a magnetic moment in a magnetic field experiences a torque, (2) torque is the temporal derivative of angular momentum, and (3) in a quantum spin system the magnetic moment is proportional to the angular momentum, we conjure an idealistic equation of motion [2] as

$$\dot{\vec{M}} = \gamma \vec{M} \times \vec{B}. \tag{1.5}$$

In a temporally (and spatially) uniform magnetic field (i.e., $\vec{B}(t) = [0\ 0\ B_0]^T$), this coupled differential equation has a simple solution:

$$\vec{M}_\perp(t) = \vec{M}_\perp(0) e^{-i\gamma B_0 t} \tag{1.6a}$$

$$\vec{M}_\|(t) = \vec{M}_\|(0). \tag{1.6b}$$

which describes perpetual clockwise rotation of transverse magnetization ($\vec{M}_\perp \equiv M_x + iM_y$) and constant longitudinal magnetization ($\vec{M}_\| \equiv M_z$). The precessional frequency of the transverse magnetization, $\omega_0 = \gamma B_0$, comfortingly, matches the frequency of the photon coupling the two spin states, Eq. 1.3.

A spin system in thermal equilibrium has no net transverse magnetization and an exceptionally uneventful time course. The perturbation necessary to initialize transverse magnetization, and induce precession, can be achieved by *very* rapidly rotating the main magnet (or the ill-informed subject) about a vector in the $\hat{x}/\hat{y}$ plane. The same result can be achieved (safely) with an additional time varying magnetic field. This resonant field rotates at the Larmor frequency in the transverse plane and possesses a time varying amplitude $B_1(t)$ such that the net magnetic field is given by [1]

$$\vec{B}(t) = \Big[B_1(t)\cos(\gamma B_0 t) \quad -B_1(t)\sin(\gamma B_0 t) \quad B_0 \Big]^T. \tag{1.7}$$

Experimentally, this field can be generated with a radiofrequency (RF) coil — an electronic resonator — tuned to the Larmor frequency. Following coordinate transformation into a rotating frame of reference[3] to mathematically conceal baseline

---

[3] We define $\hat{C}' = [\hat{x}'\ \hat{y}'\ \hat{z}']^T$ where $\hat{x}' = \hat{x}\cos(\gamma B_0 t) - \hat{y}\sin(\gamma B_0 t)$, $\hat{y}' = \hat{x}\sin(\omega t) + \hat{y}\cos(\omega t)$, and $\hat{z}' = \hat{z}$.

Larmor precession, we obtain an effective magnetic field

$$\vec{B}_{eff}(t) = B_1(t)\hat{x}'. \tag{1.8}$$

The solution to Eq 1.5, with $\vec{B} = \vec{B}_{eff}$, is analogous to Eq 1.6, but with magnetization precessing about $\hat{x}'$. For an RF pulse of finite duration τ_α, the effective field will sweep the magnetization by an angle α about $\hat{x}'$ given by:

$$\alpha = \gamma \int_0^{\tau_\alpha} B_1(t)\, dt. \tag{1.9}$$

Amplitudes and durations of these resonant RF pulses can be adjusted for specific tip angles in order to excite, or further manipulate, the equilibrium magnetization.

The idealistic equation of motion, Eq 1.5, is accurate only for impossibly isolated, non-interacting spin systems, and lacks the capacity to equilibrate. Real systems display damping of the transverse magnetization and (re-)polarization of the longitudinal magnetization. This behaviour is phenomenologically incorporated into Eq. 1.5, forming the famous — at least to me — Bloch equation [2]:

$$\dot{\vec{M}} = \gamma \vec{M} \times \vec{B} + \frac{(M_0 - \vec{M}_{\|})\hat{z}}{T_1} - \frac{\vec{M}_\perp}{T_2}. \tag{1.10}$$

In this formulation, T_1 and T_2 are time constants governing the return to equilibrium ($\vec{M}_{\|} \to M_0\hat{z}$; $\vec{M}_\perp \to 0$). The solution to this equation in a uniform magnetic field (again, $\vec{B}(t) = [0\ 0\ B_0]^T$) describes transverse precession with an exponentially decaying amplitude envelope and simultaneous regrowth of the longitudinal component:

$$\vec{M}_\perp(t) = \vec{M}_\perp(0) e^{-i\omega_0 t} e^{-t/T_2} \tag{1.11a}$$

$$\vec{M}_{\|}(t) = M_0(1 - e^{-t/T_1}) + \vec{M}_{\|}(0) e^{-t/T_1}. \tag{1.11b}$$

Examples of this evolution are shown in Fig 1.1.

Signal excitation and magnetization evolution, including precession and relaxation, can be described compactly[4] with matrices. Basic RF rotation of $\vec{M} = [M_{x'}\ M_{y'}\ M_{z'}]^T$ about x' by an angle α is approximated by the nutation operator

$$\mathbf{R}(\alpha) = \begin{bmatrix} 1 & 0 & 0 \\ 0 & \cos(\alpha) & \sin(\alpha) \\ 0 & -\sin(\alpha) & \cos(\alpha) \end{bmatrix}. \tag{1.12}$$

---

[4] This notation is, ironically, far more cumbersome than Eqs 1.9 and 1.11. The benefits are evident when one actually attempts to compute the magnetization following multiple RF pulses and free precession periods, as in section 1.3.5.

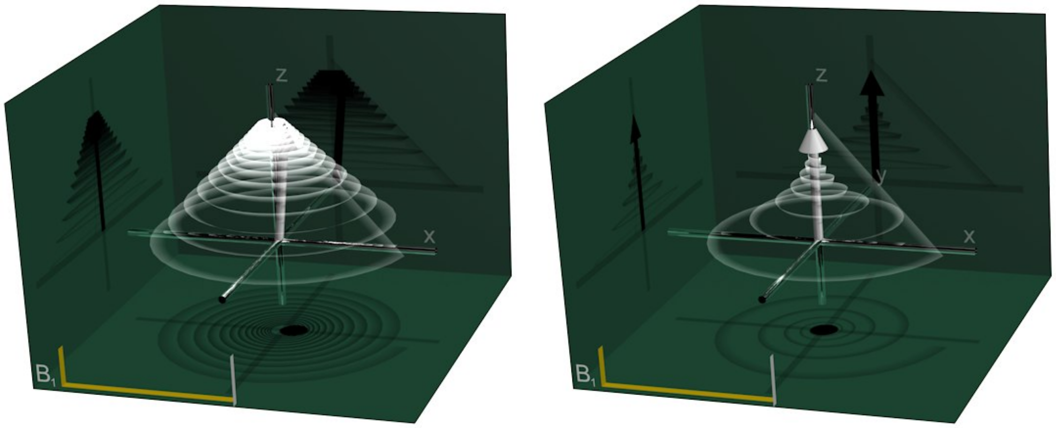

Figure 1.1: Magnetization evolution, from two spin populations in the lab frame, following 90° excitations from equilibrium. (a) $T_2 = T_1$; (b) $T_2 = T_1/3$. Magnetization precesses about the $\hat{z}$ axis while equilibrating in the transverse and longitudinal planes.

An optional phase angle (ϕ_α), permitting pulses about any vector in the x'/y' plane, can be incorporated by sandwiching the nutation operator between forward and reverse phase rotations, yielding the generalized RF operator

$$\mathbf{R}(\alpha, \phi_\alpha) = \begin{bmatrix} \cos(\phi_\alpha) & -\sin(\phi_\alpha) & 0 \\ \sin(\phi_\alpha) & \cos(\phi_\alpha) & 0 \\ 0 & 0 & 1 \end{bmatrix} \mathbf{R}(\alpha) \begin{bmatrix} \cos(\phi_\alpha) & \sin(\phi_\alpha) & 0 \\ -\sin(\phi_\alpha) & \cos(\phi_\alpha) & 0 \\ 0 & 0 & 1 \end{bmatrix}. \tag{1.13}$$

Precessional evolution of spins whose local frequency differs from the Larmor frequency by $\Delta\omega$ is procured with the precession operator

$$\mathbf{S}(t, \Delta\omega) = \begin{bmatrix} \cos(\Delta\omega\, t) & \sin(\Delta\omega\, t) & 0 \\ -\sin(\Delta\omega\, t) & \cos(\Delta\omega\, t) & 0 \\ 0 & 0 & 1 \end{bmatrix}. \tag{1.14}$$

Relaxation can be expressed independently and is excluded from the precession operator. Separation simplifies spin analysis when either relaxation or precession may be ignored. This simplification is due to the irksome re-polarization term, which irritatingly dangles from the otherwise aesthetic, and computationally straightforward, diagonal relaxation operator. The complete relaxation operator is given by

$$\mathbf{T}(t, T_{1,2}) = \begin{bmatrix} e^{-t/T_2} & 0 & 0 \\ 0 & e^{-t/T_2} & 0 \\ 0 & 0 & e^{-t/T_1} \end{bmatrix} + \begin{bmatrix} 0 \\ 0 \\ M_0(1 - e^{-t/T_1}) \end{bmatrix}. \tag{1.15}$$

With these operators, magnetization behaviour during an arbitrary sequence of RF pulses and precession/relaxation intervals can now be described, and readily computed, with an unpronounceable string of boldfaced consonants. Example: $\vec{M}(t) = \mathbf{TSR}\vec{M}(0)$ (answer: excitation and free precession). This convenience is well worth the hassle. Maybe.

Following excitation from equilibrium, inductive detection of transverse precession permits measurements of relaxation times, proton density, and precessional frequency. Measurement of this signal is the foundation of both NMR and MRI.

1.2.4 Relaxation Mechanisms

The approach to equilibrium occurs via two simultaneous processes: polarization of longitudinal magnetization and decoherence of transverse spins. Longitudinal relaxation is an energetic process involving a transition between spin states. Transitions are not spontaneous and must be stimulated by a field perturbation at the Larmor frequency. Transverse relaxation is an energetically neutral process resulting from magnetic field fluctuations at the nucleus.

Relaxation in Homogenous Materials

Nuclear dipoles are a source of field inhomogeneity and interact with precessing spins. In diffusing spins systems (such as liquids), the local magnetic field experienced by each proton is given by $B_0+b_j(t)$, where $b_j(t)$ is the local field perturbation of the j^{th} spin as a function of time. Evolution of the net transverse magnetization, Eq 1.11a, is more accurately described as [3]

$$\vec{M}_\perp(t) = \vec{M}_\perp(0)\, e^{-i\omega_0 t} \left\{ \frac{1}{N} \sum_{j=1}^{N} e^{-i\gamma \int_0^t b_j(t')} dt' \right\}. \tag{1.16}$$

The term in braces models the phase dispersal of individual spins during their journey through spatially and/or temporally heterogeneous magnetic fields. This represents the signal decay envelope. Curiously, the time evolution of $b_j(t)$ serves to dilute the phase dispersion and preserve the signal — a process termed motional narrowing.

Evaluating Eq 1.16 is rather impractical since the exact magnetic field history of each spin is unknown. A statistical approach models the decay envelope based on the autocorrelation of the magnetic field fluctuations, defined as

$$R(\tau) = \gamma^2 \left\langle b(\tau) b(0) \right\rangle, \tag{1.17}$$

where the triangular brackets represent the ensemble average over all spins. It describes the probability that the magnetic field at a time τ is related to its initial value. A possible field fluctuation and average autocorrelation function are plotted in Fig 1.2.

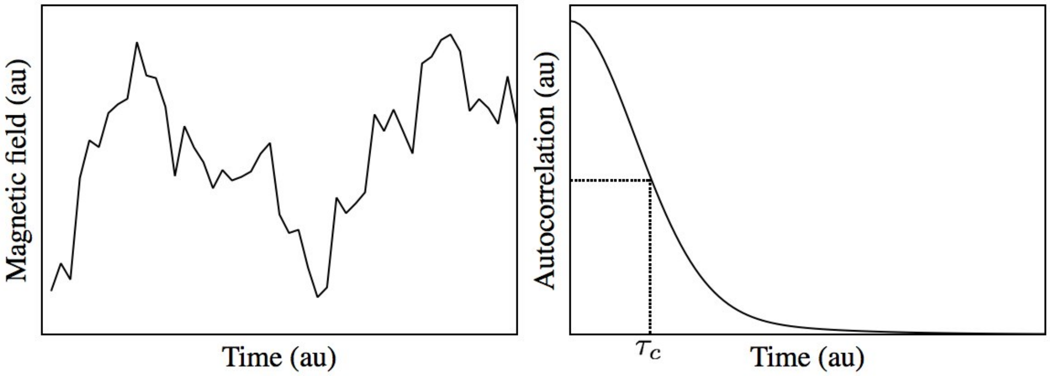

Figure 1.2: Possible magnetic field fluctuation and average autocorrelation function.

In NMR samples, the autocorrelation function decreases monotonically; it is characterized by a correlation time (τ_c) describing the duration that the local magnetic field is expected to remain relatively constant. When the correlation time is much shorter than the NMR time scale, which is typical for fluids[5], relaxation is exponential and the inverse transverse relaxation time — termed the transverse relaxation rate (R_2) — is given by [3]

$$\frac{1}{T_2} \equiv R_2 = \int_0^\infty R(\tau)\, d\tau = \gamma^2 \left\langle b^2 \right\rangle \tau_c. \tag{1.18}$$

This formulation neglects longitudinal relaxation, but emphasizes some notable dependencies: stronger, or additional field perturbations — due, for example, to additional paramagnetic ions — will drastically increase the rate of signal decay. Longer correlation times, due in part to coupling and interaction with tissue membranes and macromolecules, also accelerate signal decay.

Longitudinal relaxation requires perturbations at the Larmor frequency to modify the z-component of the magnetization. The longitudinal relaxation rate ($R_1 \equiv 1/T_1$) is proportional to the number of spins experiencing transverse field perturbations at the Larmor frequency relative to the total number of spins. This can be quantified with the spectral density function $J(\omega)$ — conveniently related to the autocorrelation function via Fourier transform. Sample spectral density functions are shown in Fig 1.3 for a hypothetical fluid, semi-solid, and solid. The spectral density function narrows with increasing correlation time, corresponding to higher viscosity liquids or solids. Initially, T_2 decreases (R_1 increases) with correlation time as the spectral density concentrates at ω_0. A T_1 minimum (R_1 maximum) occurs at a correlation time roughly corresponding to those of semi-solids such as fat and

---

[5] The correlation time of water is $\sim 10^{-11}$ s [4]; NMR relevant time scales are typically $>10^{-6}$ s.

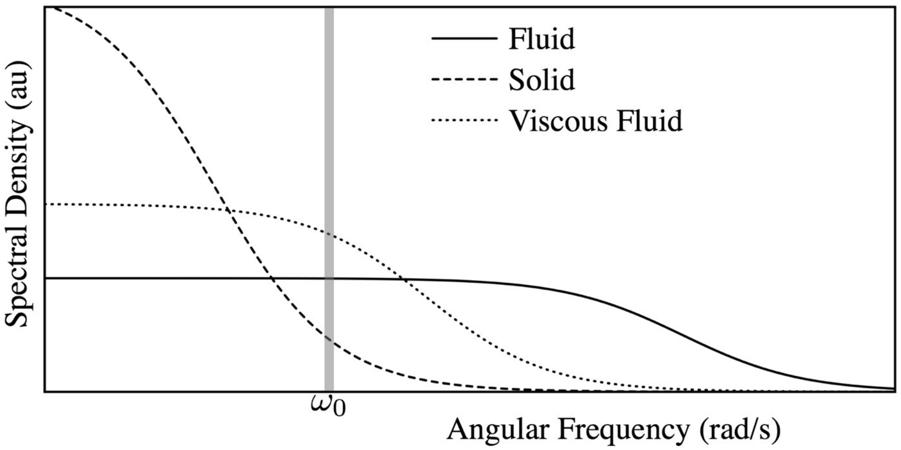

Figure 1.3: Normalized spectral density functions for a hypothetical fluid, solid, and viscous fluid. The longitudinal relaxation rate is proportional to the spectral density at the Larmor frequency.

tissue. Further increases in correlation time yield higher longitudinal relaxation times (smaller R_1) as the spectral density function narrows to exclude the Larmor frequency. This concept is formalized in the Bloembergen-Purcell-Pound (BPP) relaxation theory. Based on the spectral density function, transverse and longitudinal relaxation rates/times in a homogeneous sample are given by [4, 5]:

$$\frac{1}{T_1} \equiv R_1 \propto K \left\{ \frac{\tau_c}{1+\omega_0^2\tau_c^2} + \frac{4\tau_c}{1+4\omega_0^2\tau_c^2} \right\} \tag{1.19a}$$

$$\frac{1}{T_2} \equiv R_2 \propto \frac{K}{2} \left\{ 3\tau_c + \frac{5\tau_c}{1+\omega_0^2\tau_c^2} + \frac{2\tau_c}{1+4\omega_0^2\tau_c^2} \right\}. \tag{1.19b}$$

The constant of proportionality K contains factors related to the dipolar coupling strength. The behaviour of relaxation times is shown in Fig 1.4 at frequencies representing 1.5 T and 4.7 T. This formulation incorporates re-polarization and transverse dephasing, the latter given by Eq 1.18, into the expression for T_2. The BPP theory accurately defines $T_2 \leq T_1$ — even in the absence of dephasing, transverse magnetization decays as spins return to thermal equilibrium.

Relaxation in Heterogenous Materials

Biological tissues contain distinct, but exchanging, water compartments and display more elaborate relaxation than observed in homogeneous materials. The rate of exchange between compartments dictates the observed signal envelope. In compartments that exchange protons much more rapidly than they relax, a single transverse rate and a single longitudinal relaxation rate are observed. The net rate depends on the spin fraction in pools "A" (f_A) and "B" ($f_B = 1 - f_A$) and their respective relaxation rates (R_{2A} and R_{2B}), yielding mono-exponential transverse magnetization

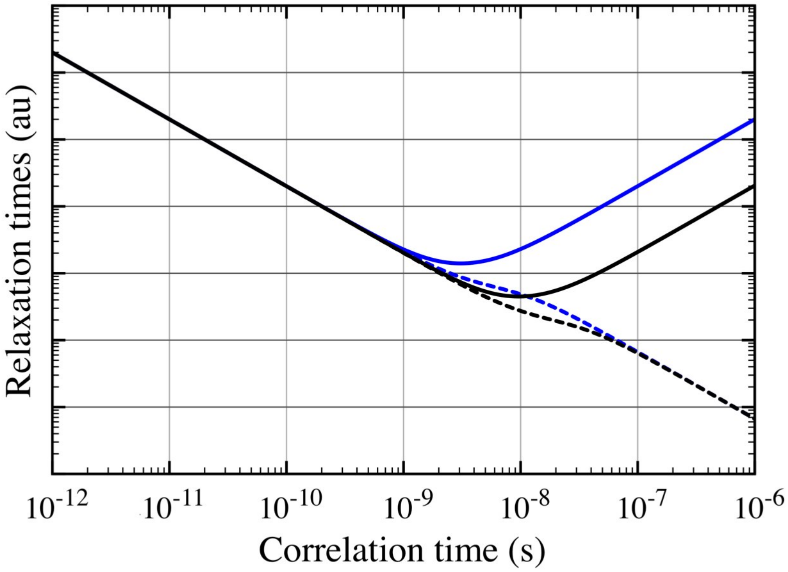

Figure 1.4: Longitudinal (solid lines) and transverse (dashed lines) relaxation times as functions of correlation time. Relaxation times at 64 MHz (black lines) and 200 MHz (blue lines) are presented. Liquids have small correlations times and nearly equivalent relaxation rates, independent of field strength. Solids have long correlation times and a large disparity between longitudinal and transverse relaxation times.

relaxation of the form

$$\vec{M}_\perp(t) = \vec{M}_\perp(0)\, e^{-i\omega_0 t}\, e^{-(f_A R_{2A} + f_B R_{2B})t}. \tag{1.20}$$

A similar expression for longitudinal relaxation can be envisioned.

Slowly exchanging spin pools display distinct relaxation rates and are described by a multi-exponential of the form

$$\vec{M}_\perp(t) = \vec{M}_\perp(0)\, e^{-i\omega_0 t}\, \left(f_A e^{-R_{2A}t} + f_B e^{-R_{2B}t}\right). \tag{1.21}$$

Again, a similar expression can be obtained for longitudinal relaxation.

1.2.5 The Signal Equation

The principle of reciprocity, expressed in NMR-friendly terms as [6]

$$S(t) = \frac{d}{dt}\int_{\vec{r}} \vec{B}_1(\vec{r}) \cdot \vec{M}(\vec{r},t)\, d\vec{r}, \tag{1.22}$$

states that a voltage (i.e., signal), $S(t)$, is induced across a conductor (the tireless RF coil) by a time varying magnetization. This magnetization exists in a volume spanned by $\vec{r}$ and its inductive effect is scaled by a coil sensitivity term, $\vec{B}_1(\vec{r})$.

Optimization of the coil sensitivity, defined as the field produced per unit current, along with appropriate spatial distribution of this sensitivity is a requirement for efficient NMR/MRI and remains an active area of research. This formulation provides insight into the MRI signal, but is a quasi-static approximation; at field strengths above approximately 1.5 T, wave propagation delays skew the $\vec{B}_1$ field. As such the transmit field, $\vec{B}_1^+$, and receive field, $\vec{B}_1^-$, differ and are distinguished from this point forward; in the rotating frame, their vector behaviour is often safely omitted.

Following a 90° excitation from equilibrium[6], magnetization evolves according to Eq 1.11 with initial conditions $\vec{M}_\perp(0) = M_0 y'$ and $\vec{M}_\parallel(0) = 0$. From the three time dependent terms in Eq 1.11, signal is induced predominantly via precession of the transverse magnetization; induction from relaxation terms is negligible since $f_0 \gg 1/T_{1,2}$. For generality, we allow the applied magnetic field to possess spatial and temporal variations superimposed on the strong static component such that precession occurs with instantaneous angular frequency

$$\omega = \omega_0 + \gamma \vec{G}(t) \cdot \vec{r} + \omega_S(\vec{r}). \tag{1.23}$$

In this expansion, $\vec{G}(t) = [G_x(t)\ G_y(t)\ G_z(t)]^T$ represents a linear gradient of the main magnetic field oriented in the $\hat{z}$ direction. Experimentally, orthogonal field gradients can be produced with three gradient coils external to the sample. All sources of time-invariant static field heterogeneities are contained within $\omega_S(\vec{r})$.

Combining Eqs 1.4, 1.11, 1.22, and 1.23, a moderately universal expression for The Signal Equation[7] can be approximated as:

$$S(t) \approx \omega_0\, B_0\, \frac{\gamma^2 \hbar^2}{4 k_B T}\, e^{-i\omega_0 t} \int_{\vec{r}} \rho(\vec{r})\, \vec{B}_1^-(\vec{r})\, e^{-t/T_2(\vec{r})}\, e^{-i\omega_S(\vec{r})t}\, e^{-i\gamma \int_0^t \vec{G}(\tau)\cdot\vec{r}\, d\tau}\, d\vec{r}. \tag{1.24}$$

This describes the NMR signal induced by magnetization with amplitude and frequency proportional to the static field strength. Signal occurs at a carrier frequency ω_0 with additional phase warping from static field heterogeneities and applied field gradients. The signal is vector-summed over a volume bounded by the proton density.

Every NMR/MRI thesis manipulates one, or more, of the terms in The Signal Equation. This thesis concentrates on generating T_2 contrast (the $e^{-t/T_2(\vec{r})}$ term) in human brain (the $\rho(\vec{r})$ term) images (the $e^{-i\gamma \int_0^t \vec{G}(\tau)\cdot\vec{r}\, d\tau}$ term) given a field strength of 4.7 T (the ω_0 and B_0 terms) and a combination of volume resonators and phased array RF coils (the $\vec{B}_1^-(\vec{r})$ term). The magnet room is known to get quite cold at times, arguably flirting with hyperpolarization (the $\gamma^2\hbar^2/(4k_BT)$ term).

---

[6] These conditions are for notational simplicity; a slight loss of generality is incurred.

[7] To be read in a loud and resounding voice for dramatic effect

1.2.6 Radiofrequency Coils

Signal excitation and detection can be performed with any conducting material near the sample. A coat hanger is rumoured to work. In practice, most RF coils are LRC circuits, tuned to resonate at the Larmor frequency (Eq 1.3) via manipulation of their inductance and capacitance.

When operating at or near the Larmor frequency, the current distribution within the coil produces/detects a transverse magnetic field within the sample. Ideal transmit coils have high sensitivity, defined as the field produced per unit current, and they generate this field uniformly across the sample. Conversely, ideal receive coils need not have high sensitivity, but rather possess an optimized spatial sensitivity[8]. An optimal receiver coil is relatively sensitive to the specific region-of-interest yet insensitive to the remainder of the sample. This minimizes thermal noise contributions from tissues outside the region-of-interest.

Imaging can be performed with a single RF coil for both transmit and receive; however, reduced noise power can often be obtained using a phased array for signal reception [8]. Volume resonators, such as the birdcage coil [9], are often ideal for transmission as they generate relatively homogeneous B_1^+ fields. Furthermore, they can operate in quadrature, generating the circularly polarized RF field needed for spin manipulation while requiring half the transmit power and yielding a $\sqrt{2}$ signal-to-noise (SNR) improvement during reception than a linearly polarized coil [10].

The signal-to-noise improvement of array coil reception relative to volume coil reception at 4.7 T is shown in Fig 1.5, along with a photograph of the four element receive only coil (PulseTeq, UK) and example images received with a birdcage volume coil (XLR, Canada) or with the array coil. Note the exceptionally increased sensitivity at the periphery of the brain and global SNR gain with the array coil relative to the volume coil image.

1.3 Magnetic Resonance Imaging

Simply put, MRI involves spatial localization of nuclear spins. The vast majority of imaging detects hydrogen protons due to their biological abundance and high gyromagnetic ratio. In general, imaging begins with signal excitation, is followed by spatial encoding — via manipulation of $e^{-i\gamma\int_0^t \vec{G}(\tau)\cdot\vec{r}\,d\tau}$ in The Signal Equation — and ends with a mathematical transform to isolate the proton density distribution.

This section commences with a description of the Fourier interpretation of The Signal Equation and its relation to imaging. Following this are descriptions of stan-

---

[8] Signal noise is sample dominated when imaging a sample greater than ∼1 ml in volume [7]; as such, electrical efficiency of the coil is largely inconsequential for signal reception in human brain imaging.

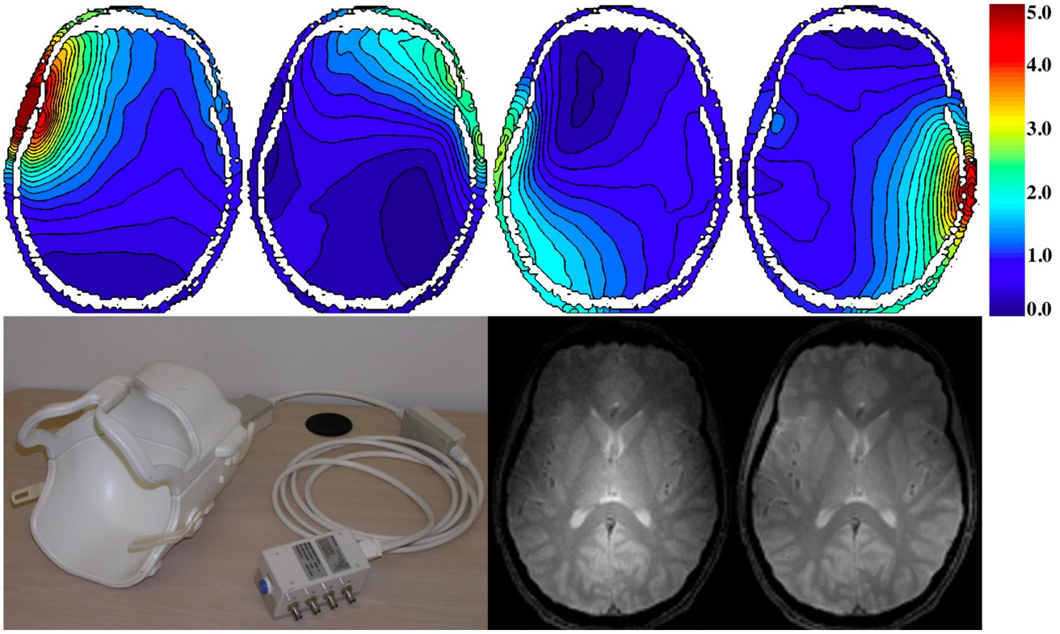

Figure 1.5: Top row: signal-to-noise of each coil in a 4-element receive array (PulseTeq, UK) relative to a birdcage coil (XLR imaging, Canada) at 4.7 T. Bottom row, left to right: a photo of the receive array, a gradient echo image acquired with the volume coil in transmit and receive mode, the same sequence using the array for reception.

dard gradient echo, spin echo, and fast spin echo imaging methods. A description of advanced FSE concepts lingers afterward. This section concludes with an overview of high field MRI.

1.3.1 The Fourier Interpretation

The Fourier transform of an arbitrary function $\psi(\vec{r})$ is defined as

$$\Psi(\vec{k}) = \int_{-\infty}^{+\infty} \psi(\vec{r})\, e^{-i2\pi\vec{k}\cdot\vec{r}}\, d\vec{r}, \tag{1.25}$$

where $\vec{k}$ has units of spatial-frequency, typically inverse-cm[9]. This transform has a striking resemblance to The Signal Equation, Eq. 1.24; comparison suggests that *the time-domain signal is the Fourier transform of a term related to the distribution of transverse magnetization. This composite term represents the desired MR image.* The image is obtained mathematically via *inverse* Fourier transform. The image intensity (and phase) at location $\vec{r}$ is related to the time domain signal, given by

---

[9] It was recently proposed this unit be termed a “Stobbe” following dismay (by the aforementioned individual) at the lack of respect this unit receives compared to its temporal brethren, the hertz.

Eq 1.24, according to

$$\psi(\vec{r}) = \int_{-\infty}^{+\infty} S(t)\, e^{i2\pi\vec{k}\cdot\vec{r}}\, d\vec{k}, \tag{1.26}$$

where

$$\vec{k}(t) = \frac{\gamma}{2\pi} \int_0^t \vec{G}(\tau)\, d\tau. \tag{1.27}$$

Image encoding can be performed in any, or all, directions; however, adequate spatial-frequency, or k-space, sampling is required (in each encoded direction) to solve this integral — or approximate it with reasonable certainty. This is achieved via systematic application of gradient pulses to traverse k-space — a process often requiring multiple spin excitations to refresh the transverse magnetization. Standard 2D Fourier transform imaging excites spins within a single slice and acquires the $k_{x,y}$ plane in a raster of readout lines as shown in Fig 1.6. Data is collected during the readout window and the waveforms are repeated, with a unique phase encode area, every repetition time (TR) to adequately sample k-space. After *all* data is collected, image formation occurs via 2D inverse Fourier transform.

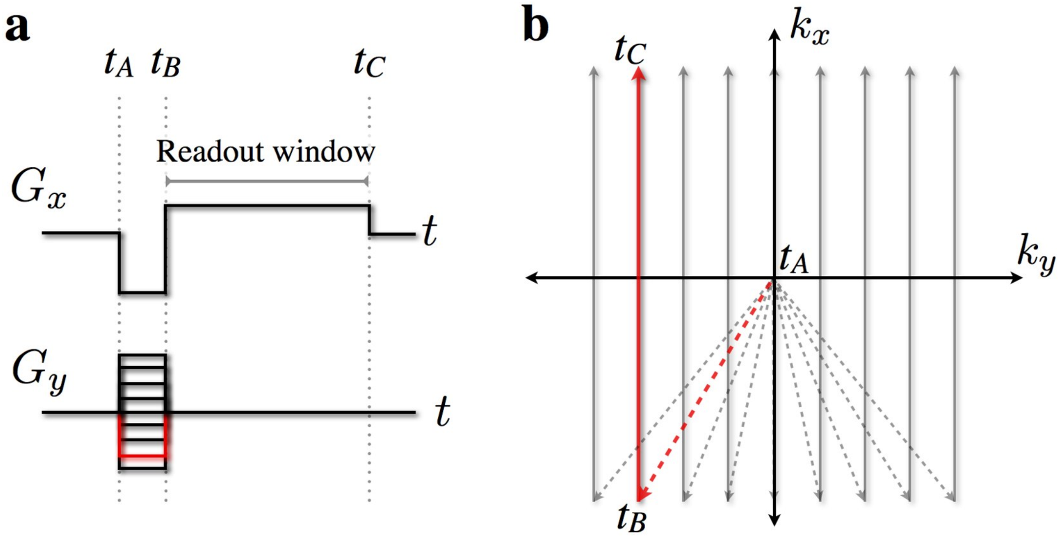

Figure 1.6: (a) Readout (x direction) and phase encode (y direction) gradient waveforms for spatial encoding in multishot 2D Fourier transform imaging. (b) The resulting k-space trajectories; data is acquired on a Cartesian grid along the solid vertical arrows.

Discrete sampling is required as it is impractical to fully sample a continuous function spanning an infinite domain. The k-space sampling intervals, $\Delta k_{x,y,z}$, are related to the image-space field-of-views, $\mathrm{FOV}_{x,y,z}$, according to

$$\mathrm{FOV}_{x,y,z} = \frac{1}{\Delta k_{x,y,z}}. \tag{1.28}$$

The field-of-view in each direction must be equal to, or larger, than the sample, in that direction, to avoid image aliasing. The maximum k-space coverage is given by $k_{x,y,z}^{max}$ and defines the voxel dimension in the respective direction. The spatial resolutions, $\Delta x, y, z$, are given by

$$\Delta x, y, z = \frac{1}{2k_{x,y,z}^{max}}. \tag{1.29}$$

The field-of-views, and resolutions, need not be equal and total acquisition time is typically the product of the number of in-plane phase encode lines (N_{PE}), the number of through-plane phase encode lines (N_{PE2}), and TR. The discrete sampling relations are summarized in Fig 1.7. Essentially, detecting small features requires collection of high spatial frequencies; imaging large objects necessitates dense sampling.

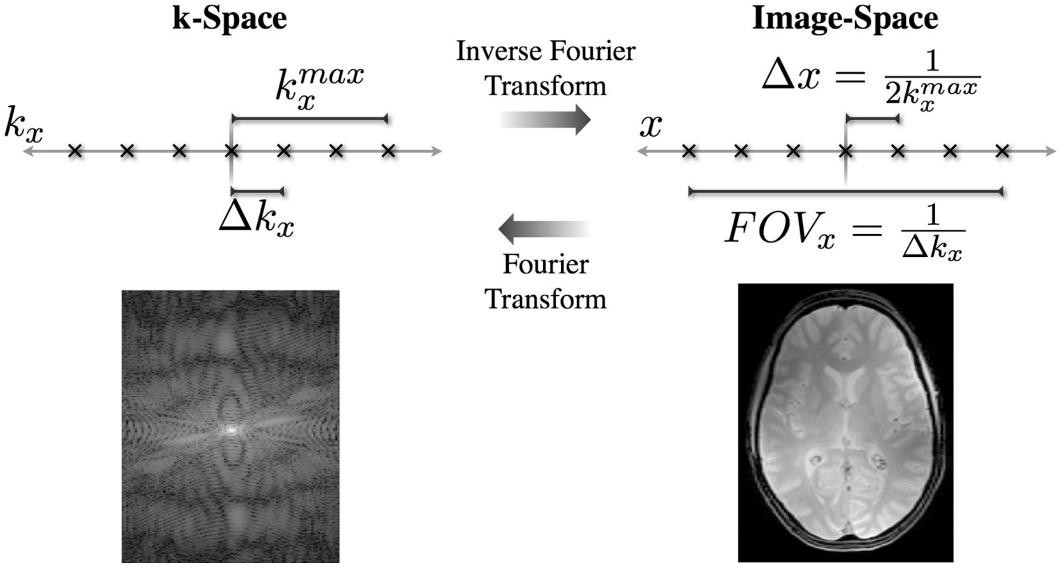

Figure 1.7: Top: overview of discrete sampling parameters and their interrelation for 1D Fourier imaging (in the x direction). Bottom: extension to multiple dimensions, such as a 2D image, is straightforward.

Fourier imaging divides the object into discrete voxels of volume $V_{vox} = \Delta x \cdot \Delta y \cdot \Delta z$. Three-dimensional imaging excites the full sample, or a large slab, and Fourier encodes all three directions, generating a volumetric representation of the object. Two-dimensional imaging employs slice selective excitation to tip magnetization from a thin slice of the sample, effectively reducing the dimensionality of the problem, and gradient encodes the remaining two in-plane directions. A stack of slices can be acquired, together forming a digital representation of the object. Simple two- and three-dimensional sequences are shown schematically in Fig 1.8.

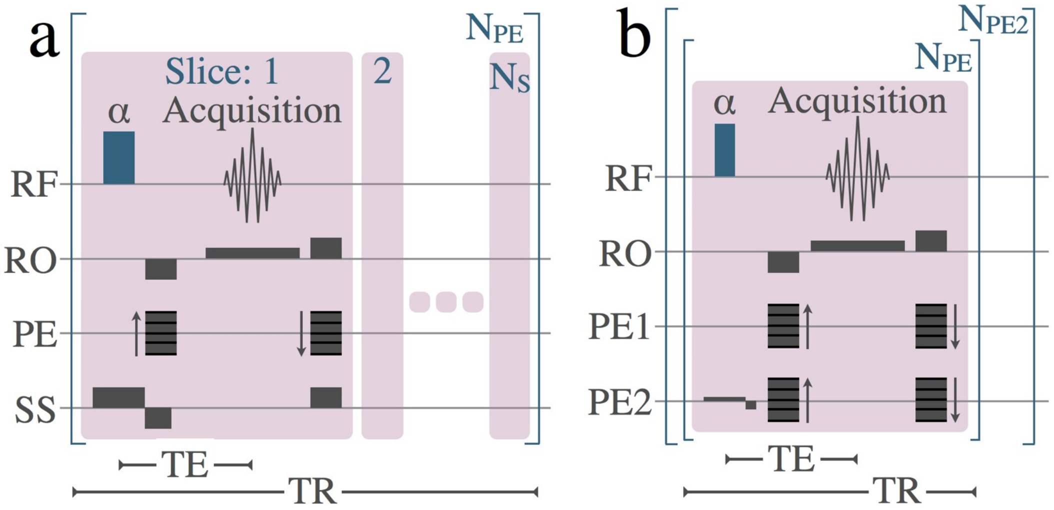

Figure 1.8: Pulse sequence diagrams for (a) multislice 2D gradient echo and (b) slab-selective 3D gradient echo. The 2D multislice sequence acquires one k-space line in each of N_S slices and loops through N_{PE} phase encode steps to acquire the full data set. The 3D approach contains two nested loops totalling $N_{PE} \times N_{PE2}$ phase encode steps.

1.3.2 Image Reconstruction

As described in Sec 1.3.1, MRI data is typically acquired in the spatial frequency domain and converted into an image via inverse Fourier transform. In practice, few situations are this simple. Optimal image reconstruction is a computational pipeline involving data manipulation and artifact suppression. Common additions to this pipeline include DC artifact suppression (to remove a central spike in image space), undersampled data reconstruction, image combination from multiple receiver coils, noise filtering, and sometimes image intensity normalization. While DC artifact suppression is trivial (subtract DC values from k-space prior to transform) and linear filters for noise reduction are well characterized, other routines are less straightforward and less universally accepted.

Images presented in this thesis were often acquired with multiple receiver coils, whose individual images must be combined. Optimal array coil image combination weights the signal from each receiver coil based on its complex-valued local sensitivity, then adds all receiver signals to form a single image. Typically, the coil sensitivities are not known. A heuristic sum-of-squares approach [8] can be employed without requiring the coil sensitivities, but exacerbates intensity bias from the coil sensitivities. Furthermore, the sum-of-squares operates on magnitude images, which rectifies the original bivariate, zero-mean Gaussian noise into a noncentral chi distribution[10] where noise is offset at low SNR values [11, 12]. Images in this thesis were

---

[10] A Rician noise distribution is observed in magnitude images from a single receiver coil

combined by estimating complex coil sensitivities from low-pass filtered versions of the image data. This generates phase-corrected images with reduced intensity bias and noise rectification [13]. Improved images are likely possible by incorporating noise covariance between receiver elements; however this has not been performed in this work.

Undersampling or acceleration schemes, which collect a subset of k-space data and rely on some form of redundancy to reconstruct an image, have become commonplace in imaging studies. Partial Fourier exploits Hermitian symmetry in k-space, but requires either zero-filling or homodyne detection [14] to reconstruct an image. Acceleration factors approaching 2× are possible in high resolution spin echo imaging. Data in parts of this thesis were collected with partial Fourier in the phase encode direction for undersampling.

There are several other undersampling methods available. Parallel imaging omits periodic phase encode lines and uses redundancy in multiple receiver coils to reconstruct images. In this case, the discrete sampling criteria (Eq 1.28) is violated, producing strong coherent aliasing artifacts. Spatial unwrapping [15] or k-space data synthesis [16, 17] can regenerate the full field-of-view. Accelerations equal to the number of receiver coils are mathematically possible; however, spatially dependent noise amplification in typical coil geometries limits acceleration to approximately 2–3× in each phase encoded direction. The self-nulling properties of incoherent aliasing artifacts is used in undersampling schemes that collect pseudo-random phase encode lines. Compressed sensing [18], a constrained reconstruction algorithm, exploits image sparsity in some mathematical domain to guide reconstruction of randomly undersampled data. Although drastic accelerations are theoretically possible — limited only by imposed data sparsity — undersampling factors of 1.5–3× per phase encoded direction are currently reported. Although not employed in this thesis, undersampling has become extremely common and hold enormous promise for neurological imaging at high field strengths.

These reconstruction methods are largely independent of data acquisition strategy. There are numerous variations in sequence layout and timing, each impacting image appearance. Acquisition schemes can be classified into two general, albeit somewhat overlapping, categories: gradient echo sequences and spin echo sequences.

1.3.3 Gradient Echo Imaging

Gradient echo sequences are, in some respects, the simpler sequence grouping: at a minimum, they involve signal excitation, encoding, and acquisition. They are available in 2D and 3D variants and can produce a wide range of image contrasts. Despite structural simplicity, magnetization behaviour can be exceptionally intricate.

Basic GRE pulse sequence diagrams are shown in Fig 1.8. The multislice 2D sequence applies a slice selective excitation pulse followed by the 2D cartesian readout module (shown in Fig 1.6). After signal readout, transverse magnetization is spoiled, via gradient lobes and possibly RF phase increments [19], to isolate new signal excitations from lingering transverse magnetization. The phase encode module is unwound to provide constant inter-shot spoiling. An echo is formed at the center of the readout gradient, at which time $k_x = 0$. The three-dimensional variant excites a slab of tissue and incorporates a second phase encode block to encode the slice direction.

The spin evolution (from gradient lobes only) of a simple GRE sequence, like those shown above, is presented in Fig 1.9. Spin behaviour can be accurately, and conveniently, summarized in a phase plot. As shown in Fig 1.10, RF and gradient waveforms (top plot) excite spins and induce spatial dephasing (middle plot) respectively. Phase coherence is recovered at the center of the acquisition window and an echo is observed (bottom plot). Only gradient induced dephasing is recuperated; phase dispersals from static field shifts are not rephased.

A single magnetization isochromat[11] at an arbitrary time τ following an α (typically $\leq 90^\circ$) excitation can be described in matrix format as

$$\vec{M}(\tau) = \mathbf{T}(\tau)\ \mathbf{S}(\tau)\ \mathbf{R}(\alpha)\ \vec{M}(0). \tag{1.30}$$

In this formulation, $\vec{M}(0)$ is the magnetization vector immediately prior to excitation; in the steady-state, it can be determined by noting that $\vec{M}(TR) = \vec{M}(0)$. Fundamentally, depletion of longitudinal magnetization with each RF pulse is balanced by T_1 recovery during the repetition time (obeys Eq 1.11) while decaying and spoiled transverse magnetization is replenished during excitation. Expanding Eq 1.30 for all relevant magnetization vectors, the steady-state signal at the echo time (TE) of a spoiled sequence is approximated as

$$S_{GE}(\vec{r}) \approx C\rho(\vec{r})\ \frac{[1 - e^{-TR/T_1(\vec{r})}]\sin(\alpha)}{1 - e^{-TR/T_1(\vec{r})}\cos(\alpha)}\ e^{-TE/T_2^\star(\vec{r})}. \tag{1.31}$$

The constant C contains scaling factors such as the coil sensitivity and all spatially invariant constants, from Eq 1.24. The observed transverse decay is often exponential(-ish); it is characterized with a relaxation time $T_2^\star$. This relaxation can be decomposed into intrinsic T_2 decay and static-field induced phase dispersion:

$$T_2^\star = \left[\frac{1}{T_2} + \frac{1}{T_2'}\right]^{-1}, \tag{1.32}$$

---

[11] An isochromat is a physical construct bridging the gap between classical and quantum spin behaviour. It represents a ensemble of spins of sufficient quantity to be described classically, yet compact enough to behave as a single coherent unit.

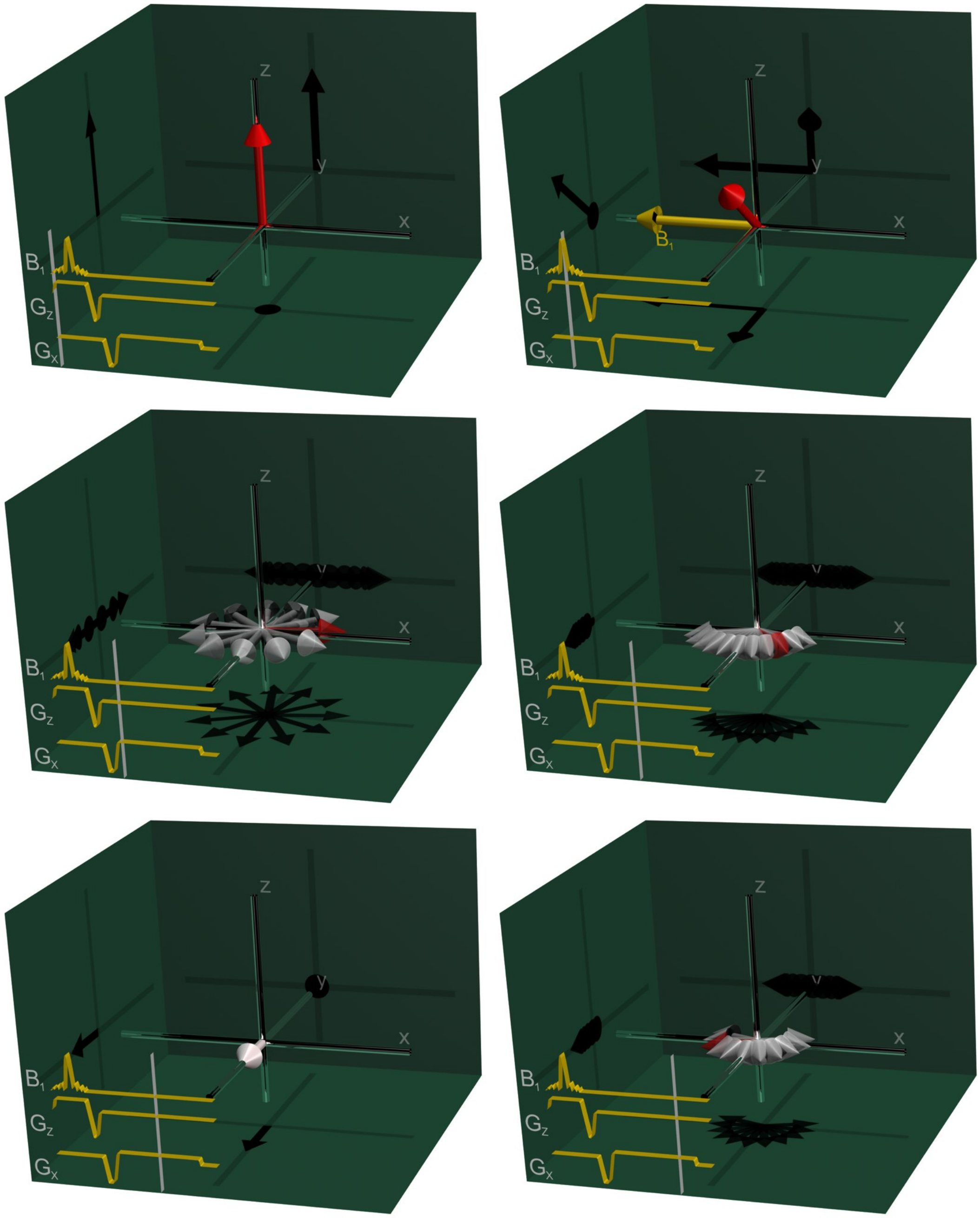

Figure 1.9: Magnetization evolution during a gradient echo sequence. Individual vectors represent magnetization isochromats evenly distributed along the readout (x') axis. From upper left, to lower right: longitudinal magnetization is excited by a slice selective pulse, is dephased by the readout pre-phasing lobe, rephases during the first half of the readout to form a coherent gradient recalled echo midway through the acquisition, and continues dephasing during the remainder of the readout lobe. Individual isochromats shrink due to T_2 decay.

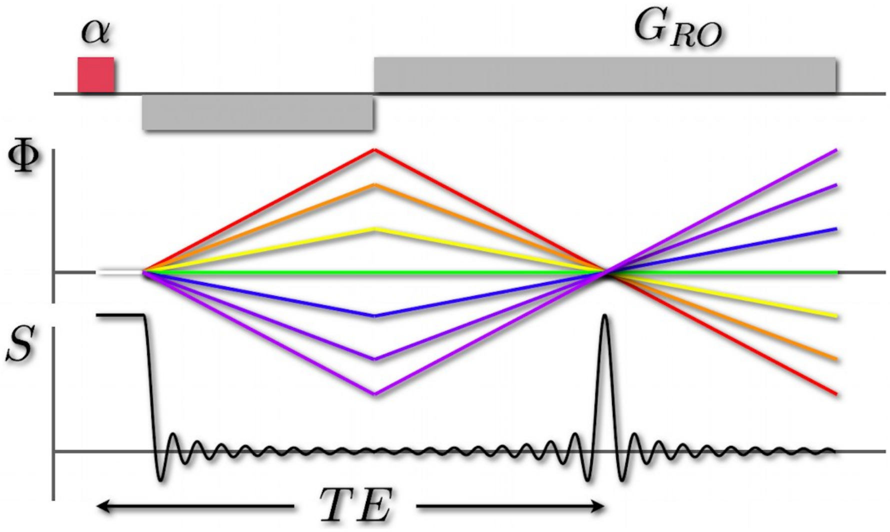

Figure 1.10: Gradient echo phase plot in the absence of static field heterogeneities and intrinsic T_2 decay. The top trace depicts RF (red) and readout gradient (gray) waveforms for a gradient echo acquisition. The center plot illustrates phase evolution of transverse magnetization during the sequence. Each line represents a unique spatial location along the readout direction. The bottom plot represents the signal amplitude, formed as the vector sum the phase plot.

where T_2' contains all intra-voxel static dephasing contributions — derived from $e^{-i\omega_S(\vec{r})t}$ integrated over the voxel. This decay is not guaranteed to be exponential [20], it's just a good approximation in most situations.

Example GRE images at 4.7 T are shown in Fig 1.11. Images are acquired with a resolution of $1 \times 1 \times 2$ mm^3 using a 3D multiecho pulse sequence. Ten echoes were collected per excitation pulse; images from the first and seventh echoes are shown.

Following excitation, spins accrue phase from off-resonant sources. These include local field shifts from susceptibility differences between tissues (a quantity of interest), non-local field shifts projecting from air/tissue interfaces (boring), and from residual encoding gradients at the echo time (bad). All of these field shifts produce phase in the complex valued image; it is often discarded when viewing magnitude images. Susceptibility weighted imaging (SWI) [21] isolates the local susceptibility field shifts to enhance or complement magnitude images. Phase images (Φ) are processed by filtering the complex 2D or 3D image, then extracting the phase. This order of operations is crucial to reduce phase wrap. High-pass filtering attenuates slowly varying phase drifts (attributed to air/tissue interfaces and residual encoding gradients) and can be performed directly on the k-space data (H) with a low-pass k-space filter (F_{LP}):

$$\Phi = \arg\left\{\frac{\mathrm{FT}^{-1}[H]}{\mathrm{FT}^{-1}[F_{LP} \times H]}\right\}. \tag{1.33}$$

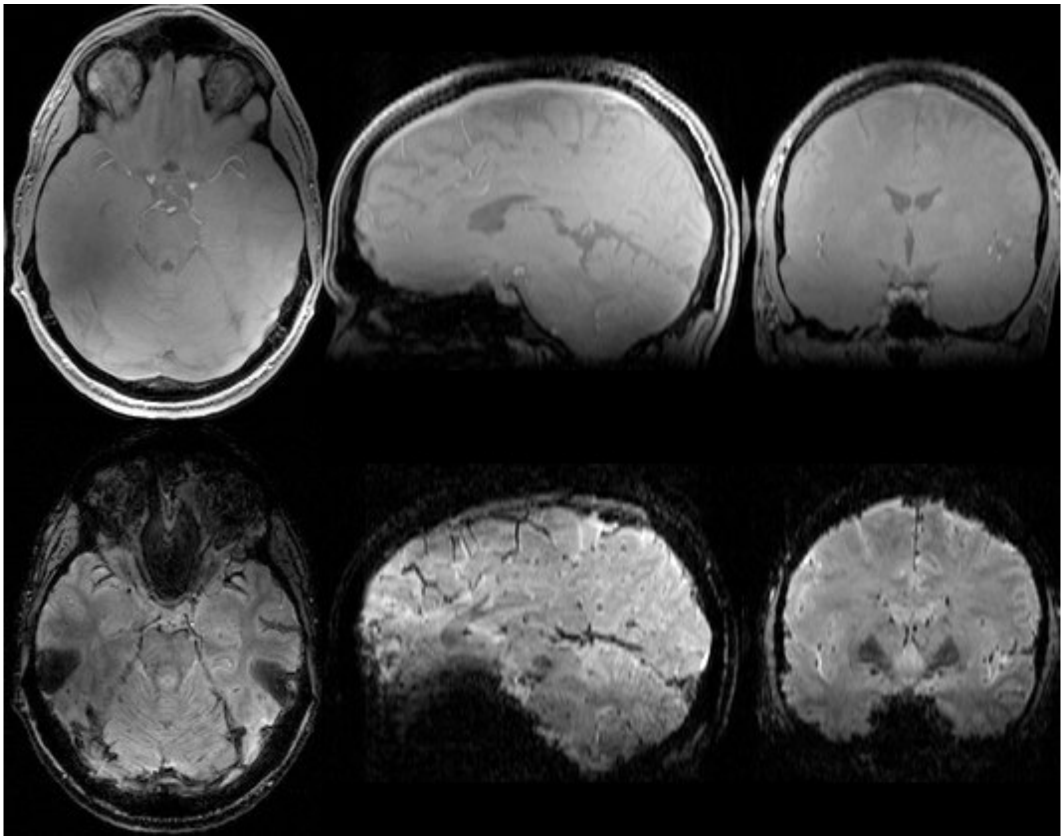

Figure 1.11: Three-dimensional gradient echo images acquired at 4.7 T with $TR = 44$ ms and $\alpha = 10^\circ$. Top row, left to right: axial, sagittal, and coronal orientations of the same $1.0 \times 1.0 \times 2.0$ mm^3 data set at $TE = 3.2$ ms. Bottom row: the same slices at $TE = 33$ ms. Stronger $T_2^\star$ weighting is obtained at longer echo times at the expense of severe signal loss around air/tissue interfaces.

In the above equation, "FT^{-1}" represents the inverse Fourier transform (in 2D or 3D, as necessary) and "arg" is the phase extraction operator (and the sound made by any reader who has made it this far). Traditional SWI images meld the magnitude image with a processed version of the phase (masked and scaled to enhance negative phase shifts) [21]. The SWI processing pipeline is summarized in Fig 1.12.

While bulk phase shifts can be exploited for contrast, intra-voxel phase dispersal reduces image intensity and is a source of serious artifact. Regions with steep field gradients — often bordering air tissue interfaces — display very short $T_2^\star$ times. These artifacts are prominent in the Fig 1.11 image set and degrade their diagnostic value. This susceptibility artifact is exacerbated at high field strength, scales with voxel dimension, and worsens with echo time. Although still useful in clinical and research environments, particularly for high resolution imaging with short echo times, sequences with minimal sensitivity to static field heterogeneities are extremely desirable.

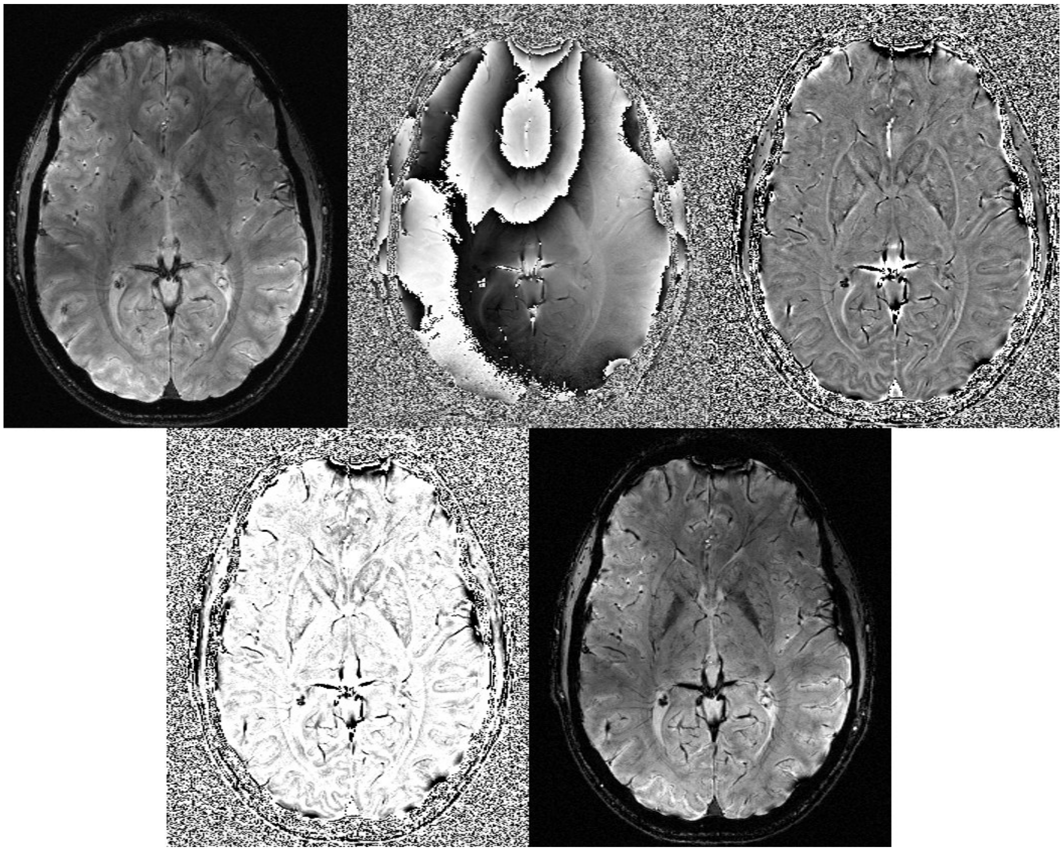

Figure 1.12: Processing pipeline for susceptibility weighted imaging. From upper left to lower right: raw magnitude image at $TE = 21.5$ ms, unfiltered phase image scaled from $-\pi$ to π, high-pass filtered phase image scaled from $-\pi/4$ to $\pi/4$, negative phase mask, susceptibility weighted image. Note the emphasized contrast venous and deep gray matter contrast in the SWI image relative to the magnitude image.

1.3.4 Spin Echo Imaging

The spin echo was first proposed, in the context of pulsed NMR spectroscopy, by Hahn in 1950 for accurate quantification of relaxation and diffusion times [22]. It has since matured into a robust and ubiquitous imaging sequence. A prototypical spin echo sequence incorporates an additional RF pulse prior to data acquisition to refocus static field induced phase evolution. This refocusing pulse, strategically placed midway between excitation and echo formation, negates any cumulative phase accrual; subsequent evolution rewinds the phase into a coherent echo. As such, spin echo based sequences are largely insensitive to static field heterogeneities; they are capable of imaging near susceptibility interfaces and can offer outstanding contrast between soft tissues.

A multislice spin echo imaging sequence is diagramed in Fig 1.13. Magnetization is initially excited by a 90° RF pulse. It undergoes free precession and relaxation, Eq 1.11, dephasing under the application of gradients and the presence of back-

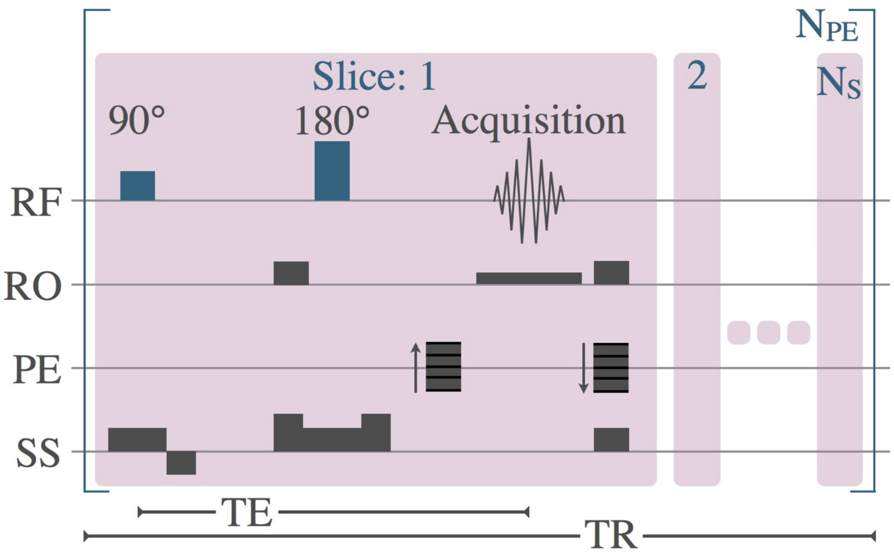

Figure 1.13: Pulse sequence diagram for 2D multislice spin echo. Spin echo sequences apply a 180° refocusing pulse midway between excitation and echo formation. One k-space line is acquired in each of N_S slices per excitation/refocusing pair; the process is repeated for N_{PE} phase encode steps every TR period.

ground heterogeneities. A 180° refocusing pulse inverts all accrued phase in the transverse plane. This pulse, shown in Fig 1.13 with a slice select gradient, is surrounded by a pair of identical crusher gradients in the slice select direction. Crusher gradients are necessary in the eventuality that the refocusing pulse differs from *exactly* 180°. These lobes spatially dephase any transverse magnetization excited by the refocusing pulse. Only transverse magnetization originating from the excitation pulse will experience *both* crusher gradients, have no net phase accrual, and contribute substantially to echo formation. The crusher gradient ($G_{x,y,z}$) and duration (τ) should be sufficient to produce at least 2π dephasing along the relevant voxel dimension,

$$G_{x,y,z} \cdot \tau \geq \frac{2\pi}{\gamma\ \Delta x, y, z}. \tag{1.34}$$

Encoding and acquisition occurs with a slightly modified cartesian readout module (Fig 1.6): the readout pre-phasing lobe is commonly inverted and executed prior to refocusing. Although signal excited during refocusing is already crushed, this prevents spatial encoding of any residual magnetization.

Magnetization evolution from a single off-resonant isochromat during a spin echo sequence is shown in Fig 1.14. Phase accrual due to off-resonant precession is reversed by the refocusing pulse; subsequent precession rewinds the phase. An echo is formed from the coherent addition of multiple isochromats. The behaviour of multiple isochromats is succinctly described in phase plot format, Fig 1.15. Phase dispersion results from both gradient encoding lobes and from static field off-resonance.

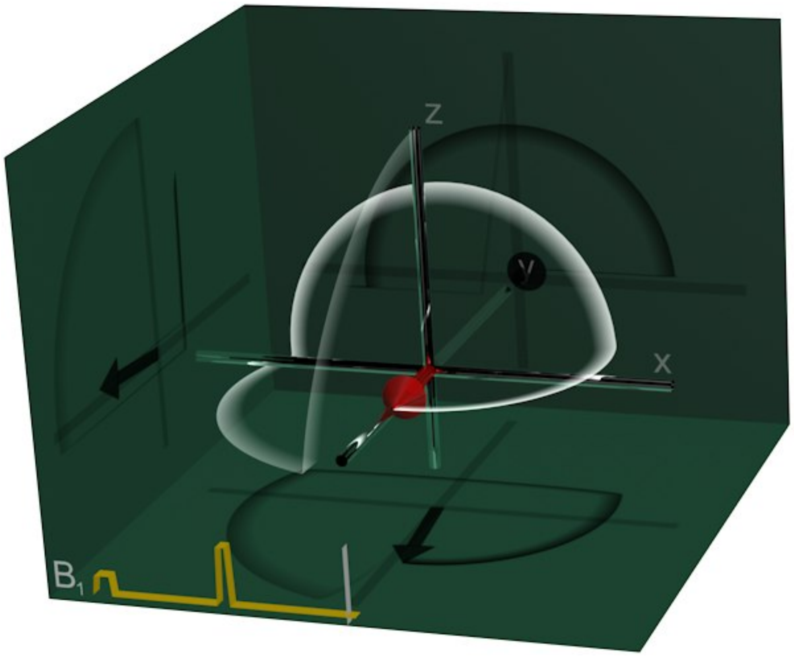

Figure 1.14: Magnetization evolution of a single off-resonant isochromat during a spin echo sequence. Magnetization, initially aligned with the z' axis, is excited into the x'/y' plane, evolves and relaxes freely in the transverse plane, is inverted by the refocusing pulse, and rephases (along with other isochromats) into a coherent echo.

Unlike GRE sequences, which only refocus gradient induced phase evolution, spin echo sequences refocus gradient and static field inhomogeneities.

A magnetization isochromat at the echo time of a spin echo experiment can be described mathematically, using matrix operators (see page 5), as

$$\vec{M}(TE) = \mathbf{TS}(\tau)\ \mathbf{R}(180^\circ)\ \mathbf{TS}(\tau)\ \mathbf{R}(90^\circ)\vec{M}(0). \tag{1.35}$$

In this case, τ represents the half echo time (i.e., $TE = 2\tau$). Each 90° excitation saturates all longitudinal magnetization; an amount $\vec{M}(0) \approx M_0(\vec{r})(1-e^{-TR/T_1(\vec{r})})z'$ is re-polarized prior to the next excitation. The detectable transverse magnetization, derived from Eq 1.35, is approximately

$$S_{SE}(\vec{r}) \approx C\rho(\vec{r})\ (1 - e^{-TR/T_1(\vec{r})})\ e^{-TE/T_2(\vec{r})}. \tag{1.36}$$

Contrast, the signal difference between two species, can be modified via manipulation of TR and TE. In addition to compulsory proton density contrast, T_1 weighting can be imposed with $TR \approx T_1$ and minimized with $TR \gg T_1$; T_2 weighting is introduced with $TE \approx T_2$ and minimized with short TE. Relatively long repetition times are required for adequate signal recovery, particularly when minimizing T_1 weighting, resulting in unnecessarily long scan times. Acquisitions can be ac-

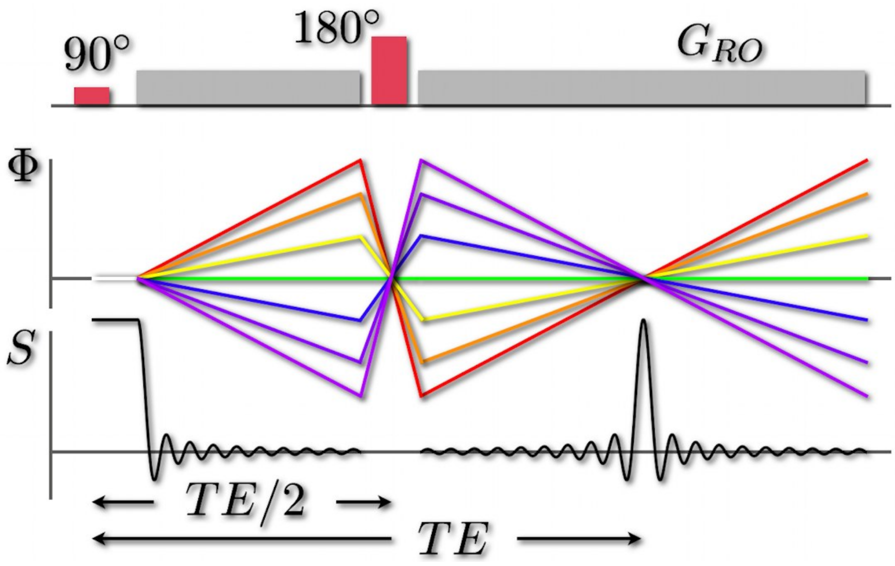

Figure 1.15: Spin echo phase plot. The top trace depicts RF (red) and readout gradient waveforms (gray) for a spin echo acquisition. The center plot illustrates phase evolution (rotation angle about z') of transverse magnetization during the sequence. Each line represents a unique off-resonant frequency. The bottom plot represents the signal amplitude, formed as the vector sum of the phase plot.

celerated by executing multiple refocusing pulses and collecting multiple echoes for each excitation pulse — a technique called fast spin echo.

1.3.5 Fast Spin Echo Imaging

Fast spin echo — also known as "rapid acquisition with refocused echoes" (RARE) and "turbo spin echo" (TSE) — is arguably the most ubiquitous sequence for clinical investigation. It offers reliable and rapid imaging almost anywhere in the human body and provides outstanding soft tissue contrast. It is typically faster and has more contrast options than does single spin echo. However, these benefits come at the cost of additional sequence intricacy, new artifacts, and complex spin behaviour.

The basic principles governing multiple RF pulses and their echoes were largely described in the 1950s using pulsed NMR techniques; fundamentally, little has changed in over 50 years — a little history is in order. The use of multiple RF pulses to induce a series of echoes was first demonstrated by Hahn [22]. In addition to discovery of the primary spin echo, a detailed analysis of the rotating frame of reference, and an innovative use of vector representations for spin visualization, this seminal work also defined the stimulated echo, which occurs following three (or more) RF pulses. Hahn noted that this echo "survives as long as T_1 permits", except in "liquids of low viscosity" whose echo amplitudes "attenuate in a time much shorter than T_1 . . . due to the diffusion factor" [22]. This "diffusion factor" degrades

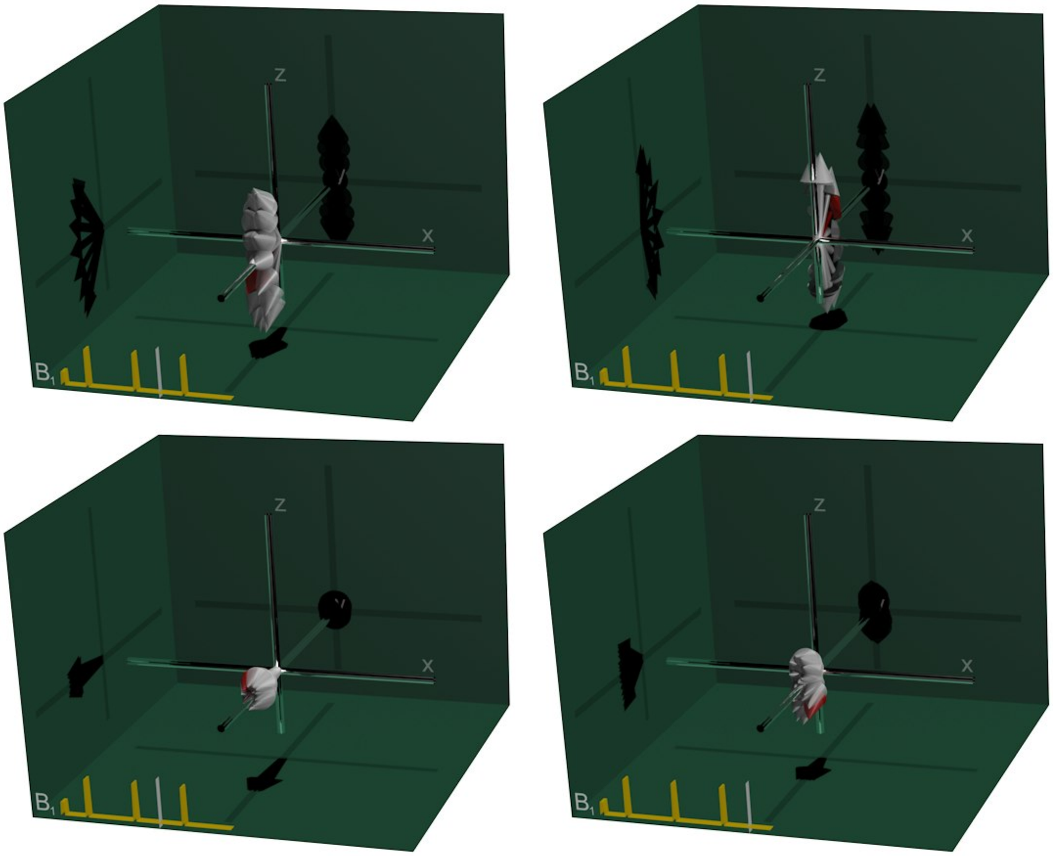

Figure 1.16: Vector representations of echo coherence during Carr-Purcell and Carr-Purcell-Meiboom-Gill echo trains refocused with 160° pulses. The upper row displays isochromats during the second and third echoes (from left to right) of the CP echo train; the lower row, isochromats from the CPMG echo train. Note the consistent echo direction and improved coherence of the CPMG train relative to the CP train.

spin coherence when pulse spacings are increased since spins can randomly traverse through background field gradients prior to rephasing.

Carr and Purcell [23] refined the multi-RF method to reduce sensitivity to molecular diffusion by employing a 90° excitation followed by multiple, evenly spaced 180° refocusing pulses with echoes forming midway between refocusing pulses. Rapid and repeated refocusing restricts inter-echo phase dispersion due to molecular diffusion. The Meiboom-Gill modification states that "the phase of the RF of the 90° pulse is shifted by 90° relative to the phase of the 180° pulses" [24]. This adjustment ensures coherent echoes along the same axis and minimizes sensitivity to errors in refocusing angle, which accrue with each pulse in the original Carr-Purcell train; this effect is demonstrated in Fig 1.16. The Carr-Purcell-Meiboom-Gill (CPMG) echo train remains the most widely used refocusing train.

Modern FSE imaging sequences, based heavily on the pioneering work of Hennig

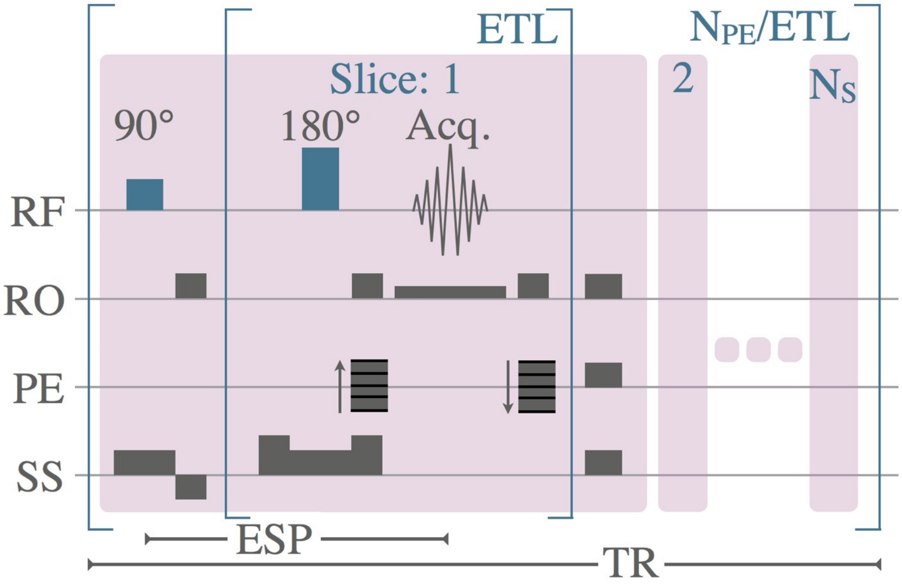

Figure 1.17: Pulse sequence diagram for 2D multislice fast spin echo. Imaging is accelerated by a factor *ETL* relative to single spin echo due to multiple refocusing pulses per excitation pulse. The excitation/echo train is repeated N_{PE}/ETL times to encode the entire image set.

et al. [25, 26], apply a CPMG train and encode the resulting echoes into a single image, offering accelerated acquisitions relative to single spin echo imaging. A typical 2D multislice FSE sequence is diagramed in Fig 1.17. It is very similar to single spin echo — until acquisition of the first echo is complete. At this point, equally spaced refocusing pulses continuously flip the transverse magnetization inducing a train of echoes. Appendix B provides an interactive visualization of this principle. Each echo is encoded with a unique phase encode value to accelerate image acquisition. The echo train length is limited by T_2 decay: echoes beyond the transverse decay time contribute little signal and are not collected. Repetition times approximately equal to, but often several times longer than, the T_1 time are required for adequate signal recovery following saturation by the high angle excitation and refocusing train. Multiple slices can be acquired during the long *TR* interval for time efficient volumetric coverage.

A position of a single magnetization isochromat at the n^{th} echo time ($TE_n = 2n\tau$) of a CPMG train is calculated via

$$\vec{M}(TE_n) = \{\mathbf{TS}(\tau)\ \mathbf{R}(180°, 90°)\ \mathbf{TS}(\tau)\}^n\ \mathbf{R}(90°, 0°)\vec{M}(0), \tag{1.37}$$

where τ represents the half echo time and the portion within the curly braces is repeated (via left multiplication) for each refocusing pulse. Eq 1.37 is an involved way of saying that transverse magnetization tries to get away, but ultimately goes nowhere. The signal at the n^{th} echo is approximately

$$S_{FSE}(\vec{r}) \approx C\rho(\vec{r})\,(1 - e^{-TR/T_1(\vec{r})})\,e^{-TE_n/T_2(\vec{r})}. \tag{1.38}$$

Typically, a single echo (n_{eff}) from the train is selected to dominate the image contrast. This "effective echo", occurring at time TE_{eff}, is encoded into central k-space regions where low spatial-frequency information is contained; other echoes are placed in the periphery of k-space and contribute to fine image structure. Encoding orders for two echo trains with different effective echoes are shown in Fig 1.18. The encoding order is designed to minimize signal discontinuities (due to T_2 relaxation between echoes) near the center of k-space, where spectral density is the greatest.

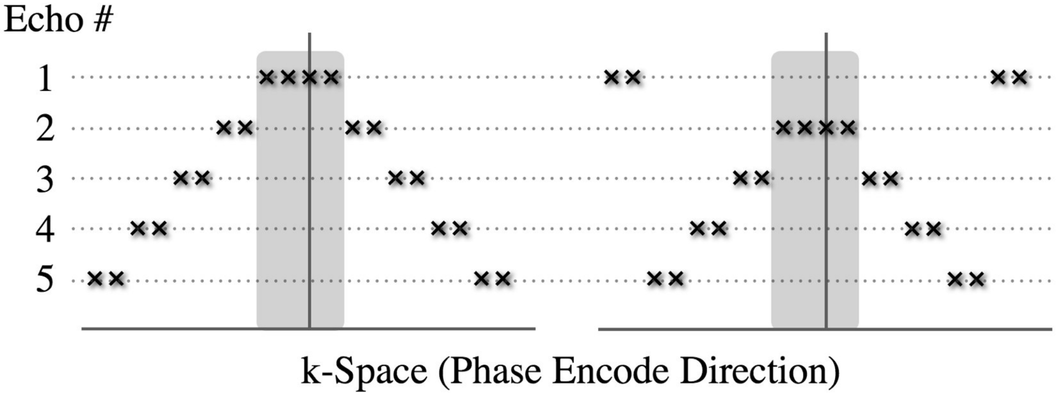

Figure 1.18: Example phase encode orderings for segmented FSE. There are 20 phase encode points and the echo train length is 5. Four shots are required for image encoding. On the left, the first echo occupies the contrast dominant region of k-space (shaded); on the right, the second echo is encoded into the contrast region.

Acquisition during the transient echo train imposes signal modulation in the phase encode direction. This modulation depends on the echo train length (ETL), inter-echo spacing (ESP), transverse relaxation time, and phase encode ordering. In general, T_2 heterogeneity within the sample precludes simple correction schemes. Transformation into the image domain produces a point spread function in the phase encode direction, typically characterized by blurring and ringing, which distorts the image and reduces resolution. This sacrifice is often worth the high contrast and acquisition efficiency of FSE. Example FSE images, obtained at 1.5 T are shown in Fig 1.19.

1.3.6 Low Angle Fast Spin Echo

The tip angle is proportional to the B_1^+ field (Eq 1.9), which is linearly dependent on the current through the RF coil according to the Biot-Savart law (see also signal reciprocity, Eq 1.22). Since electrical power scales quadratically with current, the

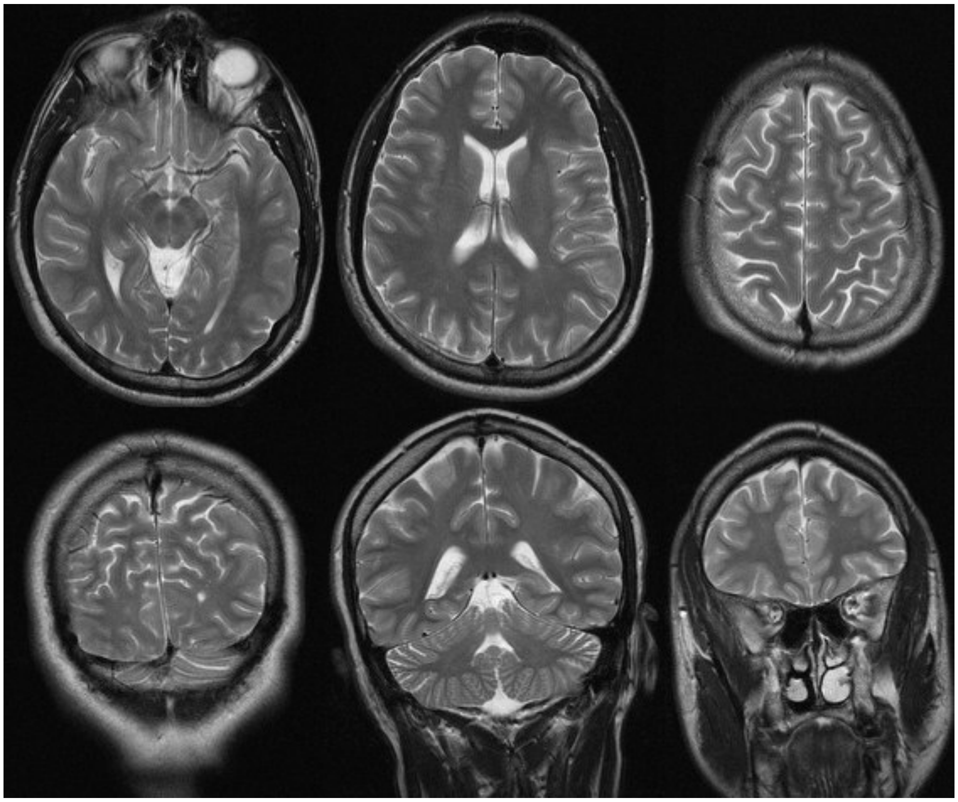

Figure 1.19: Multislice T_2-weighted fast spin echo images acquired at 1.5 T. Upper row: three axial slices; lower row: three coronal slices. Note the high contrast between brain tissues and absence of susceptibility artifacts near air/tissue interfaces.

required RF power is proportional to the tip angle squared. A quasi-static equation representing the quadrature RF power (P_{RF}) required during a hard pulse of duration τ_α producing a tip angle α within a sphere of radius R_{sphere} and conductivity σ_{cond} is [1]

$$P_{RF} = \frac{2\pi \sigma_{cond} \omega_0^2 \alpha^2 R_{sphere}^5}{15 \gamma^2 \tau_\alpha^2}. \tag{1.39}$$

Although this equation is overly specific for general use, it reveals some interesting dependencies: power scales rapidly with the object size, Larmor frequency (i.e., field strength, see Section 1.3.8), and tip angle. The energy from this pulse (equal to $\tau_\alpha P_{RF}$) is deposited as thermal energy in the patient and must be monitored to avoid excessive tissue heating.

Fast spin echo imaging employs frequent 180° refocusing pulses, often being applied every 5–20 ms. In practice, average RF amplifier output powers exceeding 160 W are required for standard FSE protocols using a body coil at 1.5 T [27]. Based on the electrical quality factors of the loaded and unloaded RF coil, over half this power is typically absorbed by the patient [27]. The specific absorption rate (SAR), defined as the power absorbed per mass of tissue, of FSE can prohibit its use on human subjects. Methods to reduce this energy deposition are required.

Lowering the refocusing angle — the excitation angle remains at 90° — is a versatile approach to SAR mitigation: the quadratic relation between pulse angle and RF power enables drastic power reductions with moderate angle reductions. The viability of this method depends on the magnetization's response. A considerable body of work has investigated and characterized magnetization behaviour at reduced, and variable, refocusing angles [26, 28, 29, 30, 31, 32, 33]. In general, the signal is insensitive to changes in refocusing angle, but these changes should be performed in a smooth and fluid manner to minimize signal oscillations and maintain high echo amplitudes.

With non-180° refocusing pulses, magnetization is not constrained to the transverse plane. This produces two major effects, which can be analyzed separately:

- Spins lose perfect coherence at the echo time (i.e., isochromats are distributed across the transverse and longitudinal directions). Vector addition of these spins produces less signal than if they were all colinear.
- Magnetization is exposed to both transverse and longitudinal relaxation mechanisms; decay occurs at a rate $R_{2eff} \leq R_2$.

Neglecting relaxation, echo amplitudes from direct refocusing angle reductions stabilize in a pseudosteady state (PSS)[12]. Following a transient oscillatory period, these echo amplitudes are given by [29]:

$$S_{FSE}(\alpha) = S_{FSE}(180^\circ) \cdot \sin\left(\frac{\alpha}{2}\right). \tag{1.40}$$

While direct angle reductions maintain impressive signal levels — a sinusoidal response ain't bad! — higher spin coherence (i.e., improved echo amplitudes), a shorter stabilization period, and lower oscillations during this stabilization are possible. An optimized spin coherence state for low angle pulses, termed the *static* pseudosteady state[13] (SPSS), occurs when spin coherence is maximized for a given refocusing angle. Its echo amplitudes are given by [34]

$$S_{FSE}(\alpha) = S_{FSE}(180^\circ) \cdot \sin^{\frac{1}{2}}\left(\frac{\alpha}{2}\right) \cdot P_{-\frac{1}{2}}\left[\sin\left(\frac{\alpha}{2}\right)\left(1 + \frac{\sin^2(\alpha)}{8\sin^4\left(\frac{\alpha}{2}\right)}\right)\right] \tag{1.41}$$

---

[12] By definition, echo trains are transient entities and true steady states are ill-defined. However, stable echo formation warrants some description, thus "pseudosteady state."

[13] "Static" describes magnetization evolution: in the optimized state, isochromats retrace an identical route to form each echo; the PSS has stable signal amplitudes, formed from *crazy* and non-repetitive magnetization evolution.

where $P_{-\frac{1}{2}}$ is a Legendre function, evaluated, in this case, via

$$P_{-\frac{1}{2}}[x] = \frac{1}{2\pi}\int_{-\pi}^{\pi}\left(x+\sqrt{x^2-1}\cos(\theta)\right)^{-\frac{1}{2}}\, d\theta. \tag{1.42}$$

The SPSS state can be approximated by modulating tip angles of the initial refocusing pulses [35, 34, 32]. In general, a smooth and gradual transition from 180° to α maintains near-optimal coherence. A graphical analysis suggests that prescribing the first refocusing pulse at $90^\circ + \alpha/2$ rapidly transitions to a reasonable approximation of SPSS(α) [30]. Magnetization vectors at the 7^{th} echo are shown in Fig 1.20 for 90° refocusing angles, either reduced directly, or prepared into the SPSS.

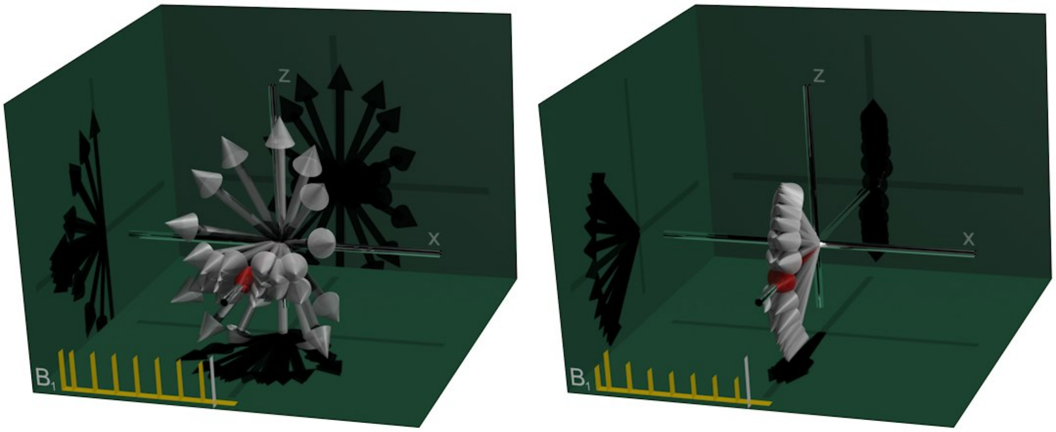

Figure 1.20: Spin coherences from low refocusing angle FSE at the 7^{th} echo. Left, spins refocused with constant 90° pulses; right, with pulse angles smoothly reduced to 90° via the "3-Ahead" algorithm (153°, 114°, 96°, 90°, ...) [32]. Note the elegant ordering when prepared into the SPSS.

Improved spin coherence, and thus a higher echo amplitude, is observed with appropriate preparation than with direct reductions. Echo amplitudes with reduced refocusing angles are shown in the left graph of Fig 1.21. Typically, low angle refocusing pulses yield signal levels somewhere between the solid blue SPSS curve and the dashed green PSS curve.

Once prepared into the SPSS, slow variations in refocusing angle maintain high coherence. Refocusing angle modulation schemes have been developed to improve SNR during acquisition of the center of k-space while reducing RF power in the periphery [36, 37]. Echo trains can also be designed to tailor the point spread function, even to compensate for relaxation, thus improving the effective resolution or to improve image SNR by filtering during acquisition [38].

Relaxation changes are observed with non-180° refocusing angles. Since magnetization evolves in the transverse plane and is stored along the longitudinal axis (see Section 1.3.7), relaxation occurs via both R_2 and R_1 processes. The effective

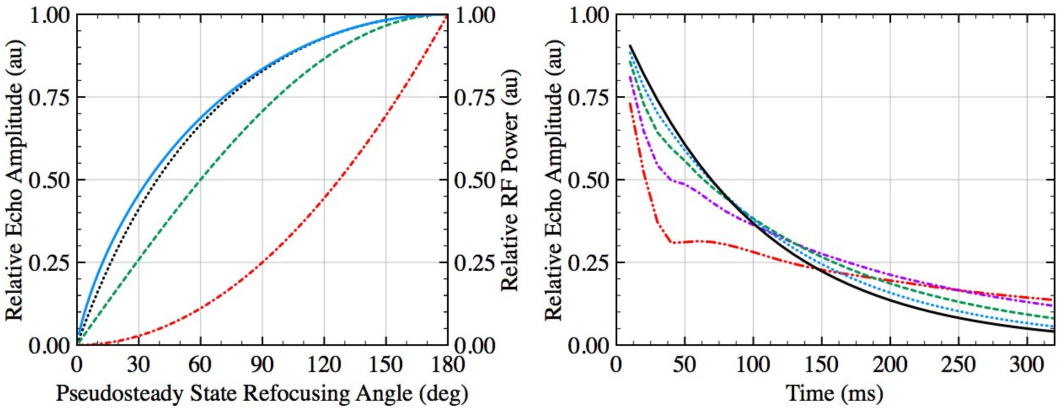

Figure 1.21: Left graph, left axis: echo amplitudes in the absence of relaxation for the SPSS (solid/blue), the SPSS approximated with an initial 90° + $\alpha/2$ (dotted/black), and the signal achieved with direct angle reductions (dashed/green). Left graph, right axis: relative RF power (dash-dot/red). Right graph: example decay curves from a sample with $T_1 = 1000$ ms and $T_2 = 100$ ms when placed and held in SPSS states for 180° (solid/black), 120° (dotted/blue), 90° (dashed/green), 60° (dash-dot/purple), and 30° (dash-dot-dot/red).

relaxation rate, R_{2eff}, is bounded between these two rates and yields slower signal decay than observed with 180° pulses. Traditional T_2-weighted images can still be obtained, but often require longer echo times for near-equivalent contrast [39]. Slower signal decay at reduced angles enables extended readout durations to reduce noise, counteracting the signal reduction from incoherent echoes. The net SNR of low angle FSE is impressively high: over 90% of the SNR at 180° is retained at 80° for tissues with $T_1 = 10 \times T_2$ [34]. Example decay curves at different refocusing angles are shown in the right graph of Fig 1.21. Note that the signal level at low angles eventually *exceeds* that of 180° pulses. This effect is discussed in more detail in Chapter 2.

Reduced refocusing angles are a robust SAR mitigation strategy, with potential for dramatic power reductions while maintaining image contrast and tailoring the point spread function. Fully exploiting these benefits requires a means of rapidly computing echo amplitudes.

1.3.7 Extended Phase Graph Algorithm

The extended phase graph (EPG) algorithm is a computational routine for approximating the MRI signal following an arbitrary sequence of RF pulses. It is an alternative to Bloch simulations of magnetization vectors (Eqs 1.12–1.15) and provides a complementary analysis of spin systems exposed to multiple RF pulses.

Unlike the vector representation, which traces the evolution of spatially distinct isochromats, the EPG algorithm partitions magnetization into distinct phase configurations. We define the complex basis set [29]

$$F(n) = \int_{\omega} M_{\perp}(\omega) e^{-i\omega n\tau} d\omega \tag{1.43a}$$

$$Z(n) = \int_{\omega} M_{||}(\omega) e^{-i\omega n\tau} d\omega \tag{1.43b}$$

representing pools of spins with similar phase dispersion history. The states $F(n)$ represent the quantity of transverse magnetization having dephased during time $n \cdot \tau$ (and thus require $n \cdot \tau$ to rephase once refocused); $Z(n)$ represents dephased longitudinal magnetization.

A CPMG train is a specific multi-pulse experiment with periodic RF pulse spacings and constant gradient area (including crushers and background field gradients) in every half echo spacing (see Sections 1.3.4 and 1.3.5). In the CPMG case, the following simplifications are justified:

- Continuous phase states are converted to discrete states with integer values of n. Constant dephasing occurs between all points of interest, namely RF pulses and echo times; non-integer states still physically exist, but are neither detected nor nutated via RF pulses. This is a crucial concept, as it vastly reduces the number of states requiring evaluation.

- Strong crusher gradients fully dephase non-refocused magnetization; only rephased magnetization (i.e., the $F(n = 0)$ state) contributes signal.

- Relaxation during the echo train occurs via R_1 and R_2 processes; spin re-polarization can be neglected since any re-polarized spins that get excited by refocusing pulses are dephased by the crusher gradients.

With these assumptions, we can define simple rules to determine phase state populations during an echo train. Initially, a 90° excitation pulse tips the equilibrium longitudinal magnetization, which exists in state $Z(0)$, into the transverse plane. This magnetization is fully coherent in the transverse plane, yielding (normalized) states

$$F(0) = 1 \tag{1.44a}$$

$$F(n \neq 0) = 0 \tag{1.44b}$$

$$Z(n) = 0 \tag{1.44c}$$

During each half echo period, magnetization will undergo dephasing and relaxation. Transverse states will naturally increment their phase state, longitudinal states do not dephase. A transition rule can be defined as [38]

$$F'(n) = F(n-1) \cdot e^{-\tau/T_2} \tag{1.45a}$$

$$Z'(n) = Z(n) \cdot e^{-\tau/T_1} \tag{1.45b}$$

where F' and Z' are the final states. A refocusing pulse with angle α will mix states according to [40, 38]

$$\begin{bmatrix} F'(n) \\ Z'(n) \end{bmatrix} = \begin{bmatrix} \frac{1}{2}\left[1+\cos(\alpha)\right] & \frac{1}{2}\left[1-\cos(\alpha)\right] & \sin(\alpha) \\ -\frac{1}{2}\sin(\alpha) & \frac{1}{2}\sin(\alpha) & \cos(\alpha) \end{bmatrix} \begin{bmatrix} F(n) \\ F(-n) \\ Z(n) \end{bmatrix} \tag{1.46}$$

Equations 1.45 and 1.46 can be applied to compute magnetization evolution during an echo train. Echoes are formed at $n = 0$, when the phase history has been fully refocused; the echo amplitude is given by

$$S_{FSE} = F(0). \tag{1.47}$$

An EPG diagram for a CPMG train is shown in Fig 1.22. The EPG algorithm and graph provide insight into magnetization behaviour, which is often lost when analyzing the vector representation, Fig 1.20. This model allows visual representation of abstract concepts like stimulated and indirect echoes.

1.3.8 High Field Systems

High field imaging systems offer improved resolution, faster acquisitions, and improved tissue contrast than do lower field systems. Or so the vendors tell us. Clinical systems are available at fields strengths up to 3.0 T, pre-clinical systems operate up to 7.0 T, a few 9.4 T research machines exist, and an experimental 11.7 T system is scheduled for eventual delivery [41]. From an imaging perspective, the *only* irrefutable advantage of increasing the static field strength is an approximately linear improvement in SNR. Most changes are of questionable virtue: modified relaxation times, reduced RF homogeneity, stronger susceptibility gradients, and expanded spectral separation can all be exploited, but these typically just impede imaging. Some effects — intense acoustic noise, large and expensive magnets and amplifier systems, and high siting costs — are like banana flavoured medicine: universally disliked, yet an integral part of the package. Consequences of high RF power deposition range from mildly restrictive to entirely prohibitive.

The additional SNR available at high field strength can be converted into improved image resolution — a strategy that may improve disease detection and diagnosis. Investing SNR into enhanced resolution is costly option that rapidly depletes

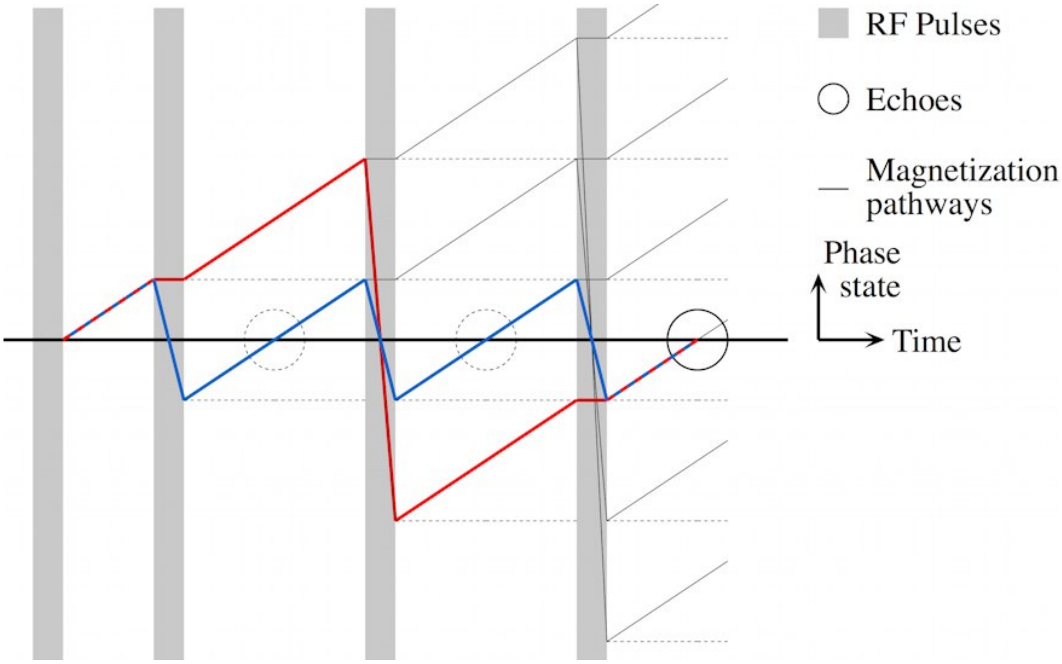

Figure 1.22: Extended phase graph diagram for a CPMG echo train. Solid lines represent $F(n)$ states that accrue phase and evolve at a diagonal between RF pulses. $Z(n)$ states are shown by horizontal dotted lines and do not evolve in phase space. Refocusing pulses serve to mix states. Negative phase states (those below the horizontal center line) have been inverted and are in the process of re-phasing. After several RF pulses, there are multiple pathways leading to echo formation. Two pathways contributing to the third echo are emphasized: in blue, a direct spin echo; in red, an indirect echo.

the high field advantage and increases scan time.

In theory, scan time can be drastically reduced with the additional SNR available at high field. The advantages of this SNR expenditure are palpable: additional contrasts can be obtained in the same total scan time, patient compliance is increased while motion artifacts are decreased, patient throughput can be increased, and detection of dynamic processes (i.e., cardiovascular, blood flow, even vocal tract shaping [42]), can be enhanced. To fully achieve reduced acquisition times, drastic undersampling strategies are necessary, as introduced in Section 1.3.2.

Strong sensitivity to magnetic susceptibility differences are observed at high field strengths. Functional MRI exploiting blood oxygenation levels to map brain activity benefits from larger signal changes between rest and activation states when measured at higher field strengths than at lower strengths [43]. Susceptibility weighted imaging benefits from more rapidly evolving bulk phase shifts at high field to drastically improve contrast-to-noise and acquisition efficiency over lower field scanners.

Strong sensitivity to non-heme iron has been reported at high field. High correlations between non-heme iron estimates and R_2, R_2' and R_1 have been reported at 3.0 T [44, 45]. Furthermore, a near linear increase in sensitivity to non-heme iron was demonstrated at fields between 1.5 and 4.0 T. A report from the other 4.7 T group claimed to isolate iron induced relaxation from other processes and published a correlation coefficient of 0.99 between non-heme iron content and this iron-specific relaxation rate [46]. Gradient echo phase values have been attributed (over-ambitiously?) to non-heme iron concentration in both quantitative [47] and qualitative [48, 49] manners. Although confounds exist and the exact relation between iron and MR parameters has not been established, there is a correlation — and it increases with field strength [50]. This iron rant continues in Sections 1.4.3 and 5.1.

At high field strength, extreme RF power deposition limits the imaging techniques available for *in vivo* studies. Equation 1.39 contains a quadratic relationship between RF power and field strength. If RF pulse durations are adjusted to maintain a constant ratio between pulse bandwidth and chemical-shift — the latter scales with field strength — the instantaneous RF power develops a *quartic* dependence on field strength [51]. Fortunately, the quasi-static model fails at high field strength and full-wave simulations are required to accurately estimate power requirements; numerical [52, 53] and experimental [54] evidence suggest that the quadratic dependence between RF power and field strength in Eq 1.39 overestimates the actual RF power requirements at field strengths above ∼4.7 T. Regardless of the exact dependence, intense RF power deposition precludes traditional FSE, with densely packed 180° pulses, at high field strengths. With a head-only transmit coil at 4.7 T, a clinical-like FSE protocol requires ∼60 W (∼20 W/kg) of average power. Clearly, modifications are required to enable time-efficient FSE imaging at high field. As described in Section 1.3.6, low refocusing angles enable drastic power reductions. This approach is viable at clinical field strengths; however, its utility has not been demonstrated at high field strengths, where substantial power reductions are required and non-uniform RF fields may obfuscate tissue contrast.

As imaging frequency increases, the RF wavelength decreases and its tissue penetration is attenuated. These effects produce heterogeneous transmit and receive fields. At 4.7 T, wavelength interference effects [55] produce a central brightening while destructive interference attenuates the B_1 fields at the periphery of a head. This is problematic as contrast typically depends on RF tip angles, which can vary substantially across the imaging volume. Fast spin echo, which employs multiple RF pulses prior to acquisition, could potentially suffer compound errors and significant variations in signal intensity and contrast. Furthermore, quantitative T_2 mapping requires perfect 180° refocusing to ensure the signal decay is modulated exclusively by T_2; this condition cannot be satisfied at high field.

1.4 The Brain, Multiple Sclerosis, and Non-Heme Iron

The brain is the primary component of the central nervous system. It is composed predominantly of neurons, support cells, and vasculature. It is an exceptionally ordered organ with countless neural connections and many structural and functional divisions. This section very briefly describes some major components of the human brain, introduces multiple sclerosis (MS), describes the role of iron in brain metabolism, and notes possible dysfunctions in iron storage and use that may be associated with MS and other neurodegenerative diseases.

1.4.1 Macroscopic Divisions of the Human Brain

The human brain is divided into three primary structures: the cerebrum, the brainstem, and the cerebellum. The cerebrum is divided into two hemispheres with the majority of inter-hemispheric connections passing through the corpus callosum. It is further divided into frontal, temporal, parietal, and occipital lobes — these designations are based on a combination of anatomical location and functional division. The cerebrum also contains the basal ganglia and limbic systems. As a whole, the cerebrum is associated with sensory, motor, memory, and higher functions, such as personality. The brain stem contains neural connections between the brain and body; it also regulates breathing, digestion, and heart rate. The cerebellum is best known for its role in coordinating movement.

The human brain displays substantial corticalization — the reassignment of functional tasks from sub-cortical centres to the cortex. Gray matter (GM), which occupies the cerebral and cerebellar cortices and certain sub-cortical regions, is composed of neural cell bodies, their dendrites and axons, as well as glial cells, and capillaries. White matter (WM) is composed of myelinated axons, bundled into fasciculi that connect brain regions, and glial cells. The ventricular system is filled with cerebrospinal fluid (CSF) and serves to cushion the brain and spinal cord.

Numerous sub-cortical GM regions are partially responsible for a variety of crucial tasks[14]. Of relevance to this thesis, the basal ganglia — a networked grouping comprised (primarily) of the caudate, putamen, globus pallidus, substantia nigra, and subthalamic nucleus — are associated with with initiation and modulation of motor control [56]. The basal ganglia contain feedback loops that facilitate or attenuate activation to provide a controlled and coordinated motion. Afferent neurons from the cortex enter the basal ganglia through the striatum (a spatially disparate grouping, comprised primarily of the caudate and putamen). After looping through the basal ganglia, efferent neurons return to the cortex, often via the thalamus. The thalamus is a compound structure with numerous sub-nuclei adjacent to the

---

[14] Possibly the most vague sentence in this thesis

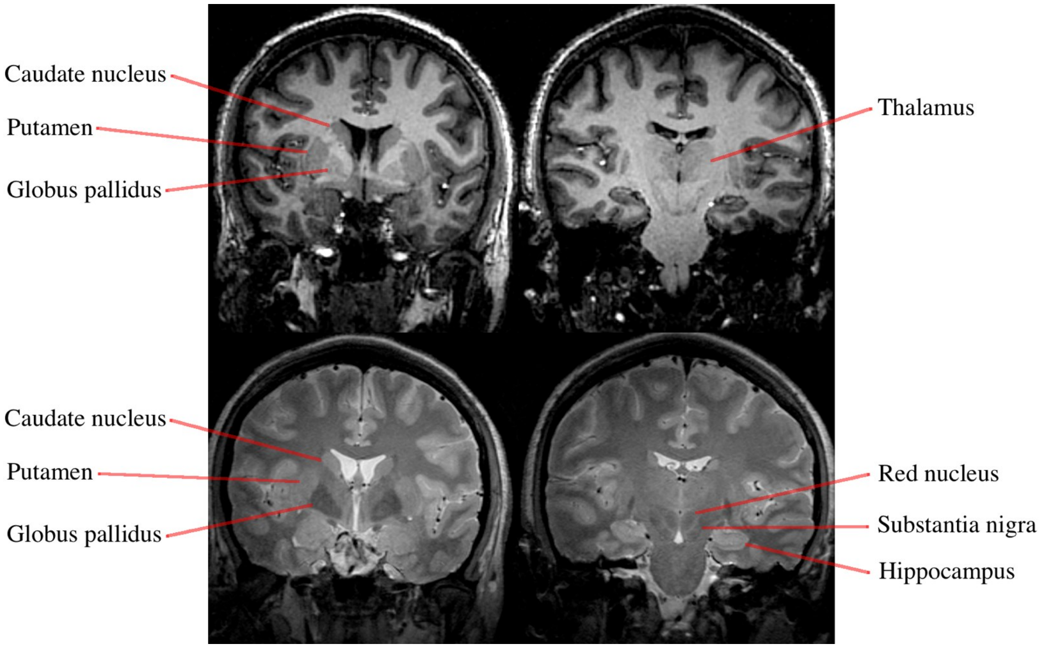

Figure 1.23: Coronal T_1 (top row) and T_2 (bottom row) weighted magnetic resonance images showing several deep gray matter structures.

lateral wall of the third ventricle. Often termed “the gateway to the cortex”, it relays sensory, cerebellar, and limbic information to the cortex. The basal ganglia and thalamus are shown in Fig 1.23; the hippocampus and red nucleus is also prominent. The hippocampi are associated with information assimilation and memory. The red nuclei play a role in muscle tone, particularly in the arms and shoulders.

1.4.2 Multiple Sclerosis

There are numerous neurodegenerative diseases that degrade neural integrity and produce a progressive loss of function. Presented is a brief overview of multiple sclerosis, a demyelinating condition in which MRI plays a role in diagnosis and research.

Multiple sclerosis is an autoimmune disease involving, among other things, the breakdown of myelin sheaths and the formation of white matter scleroses. This reduces neural conduction and severs connections. Numerous neurological symptoms are possible, but the most commonly occurring are hypoesthesia, motor and coordination impairments, cognitive decline, and depression. It is idiopathic and has no cure. Onset usually occurs in young adulthood and is up to twice as common in females as in males [57]. Global incidence varies drastically: prevalence rates below 5 cases per 100,000 occur in parts of Asia, Africa, and South America [58]. Overall prevalence in Canada is 240 cases per 100,000, with regional variation between 80 and 350 cases per 100,000 [59].

The diverse neurological symptoms associated with MS preclude a simple diagnostic test. The disease is diagnosed via neurological evidence — occasionally supported via radiological and laboratory findings. A diagnosis of MS requires evidence of spatial and temporal disease dissemination in conjunction with exclusion of alternate neurological conditions [60]. According to the McDonald criteria, diagnosis requires clinical presentation of two or more attacks *and* evidence of two or more disparate lesions; other diagnostic tests, such as MRI or CSF analysis, can replace one or more criteria [61]. Diagnosis always involves a neurological exam to assess motor and sensory functions and to test for signs indicative of dysfunction in specific neurological systems. MRI can be performed to supplement or replace neurological indicators; an MRI exam supporting the MS diagnosis requires three of the following four criteria:

- One gadolinium enhancing lesion or nine T_2 hyperintense lesions.
- At least one infratentorial lesion.
- At least one juxtacortical lesion.
- At least three periventricular lesions.

Patient disability is commonly assessed using the Kurtzke expanded disability status scale (EDSS) [62]. This method compiles disability in eight functional systems into a single numerical value ranging from 0 to 10. It measures disability in pyramidal, cerebellar, brainstem, sensory, bower/bladder, visual, cerebral, and other functional systems. EDSS scores between 1.0–4.5 represent ambulatory MS patients while scores between 5.0–9.5 are assigned to patients with considerable ambulatory impairment. A score of 0 indicates a normal neurological exam; a score of 10 is defined as death due to MS.

There are four broad disease subtypes: relapsing-remitting, secondary-progressive, primary-progressive, and progressive-relapsing. The majority of MS patients are categorized as relapsing-remitting; they experience unpredictable relapses separated by periods of relative inactivity. Disability gradually worsens and within 10 years most relapsing-remitting patients eventually enter the secondary-progressive classification, where disability progresses continuously despite few or minor relapses.

Pathophysiologically, MS is partially characterized by formation of plaques in the brain. These lesions often occur in WM, but can also form in cortical and sub-cortical GM. Lesion formation is thought to occur by infiltration and activation of various T-lymphocytes and microglia during disruption of the blood brain barrier [63, 64]. An autoimmune response is triggered which degrades the myelin sheath, destroys oligodendrocytes, and damages neurons [65]. An initial demyelination stage occurs during immune cell infiltration and is followed by a period of partial remyelination. Repeated demyelination/partial-remyelination cycles eventually form a permanent plaque. Although classically considered a WM disease, extensive damage has been reported in the cortex, normal appearing WM, and in deep GM [63]. Furthermore, evidence of progressive astrogliosis, demyelination, and remyelination have been detected in normal appearing tissue during clinical remission in a relapsing-remitting population [66]. Neuronal loss and atrophy have been observed histochemically in deep gray matter nuclei [67]; abnormalities in these regions are supported by MRI findings, which report T_2 hypointensity [68, 69], suggestive of increased iron accumulation [70]. MS, in all its forms, clearly produces widespread neurodegeneration; however, the extent of this degradation, its cause, and the considerable inter-patient variability is poorly understood. Improved imaging methods could potentially improve our understanding of this disease and aid in the design and administration of therapies.

Magnetic resonance imaging assists with disease diagnosis and has increased our understanding of the pathology. WM lesions typically appear hyper-intense on T_2 weighted acquisitions and can be distinguished from CSF with a fluid attenuated scan. Some acute lesions are abnormal on T_1 weighted images but partially recover as they evolve into chronic lesions [71]. A hypo-intense (increased T_1) core is attributed to demyelination and loss of glial and neuronal cells; partial remyelination may explain gradual T_1 recovery. A hyper-intense (decreased T_1) ring can also be present, but its cause is unknown [72]. Contrast enhancement with chelated gadolinium compounds reveal blood brain barrier leakage and indicate sites of active disease. These traditional imaging methods are employed to aid clinical diagnosis but typically correlate poorly with patient symptoms [73, 74].

Advanced imaging techniques have been developed to probe specific alterations in tissue structure and composition and have been applied to study MS [75]. Magnetization transfer imaging is sensitive to interactions between the semi-solid and mobile water pools [76]; furthermore, quantitative magnetization transfer measures are related to myelin content [77]. Multicomponent T_2 analysis enables extraction of the myelin water fraction [78]. Reduced myelin water has been observed in normal appearing white matter and in white matter lesions [79]. Susceptibility weighted imaging is sensitive to the magnetic susceptibility of tissues, which is particularly altered in the presence of iron. Susceptibility phase enhancement has been observed in lesions [80, 81] and in deep gray matter structures [48]. There is considerable histological [82] and imaging [80, 48] evidence that iron accumulates in the brains of MS patients, but its role in disease progression is poorly understood. Furthermore, optimal detection methods have not yet been established.

1.4.3 Non-Heme Brain Iron

The human brain contains a variety of essential metals; of these, only copper, manganese, and iron are paramagnetic and alter MR relaxation rates. Except under abnormal conditions, copper and manganese concentrations are insufficient to noticeably alter the MRI signal, but iron occurs with sufficient concentration (above ∼0.1 mM) to be detected indirectly [83].

Iron is a crucial element of cellular metabolism. Notably, it is used in the mitochondrial electron transport chain, and it may also have a role in myelin formation in the central nervous system [84]. Iron readily accepts or donates an electron making it extremely redox active and potentially toxic. As such, it is carefully regulated via transport proteins (like transferrin), bound to chelating ligands, and is stored in an accessible, but non-reactive form.

The human brain contains an estimated 60 mg of non-heme iron [85]. It is stored primarily in ferritin and hemosiderin and is likely concentrated in oligodendrocytes. Ferritin is a protein that forms a water-soluble shell, housing up to 4500 iron atoms [86]. Within the ferritin shell, iron is believed to be stored as a ferrihydrite crystal [87]; however, its exact form and magnetic properties are poorly understood [88, 89]. Hemosiderin is associated with iron overload and storage diseases and appears to be a degraded form of ferritin — potentially damaged by lysosomes [90].

Excess unchelated iron ions are extremely toxic to tissues because they are known to catalytically enhance reactive oxygen species. The Fenton reactions describe production of extremely reactive hydroxyl radicals (OH• and OOH•) in the presence of ionic iron [91]. These free radicals react almost immediately and can damage most macromolecules, such as lipids (including membranes and myelin), nucleic acids, and amino acids. Iron storage, chelation, or transport deficiencies are thus hypothesized as a potential cause or contributor to neuronal loss in neurodegenerative diseases [92].

In Parkinson's disease, increased iron has been reported in midbrain and basal ganglia structures [93, 94, 95]; Unfortunately, its specific form and reactivity is rarely noted. The pattern of signal loss in magnetic resonance images is consistent with suspected neuronal loss [96], suggesting that MRI is capable of detecting iron and that it may serve as a disease biomarker.

In MS, oligodendrocytes are preferentially destroyed. Although possibly coincidental, these cells contain a large proportion of the non-heme brain iron. As discussed in Section 1.4.2, increased iron has been observed in the brains of MS patients; however, its role in the pathology is poorly understood.

Measuring iron with MRI has proven surprisingly challenging considering its presence can strongly alter relaxation rates and bulk susceptibility. Numerous reports have described T_2 hypo-intensity and shortening on quantitative measures in regions of probable iron content. Truly quantitative iron measurements have been elusive given the complex nature of relaxation: macromolecules and unpredictable water content obfuscate iron induced relaxation. Despite confounds in quantitatively measuring iron, imaging methods that are sensitive and specific to iron are required to assess the role of iron in neurodegenerative diseases. An additional discussion of iron sensitive imaging is deferred to Section 5.1.

1.5 Thesis Objectives

High field scanners have the potential for high resolution or rapid imaging with emphasized susceptibility contrast. Current imaging methods are inadequate to fully exploit these advantages: spin echo sequences require prohibitive RF power deposition and may be excessively sensitive to RF heterogeneity. Transmit field heterogeneity certainly precludes traditional quantitative T_2 measurement techniques. Gradient echo sequences are highly sensitive to background field variations and excessive artifacts occur at the echo times required to maximize relaxation weighting and susceptibility phase contrast.

This thesis aims to improve certain critical imaging methods for qualitative and quantitative imaging at high field strengths; a focus is placed on developing sequences and reconstruction tools for a 4.7 T human scanner. The specific objectives of this work are to:

- Demonstrate the efficacy of low refocusing angles for FSE imaging in a SAR constrained regime.
- Enable time-efficient FSE imaging at 4.7 T for high resolution and rapid T_2 weighted imaging.
- Develop a quantitative method for measuring the transverse relaxation times in heterogeneous RF fields.
- Improve GRE imaging for robust qualitative and quantitative imaging, despite intense background field gradients.
- Demonstrate the utility of these methods, and high field strengths in general, for investigating neurodegenerative disease.

These objectives are systematically addressed in the following chapters. Before proceeding, I strongly recommend a snack break and perhaps a dram of Laphroaig.

Chapter 2

Qualitative Fast Spin Echo Imaging

Fast spin echo imaging requires major modifications for efficient acquisition at high field strengths where extreme RF power deposition precludes consecutive high angle pulses. Refocusing angles reduced from 180° offer significant power savings and represent a viable and flexible strategy for imaging at high field strengths. Previous works have mathematically described the effects of reduced refocusing angles in terms of signal levels and relaxation rate changes; however, their utility at high field remains unclear. Section 2.1 describes the use, and consequences, of reduced refocusing angles for time-efficient multislice acquisitions with T_2 weighting. It presents a range of protocols for fast or for high resolution imaging. This chapter also presents two technical notes investigating the behaviour and use of low, and highly variable, angle echo trains. A geometrical interpretation of variable angle echo trains is presented in Section 2.2 along with simple guidelines for echo train modulation. Section 2.3 presents the "Virtual 180", a new class of short echo trains with highly variable refocusing angles for high resolution imaging with extreme power reductions.

2.1 Time-Efficient Fast Spin Echo Imaging at 4.7 T With Low Refocusing Angles[1]

2.1.1 Abstract

An implementation of fast spin echo at 4.7 T designed for versatile and time-efficient T_2-weighted imaging of the human brain is presented. Reduced refocusing angles ($\alpha < 180°$) are employed to overcome SAR constraints and their effects on image

---

[1] A version of this section has been published. Lebel RM, Wilman AH. Time-efficient fast spin echo imaging at 4.7 T with low refocusing angles. Magn Reson Med 2009;62:96-105.

quality are assessed. Image intensity and tissue contrast variations from heterogeneous RF transmit fields and incidental magnetization transfer effects are investigated at reduced refocusing angles. We found that intra-slice signal variations are minimized with refocusing angles near 180°, but apparent gray/white matter contrast is independent of refocusing angle. Incidental magnetization transfer effects from multislice acquisitions are shown to attenuate white matter intensity by 25% and gray matter intensity by 15% at 180°; less than 5% attenuation was seen in all tissues at flip angles below 60°. We present multislice images acquired without excess delay time for SAR mitigation using a variety of protocols. Sub-second half Fourier acquisition single shot turbo spin echo (HASTE) images are obtained with a novel variable refocusing angle echo train ($20° < \alpha < 58°$) and high-resolution scans with a voxel volume of 0.18 mm^3 are acquired in 6.5 minutes with refocusing angles of 100°.

2.1.2 Introduction

Fast spin echo imaging, also known as RARE [25] and TSE, is a robust imaging sequence with numerous clinical and research applications. Prototypical FSE uses a 90° excitation pulse and a train of 180° refocusing pulses repeated every *TR* to form a single image. These refocusing pulses render FSE largely insensitive to static field inhomogeneities.

High field imaging systems — loosely defined here as those exceeding 3.0 T — pledge exceptional capabilities including faster or higher resolution imaging with altered, and possibly enhanced, tissue contrast mechanisms. Unfortunately, there are impediments to high field imaging [97]: First, static magnetic field heterogeneities scale linearly with main field strength and exacerbate signal losses and geometric distortions. Second, short RF wavelengths cause non-uniform sensitivity profiles for excitation and reception [54]. Third, RF power deposition scales approximately quadratically with static field strength [52]; patient safety requirements can limit successive high flip angle pulses, as required by FSE.

Nevertheless, high-resolution FSE images of the human brain have previously been obtained at 4.7 T [98, 99] using long inter-echo spacings (22 ms) to reduce the temporal density of RF pulses, short echo trains (8 refocusing pulses), slightly reduced refocusing flip angles (162°), and likely also long RF pulses, to constrain SAR within safety regulations (4 W/kg for short exposure times). These works demonstrate that FSE and high field are not mutually exclusive; however, this implementation is ill-suited for variants, such as HASTE, where short echo spacings and long echo trains are required and would produce extreme SAR levels due to a large number of brief, high angle pulses per unit time. SAR mitigation strategies such as RF pulse elongation and bandwidth reduction provide modest power savings and can be applied to high-resolution imaging, but are, in general, of limited versatility and are insufficient to compensate for power levels at very high field. Limited reports from 7.0 T have presented 2D FSE images of the human head [100, 101], but at the expense of the number of slices and with excess delay time for SAR reduction.

Previous works have shown that reducing, and often modulating, the refocusing angles of the FSE echo train is a viable means of RF power reduction, contrast manipulation, and point spread function modification. A favorable non-linear relationship between echo amplitude and refocusing angle [26] permits drastic power reductions with relatively minor signal penalties. The favorable magnetization behaviour results from a superposition of spin, stimulated, and indirect signal pathways [26, 28]. The latter two pathways introduce T_1 components into the echoes, thus producing longer effective transverse relaxation times [39], particularly in tissues with large T_1/T_2 ratios, such as GM and WM at high field. The optimized SPSS, in which coherent and intense echoes are formed, is achieved via modulation of the first few refocusing angles [34, 30, 32].

Refocusing angle reduction and modulation is a robust technique for RF power mitigation and will play an important role in time-efficient (i.e., without excessive delays for SAR reduction) FSE at high field; however, the effects of reduced flip angles on tissue contrast and image homogeneity in the presence of heterogeneous transmit RF fields have not yet been described. Here, we examine the utility of reduced refocusing flip angles in an implementation of 2D multislice FSE at 4.7 T designed for time-efficient anatomical imaging with diverse resolution requirements and time constraints. We examine the properties of reduced refocusing angles, including image contrast and intensity variations due to transmit inhomogeneities and incidental magnetization transfer effects during multislice imaging. We present example protocols and images illustrating the capabilities of reduced refocusing angle FSE at 4.7 T.

2.1.3 Methods

Following informed consent from healthy volunteers, human brain imaging was performed using a 4.7 T whole-body imaging system controlled by a Varian Unity Inova console. Maximum gradient strength was 35 mT/m with a rise time of 300 μs. All imaging used a 27 cm diameter birdcage RF coil (XLR imaging, Canada) [102] for transmission. Unless otherwise stated, a closely coupled 4-element array coil (PulseTeq, United Kingdom) [103] was used for signal reception. In all cases, transmit power was calibrated in the center of the brain; excitation pulses were prescribed at 90° while refocusing angles, applied orthogonally to the excitation pulse, were varied. Gradient waveforms were optimized for coherent spin/simulated echo formation using the pre-scan method proposed in [104].

Contrast and Intensity Variations

Prescribing reduced refocusing angles diminishes the initial echo amplitudes and prolongs the effective transverse relaxation times; inadvertent angle reductions from inhomogeneous transmission may introduce contrast and intensity variations between and within images. Simple intensity variations are relatively benign, since they alter image uniformity but may be rectified during post-processing. However, contrast variations, which inherently include some correctable intensity changes, have the potential to alter the relative signal between different tissue types, effectively degrading the information content of the image set. Of particular concern are changes in visible contrast — changes in the hierarchy of tissue intensity. For T_2 weighting, we typically expect fluid to be brightest, followed by GM, then by WM. This order may be altered, and our ability to delineate tissues lost, if apparent relaxation times of brain tissues vary sufficiently and independently. We investigated contrast and intensity variations by experimentally measuring the relative tip angle distribution in an image slice, then by modeling their variations using this distribution; these predictions are validated with experimental imaging sets.

The relative tip angle from a birdcage volume coil was measured via the double angle method [105] implemented on a multislice spoiled gradient echo sequence. Tip angles were 60° and 120° with a *TR* of 13 sec. Echo time was 4 ms; field-of-view was 22.0×21.0 cm^2; imaging matrix size was 128×46 with 46 slices, each 5 mm thick with no intra-slice gap. A profile was measured along the anterior/posterior direction of an axial slice that was spatially smoothed and normalized to the peak intensity. Variation is reported as the percent difference between the maximum transmit field near the center of the profile, and the minimum field at the edge of the head.

Following previously published methodology [39, 36, 38], the relative amplitude of the transverse magnetization, $M_\perp$, at the n^{th} echo can be described by:

$$M_\perp(n) = f_{coherence}(n) \cdot f_{relaxation}(n), \tag{2.1}$$

where $f_{coherence}$ describes the spin state derived from the full history of refocusing pulses, neglecting relaxation, while $f_{relaxation}$ accounts for the variation between the full transverse magnetization and the coherence term and is attributed to T_1 and T_2 relaxation. The magnetization and coherence terms may be computed with the EPG algorithm [26, 38]; the relaxation term may then be determined by reorganizing Eq 2.1. Expressing the magnetization as separable coherence and relaxation terms isolates intensity and contrast modulations due to transmit variations, intentional or otherwise.

The coherence term is independent of relaxation parameters, so it does not contribute to contrast variations. Its response to intentionally reduced flip angles has been well described elsewhere [26, 34, 32]. The relaxation component depends on flip angle history and tissue relaxation rates; this component alters image contrast. It may be approximated as an exponential decay with an effective decay rate R_{2eff} (12). We calculate R_{2eff} changes, relative to R_2 ($R_2 = 1/T_2$), as a function of prescribed refocusing flip angle for three tissues with relaxation times approximating those of CSF ($T_1/T_2 \approx 4500/2000$ ms), GM ($T_1/T_2 \approx 2000/60$ ms), and WM ($T_1/T_2 \approx 1200/50$ ms) [106, 107, 108] at 4.7 T to illustrate the prolonged effective relaxation times at reduced flip angles.

Using the EPG algorithm, we calculate $f_{coherence}$ and $f_{relaxation}$ from Eq 2.1 along the transmit profile for a range of prescribed refocusing angles. Fourth echo profiles are obtained following three catalyzing pulses for SPSS preparation whose flip angles are computed with the “3-ahead” algorithm [32]. For symmetry with coherence terms, $f_{relaxation}$ components are presented as fractional rate reductions and are based on the relaxation times for GM.

Single-slice FSE images were collected with refocusing angles of 200°, 180°, 120°, 90°, 60°, and 30° to demonstrate the cumulative effect of heterogeneous RF fields. In this case, the volume coil was used for both transmission and reception. The first three refocusing angles were computed with the “3-ahead” algorithm; the remaining angles were held constant. The effective echo time (TE_{eff}) was 38 ms, ESP = 9.5 ms, $TR = 3.5$ s, FOV = 25.6×19.2 cm^2, matrix size = 256×192, and slice thickness = 5.0 mm.

Incidental Magnetization Transfer Contrast

Magnetization transfer (MT) effects significantly alter tissue contrast in multislice FSE [109], are enhanced at high field, and depend on the refocusing flip angles [110], and make accurate contrast predictions difficult [39]. We demonstrate MT effects in 2D FSE at various refocusing flip angles by plotting ratios of multislice to single-slice image intensities in regions of CSF (body of the left lateral ventricle), GM (left posterior cingulate gyrus), and WM (splenium of the corpus callosum). Images were acquired with a TR of 3 sec, TE_{eff} of 15 ms, ESP of 15 ms, and ETL of 9. Imaging matrix was 220×129 reconstructed from 70% partial Fourier, the FOV was 22.0×18.0 cm, and the slice thickness was 3.0 mm. For simplicity, we employed 4.0 ms Gaussian pulses with a time-bandwidth product of 2.0 for both excitation and refocusing. Multislice images were acquired with 13 interleaved slices with a 12.0 mm gap on either side of the central slice and no gap between the remaining slices. This arrangement minimized direct saturation while retaining off-resonant irradiation typical of multislice imaging. Eight image sets were collected with refocusing angles between 40° and 180°, in increments of 20°. For rapid SPSS preparation and echo train stability, the first refocusing pulse was set to $90° + \alpha/2$, where α was the prescribed refocusing angle of the remaining echo train [30].

Imaging Protocols

Three drastically different FSE protocols were developed: single-shot, fast intermediate resolution, and high-resolution imaging. Parameters are chosen for optimal image quality. Specifically, refocusing angles were selected, or computed, to balance SNR and SAR while TE_{eff} was selected for T_2 weighting with consideration given to incidental MT and reduced effective relaxation times. For all cases we report the acquisition duty cycle, which is defined as the ratio of time spent during gradient events to the total imaging time. We also report the 10 second average RF transmit power, measured from RF amplifier output without accounting for system losses. Power is deposited to the whole head and a portion of the neck (∼3 kg).

HASTE images were acquired from a healthy 22 year-old in the sagittal and axial planes with a novel refocusing scheme based on the extended echo-train acquisition [38]. The original method modulates refocusing angles to provide a near constant signal level in the first half of the echo train; flip angles are ramped to a higher value (115° in Ref. [38]) in the later half of the train, during which time the signal decays gradually. In this scheme, RF power is concentrated in the second half of the echo train, where the angles are relatively high. Our low-power version modulates the initial refocusing angles for constant signal, but then constrains the maximum flip to conserve RF power. In our implementation, the first 28 refocusing pulses were computed with the "1-ahead" algorithm [32] to yield a constant relative signal level of 0.22 for GM ($T_1/T_2 \approx 2000/60$ ms). Refocusing angles were then prohibited from exceeding 45°. ETL=63, ESP = 5.5 ms, TE_{eff} = 77 ms, FOV = 25.6×17.9 cm^2 (RO, anterior/posterior), bandwidth = 62.0 kHz. Images were homodyne reconstructed with a matrix size of 102×146 with the central 28 echoes used for phase estimation. Images were then interpolated to 358×512. Each slice was acquired in 347 ms with an interslice delay of 122 ms (for gradient duty cycle reduction). A total acquisition time of 15 seconds (one *TR* period) provided full brain coverage with 32 contiguous slices, each 5.0 mm thick.

Intermediate resolution images were collected from a healthy 24 year-old in the axial plane with refocusing angles ramped down via 151°, 110°, and 96° pulses, as prescribed by the "3-ahead" algorithm, then held constant at 90° for the remainder of the train. Refocusing angles were chosen to provide over 83% of the signal (estimated with the EPG algorithm, neglecting relaxation), with only 32% of the RF power required for an equivalent train of 180° pulses. Echo train length was 9; ESP, 15 ms; TE_{eff}, 60 ms; *TR*, 5.0 sec; FOV, 22.0×21.6 cm^2 (RO, anterior/posterior × PE, left/right); imaging matrix size, 256×252 with 32 continuous 5 mm thick slices;

bandwidth, 40.0 kHz. Total acquisition time was 2.3 min. Images are unfiltered and interpolated to 512 × 504. We present images before and after processing with a local polynomial fitting algorithm for intensity correction.

High-resolution images were acquired from a healthy 25 year-old in the axial plane with 100° refocusing angles, except for the first refocusing pulse at 140° [30]. This refocusing scheme retained 83% of the signal, but required only 35% of the RF power of an equivalent train of 180° pulses. Echo train length was 8; ESP, 20.5 ms; TE_{eff}, 41.0 ms; TR, 6.1 sec; bandwidth, 50.0 kHz; FOV, 22.0×22.0 cm^2 (RO, anterior/posterior × PE, left/right); imaging matrix, 512 × 512 with 30 contiguous 1 mm thick slices yielding a voxel volume of 0.18 mm^3. Total image acquisition time was 6.5 min. Images were processed with a mild 3D low-pass Butterworth filter (relative cutoff frequency of 1.0) for noise reduction, interpolated to 1024 × 1024, then intensity-corrected.

2.1.4 Results

Contrast and Intensity Variations

Effective transverse relaxation rates for three main brain tissues at 4.7 T as functions of refocusing pulse angle are shown in Fig 2.1. WM and GM display similar fractional rate changes resulting from large, and nearly equivalent, T_1/T_2 ratios at high field; CSF, whose T_1/T_2 ratio is near unity, shows minor relative rate reductions. Drastically prolonged signal decay can be achieved using reduced flip angles: effective relaxation times for WM and GM are doubled at 60° and more than tripled at 30°.

A relative flip angle map through the center of the head in the axial plane is shown in Fig 2.2a. The transmit field from a volume coil at 4.7 T is highly heterogeneous: a maximum variation of 44% was found along a profile in the anterior/posterior direction, as shown in Fig 2.2b. This variation is responsible for numerous intensity and contrast variations within the imaging plane. Transverse magnetization following excitation, modulated by the sine of the excitation angle, will display a maximum intensity variation of 23%. If the same coil is used for reception, and assuming the reception field is similar to the transmit field, an additional 44% intensity variation will be observed.

Intraslice coherence and effective relaxation rate changes following SPSS preparation with the "3-ahead" method are shown in Fig 2.3. As seen in Fig 2.3a, variation in the coherence term is minimized at refocusing angles slightly above 180°, where the center of the slice is attenuated but edges show improved coherence. A larger percent difference between slice center and edge is observed at lower prescribed angles despite less absolute flip angle variation. Intraslice effective relaxation rate changes, shown in Fig 2.3b, have a local minimum at high refocusing angles and

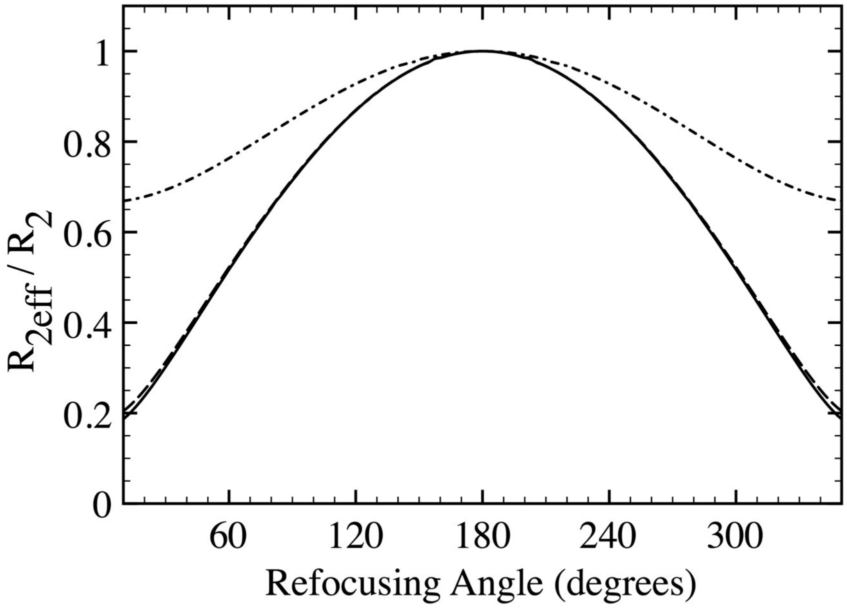

Figure 2.1: Effective transverse relaxation rates for tissues approximating GM, WM, and CSF at high field (solid line, dashed line, and dot-dashed line, respectively), are plotted versus the refocusing flip angle. Large T_1/T_2 ratios of GM and WM yield similar fractional enhancements while CSF, with a T_1/T_2 ratio near unity, shows less dependence on refocusing angle.

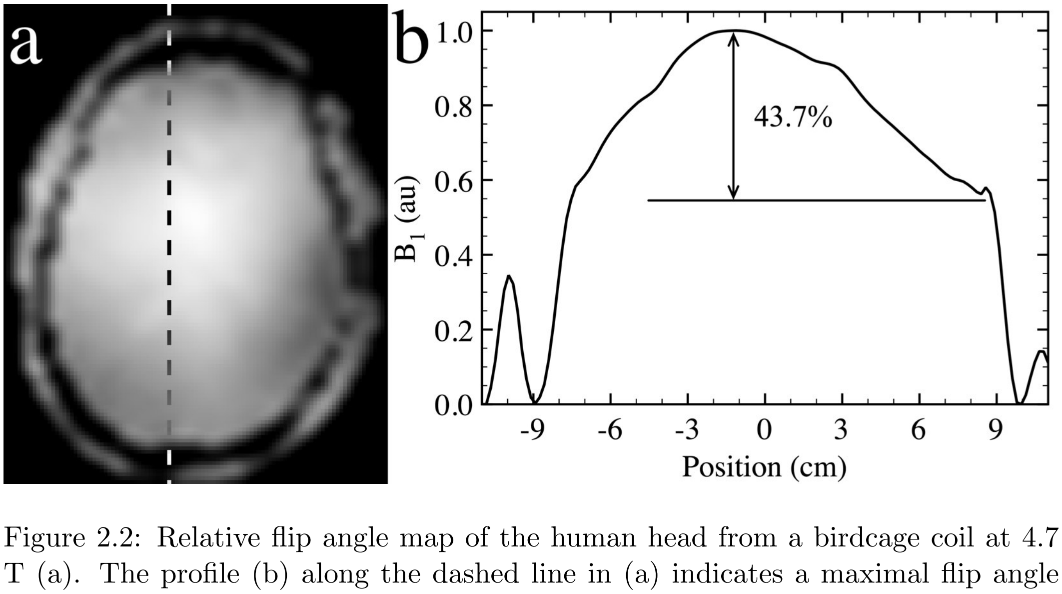

Figure 2.2: Relative flip angle map of the human head from a birdcage coil at 4.7 T (a). The profile (b) along the dashed line in (a) indicates a maximal flip angle variation of 44% in the anteriorposterior direction.

are largest at angles around 90°. As expected from Fig 2.1, intraslice relaxation variations for WM (not shown) are similar to those of GM, while CSF (not shown) has considerably less change. Note that coherence and relaxation terms generate opposing signal changes: coherence reductions lower signal intensities while effective relaxation rate reductions maintain higher signal levels. The net signal variation depends on flip angle history and echo time.

The combined effect of heterogeneous RF fields on signal excitation, refocusing, relaxation, and reception is demonstrated in the Fig 2.4 image series. Global image intensity is similar with refocusing angles of 200°, 180°, and 120° (top row, left to right) while intensity reductions are visible with refocusing angles of 90°, 60°, and 30° (bottom row, left to right). To assess relative intensity and homogeneity, profiles through the image set shown in Fig 2.4, relative to the profile through the 180° image, are displayed in Fig 2.5. From Fig 2.3a alone, one would expect noticeable intensity reductions at 120°; however, reduced effective relaxation rates, described in Fig 2.1 and Fig 2.3b, maintain WM and GM signal intensities. With refocusing angles less than or equal to 90° at this 38 ms echo time, low echo coherence dominates slow signal decay of GM and WM and produces visible intensity reductions. CSF (gray bands in Fig 2.5) is the only component to display actual visible contrast variations with refocusing angle as evidenced by its deviation from surrounding tissues. With slight concavity, the 200° profile shows improved intensity homogeneity over the 180° profile; image homogeneity decreases with refocusing angle reductions from 180°, as demonstrated by increasing convexity of the profiles. These results are in agreement with predictions from Fig 2.3.

Incidental Magnetization Transfer Contrast

Presented in Fig 2.6 are multislice to single-slice image intensity ratios from regions of CSF, GM, and WM at various refocusing angles. WM signal is attenuated by 25% with 180° flip angles, GM by 15%, and CSF shows no attenuation. Less than 5% signal change was measured in all tissues with refocusing angles less than or equal to 60°.

Imaging Protocols

Our single-shot low-power extended echo train is shown in Fig 2.7a. The refocusing angles and resulting EPG computed signal levels from GM, WM, and CSF are plotted. Flip angles early in the echo train are modulated to provide uniform GM signal during acquisition of the center of k-space — the portion used for homodyne phase correction. Exponential signal decay is observed during the remainder of the echo train where refocusing angles are constrained to 45°. This refocusing scheme yields narrow point spread functions (Fig 2.7b), with full-width-at-half-maximum

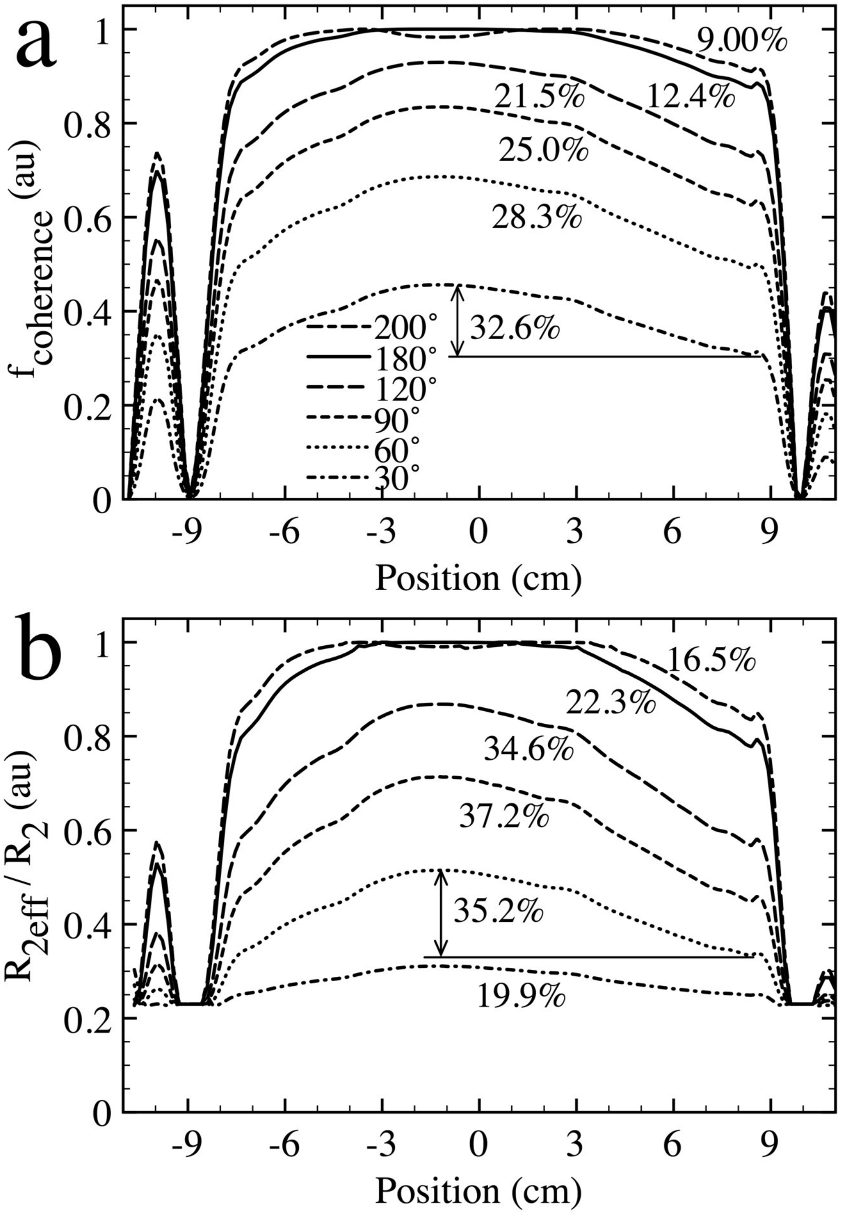

Figure 2.3: Coherence (a) and fractional GM relaxation rate changes (b) along the profile in Fig 2.2 due to heterogeneous RF transmission, plotted for several prescribed refocusing angles, as annotated. Signal variations due to relaxation and spin coherence are simultaneously minimized at high refocusing angles.

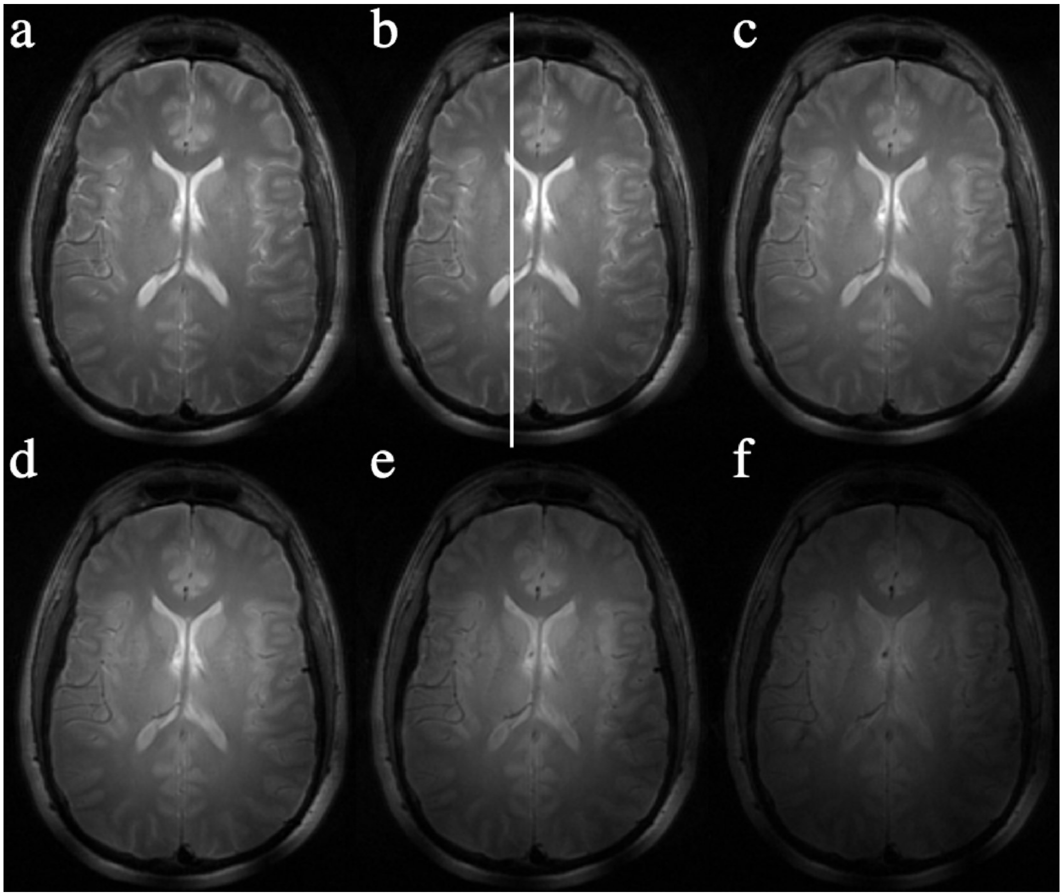

Figure 2.4: FSE images with refocusing angles of 200°, 180°, 120°, 90°, 60°, and 30° (af), respectively, shown at the same window and level. At an echo time of 38 ms, overall image intensity is reduced at lower flip angles, but the visually apparent image contrast remains largely unchanged: CSF is brightest, followed by GM, then WM. The vertical line in (b) indicates the region of signal profiles in Fig 2.5.

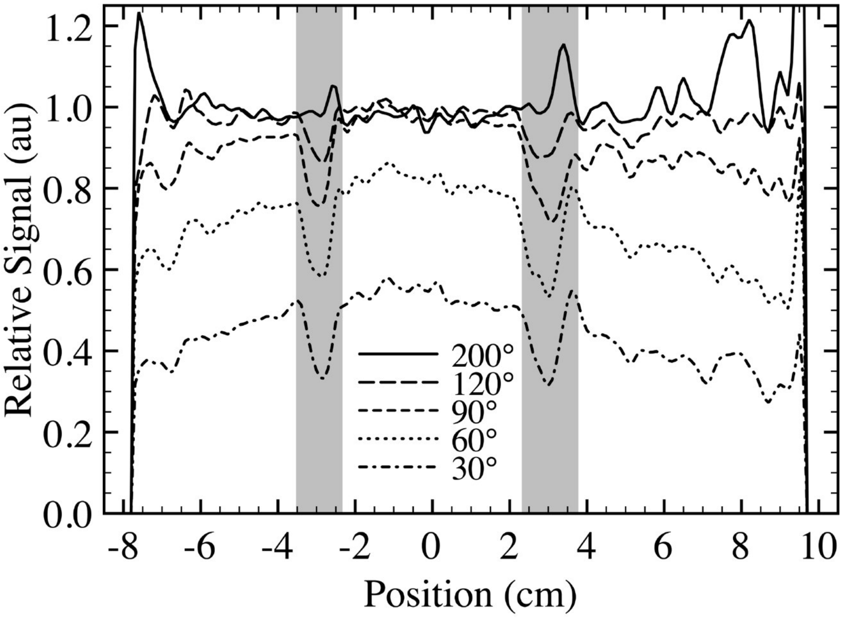

Figure 2.5: Signal profiles in the anterior/posterior direction through slices shown in Fig 2.4, normalized by the 180° profile. Gray bands represent regions of CSF. Relative concavity of the 200° profile confirms improved signal homogeneity over the 180° profile while increasingly pronounced convexity at lower angles supports our prediction of reduced homogeneity. Reduced effective signal decay rates from WM and GM at low angles are apparent when compared to CSF.

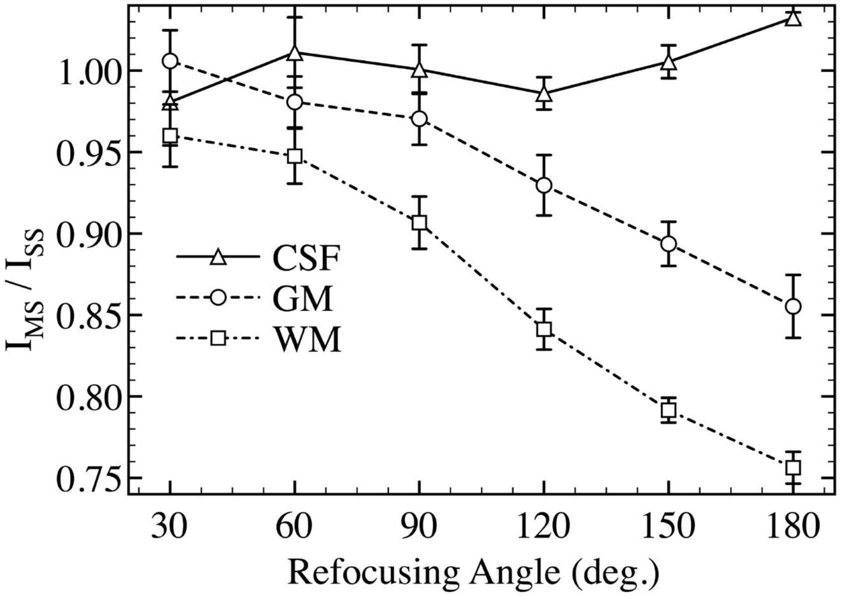

Figure 2.6: Multislice (I_{ms}) to single-slice (I_{ss}) signal intensities in regions of GM, WM, and CSF at various refocusing angles. Error bars represent standard deviation within the regions of interest. Signal attenuation from MT can drastically affect tissue contrast, particularly at high refocusing angles, but has little influence below 60°.

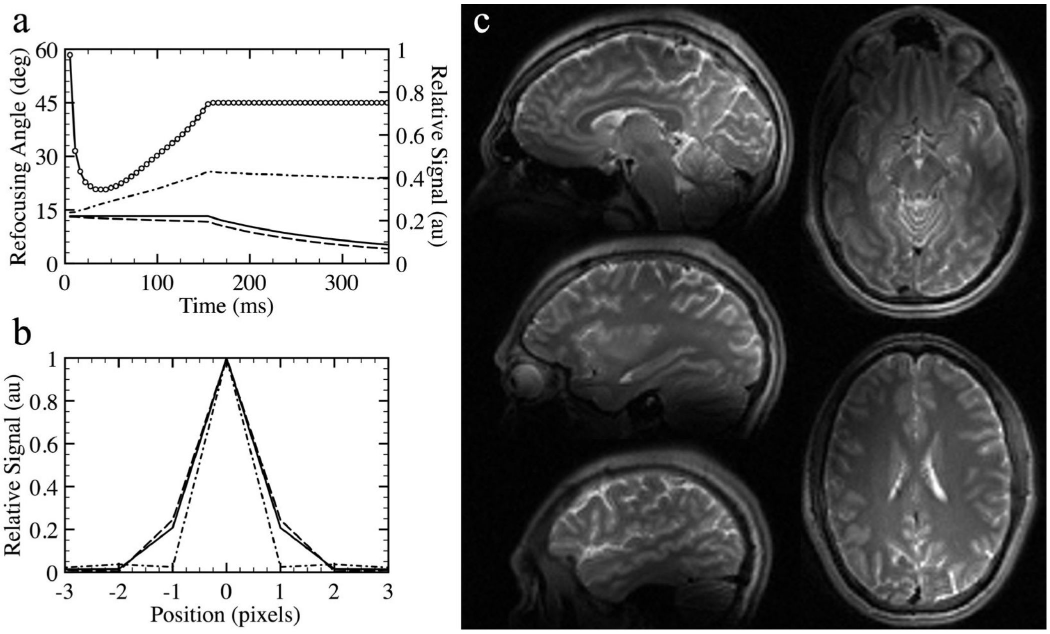

Figure 2.7: Low-power extended echo train refocusing angles (solid line with open circles) on the left axis and signal levels for GM (solid line), WM (dashed line), and CSF (dash-dotted line) on the right axis (a). Resulting point spread functions for the above tissues (same line types) acquired with a half-Fourier single shot echo train (b). An assortment of sagittal and axial HASTE images ($1.75 \times 1.75 \times 5.00$ mm^3) acquired in 347 ms/slice (c).

values of 1.26, 1.32, and 1.02 pixels for GM, WM, and CSF, respectively. This echo train generates detailed images (Fig 2.7c), acquired in 347 ms per slice (plus 122 ms gradient delay time) with a net multislice acquisition duty cycle of 77%. Short-term average RF power was 3.8 W (1.3 W/kg) — roughly 5% of that required by an equivalent train of 180° pulses and sufficiently low for continuous exposure.

Axial slices taken from a full-brain dataset acquired in 2.3 min are shown in Fig 2.8a–c; intensity-corrected versions in Fig 2.8d–f. Resolution was $0.86 \times 0.86 \times 5$ mm^3, acquisition duty cycle was 86%, and the RF power was 6.5 W (2.2 W/kg). Array coil reception sensitivity and transmit intensity variations were effectively removed with intensity correction to provide uniform T_2-weighted images. Very high-resolution T_2-weighted FSE images are shown in Fig 2.9a,b; inverse contrasts in Fig 2.9c,d. Resolution was $0.43 \times 0.43 \times 1.0$ mm^3 — resulting in a voxel volume of only 0.18 mm^3. The duty cycle was 81% and RF power 4.8 W (1.6 W/kg). Acquisition time for the 30-slice volume was 6.5 min.

2.1.5 Discussion

The use of reduced refocusing flip angles is a robust SAR mitigation strategy for FSE at high field strength; significant power reductions are possible with only modest

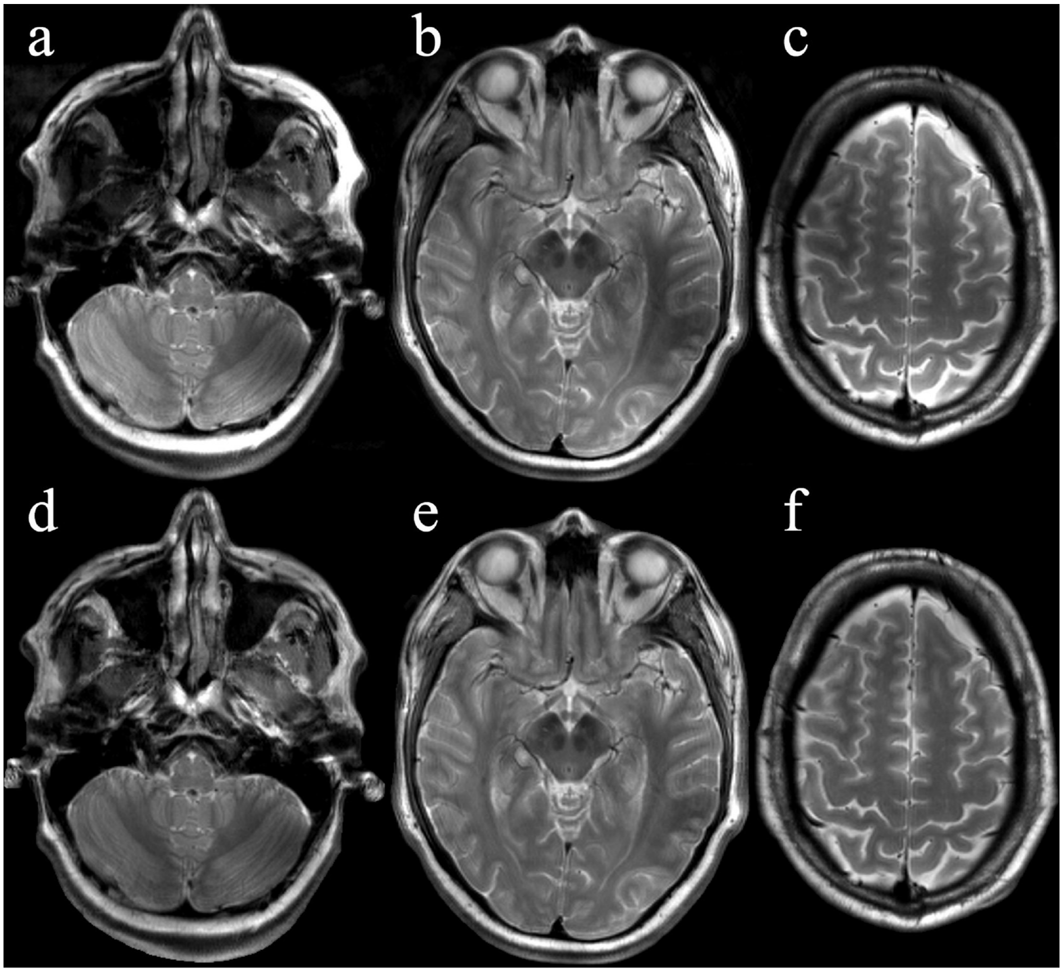

Figure 2.8: Intermediate resolution images ($0.86 \times 0.86 \times 5$ mm^3) taken from a 32-slice dataset acquired in 2.3 min. Images without, (a–c), and with, (d–f), intensity correction are shown. Full brain T_2-weighted images can be obtained in a clinically acceptable scan time with refocusing angles ramped down to 90°. Intensity-corrected images illustrate uniform apparent contrast between brain tissues despite transmit and reception heterogeneity.

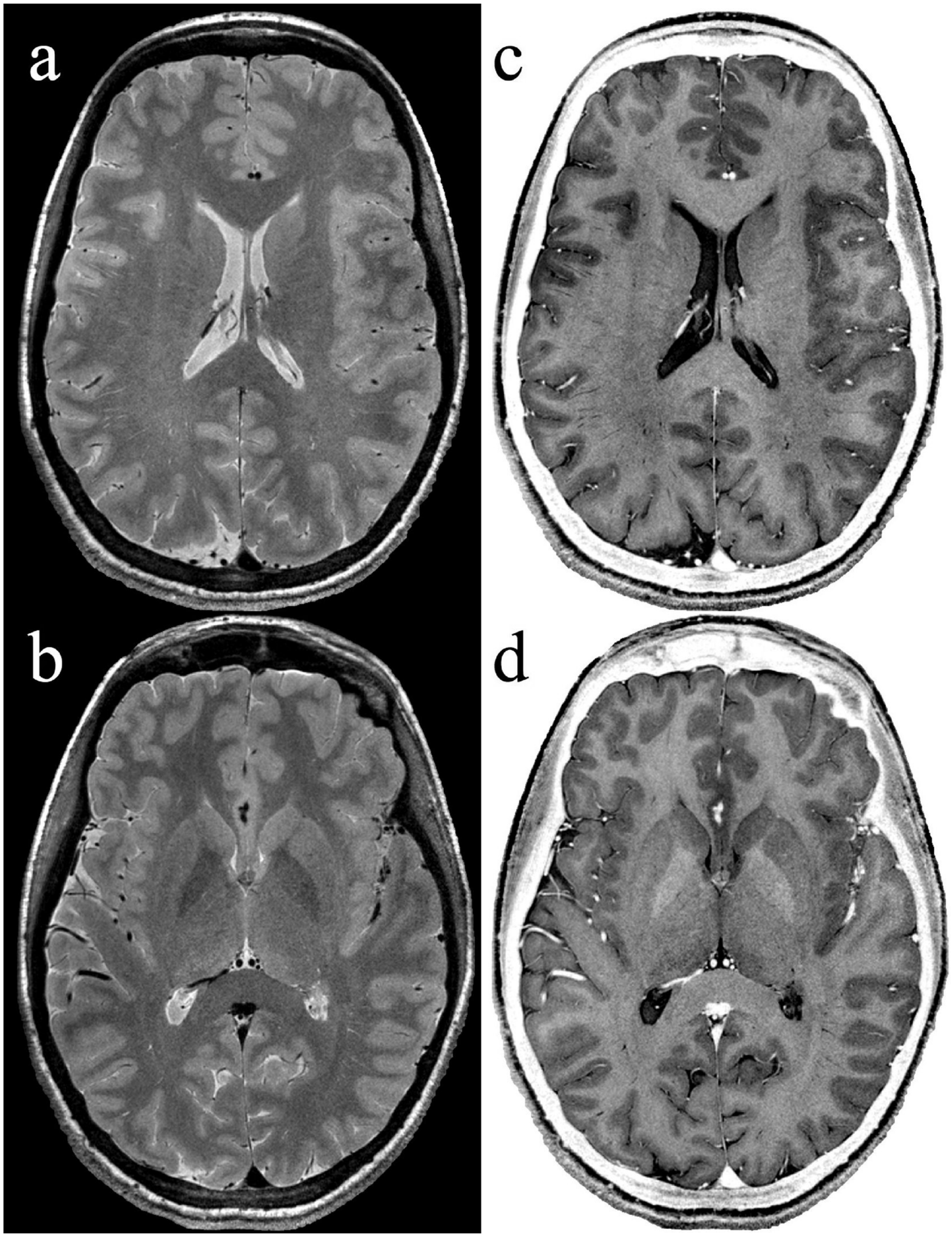

Figure 2.9: Representative images taken from a 30-slice dataset with 0.43×0.43 mm^2 in-plane resolution and 1.0 mm slice thickness (voxel volume of 0.18 mm^3) acquired in 6.5 min with 100° refocusing pulses, prepared with an initial 140° refocusing pulse. T_2-weighted images, (a,b), and their inverse contrasts, (c,d), are shown. Images have been intensity-corrected to demonstrate uniform visual contrast.

signal decreases. Furthermore, low refocusing angles elicit reduced signal decay rates, which are particularly pronounced for WM and GM at high fields. Effective relaxation rate changes are determined by T_1/T_2, and are maximized at ratios above $\sim$15 [34], which occurs for WM and GM at high field. Furthermore, slower signal decay permits longer readout periods or more refocusing pulses and nearly restores lost SNR due to initial signal drops. Despite the attractiveness of reduced flip angles for high-field FSE, apparent image contrast in the presence of transmit heterogeneity must be characterized.

Contrast and Intensity Variations

Throughout this work, the transmit coil was calibrated at the center of the brain, where the transmit field is maximized. This calibration was chosen because it is one of several standard methods [52] and it provided a worst-case scenario for signal variation assessment. A volume RF coil at 4.7 T produced a maximum 44% transmit B_1^+ variation within a single axial slice of the human head at 4.7 T.

At clinical field strengths, with nearly uniform RF fields, traditional T_2-weighting can be maintained at reduced refocusing angles with longer effective echo times [39, 38]. In the presence of heterogeneous fields, tissue contrast and signal intensity variations within an image, or a set of images, are of concern with reduced refocusing angles. Note that the first echo is unique: it is comprised exclusively of spin echo components and lacks stimulated echo contributions observed in later echoes. Its intensity is modulated by $\sin^2(\alpha_1/2)$, where α_1 represents the first refocusing angle, and signal relaxation is independent of the refocusing angle. This echo can be used for applications requiring spatially uniform relaxation rates; however, as described by Thomas et al. [99], it displays larger intensity variations than do subsequent echoes. Unlike the first echo, later echoes exhibit effective relaxation rates that are dependent on refocusing angle. Our analysis describes the magnetization following its transient behavior observed during the first few echoes. During this period, flip angles are intentionally modulated (via computational [32] or geometric methods [30, 111]) for SPSS preparation to provide increased signal levels and reduced oscillations relative to echo trains lacking initial flip angle preparation. Following this preparation, magnetization during the remainder of the echo train can be modeled according to Eq 2.1 as a separable function of echo coherence and relaxation.

Coherence and effective relaxation rate variations resulting from 44% transmit variation at 4.7 T are simultaneously minimized with refocusing angles slightly above 180°. In this case, magnetization at the image center is attenuated in order to enhance magnetization at the edges. Images acquired at or above 180° are thus expected to appear the most uniform; this was confirmed experimentally with the image set in Fig 2.4 and profiles in Fig 2.5. Image profiles are normalized by the 180° profile to remove reception sensitivity and baseline tissue contrast, effectively isolating intensity and effective relaxation rate changes due to the refocusing angle. Increasingly pronounced profile convexity as refocusing angles are reduced indicates more extreme intensity variation across the slice. While deleterious to SNR, transmit-based intensity modulations may be remedied with edge-enhancing array coil reception and image post-processing, both of which were employed in this work. Relaxation variations are more troublesome: anatomy and pathology may be obscured if tissue intensity inversions occur. Fortunately, WM and GM have equivalent fractional rate changes (Fig 2.1). While magnetization in the center of the brain may decay faster than at the edges (Fig 2.3b), visual contrast remains similar within and between images. There is clear visual delineation of brain tissues in all images shown in Fig 2.4: CSF has a higher intensity than GM, which is brighter than WM. Only CSF displays a marked contrast change in the relative signal profiles of Fig 2.5. Any actual contrast variations are dwarfed by the diversity of GM relaxation rates at high field due to tissue iron (21,27). The latter reference found GM at 4.7 T to have apparent (including diffusion proximal to non-heme iron) relaxation times ranging from 38 ms up to 64 ms. We conclude that although intensity and contrast variations exist between and within image slices, FSE images with reduced refocusing angles at 4.7 T retain conventional T_2-weighting.

Acquisition schemes, such as those of Busse [37] and Hennig et al. [36], where the center of k-space is acquired with high refocusing angles, while the periphery of k-space is acquired with much lower angles, will likely be advantageous at high field. 3D variants with low refocusing angles [112, 113] are also very promising at high field and warrant further investigation.

Through-plane transmit changes are a concern for multislice image homogeneity; however, an active power modulation technique that adjusts transmit gain based on slice position has been demonstrated to reduce apparent inhomogeneities for multislice FSE imaging [99]. Thomas et al. acknowledge SAR as a serious limitation of active power modulation. We expect the combination of reduced refocusing angles and active power modulation will provide more uniform FSE imaging volumes at high magnetic field strengths.

Approaches to compensate for intraslice RF signal variations are far more complex than active power modulation for interslice variations. Multidimensional pulses may be used at a cost of additional RF power and duration, and, once matured, multicoil transmission technology may provide uniform transmit fields at high field [114]. At most centers, intraslice signal variations are currently unavoidable, but may be minimized with appropriate acquisition parameters and postprocessing.

Incidental Magnetization Transfer Contrast

Magnetization transfer effects are well known to alter contrast with multislice FSE [109]. A recent work at 4.7 T demonstrated signal differences of 20–25% in edge slices when using refocusing angles of 162°, and attributed these differences to MT signal attenuation [99]. While the experimental methodologies differ, our results (Fig 2.6) show the same reductions of WM intensity with flip angles between 150° and 180°. It was recently reported that MT attenuation and refocusing angle were correlated in WM and GM at 1.5 T and 3.0 T [110]. Weigel et al. demonstrated increased MT contrast at 3 T relative to 1.5 T and ∼7% signal attenuation in WM with 60° refocusing pulses. This is consistent with our findings at 4.7 T, where refocusing angles below 60° showed less than 5% variation in WM. Recent works with inversion recovery FSE noted T_1 reductions in multislice [115] and multislab [116] imaging, an effect attributed to MT. Incidental MT is clearly a major — possibly dominant — contrast mechanism with FSE at high refocusing angles and at high field. Fortunately, as with proton density, incidental MT operates in conjunction with T_2 processes to enhance signal differences between brain tissues with FSE. This helps explain the strong T_2-like weighting observed in images formed from early echoes with high refocusing angles [99], but makes contrast prediction and protocol design challenging.

Incidental MT contrast will depend on factors including RF pulse shape and echo train length in addition to the refocusing angle, investigated here. We restricted our analysis to a single parameter set since an exhaustive study of the numerous variables influencing MT contrast is beyond the scope of this work. Our short echo train (9 pulses) parameter set was selected as a compromise between common imaging configurations and RF power deposition. We did not investigate longer echo trains since dangerously high SAR levels are required for multislice imaging with large echo train lengths at high refocusing angles — which necessitate short and powerful RF pulses. While our findings indicate negligible MT contrast at refocusing angles below 60°, this result is only applicable to acquisition parameters resembling those used here; incidental MT may contribute significantly with extended low angle echo trains. Further investigation is warranted.

Imaging Protocols

High-field HASTE images can be obtained with reduced and modulated refocusing angles, as shown in Fig 2.7. This application benefits considerably from reduced effective relaxation rates at low refocusing angles; slow signal decay permits the extended echo trains required for spatial encoding. Initial flip angle modulation, computed for constant GM signal, yields a narrow point spread function for all tissue types, thus producing crisp images despite relatively low resolution and very low refocusing angles. In spite of considerable image nonuniformity using the reduced refocusing angles, due in part to array coil reception, there remains a clear visual distinction between brain tissues. From our RF power deposition measurement and refocusing scheme, we expect multislice HASTE with 180° refocusing pulses would require in excess of 75 W. Obviously, conventional HASTE is not usable at 4.7 T, or at higher field strengths.

Images mimicking T_2-weighted clinical scans can also be achieved with refocusing angles ramped down to 90° (Fig 2.8). Full brain coverage with sub-millimeter in-plane resolution can be obtained in 2.3 min at power levels below RF exposure limits, without parallel imaging or partial Fourier. Regions with high iron content, such as the red nucleus and substantia nigra, are prominent in Fig 2.8b–e. Images show uniform apparent contrast between brain tissues, particularly following intensity correction, despite 90° refocusing pulses, which cause the largest intraslice relaxation variation (37%, as shown in Fig 2.3b). Low refocusing angles are also applicable to high-resolution imaging. Images shown in Fig 2.9 were taken from a multislice dataset acquired with about one-third the power that would be required with 180° pulses.

2.1.6 Conclusion

Robust FSE imaging can be achieved at 4.7 T with reduced and variable refocusing flip angles. This approach provides flexible SAR management, effectively removing the major obstacle to efficient multislice FSE at high field. While reduced refocusing angles decrease initial signal intensities, they prolong signal decay. WM and GM at 4.7 T (and higher field strengths) display similar relative rate reductions, permitting classic T_2 contrast to be obtained despite a highly heterogeneous transmit field. Intraslice signal variation is largest at low refocusing angles and minimized at angles slightly above 180° in the center of the brain. These variations are largely intensity-based and do not drastically alter contrast; therefore, they can be corrected with post-acquisition processing. Incidental MT effects during multislice imaging significantly bias image contrast at high refocusing angles, but are negligible at angles below 60°. With reduced refocusing angles, we efficiently acquired a variety of multislice T_2-weighted FSE images including sub-second HASTE images with a novel low-power extended echo train, fast images at standard clinical resolution with 90° refocusing angles, and high-resolution images with 100° pulses.

2.2 The Transition Pulse: A Geometric Analysis of Variable-Angle FSE[2]

2.2.1 Abstract

We present a simple and intuitive means for determining the flip angles required for smooth transitions between static pseudosteady-states in fast spin echo imaging with variable flip angle echo trains. We demonstrate the effectiveness of single and multiple transition pulses to successfully vary refocusing flip angles while retaining high signal levels. The graphical interpretation presented here is consistent with previous analytic techniques and permits accurate signal intensity predictions along the echo train.

2.2.2 Introduction

Fast spin echo imaging (or RARE [25]) is capable of generating detailed images with an assortment of contrast weightings, and is highly insensitive to static magnetic field inhomogeneities. However, even at low magnetic fields, FSE can be limited by RF power deposition arising from the use of closely spaced, high flip angle refocusing pulses. At higher magnetic fields, RF power becomes an even greater limitation, precluding a direct implementation of the standard low field version of FSE. Thus, considerable effort is currently invested in the development of reduced power versions of FSE suitable for imaging at all field strengths.

Recent work has focused on designing reduced, and often variable, flip angle echo trains for the purpose of RF power reduction, contrast manipulation, and point spread function modification. Considerably more signal is obtained from a train of reduced flip angles if the magnetization is initially prepared into the SPSS [34, 30] relative to a train lacking preparation [26]. In this prepared state, magnetization isochromats form a coherent and intense echo. Preparation into a reduced flip angle SPSS can be performed with either a single initial pulse [30], or with multiple pulses to provide a smoother passage from high flip angles [32, 38]. Following preparation, the flip angle can be modulated while maintaining the SPSS in order to tailor the signal response along the echo train. Recently, Hennig *et al.* employed low flip angles to collect the periphery of k-space to preserve magnetization and reduce RF power, then temporarily ramped the flip angle to 180° during acquisition of the central portion of k-space to increase the signal intensity and generate T_2 contrast [36]. Busse proposed a related method in which the center of k-space is collected near the beginning of the echo train with relatively high flip angle pulses, and the periphery is acquired later in the echo train with much lower flip angle pulses [37].

---

[2] A version of this section has been published. Lebel RM, Wilman AH. Intuitive design guidelines for fast spin echo imaging with variable flip angle echo trains. Magn Reson Med 2007;57:972-975.

He was also able to correct for the SPSS intensity changes encountered during the variable flip angle echo train to reduce blurring. Numerous flip angle schemes have been proposed to integrate k-space filtering envelopes into the echo train and to compensate for relaxation to minimize point spread function distortions [32, 38]. Reduced and variable flip angle echo trains show extreme promise for RF power management and contrast manipulation; however, current algorithms for computing flip angles provide little insight into the rules governing SPSS transitions and are frequently computationally complex.

This work provides an intuitive approach to the design of variable flip angle echo trains. Based on the geometrically derived preparation pulse proposed by Hennig and Scheffler [30], we describe generalized transition pulses used to initialize and convert between static pseudosteady-states. Since the transition pulses are based on a simple geometric argument, the flip angles can be readily calculated to provide rapid and smooth SPSS variations. In addition, our analysis tracks the SPSS during flip angle changes, permitting analysis of subsequent pulses and signal prediction along the variable echo train.

2.2.3 Theory

The SPSS describes the ideal magnetization arrangement during reduced flip angle refocusing trains. In this state, transverse magnetization forms a coherent echo midway between refocusing pulses. This is contrary to the dynamic pseudosteady-state achieved during a reduced flip angle sequence lacking SPSS preparation, in which a coherent echo is not observed. More detailed descriptions and illustrations of the SPSS for reduced flip angles are provided elsewhere [30, 32].

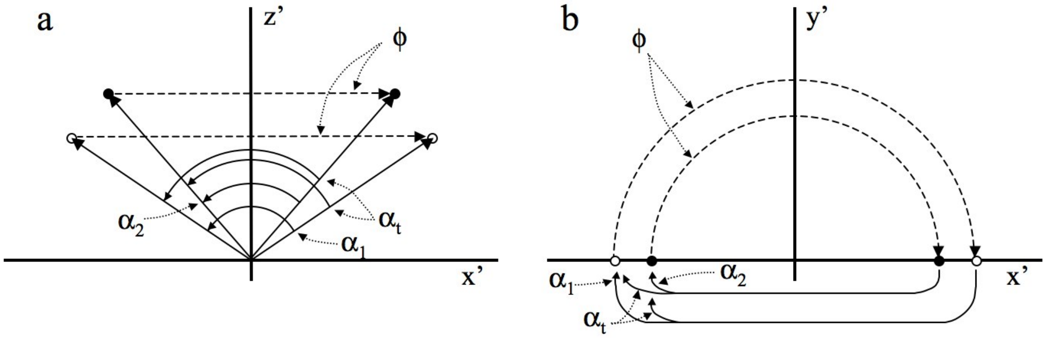

Figure 2.10: Illustration of an isochromat with precession angle $\phi = \pi$ for two reduced refocusing angle SPSS(α_1) and SPSS(α_2) as viewed from the (a) $-y'$ and (b) z' directions. The transition angle α_t will approximately convert between the two states.

Hennig and Scheffler presented an elegant geometrical argument justifying an initial $90° + \alpha/2$ preparation pulse to approximate the SPSS for subsequent refocusing pulses with flip angle α [30]. This was based on the observation that the SPSS magnetization immediately following a refocusing pulse resides on a plane rotated away from the transverse plane about the y' axis of the rotating frame. Assuming the magnetization following excitation is initially distributed in the transverse plane, a single $90° + \alpha/2$ refocusing pulse in the y' direction places the magnetization in a state resembling SPSS(α). We generalize this preparation pulse into a transition pulse, with flip angle α_t, applied to convert the magnetization from SPSS(α_1) into SPSS(α_2), as shown in Fig 2.10 for an isochromat with precession angle $\phi = \pi$. The precession angle was chosen purely for diagrammatic clarity, the same flip angle relations apply to all isochromats. The relationship between the transition flip angle and the two SPSS flip angles is obtained from geometric analysis of Figure 2.10 and is simply their mean value:

$$\alpha_t = \frac{\alpha_1 + \alpha_2}{2}. \tag{2.2}$$

It is useful to solve Eq 2.2 for α_2 in order to predict the SPSS flip angle following a transition pulse:

$$\alpha_2 = 2\alpha_t - \alpha_1. \tag{2.3}$$

The generalization of the single preparatory pulse into a transition pulse permits the passage between static pseudosteady-states at arbitrary points during the echo train and provides a simple tool for the design and analysis of arbitrary flip angle trains.

It is important to distinguish between the SPSS flip angles, α_1 and α_2, and the transition flip angle, α_t. The SPSS flip angles are those which define, and are required to maintain, the SPSS. They are also related to the inclination of the magnetization relative to the transverse plane. A transition pulse mediates the passage from SPSS(α_1) into SPSS(α_2) rather than enter into its own. For example, a direct step from α_1 to α_2 will transition into SPSS($2\alpha_2 - \alpha_1$) rather than SPSS(α_2). Subsequent applications of α_2 will result in oscillatory echo behaviour and degrade magnetization coherence; a passage pulse would transition to the proper SPSS.

The mean-angle transition pulse if also applicable to the design of multiple pulse transitions such as initial SPSS preparation and continually varying flip angle echo trains. Multiple pulse transitions can be decomposed into recursive applications of single transition pulses. Transition pulse design begins by selecting a function such as a linear ramp or a smoother windowing function [37] to define the intermediate SPSS states. The transition flip angles are then chosen from the desired sequence of static pseudosteady-states via iterative application of Eq 2.2.

2.2.4 Materials and Methods

Experiments were performed on a 4.7 T system using a one-dimensional single shot FSE sequence on a water phantom ($T_1 \approx T_2 > 3$ s). Gaussian refocusing pulses of 1.6 ms duration were used with an echo spacing of 8.4 ms and an echo train length of 32. Hardware limitations restricted the transmit gain to 1 dB increments. All echo trains were prepared into the SPSS during the first three pulses according to the "3-Ahead" algorithm in Table 1 in [32], then transitioned to a second SPSS commencing at the 17^{th} echo. Echo amplitude plots were generated to illustrate signal variations around this transition echo. Normalization of the plotted echo amplitudes was performed in two ways. First, relaxation along the echo train was compensated for by normalizing to an echo train remaining in the first SPSS, without transition. Second, to provide a meaningful vertical scale, the plots were globally scaled such that the initial SPSS echo intensities matched their theoretical values.

Bloch magnetization simulations were performed to complement the experimental data by computing echo intensities and remnant signal oscillations following flip angle jumps mediated by a more complete range of transition nutation angles. Relaxation was excluded to isolate flip angle induced signal variations. Simulated magnetization was prepared into an initial SPSS with three catalyzing pulses selected using the "3-Ahead" algorithm. Flip angle changes commencing at the 17^{th} echo and mediated by one and two pulses were investigated. We report the average and standard deviation of the signal of the 19^{th} to 32^{nd} echoes to assess the signal level attained and oscillations following various transition flip angles.

2.2.5 Results

Figure 2.11 shows experimental echo intensities surrounding a 17^{th} echo transition from 90° to 140° using either a direct step or a single intermediate 115° pulse. The mean flip angle pulse efficiently shifts between states given that the signal intensity following the move to 140° corresponds to its theoretical value of 0.97. Following the transition pulse, residual oscillations still occur due to the large flip angle jump, the approximate nature of these transition angles, and the use of slice selective RF pulses.

While it is apparent that a single transition pulse improves the signal response relative to a direct jump, Fig 2.12 demonstrates that a mean flip angle pulse provides the maximum signal intensity with near minimal residual oscillations relative to other mediating pulse angles. For the specific example shown, a transition from 90° to 140°, simulations indicate a 115° pulse yields the maximum signal with a gradual and symmetric drop off at higher and lower angles. Signal oscillations are nearly minimized at the mean angle with the global minimum occurring at 121°.

Figure 2.13 reports the experimental signal intensities surrounding a transition

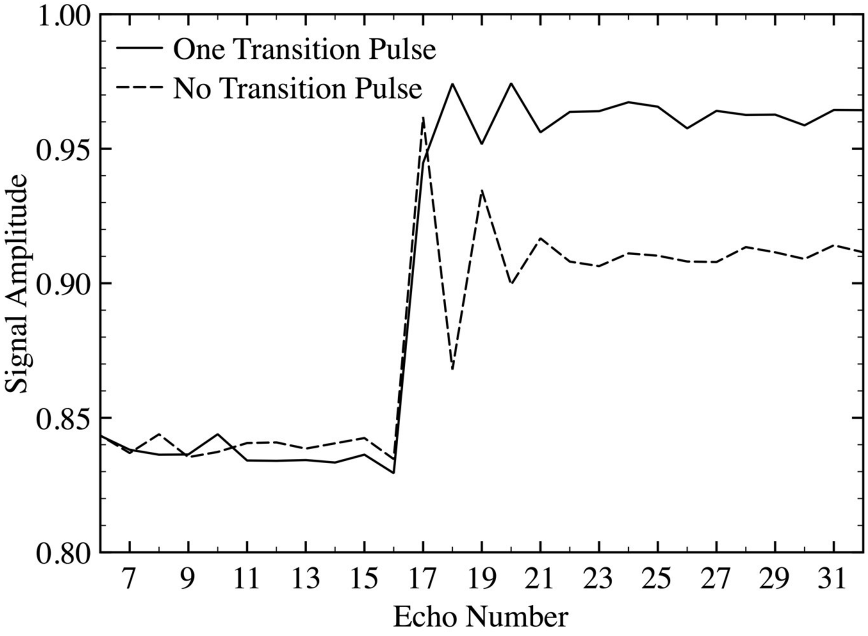

Figure 2.11: Experimental signal intensities from echo trains initially prepared into SPSS(90°), which then transition from 90° to 140° with either a single 115° transition pulse at the 17^{th} echo (solid line) or no transition pulse (dashed line).

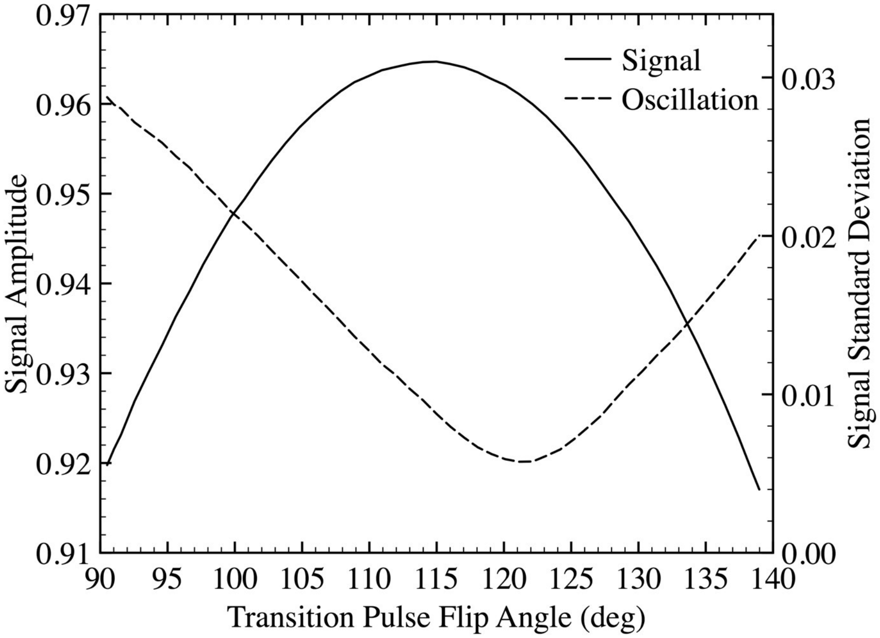

Figure 2.12: Simulated average echo amplitudes (solid line, left axis) and standard deviations (dashed line, right axis) following flip angle transitions from 90° to 140° as a function of the transition pulse flip angle.

between 60° and 150° commencing at the 17^{th} echo occurring either directly or assisted by sequential 75° and 120° transition pulses. Note that transition flip angles were not computed from a windowing function as described previously, but were selected from discrete transmitter powers that approximately satisfy the transition guidelines described above. Despite this hardware limitation, Fig 2.13 demonstrates that multiple pulse transitions can be employed to smoothly shift between states provided the final SPSS resulting from repeated transition pulses corresponds to the final flip angle.

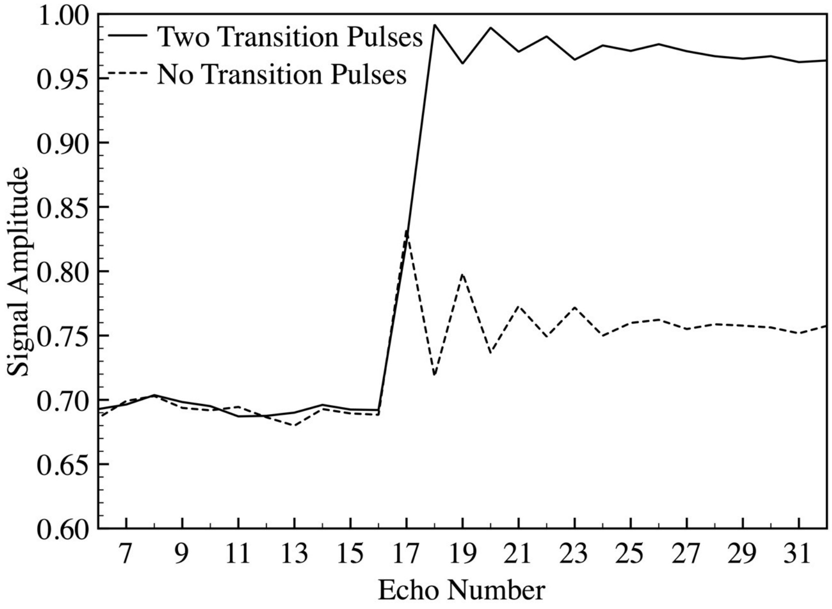

Figure 2.13: Experimental signal intensities from echo trains initially prepared into SPSS(60°), which is then transition from 60° to 150° with either sequential 75° and 120° transition pulses commencing at the 17th echo (solid line) or no transition pulses (dashed line).

The colour scales in Fig 2.14(a, b) represent the mean and standard deviations of the simulated signal intensities following transitions from 60° and 150°, respectively, as a function of two sequential transition pulses, α_{t1} and α_{t2}. The maximum signal intensity and minimum signal oscillations closely follow the mean flip angle transition guideline, indicated by the diagonal black line. The signal response displays a broad peak nearly centered about the mean flip angle condition, effectively permitting alternate ramp designs, including those not strictly satisfying the mean flip angle criteria, to provide efficient SPSS modulation. Design flexibility is expected due to the approximate nature of the mean flip angle theory, however, SPSS coherence is destroyed when flip angle combinations deviate sufficiently from the mean transition pulse requirement. Although we limit our investigation to two pulse transitions, extensive simulations indicate our analysis is equally valid for longer pulse ramps.

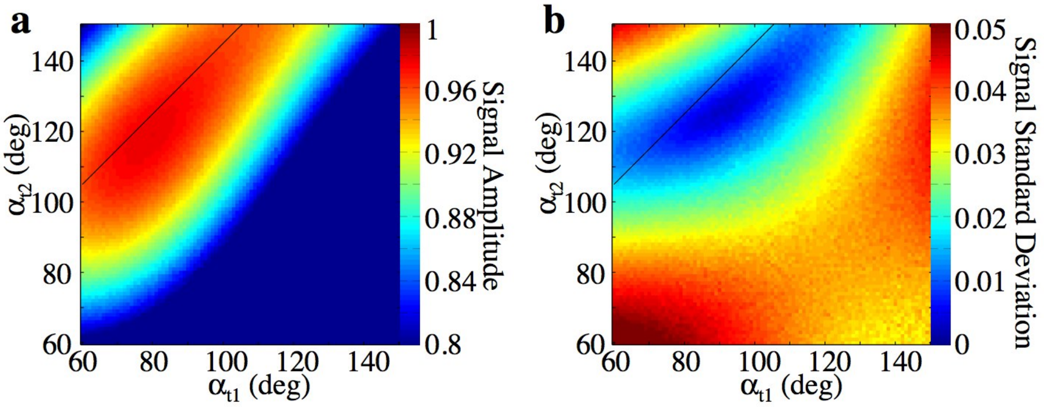

Figure 2.14: Simulated average echo amplitudes (a) and standard deviations (b) following a two-step transition from 60° to 150° using flip angles α_{t1} then α_{t2}. The diagonal lines indicate transition pulse combinations yielding magnetization in SPSS(150°) following two iterative applications of Eq 2.3.

2.2.6 Discussion

The $90° + \alpha/2$ preparation pulse can be generalized to a mean flip angle transition pulse that provides a technique for approximate SPSS modulations during reduced and variable flip angle echo trains. We have shown that transitions between flip angles should be mediated with at least one pulse to retrain SPSS coherence and reduce signal oscillations. Multiple pulse transitions are easily designed by selecting a smooth windowing function to define intermediate SPSS values then computing the required flip angles according to Eq 2.2.

These transition pulses are compatible with those used in previous works and provide an intuitive interpretation of their effect. The single $90° + \alpha/2$ preparation pulse can be recast as $(180° + \alpha)/2$ since the excitation pulse initializes the magnetization into the SPSS defined for 180° refocusing pulses. Upon rewriting, the preparation pulse becomes a mean flip angle transition pulse as described in this work. The extended phase graph algorithm has been used to compute and tabulate the first three transitory pulses required to approximate the SPSS for a broad range of final flip angles [32]. The preparation angles for final flip angles above 40° computed according to the preferred "3-Ahead" algorithm conform closely to the transition requirements presented in this work. Rapid SPSS preparation to flip angles below 40° in only three pulses is difficult to achieve with the approximate transition pulses presented here; for those cases, more advanced techniques, like the extended phase graph algorithm, are preferred. The normalized windowing functions suggested by Busse to transition from high (α_{high}) to low (α_{low}) flip angles by decrementing each flip angle ($\Delta\alpha_i$) [37] are also consistent with this work. The normalization condition imposed to scale the windowing function ($\sum \Delta\alpha_i = \alpha_{low} - \alpha_{high}$) is equivalent to our series of mean transition pulses whose incremental differences satisfy the same normalization.

The mean flip angle transition pulse theory can be employed to predict and compensate for signal intensity variations resulting from SPSS changes during variable flip angle echo trains. The theoretical signal intensity following the transition pulse can be determined analytically [34] using α_2, which is computed according to Eq 2.3. The theoretical SPSS signal intensities can be used to compensate for intensity variations along the echo train [37]. The latter reference employed heuristic effective flip angles, extrapolated from the local derivatives of a smooth function, rather than the applied flip angle to compute the SPSS echo intensities. This approximately compensates for the difference between transition and SPSS flip angles, as described in this work. Simulations of a linear flip angle ramp from 60° to 180° over 8 pulses indicate that signal predictions employing the SPSS flip angles are within 3% of simulated values (data not shown) and provide the same degree of accuracy as the effective flip angle approach of Busse [37], yet provide an intuitive geometrical justification.

2.2.7 Conclusion

The present work demonstrates that the numerous flip angle modulation techniques for FSE imaging with reduced and variable flip angle echo trains all execute similar geometric rotations of the SPSS magnetization. We have described a mean flip angle transition rule to unify previous works and to assist in the design of computationally simple variable flip angle refocusing schemes that maintain the coherent static pseudosteady-state. This analysis also permits signal intensity predictions along the echo train, which can be used for echo intensity correction.

2.3 The Virtual 180[3]

2.3.1 Abstract

We present an approach for designing short echo trains (fewer than ~16 echoes) with highly variable refocusing angles for 2D fast spin echo imaging with drastic SAR reductions. Using established computational techniques and an understanding of the transient signal response to a large change in refocusing angle, short echo trains with beneficial signal responses can be designed. We demonstrate echo amplitudes approaching those afforded by 180° refocusing pulses can be achieved, albeit temporarily, with angles considerably below 180°. Encoding this “Virtual 180” echo into

---

[3] A version of this section has been presented. Lebel RM., Wilman AH. The Virtual 180: Application to High Field Fast Spin Echo Imaging. In Proceedings of the 16th Annual Meeting of ISMRM, Toronto, Ontario, Canada, 2008. p. 230.

the center of k-space yields high SNR images with strong T_2 weighting. RF power levels can be reduced to ∼20% of the standard 180° echo train without significant image degradation. This method is particularly applicable to high resolution imaging at high magnetic field strengths; we demonstrate the utility of this technique for imaging the human brain at 4.7 T.

2.3.2 Introduction

Fast spin echo imaging (also known as RARE [25] and TSE) plays an important role in both routine clinical imaging and research investigation. Traditional FSE employs repeated trains of 180° refocusing pluses to rapidly encode images with very little sensitivity to static field variations. The approximately quadratic increase in RF power with field strength precludes a direct implementation of conventional multislice FSE at field strengths exceeding ∼3 T. A high field compatible version is particularly desirable given the strong susceptibility induced variations encountered at these strengths.

Reduced refocusing angles have been employed to moderate SAR levels, enabling time-efficient FSE imaging of the human head at field strengths up to 4.7 T [117]. Spin dynamics and echo amplitudes have been well characterized for both directly reduced refocusing angles [26] and for smoothly ramped angles [35, 34, 32]. In general, low refocusing angles degrade spin coherences (and thus attenuate signal amplitudes) at the echo times. Echo coherence is not simply a function of the previous refocusing angle, but rather of the entire refocusing angle history. Refocusing angle reductions achieved via smooth passage from 180° maintain the SPSS, whereby spin coherence is optimized and maximal signal amplitudes are observed. Following preparation into the SPSS, which can be approximated with one [30] or more [32] initial refocusing pulses, maximal coherence can be maintained with smoothly varying refocusing angles.

Flip angle modulation schemes, such as TRAPS, have been proposed to exploit this adiabatic coherence behaviour [36, 37]. These approaches employ high refocusing angles while traversing the center of k-space to provide high signal levels and lower angles during acquisition of peripheral k-space lines to reduce the average RF power deposition. These approaches permit RF power reductions of ∼50–80%, relative to a 180° pulse train, while maintaining signal levels nearly equivalent to those of 180° pulses for central k-space acquisition [36]. These approaches require long echo trains, involving a minimum of ∼15, but typically 27 or more pulses, to slowly modulate refocusing angles and maintain the SPSS. With gradual refocusing angle modulations, echo amplitudes are (nearly) in-phase and vary smoothy with refocusing angles. These approaches necessitate short echo spacings (∼5–10 ms) to limit the total train duration and require relatively brief RF pulses (∼2 ms) to avoid eroding readout time. As such, they are of limited utility for high resolution imaging or very high field applications where sizeable encoding gradients are required and long RF pulses may be needed in conjunction with refocusing angle reductions to abate extreme RF power deposition, respectively. Additionally, despite substantial net power reductions, the RF energy in these echo trains is concentrated in a small number of high angle pulses. An example TRAPS protocol (sequence 5 listed in Table 1 of [36]) deposits 32% of its RF energy via 11% of its refocusing pulses. Schemes to further reduce the average RF power deposition must be additionally frugal with pulses nearing 180°.

We have recently described variable refocusing angles in terms of transition pulses that convert between static pseudosteady states [118]. This formalism is particularly relevant to large flip angle changes where the SPSS does not track smoothy with the applied refocusing angle but rather, is launched into a new one. Large refocusing angle changes induce a signal response associated with distant angles. This implies that an intense echo can be produced without a high angle pulse.

In this work, we present a class of short echo trains with variable refocusing angles that provide high signal intensities during the acquisition of central k-space lines. Using the transition pulse principle, near optimal echo coherence and high signal levels can be temporarily achieved without requiring 180° pulses. These trains provide drastic RF power reductions while enabling long RF pulses and high resolution imaging.

2.3.3 Theory

The transition pulse framework defines a refocusing pulse of angle $\alpha_t = (\alpha_1 + \alpha_2)/2$ that mediates SPSS(α_1) and SPSS(α_2). This transition pulse can be used at the beginning of an echo train to convert between SPSS(180°) and SPSS(α). In this case, $\alpha_t = 90° + \alpha/2$, as described by Hennig and Scheffler [30]. The converse is also true: once prepared into a low angle SPSS, one (or more) transition pulses can approximately restore the coherence state associated with 180° refocusing pulses. In this case, transverse magnetization will nearly completely rephase and magnetization stored in the longitudinal state will be reclaimed to form an exceptionally coherent echo — a "virtual 180".

Echo Train Design

The concept of a transition pulse provides insight into magnetization behaviour during highly variable refocusing angles and suggests that SPSS(180°) can be approximated without 180° pulses, but is a relatively crude tool for designing echo trains. We propose a windowing function, centered on the contrast dominant echo, to define the desired signal followed by the "1-ahead" algorithm [32, 38] to compute the refocusing angles needed to provide this signal amplitude.

Any envelope with a flat baseline and abrupt peak may be employed. We investigate an offset, symmetric exponential signal envelope of the form

$$S_{envelope}(n) = [1 - (S_0 + \zeta)] \exp\left(\frac{-|n - n_{eff}|}{w_{envelope}}\right) + S_0. \tag{2.4}$$

In this expression, S_0 is a baseline signal, ζ is an amplitude attenuation factor ($\zeta \leq 1 - S_0$) to account for unobtainable signal levels due to imperfect echo formation, n is the echo number (an integer from 1 to ETL), n_{eff} is the effective echo, and $w_{envelope}$ defines the envelope width.

With short echo trains, SPSS preparation must occur very rapidly. Improved coherence can be obtained by requesting slightly increased signal levels. We have empirically noted that an additional exponential window with amplitude S_{prep} and width w_{prep}, centered around the first echo provides sufficient and rapid SPSS preparation. The target signal for the virtual 180 echo train is given by

$$S_{V180}(n) = S_{envelope}(n) + S_{prep} \exp\left(\frac{-(n-1)}{w_{prep}}\right). \tag{2.5}$$

To maintain feasible signal levels, $S_{prep} \leq 1 - S_{envelope}(1)$, but is typically much smaller; additionally, $w_{prep} \leq 1$, for rapid SPSS preparation.

The relaxation free "1-ahead" algorithm [32] is employed to compute the refocusing angles required to produce the requested signal. This algorithm is recursive, yet deterministic; it is based on the population of spin ($F(0)$), indirect ($F(-2)$), and stimulated ($Z(1)$) echo components at the previous echo, or immediately following excitation. Neglecting relaxation, a refocusing angle α mixes these states into an echo of amplitude [40]

$$S = F(-2)\cos\left(\frac{\alpha}{2}\right)^2 + F(0)\sin\left(\frac{\alpha}{2}\right)^2 + Z(1)\sin(\alpha). \tag{2.6}$$

Solving this equation for α provides two refocusing angles — the lowest angle is selected — that produce a desired signal [32],

$$\alpha = 2\arctan\left(\frac{-Z(1) \pm \sqrt{Z(1)^2 - [F(-2) - S][F(0) - S]}}{F(0) - S}\right). \tag{2.7}$$

If the root in Eq 2.7 is negative, the requested signal cannot be achieved with the current phase state; the requested signal envelope must be modified. This can be achieved by heuristically increasing ζ and recomputing all refocusing angles, or by reducing the target signal of the specific offending echoes.

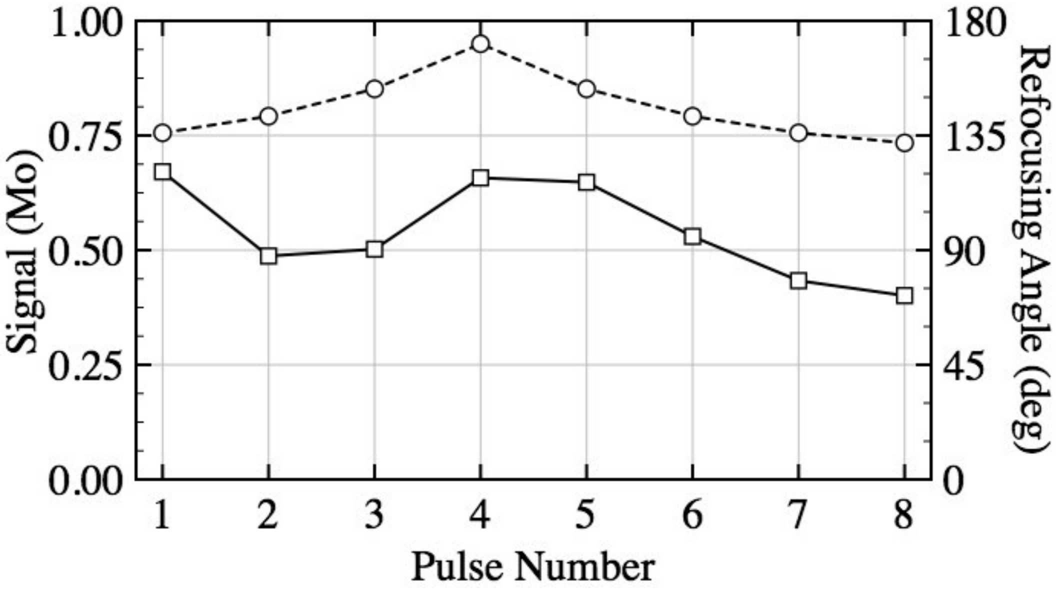

Figure 2.15: A typical virtual 180 echo train (sequence 1 in Table 2.1) designed with a symmetric exponential signal envelope. Signal is shown with a dashed line and circles; refocusing angles with a solid line and squares. The maximum refocusing angle required to produce 95% of the 180° signal is 121°; average RF power is 30% of that required by an equivalent train of 180° pulses.

Using the "1-Ahead" algorithm, a set of refocusing angles can be determined that will produce the virtual 180 echo train. An example signal envelope and required refocusing angles are shown in Fig 2.15. It is important to note that the virtual 180 is a transient phenomena resulting from rapid refocusing angle modulations. There are several restrictions to its existence:

- The virtual 180 cannot occur at the first echo (i.e., $n_{eff} > 1$).
- Narrow signal envelopes (i.e., $w_{envelope} \approx 1$) are required to form the virtual 180; broad envelopes resemble the TRAPS sequence, which employs high angle pulses.
- The virtual 180 is a transient phenomena; high signal levels can only be maintained with subsequent pulses near 180°.

Point Spread Function Correction

The imposed signal envelope produces an intensity modulation across k-space; this results in a point spread function (PSF) in image space. The blurring and ringing associated with this PSF can be corrected by scaling the raw data. Scaling factors are obtained by simply inverting the signal envelope.

Table 2.1: Virtual 180 design parameters

	$S_{envelope,\ prep}$	ζ	ETL	n_{eff}	$w_{envelope,\ prep}$	RFP	σ
1	0.70, 0.00	0.050	8	4	2.0, 0.0	0.30	1.18
2	0.70, 0.00	0.050	8	2	2.0, 0.0	0.29	1.21
3	0.50, 0.08	0.075	8	4	1.5, 0.5	0.20	1.44
4	0.33, 0.15	0.075	5	2	1.0, 0.1	0.24	1.86
5	0.33, 0.15	0.075	8	2	1.0, 0.1	0.16	2.24

This correction process amplifies high spatial frequency noise — an unavoidable cost of PSF correction. Overall noise power is amplified by a factor [37]:

$$\sigma = \sqrt{\frac{1}{ETL}\sum_{j=1}^{ETL}\left[\frac{S_{V180}\left(n_{eff}\right)}{S_{V180}(n)}\right]^2}. \tag{2.8}$$

This PSF correction is an optional procedure. We reconstruct raw and corrected data sets to ensure all available information is visible. Design parameters for virtual 180 trains employed in this work are listed in Table 2.1.

2.3.4 Materials and Methods

Imaging was performed on a Varian Inova whole-body 4.7 T MRI with a maximum gradient strength of 60 mT/m and slew rate of 120 T/m/sec. Images of a resolution phantom filled with tap water and 250 mM sodium chloride were collected with a TEM coil (MR Instruments Inc, USA) for transmit and receive; for human imaging, a 27 cm birdcage transmit coil (XLR imaging, Canada) was paired with a 4-element receive array (PulseTeq, UK). All volunteers provided informed consent in compliance with institutional regulations.

Virtual 180 images of the resolution phantom were collected using the 3^{rd} and 4^{th} protocols in Table 2.1; equivalent images with 180° echo trains were also collected. In-plane resolution was 0.50×0.50 mm^2. Virtual 180 images were reconstructed with, and without, PSF correction. The SNR was evaluated as the average signal in a homogeneous region divided by the average noise signal in a region outside the phantom in the frequency encode direction.

Human brain images were collected with an in-plane resolution of 0.40×0.40 mm^2 and a slice thickness of 2.0 mm. *TR* was 4300 ms, ESP was 15.0 ms, bandwidth was 111 Hz/pixel. Thirty slices were collected with a 1.0 mm gap between edges. Echo times were either 30 ms or 60 ms, based on the protocol. The 2^{nd}, 3^{rd}, and 5^{th} virtual 180 trains from Table 2.1 were employed. Equivalent 180° FSE images could not be collected due to prohibitive RF power deposition. Scan time was 4.6

minutes.

Selection of design parameters is a compromise between RF power, SNR and image blurring (noise amplification upon PSF correction). For typical parameters $w_{envelope} = 1.5$, $w_{prep} = 0.5$ and preparation amplitude $S_{prep} = (1 - S_{envelope})/5$, we compute virtual 180 echo trains with different baseline signal amplitudes and report their relative RF power and noise amplification factors as functions of their maximum echo amplitude (given by $1 - \zeta$).

2.3.5 Results

Cropped images of the resolution phantom are shown in Fig 2.16. Images acquired with 180° refocusing pulses produce crisp images — blurred only by relaxation, which is minimal in this water phantom. All resolution grids (the finest grid contains 1.0 mm diameter holes with a 1.0 mm gap) are resolvable, although the leftmost hole on the finest grid is not seen with an ETL of 8. The second virtual 180 sequence in Table 2.1 employed refocusing angles of 135°, 121°, 111°, 96°, 81°, 73°, 69°, 68°, required 29% relative RF power, and produced 99% of the large structure SNR as the equivalent 180° echo train, Table 2.2. The virtual 180 echo is achieved with a refocusing angle of only 121°. The virtual 180 sequence displays blurring as evidenced by incomplete separation of the finer resolution grids. PSF correction restores lost resolution, at the expense of a measured 16% noise amplification, Table 2.2. Images from the fourth virtual 180 train, using angles of 113°, 124°, 79°, 53°, 37°, are shown in the bottom row of Fig 2.16. Signal intensities between 0.925 and 0.333 are requested in the virtual 180 protocol yet the measured SNR exceeds 98% of the 180° train. Again, blurring can be seen in the virtual 180 image, but is efficiently corrected with a measured noise amplification of 1.75.

Table 2.2: Signal-to-noise ratios and noise amplification factors of conventional and virtual 180 FSE, without and with PSF correction, in the resolution phantom.

	SNR		σ	
Protocol	Raw	PSF Corr.	Measured	Theory
FSE (ETL 8)	14.9	—	—	—
V180 (#2)	14.7	12.7	1.16	1.21
FSE (ETL 5)	15.2	—	—	—
V180 (#4)	14.9	8.5	1.75	1.86

Virtual 180 images of the human brain are shown in Fig 2.17. Two axial slices — the midbrain slice is cropped and enlarged — from three protocols are presented. SNR and artifact levels of the selected slices are representative of the entire volume.

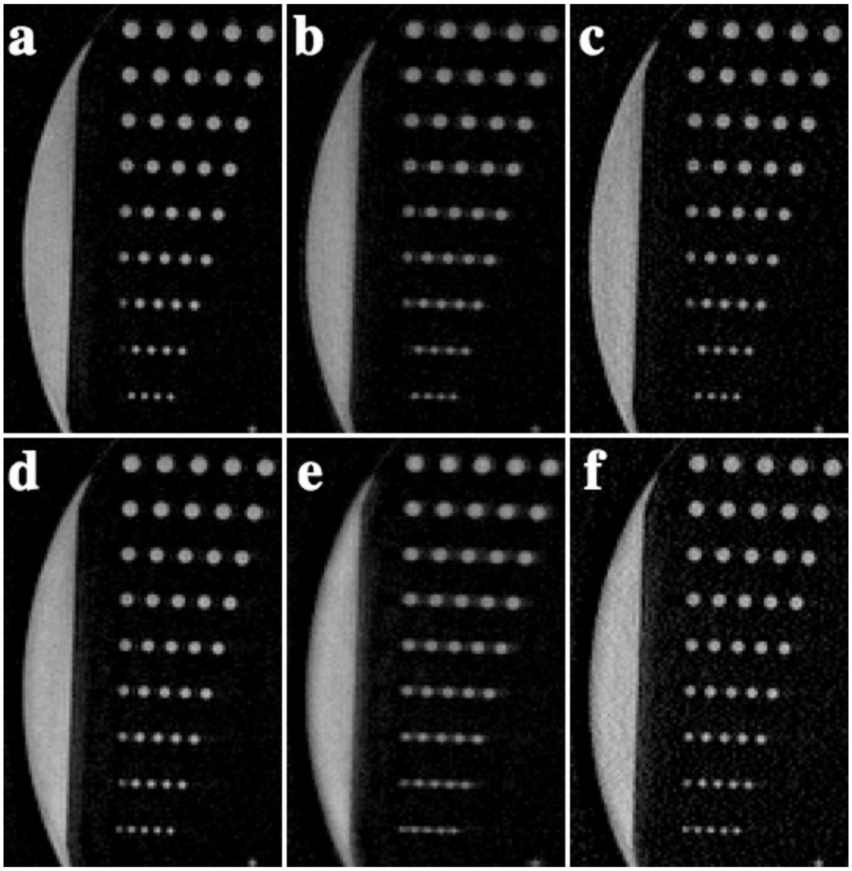

Figure 2.16: FSE and virtual 180 images of a resolution phantom. The top row compares standard 180° FSE with an ETL of 8 (a) to the 2^{nd} virtual 180 sequence from Table 2.1 before (b) and after (c) PSF correction. The bottom row compares standard FSE with an ETL of 5 (d) to the 4^{th} virtual 180 sequence without (e) and with (f) PSF correction. Window and level is constant throughout.

The highly variable refocusing angles of the virtual 180 trains enabled acquisition of multislice high resolution T_2 weighted FSE images in a clinically tolerable 4.6 minute scan. The 10 s average RF power, measured from amplifier output and deposited in the head and neck (∼3 kg), was 7.5 W for protocol 2 (left column), 5.6 W for protocol 3 (center column), and 4.4 W for protocol 5 (right column). An equivalent train of 180° pulses would require an estimated 27 W and exceed SAR limitations by a factor of 3. Blurring produces a relatively minor loss of resolution: structural and vascular detail is nearly equivalent in all image sets, although edges are enhanced — particularly Fig 2.17(l) — following PSF correction.

Traditional T_2 weighting is observed in these virtual 180 images despite low refocusing angles. Protocols 2 and 5 (left and right columns in Fig 2.17) have an echo time of 30 ms, but stronger T_2 weighting is observed with protocol 2. This is attributed to higher refocusing angles and lower stimulated echo contributions in

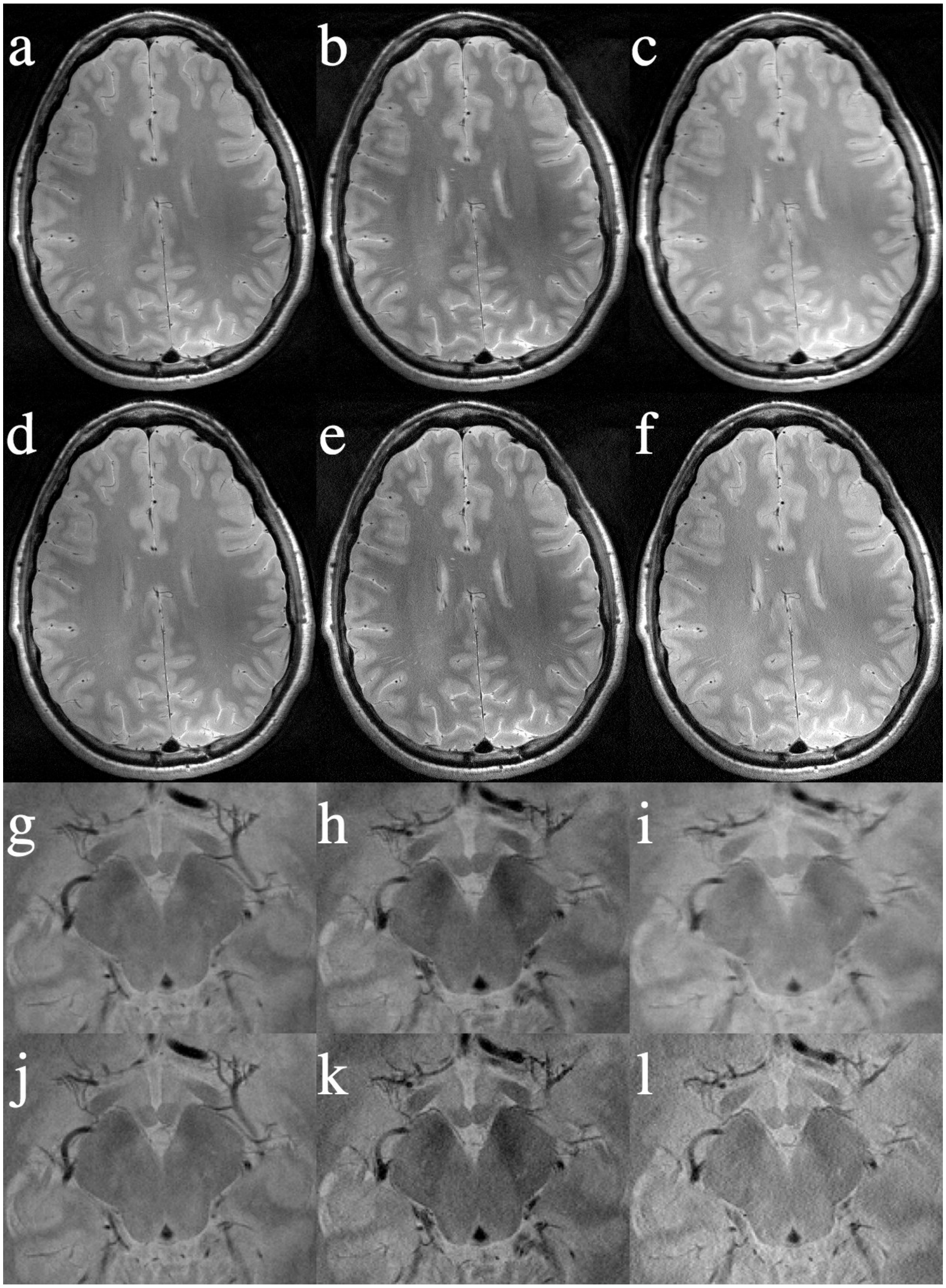

Figure 2.17: Representative axial images from three virtual 180 protocols. Images (a, d, g, j) were acquired with protocol 2 from Table 2.1, (b, e, h, k) with protocol 3, and (c, f, i ,l) with protocol 5. Images d–f and j–l have PSF correction. Frames g–l are cropped from full field-of-view slices through the mid-brain.

protocol 2 than in 5.

The RF power and noise amplification factors of virtual 180 echo trains are plotted in Fig 2.18 as functions of their maximum echo amplitudes, which are defined by the linear attenuation factor ζ. Nine baseline signal amplitudes, equally spaced between $S_0 = 0.1$ and 0.9 are investigated. This analysis illustrates the compromise between virtual 180 echo amplitude, RF power, and noise amplification/image blurring. Multiple baseline signal amplitudes can achieve a target SNR, *or* desired RF power. The choice of S_0 then impacts the noise amplification upon PSF correction. Typically, a larger baseline signal requires more RF power, but produces less signal modulation during the echo train, yielding less noise amplification or blurring. Each curve is defined over a limited domain: it's minimum signal is equal to S_0 — this represents a standard low angle echo train with no virtual 180 envelope. The maximum possible echo amplitude is constrained by degradation of ideal SPSS coherence due to large and rapid refocusing angle modulations. Selection of a baseline signal near its maximal SNR is inadvisable: this produces a larger than necessary noise amplification and fails to minimize the RF power.

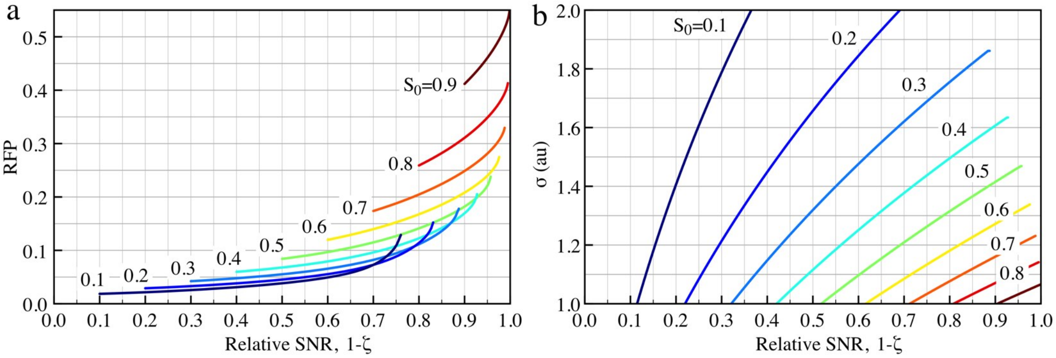

Figure 2.18: (a) Relative RF powers and (b) noise amplification factors versus the virtual 180 echo amplitudes, which are given by $1 - \zeta$, for 9 baseline signal amplitudes. For a given RF power, baseline signal selection involves a compromise between SNR and noise amplification/blurring.

2.3.6 Discussion

The virtual 180 echo train is a low RF power variant of the CPMG echo train [23, 24]: it retains the 90° excitation pulse and RF phase shift between excitation and subsequent refocusing pulses, but varies the refocusing angles. It is based on the transient magnetization response of a large change in refocusing angle. When prepared into a low refocusing angle SPSS, magnetization can be rapidly driven back into the transverse plane to form a coherent echo, resembling that from a 180° pulse. Encoding this echo into the center of k-space generates high SNR images at a fraction of RF power requirement of a traditional CPMG train.

The virtual 180 can be considered a short echo train TRAPS sequence [36]. In both cases, the contrast dominant regions of k-space are collected with high signal levels, while the periphery of k-space is acquired with reduced signal amplitude. These sequences differ in the refocusing angles required to generate the signal modulation across the echo train. The TRAPS approach slowly and smoothly varies the refocusing angles; to achieve full echo coherence, power intensive 180° refocusing angles are required. The virtual 180 sequence employs rapid refocusing angle modulations to transition into the 180° SPSS. Very high echo coherence can be obtained with exceptionally low refocusing angles. In train 3, Table 2.1, a 106° pulse is sufficient to induce an echo with 92.5% of the 180° signal. Complete elimination of high angle pulses enables the drastic RF power reductions afforded by the virtual 180 train. Furthermore, compatibility with long echo spacings enables long RF pulses for further SAR mitigation without excessively eroding the available readout time.

The rapid refocusing angle modulations employed in virtual 180 trains necessitate a loss of spin coherence and thus fail to fully maintain the SPSS. The parameter ζ provides leeway for this loss of coherence and enables intentional reduction of the echo amplitude in favour of RF power savings and reduced blurring. As shown in Fig 2.18, minimizing ζ is a sub-optimal solution that requires unnecessary RF power and produces excess noise amplification upon PSF correction.

We employ an offset and symmetric exponential signal envelope for virtual 180 echo formation. This envelope was selected empirically but appears favourable for this purpose. The virtual 180 requires a rapid signal modulation to avoid high angle pulses and should not have multiple echoes with high signal amplitude. The symmetric exponential satisfies these criteria and is defined succinctly by its decay constant, baseline signal, and echo amplitude. Additional investigation into optimal signal envelopes is warranted.

This method is ideally suited to high resolution T_2 weighted imaging in SAR constrained regimes. As presented in Section 2.3.3, the virtual 180 cannot occur at the first echo — this restriction imposes T_2 weighting and obstructs efficient T_1 weighted imaging. As observed with TRAPS [36], hyperecho [31], and other low angle CPMG echo trains, the degree of T_2 weighting is reduced as the stimulated echo contribution increases [39]. We hypothesize that 180°-equivalent T_2 weighting could be achieved by extending *TE* to account for the fraction of time magnetization is exposed to longitudinal relaxation [39].

This method is hindered by image blurring and ringing caused by signal modulation along the echo train. This flip angle induced signal modulation can be readily corrected although high spatial frequency noise is amplified as peripheral k-space is scaled. This process is optional and performed via post-processing; reconstructing both data sets is a feasible option. We anticipate the PSF corrected images will be compatible with linear and non-linear noise filters, which are effective at suppressing high spatial frequency noise. Relaxation blurring is not corrected, but is expected to diminish with the virtual 180 train relative to the 180° train since the effective transverse signal decay is diminished at low refocusing angles.

2.3.7 Conclusion

We have demonstrated that highly modulated refocusing angles can drastically reduce the RF power required for T_2 weighted FSE imaging. An echo amplitude approaching that of 180° pulses can be achieved, temporarily, without requiring high angle pulses. When encoded into the center of k-space, this echo, termed a "virtual 180", enables T_2 weighted FSE at a small fraction of the RF power of a 180° train, yet with no loss in SNR performance. Image blurring is observed, but if required, can be corrected at the cost of spatial frequency dependent noise amplification. The utility of this method has been demonstrated for high resolution human brain imaging at 4.7 T.

Chapter 3

Quantitative Fast Spin Echo Imaging

Low and modulated refocusing angles effectively moderate the extreme RF power deposition of FSE imaging at high magnetic field strengths and are relatively tolerant of heterogeneous RF fields. Conversely, traditional quantitative T_2 measurement techniques are extremely sensitive to variations in refocusing angle. This chapter describes a method for data processing to reduce sensitivity to sub-optimal refocusing conditions, thus enabling quantitative measures at high field strengths.

3.1 Transverse Relaxometry with Stimulated Echo Compensation[1]

3.1.1 Abstract

Presented is a fitting model for transverse relaxometry data acquired with the multiple-refocused spin echo sequence. The proposed model, requiring no additional data input or pulse sequence modifications, compensates for imperfections in the transmit field and radiofrequency profiles. Exploiting oscillatory echo behavior to estimate alternate coherence pathways, the model compensates for prolonged signal decay from stimulated echo pathways yielding precise monoexponential T_2 quantification. Verified numerically and experimentally at 4.7 T in phantoms and the human brain, over 95% accuracy is readily attainable in realistic imaging situations without sacrificing multislice capabilities or requiring composite or adiabatic RF pulses. The proposed model allows T_2 quantitation in heterogeneous transmit fields and permits thin refocusing widths for efficient multislice imaging.

---

[1] A version of this section has been published. Lebel RM, Wilman AH. Transverse relaxometry with stimulated echo compensation. Magn Reson Med 2010; in press.

3.1.2 Introduction

Relaxation of transverse magnetization is a fundamental MRI contrast mechanism; it aids tissue and pathology delineation and is indicative of tissue microstructure. It is characterized by the exponential decay of magnetization with a time constant T_2 (or a rate $R_2 = 1/T_2$). Transverse relaxometry — the quantification of T_2 times — is important for protocol optimization, disease detection [75, 119, 83], and tissue characterization in the brain [120, 121] and body [122, 123, 124, 125].

Spin echo techniques are typically regarded as the gold standards for *in-vitro* NMR transverse relaxometry [23, 24]. The imaging variant forms complete images at each echo time and relaxation times are extracted via mono- or multiexponential fitting [126]. Spin echo approaches require 180° refocusing angles to generate echo amplitudes modulated exclusively by T_2 decay [127, 128, 129]. In practice, the ideal refocusing stipulation is chronically violated: finite refocusing thickness, nonrectangular slice profiles, transmit calibration errors, and radiofrequency interference effects [55] — a pronounced phenomena at high field — all collude to alter the refocusing angles. This introduces T_1 weighted stimulated echo pathways into echo formation, confounding the pure spin echo T_2 measurement. The hallmark of echo contamination, for any of the above reasons, is a hypointense first echo (lacks stimulated echo contribution) [26]; subsequent echoes display roughly monoexponential relaxation, but with an artificially long time constant.

A partial remedy prescribes the refocusing width (W_R; units of distance), at approximately three times the excitation width (W_E) [130]. This minimizes refocusing profile errors, but limits multislice imaging efficiency and fails to address RF calibration errors or inhomogeneity within the image plane. Several works have discarded the first echo [131, 132], favoring improved fits; while accuracy is improved, this necessity indicates T_1 contamination and systematic T_2 misestimation. Additionally, first echo rejection may compromise quantification of short T_2 components, such as myelin, cartilage, and muscle, whose signals will decay appreciably prior to the second echo. Echo editing techniques, which vary the crusher gradient area surrounding each refocusing pulse to isolate the desired spin echo pathway [126, 127, 128, 129, 26], permit accurate relaxometry at clinical field strengths. These approaches use nonselective composite refocusing pulses to minimize sensitivity to transmit (B_1^+) and static (B_0) field heterogeneities, necessitating a single slice excitation. The accuracy of these methods still deteriorates in regions lacking ideal refocusing as magnetization is lost to alternate coherence pathways. Signal-to-noise is degraded in these regions and a correction scheme may be needed for accurate measurements [133, 134].

Alternative T_2 mapping techniques exist, but none are perfect. Inversion recovery balanced steady-state free precession can be used to simultaneously map T_1,

T_2, and proton density [135], but requires accurate knowledge of the tip angle, is sensitive to static field inhomogeneities, and accuracy is affected by the slice profile in two-dimensional acquisitions. A three-dimensional method, DESPOT2 [136], extracts T_2 from images at two different flip angles, but requires prior T_1 information — typically provided by its companion method, DESPOT1. This method offers full brain quantification in clinically acceptable durations, but without additional corrective data is sensitive to B_1^+ [137] and B_0 [138] heterogeneities.

The EPG algorithm [26, 29] computes echo amplitudes given T_1, T_2, the ESP, and an arbitrary sequence of refocusing angles. It has been used to accurately predict and tailor image contrast with reduced refocusing angle echo trains [39, 38]. Jones *et al.* [139] demonstrated an inverse solution was possible: refocusing angles and relaxation times could be estimated from echo train amplitudes. While novel, this work neglected imperfect slice profiles, which are a significant source of stimulated echoes. Furthermore, they omitted discussion of T_1, a required input into the EPG algorithm and a potential confound in the T_2 measurement.

Here, we present a more complete fitting model for transverse relaxometry data acquired with the standard (phase-encode rewound, constant crusher area) multiple-refocused spin echo sequence based on Jones *et al.*'s approach. Our proposed stimulated echo compensated model, accounts for imperfect RF slice profiles, requires no additional data input, and is validated for a wide range of imaging situations and relaxation times. The proposed model estimates the relative transmit field from oscillatory signal behavior and compensates for alternate echo pathways. It allows accurate T_2 quantitation in heterogeneous transmit fields and permits spatially thin refocusing widths relative to the excitation width for efficient multislice imaging.

3.1.3 Materials and Methods

All experimental data were acquired using a Varian Unity Inova 4.7 T whole-body imaging system. Maximum gradient strength was 60 mT/m with a slew rate of 120 T/m/s. Data from phantoms were acquired with an 18 cm diameter birdcage coil; human brain images with a 27 cm birdcage coil. Gaussian pulses (time-bandwidth product, 2.69) were used throughout as they deposit less RF power than most conventional shaped pulses, enabling RF power-constrained human imaging at 4.7 T. Substandard gaussian slice profiles also provide a worst-case scenario assessment of our proposed model.

Stimulated Echo Compensation

Any accurate fitting model for transverse relaxometry generates signal decay curves — typically via numerical modeling of salient spin behavior — for comparison with experimental data. For multiple-refocused spin echo, decay curves can be generated via Bloch magnetization simulations of the RF pulses and the spin evolution and relaxation during the interpulse spacings. Unfortunately, this process is computationally intense, necessitating a large digital sampling density across the slice, and becomes impractical for multivoxel curve fitting.

An accelerated approach employed in this work uses the EPG algorithm, which given T_1, T_2, ESP, and refocusing angles, efficiently computes echo amplitudes. Its computational implementation is detailed elsewhere for general [26, 29] and spin echo specific [38] cases. This algorithm partitions magnetization following excitation into numerous coherence pathways; it evaluates T_1 and T_2 relaxation along each pathway to accurately compute amplitudes of echoes formed from the mixture of these pathways.

Our proposed fitting routine is a nonlinear least-squares algorithm whose objective function is an aggregate decay curve representing EPG-generated echo train amplitudes integrated over the slice profile. Required inputs are the distribution of prescribed excitation angles along the slice profile (for simplicity, the z direction), $\alpha_{EX}(z)$, and the distribution of prescribed refocusing angles, $\alpha_j(z)$, at the j^{th} echo. These distributions can be approximated from the frequency responses of the RF pulses, obtained from the Fourier transform of their time modulation. Implications of this assumption are investigated in this work. Also required are key sequence parameters, namely the ESP and the ETL. Unknown are relaxation times T_1 and T_2; a relative RF transmit scaling factor, $B_1^{+\,rel}$ (unitless and near unity); and a global amplitude scaling factor, A_{scale}.

The EPG based fitting routine computes its objective function by first approximating $M_{EX}(z)$, the transverse magnetization along the slice profile immediately following excitation, according to:

$$M_{EX}(z) = M_z^{(0)} \sin\left[B_1^{+\,rel} \cdot \alpha_{EX}(z)\right] \tag{3.1}$$

$M_z^{(0)}$ is the longitudinal magnetization prior to excitation. It is assumed to be uniform along the slice direction due to the combination of saturation during the previous echo train and recovery during the repetition time. The excitation angle across the slice profile is set, presumably but not strictly necessarily, at 90°. The fitting parameter $B_1^{+\,rel}$ further scales the excitation angle. The coherent transverse magnetization of the j^{th} echo as a function of slice position $M_j(z)$ is then calculated using the EPG algorithm:

$$M_j(z) = M_{EX}(z) \cdot \mathrm{EPG}\left[T_1, T_2, ESP, B_1^{+\,rel} \cdot \alpha_{1\ldots j}\right] \tag{3.2}$$

The entire refocusing angle history, $\alpha_{1\ldots j}$, is relevant to the j^{th} echo. The slice profile dependence is determined by the refocusing shape and spatial width. Refocusing angles are traditionally all prescribed at 180°; like the excitation pulse, they are scaled by $B_1^{+\,rel}$. Finally, the aggregate decay curve C — the objective function for nonlinear fitting — is the time course of the above echo magnetization, globally scaled by A_{scale} (accounts for $M_z^{(0)}$, coil sensitivity, receiver gain, etc.) and integrated over the slice profile:

$$C_j = \left\{ A_{scale} \int_z M_j(z')\, dz' : j \text{ is an integer} : 1 \leq j \leq ETL \right\} \tag{3.3}$$

This process is summarized in Fig 3.1, where signal decay, computed with the EPG algorithm, is plotted at discrete locations along the slice profile and the aggregate decay is projected on the far slice axis. Harsh conditions (gaussian RF envelopes, $B_1^{+\,rel} = 0.5$, $W_R = 2.0W_E$) were used to generate this figure to demonstrate signal oscillations from alternate echo pathways and to emphasize variation in decay times across the slice profile. Our implementation uses 85 discrete points spanning ±5 standard deviations across the gaussian excitation envelope.

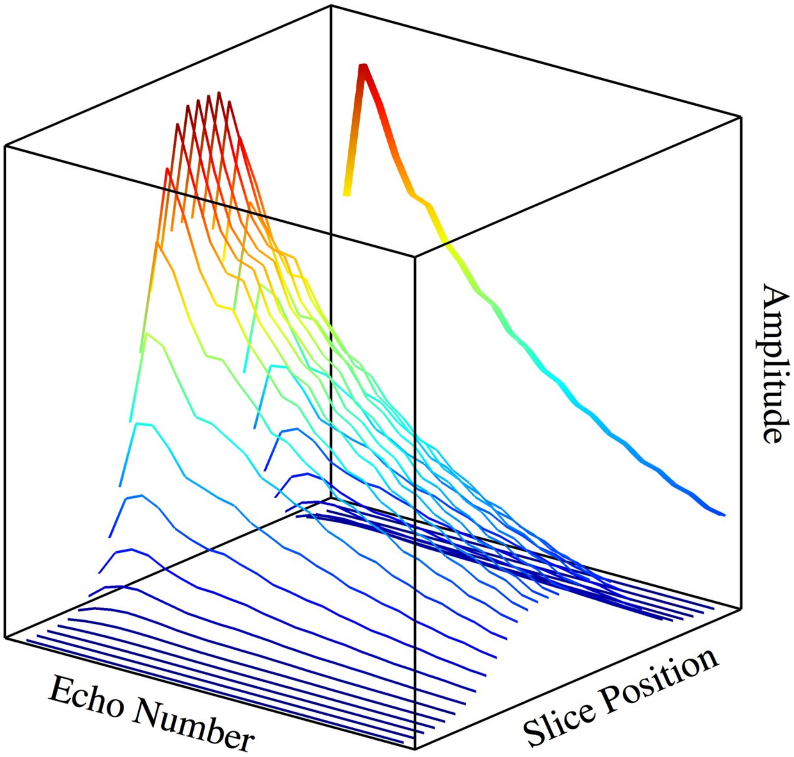

Figure 3.1: Simulated signal decay at discrete locations along the slice profile for a multiecho spin echo acquisition and the net signal, scaled and projected onto the far slice position axis. Signal oscillations arise from stimulated echo contributions due to finite refocusing width ($W_R = 2.0W_E$) and miscalibrated transmit ($B_1^{+\,rel} = 0.5$). The net signal serves as the objective function for least squares fitting.

Symmetry of the spin echo signal at refocusing angles surrounding 180° permits two distinct $B_1^{+\,rel}$ solutions with the proposed fit, one above unity (i.e., $\alpha_j > 180°$), and one below (i.e., $\alpha_j < 180°$). This precludes true transmit filed extraction but permits estimation of refocusing angle deviation from 180°. Since the relaxation times are unaffected, we add the constraint $0 < B_1^{+\,rel} \leq 1$.

Given a multiecho spin echo decay curve, T_1 and T_2 components are indistinguishable, as illustrated in Fig 3.2. In this example, we have purposely chosen three species with different relaxation times (A: $T_1/T_2 = \infty/100$ ms; B: 1000/100 ms; C: 115/115 ms) that display nearly identical decay when refocused with 120° pulses. The above species have similar T_2 values and contrasting T_1 values: a maximum 15% deviation in T_2 is observed between extreme limiting cases of long and short T_1. Magnetization exposed to longitudinal decay via stimulated echo pathways is largely preserved for subsequent echo formation — even when T_1 is short. The result is an effective relaxation time appearing longer than the true transverse relaxation time. To compensate for this effect and to permit T_2 estimation, we assume $T_1 \gg T_2$. With this assumption, all remaining unknowns in the proposed fit — T_2, $B_1^{+\,rel}$, and A — can be estimated. The remainder of this work focuses on validating the assumptions intrinsic to this model.

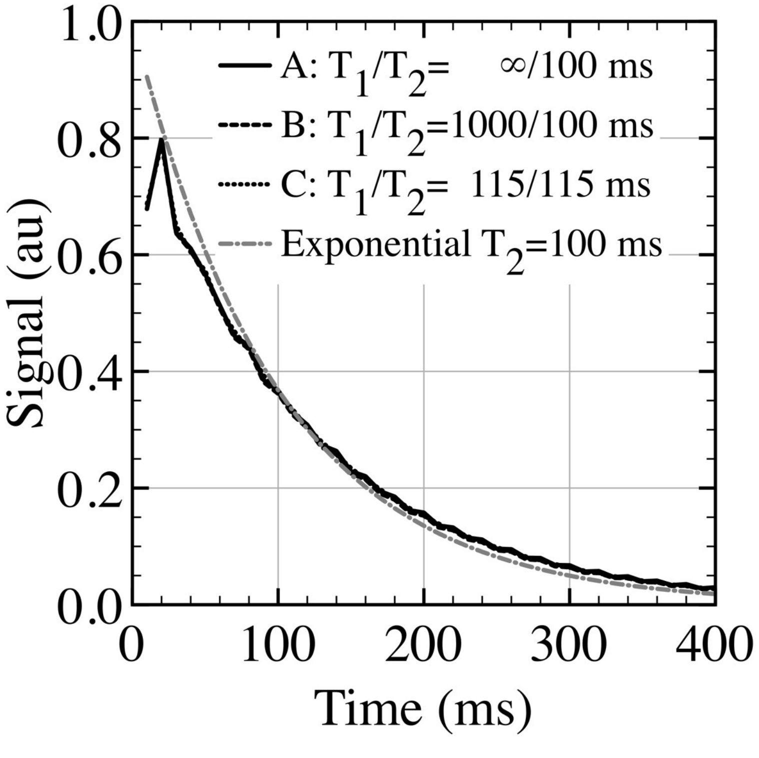

Figure 3.2: Simulated signal decay with 120° refocusing pulses from three species with relaxation times chosen for overlapping decay curves. A pure exponential decay curve with $T_2 = 100$ ms is shown for reference. Note the signal oscillations and slower apparent decay in the three species relative to the exponential. This behavior is largely independent of T_1.

Numerical Validation

To validate the approximations used in our proposed fit, namely using the RF frequency response as input to the EPG routine and assuming infinite T_1, simulated multiecho spin echo decay curves were generated using Bloch simulations then fit using the proposed method. Simulations of the slice-selective excitation and refocusing pulses, via hard pulse decomposition, as done in the Shinnar-LeRoux transform [140], account for Bloch equation nonlinearity; evaluation of T_1 and T_2 relaxation between RF pulses models the full relaxation behavior. These curves were fit with the traditional exponential model and with our stimulated echo compensating model to probe the effects of noise, finite T_1, $B_1^{+\,rel}$ variation, and relative RF pulse widths. Unless stated otherwise or used as an independent variable, the following standard simulation parameters were assumed: $T_1 = 1000$ ms, $T_2 = 100$ ms, $W_R = 1.75W_E$, $B_1^{+\,rel} = 1.00$, ESP = 15.0 ms, and ETL = 32.

Noise stability was investigated with the addition of zero-mean gaussian white noise to a simulated data set generated with the above parameters. This mimics a phase sensitive reconstruction where the image signal and noise are real-valued. Noise was generated with a predefined standard deviation; signal-to-noise (SNR) was defined as amplitude of the first, noise-free echo divided by the requested noise deviation. At each SNR value, 4096 independent trials were characterized with the exponential and proposed models.

Phantom Validation

Ten solutions with manganese concentrations exponentially spaced between 0.039 and 1.5 mM were placed in 1.0 cm diameter (15 mL) cylindrical plastic laboratory tubes. Samples were scanned individually; transmit power and shim settings were calibrated for each sample. Slice-selective profiles (i.e., orthogonal slice-select and readout gradients, no phase-encode gradients) were obtained with the slice-select direction parallel to the long axis of the tube. Repetition time was 4.00 s, ESP was 7.25 ms, and ETL was 256 echoes. Excitation and refocusing pulse durations were 2.00 ms (bandwidths of 1.35 kHz). Profiles were collected with a 10.0 mm excitation width and with refocusing widths of 35.0 mm, 17.5 mm, and 10.0 mm. At each refocusing thickness, the transmit gain (i.e., $B_1^{+\,rel}$) was adjusted for refocusing angles of 180°, 150°, 120°, 90°, 60°, and 30° and correspondingly reduced excitation angles. Decay curves were fit with a monoexponential curve and with our proposed model. True T_2 values were measured with 50.0 mm refocusing widths and 180° refocusing angles and were fit with the exponential model. T_1 was measured with slice-selective inversion recovery spin echo. Adiabatic inversion pulses were used with inversion times arrayed between 25.0 and 2500 ms; T_1 was extracted with a least-square fit. Repetition time for T_1 measurements was 11.0 s.

To assess the performance of our model in an imaging situation with large B_1 variation we obtained multiecho spin echo images of an 11 cm diameter cylindrical phantom. The phantom was doped with 0.15 mM manganese chloride and 3.0 mM sodium chloride. Transmit power was calibrated on a readout profile; a prescribed angle represents the mean (weighted by reception sensitivity) of the tip angle distribution in the center of the profile. Repetition time was 2.00 s, ESP was 15.0 ms, ETL was 20, field-of-view was 16 cm × 16 cm, and the imaging matrix, homodyne reconstructed from 75% phase partial Fourier, was 128 × 128. Excitation profiles were 5.0 mm thick and the refocusing widths were 17.5 mm; excitation pulses were 7.00 ms long (bandwidth, 384 Hz) while the refocusing pulses were 2.00 ms (bandwidth, 1.35 kHz). Images were fit on a pixel-by-pixel basis with a monoexponential and with our proposed fitting algorithm. T_1 was measured as described above for the small phantoms.

In Vivo Validation

Multiecho spin echo images of the human head were obtained in multislice mode to assess the accuracy of our proposed fit model. Relaxation maps of the human brain were obtained from six healthy consenting adults (five men, one woman; mean age: 29 years, standard deviation: 3 years). Three transverse slices with 5.0 mm excitation widths were collected twice: once with refocusing widths of 25.0 mm and again with 5.0 mm widths. A 30.0 mm gap between slices was prescribed to avoid crosstalk. Excitation and refocusing pulses were 6.00 ms in duration (bandwidth, 448 Hz). Excitation and refocusing angles were prescribed at 90° and 180°, respectively. As above, transmit power was calibrated on a readout profile. Additional imaging parameters include: a repetition time of 4500 ms, an ESP of 15.0 ms, an ETL of 20, a field-of-view of 23 cm × 16 cm, and an imaging matrix, homodyne reconstructed from 60% phase partial Fourier, of 192 × 133. Acquisition time was 6.0 min per image set. Slice coverage, train length, and acquisition efficiency were limited by RF power deposition. Images were fit on a pixel-by-pixel basis with the proposed and exponential models. Bilateral regions-of-interest were drawn on representative sections of frontal white matter (WM), splenium of the corpus callosum, thalamus, putamen, globus pallidus, and head of the caudate nucleus. Frontal, motor, and occipital cortices were sampled with sets of discrete points selected to minimized partial voluming.

3.1.4 Results

Experimental echo amplitudes from a small 0.3 mM manganese phantom and fits are shown in Fig 3.3. Data acquired under near-ideal conditions are shown in black and decay with a relaxation time of 27.0 ± 0.5 ms, as estimated with the exponential

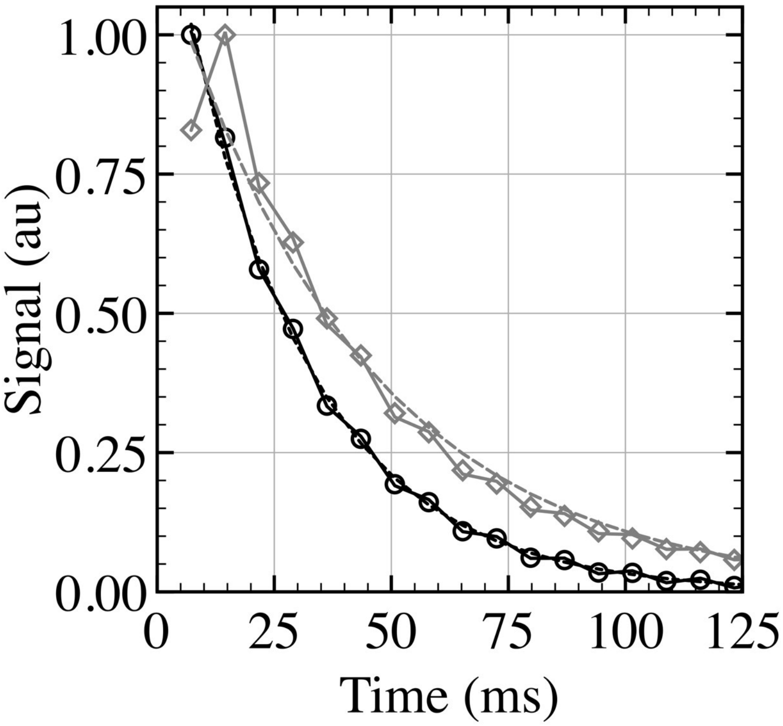

Figure 3.3: Experimental signal decay and fits from a 0.30 mM manganese phantom. The near-ideal measurement with $W_R = 5.00W_E$ and $B_1^{+\,rel} = 1.00$ (open circles), its exponential fit (dashed line), and our proposed fit (solid line) are shown in black. A nonideal acquisition with $W_R = W_E$ and $B_1^{+\,rel} = 0.67$ (open diamonds), its exponential fit (dashed line), and our proposed fit (solid line) are shown in gray.

model. The proposed fit yields 26.4 ± 0.3 ms. Data and fits using equal refocusing and excitation widths and 120° refocusing angles ($B_1^{+\,rel} = 0.67$) are shown in gray. Pronounced initial oscillation is superimposed on prolonged exponential decay. Exponential fitting estimates an erroneous decay time of 42.0 ± 2.9 ms; our proposed fit yields a more accurate value of 25.3 ± 0.5 ms. Error bounds represent the 95% confidence intervals in the fitting procedure — they do not account for model inaccuracy. In both examples, our proposed model incorporates signal oscillations and prolonged decay from stimulated echo contributions and provides accurate T_2 estimates with narrower confidence bounds than the exponential fit, which fails to address these issues. The data and fit quality shown in Fig 3.3 are representative of all phantom data. The T_1 in this sample was measured at 376 ms, giving a T_1/T_2 ratio of ~14. Transverse relaxivity of the manganese phantoms was measured as 122 $\text{mM}^{-1}\text{s}^{-1}$; longitudinal relaxivity was 7.86 $\text{mM}^{-1}\text{s}^{-1}$. The T_1/T_2 ratio varied smoothly between 7.77 at low-ionic concentration (0.039 mM) and converged at 15.2 at high concentration (1.5 mM).

Using the standard Bloch simulation parameters ($T_1 = 1000$ ms, $T_2 = 100$ ms, ESP = 15 ms, ETL = 32, $W_R = 1.75W_E$), stabilities of both fitting procedures at finite SNR values are shown in Fig 3.4. The median relaxation time provided by the exponential fit is uniformly erroneous at all SNR levels due to the narrow refocusing thickness. The median relaxation time from the proposed fit provides improved accuracy over the exponential at all SNR levels, but deviates at very low SNR levels where erroneous $B_1^{+\,rel}$ estimates reduce the reported relaxation time. Shaded areas represent the first and third quartile in reported transverse relaxation times. With an extra fitting parameter for $B_1^{+\,rel}$, the stimulated echo compensated approach provides reduced precision than the exponential fit: over the entire SNR range, the proposed fit has an interquartile range 1.6 times larger than the exponential.

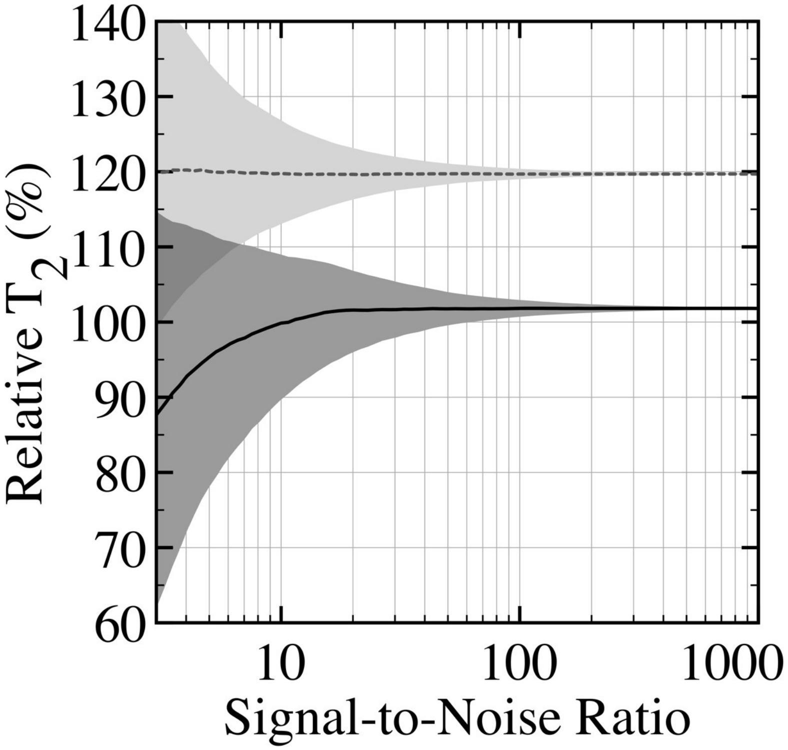

Figure 3.4: Simulated median accuracy of the proposed fit (solid black line) and exponential fit (dashed gray line) as functions of the SNR. Shaded areas represent the first and third quartile of reported relaxation times observed during 4096 random trials at each SNR value.

Simulated accuracies of both fit models for species with finite T1 values are shown in Fig 3.5 for two refocusing angles and three refocusing widths. In Fig 3.5a, $B_1^{+\,rel}$ is unity; in Fig 3.5b, $B_1^{+\,rel} = 0.67$. In both parts, the upper three gray curves represent exponential fits at different refocusing widths; the lower three black curves represent the proposed EPG based fits. With $B_1^{+\,rel}$ at unity and T_1/T_2 above five, the proposed fit has <5% error at all refocusing widths while accuracy of the exponential fit decreases rapidly as the refocusing width is reduced. Transmit

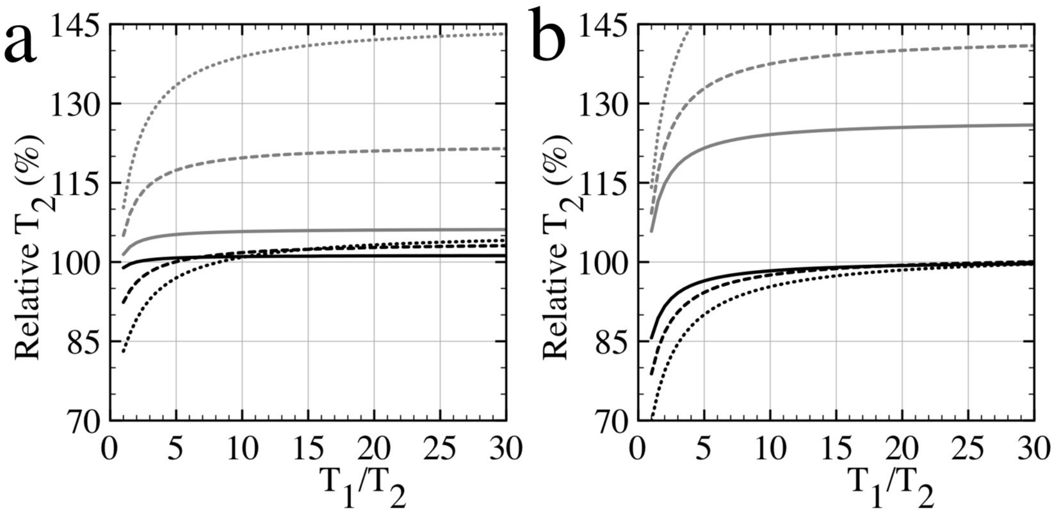

Figure 3.5: Simulated accuracy of the exponential (upper three curves, gray) and proposed (lower three curves, black) models as functions of T_1/T_2. Computed T_2 values are shown as a percentage of true T_2 at refocusing widths of $3.50W_E$ (solid lines), $1.75W_E$ (dashed lines), and $1.00W_E$ (dotted lines) for (a) $B_1^{+\,rel} = 1.0$, and for (b) $B_1^{+\,rel} = 0.67$.

heterogeneities affect both fit models, as shown in Fig 3.5b. The exponential fit massively overestimates T_2 at nearly all T_1/T_2 ratios while the proposed fit remains within 5% error at T_1/T_2 ratios above ten. The proposed fit overestimates T_2 due to the assumption that the tip angle distributions result from the frequency response of the RF pulses; this is most evident when $B_1^{+\,rel}$ is unity, T_1/T_2 is large, and $W_R = W_E$, where a 4.1% overestimation is observed.

The effect of finite refocusing width on fit accuracy, investigated in more detail, is shown in Fig 3.6. In Fig 3.6a, simulated accuracy is presented for both models at T_1/T_2 ratios of 5, 10, and 20. Considerably improved results are obtained from our proposed model relative to the exponential model at all refocusing widths. Our proposed method deviates by <5% as the relative refocusing width is reduced to unity. Experimentally determined slopes, relating estimated T_2 versus true T_2, as measured with near-ideal conditions in all small Mn^{2+} phantoms, are shown in Fig 3.6b. The exponential fit displays considerable overestimation, particularly with thin refocusing widths, while the proposed model provides <5% error in all cases investigated.

The effects of transmit variations are shown in Fig 3.7. Fig 3.7a plots simulated accuracy of both fit models, at three T_1/T_2 ratios, versus $B_1^{+\,rel}$. The proposed fit outperforms the exponential at all $B_1^{+\,rel}$ values, the latter has a minimum 17% error when $W_R = 1.75W_E$ (consistent with Fig 3.6a). Our proposed fit underestimates T_2 at very low or high $B_1^{+\,rel}$ values, particularly when T_1 is short, as the fraction of

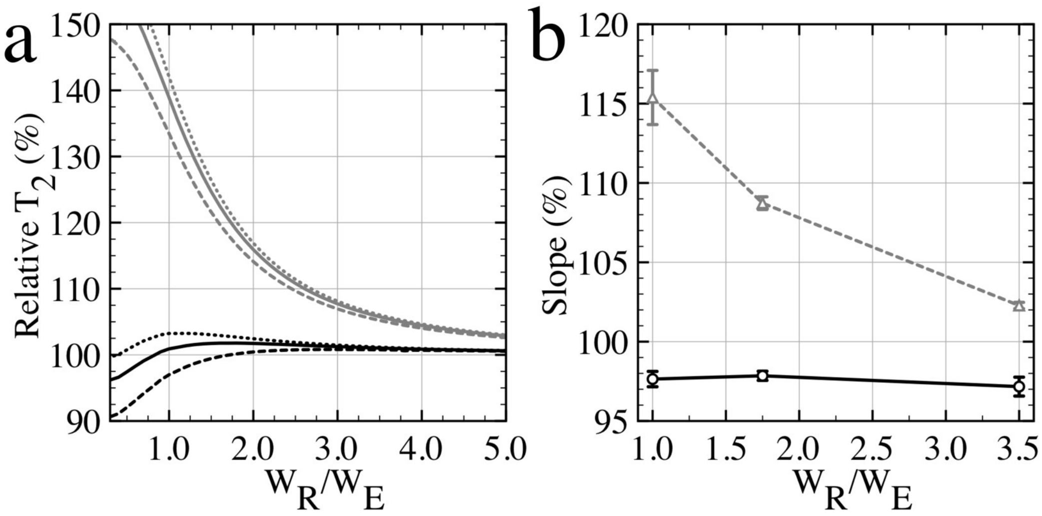

Figure 3.6: Simulated accuracy of the exponential fit (upper three curves, gray) and the proposed fit (lower three curves, black) as functions of refocusing width. Three T_1/T_2 ratios are investigated: 5 (dashed lines), 10 (solid lines), and 20 (dotted lines). b: Experimental slopes (relating estimated T_2 to true T_2), expressed as a percentage, for the exponential fit (triangles, dashed line) and the proposed fit (squares, solid line) at three refocusing widths. $B_1^{+\,rel}$ is unity throughout this figure.

stimulated echo pathways increase. Experimental results, Fig 3.7b, confirm that our proposed method is far less sensitive to transmit deviations than the exponential; only 5% underestimation is observed at $B_1^{+\,rel} = 0.5$ (i.e., 90° refocusing) with our method compared with 37% overestimation with the exponential. A full list of experimentally measured slopes relating estimated T_2 values to true T_2 values in all small Mn^{2+} phantoms are listed in Table 3.1. The proposed fit is robust to variations in refocusing width with no measured change in slope at any $B_1^{+\,rel}$ value. Over 95% accuracy is maintained at $B_1^{+\,rel}$ values greater than or equal to 0.5; loss of accuracy is only observed at very low $B_1^{+\,rel}$ values.

Transverse relaxation maps from the large uniform phantom are presented in Fig 3.8. In Fig 3.8a, T_2s are estimated with the exponential fit; in Fig 3.8b, with the proposed fit. The $B_1^{+\,rel}$ map, from the proposed method, is shown in Fig 3.8c. The exponential fit returns a heterogeneous distribution of relaxation times while the proposed fit yields a flat map unaffected by transmit variations. Profiles through the T_2 maps are shown in Fig 3.8d. Along this profile, the exponential fit predicts values between 60 and 180 ms while the proposed fit ranges between 53 and 59 ms; the relative transmit field along this profile ranges from 0.32 and 0.92. A scatter plot of T_2 versus $B_1^{+\,rel}$ for all signal containing pixels is shown in Fig 3.8e, confirming, as shown in Fig 3.7, that the proposed fit is resilient to $B_1^{+\,rel}$ variations. The true T_2 value of this phantom is estimated at 60 ms — the intersection point of both methods as $B_1^{+\,rel}$ approaches unity. The T_1 was measured at 690 ms, yielding a

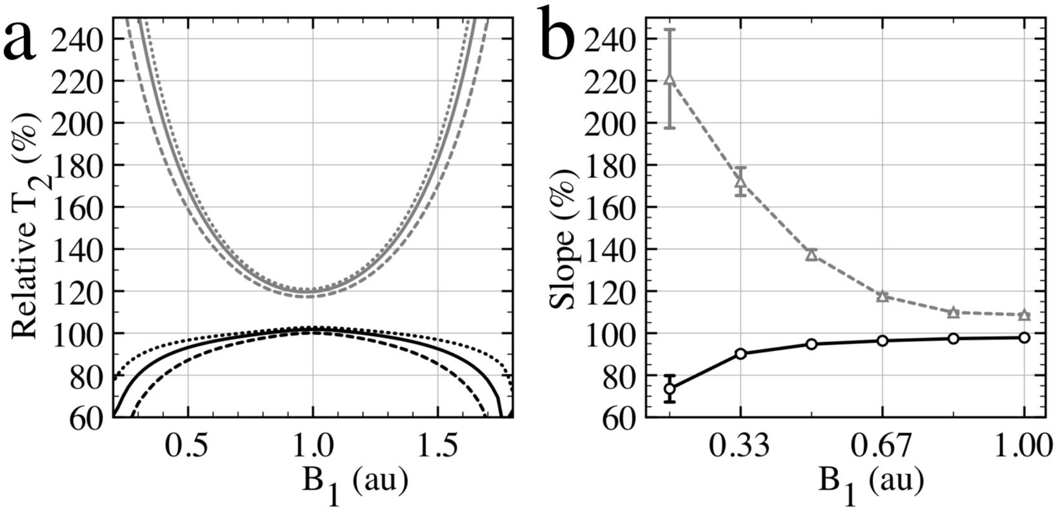

Figure 3.7: Simulated accuracy of the exponential fit (upper three curves, gray) and the proposed fit (lower three curves, black) as functions of $B_1^{+\,rel}$. Three T_1/T_2 ratios are investigated: 5 (dashed lines), 10 (solid lines), and 20 (dotted lines). b: Experimental slopes, determined via linear regression of estimated T_2 versus measured T_2 under ideal conditions at all manganese concentrations in the small phantoms, expressed as a percentage, for the exponential fit (triangles, dashed line) and the proposed fit (squares, solid line). Error bars are occasionally smaller than the data points. Refocusing widths of 1.75 times the excitation width were used in this figure.

Table 3.1: Experimentally Measured slopes, expressed as percentages, relating estimated T_2 values to true T_2 values for the proposed and exponential fits at low transmit amplitudes and finite refocusing widths. Average uncertainty: ±3%.

$B_1^{+\,rel}$	Stimulated echo compensated fit			Exponential fit		
	$W_R/W_E = 3.50$	1.75	1.00	$W_R/W_E = 3.50$	1.75	1.00
1.00	97	98	98	102	109	115
0.83	98	97	96	103	110	117
0.67	96	96	95	110	118	125
0.50	94	95	95	129	137	145
0.33	87	90	91	159	172	179
0.17	73	74	70	196	221	224

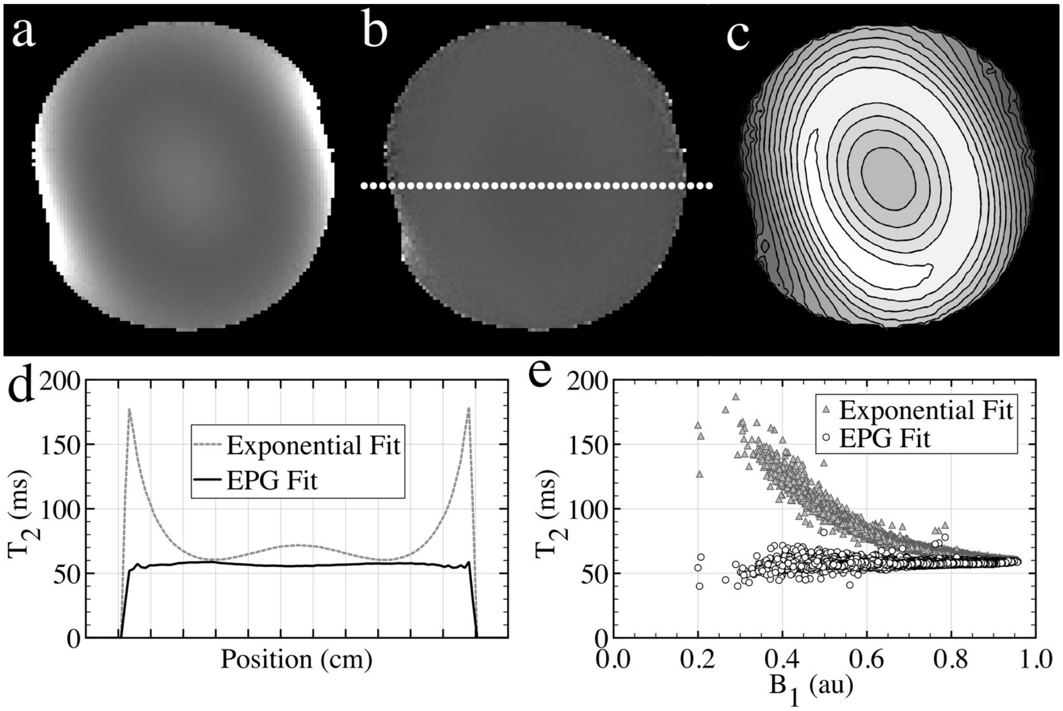

Figure 3.8: Comparison of the exponential and the proposed relaxation models on a uniform, manganese-doped water phantom. a: T_2 map derived with the exponential fit. b: T_2 map estimated with the proposed fit. Intensity scale for (a, b) is from 10 to 200 ms. c: Contour plot of the $B_1^{+\,rel}$ transmit field, as estimated with the proposed model, scaled from 0 to 1 with contours every 0.05 units. d: Profiles through the T_2 maps along the dotted line in (b). e: Scatter plot of T_2 values versus estimated $B_1^{+\,rel}$ from all signal containing voxels.

T_1/T_2 ratio of 11.5.

In vivo results are shown in Fig 3.9. With wide refocusing pulses (upper row), both models yield very similar results in regions of ideal $B_1^{+\,rel}$. The models deviate in the upper left and lower right of the images, where the estimated $B_1^{+\,rel}$ field is low. With thin refocusing pulses (middle row), the exponential yields a 30% baseline overestimation of T_2, with further exaggeration in regions of low $B_1^{+\,rel}$. Profiles through the four maps, along the region indicated in Fig 3.9b, show the stimulated echo compensated fit returns equivalent relaxation times at both refocusing widths while the exponential is incompatible with thin refocusing. Average transverse relaxation times in various brain structures are presented in Table 3.2.

3.1.5 Discussion

Stimulated echoes are a major source of error in multiecho spin echo relaxometry. Most approaches aim to minimize their contribution via wide refocusing pulses and faith in uniform transmit fields, or by excluding alternate echo pathways then,

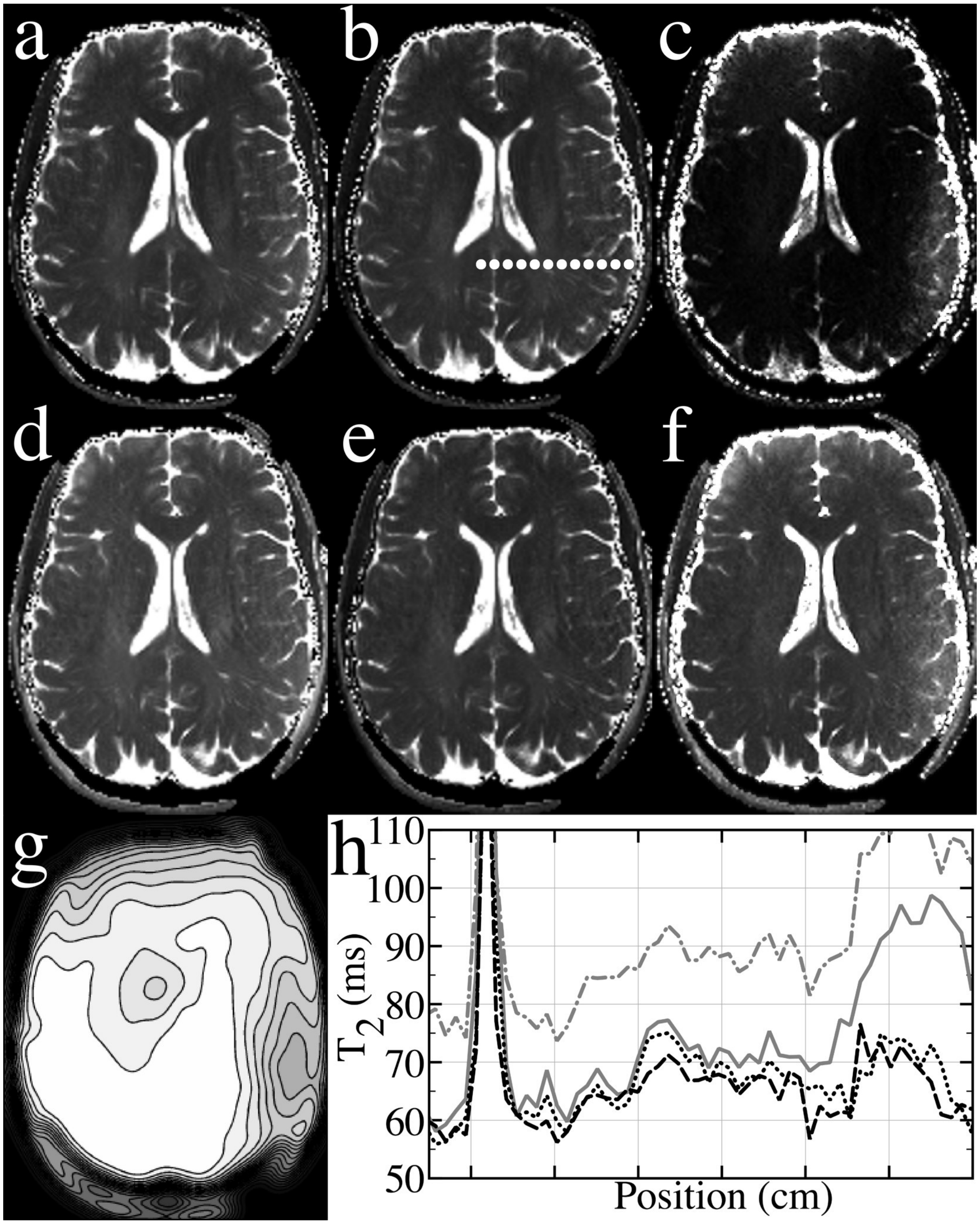

Figure 3.9: *In vivo* T_2 maps with $W_R = 5W_E$ are shown in (a) and (b); maps with $W_R = W_E$ in (d) and (e). An exponential fit was used to generate (a) and (d) while the proposed fit was used in (b) and (e). Intensity scale is from 10 to 300 ms. Image (c) is the difference between maps (a) and (b); image (f) is the difference between (d) and (e). Difference images are scaled between 0 and 100 ms. The $B_1^{+\,rel}$ map, estimated with the proposed fit and scaled from 0 to 1, with 0.05 contour separations, is shown in (g). Profiles through the four T_2 maps, along the dotted line in (b) are shown in (h). Gray lines represent the exponential fit, the solid line shows $W_R = 5W_E$, the dash-dot line depicts $W_R = W_E$. Black lines represent the proposed fit, the dotted line represents $W_R = 5W_E$; the dashed line, $W_R = W_E$.

Table 3.2: Average T_2 values, estimated with the proposed fit at 4.7 T, reported as the inter-subject mean ± standard deviation in specific brain regions from six healthy volunteers. Regions marked * are averaged over five individuals due to unreliable slice location.

	Frontal WM	Splenium*	Frontal cortex	Motor cortex*	Occipital cortex
T_2 (ms)	53 ± 3	64 ± 4	72 ± 2	55 ± 3	55 ± 1

	Thalamus*	Putamen*	Globus pallidus*	Caudate
T_2 (ms)	53 ± 2	55 ± 3	38 ± 2	60 ± 3

if need be, correcting for lost signal. We have presented a fitting model embracing stimulated echoes to permit relaxometry in heterogeneous transmit fields and improve multislice imaging efficiency. Our proposed method requires no sequence modifications but needs the shapes and spatial widths of excitation and refocusing pulses.

The proposed model assumes magnetization evolving in alternate coherence pathways experiences negligible T_1 relaxation. Accurate results are obtained when either T_1 is much longer than T_2 or when magnetization is concentrated in primary spin echo pathways. This is an improvement over the exponential model, which relies exclusively on the latter condition. As shown in Figs 3.5-3.7 and Table 3.1, the proposed model is insensitive to variations in refocusing width, transmit variation, and even T_1/T_2 ratio; it matches or outperforms the exponential fit in all cases. From simulated and experimental data, accuracy below 95% is rarely observed.

In practice, the above combinations yielding inaccurate T_2 relaxometry with our method occur very rarely. Most biological tissues of interest have large T_1/T_2 ratios. At 1.5 T, ratios for gray matter range between ∼11 and ∼15 [141], WM between ∼8.5 and ∼11 [141], muscle and cartilage have ratios of ∼32 and ∼25, respectively [142]. Several tissues, notably fat and cerebrospinal fluid, have small T_1/T_2 ratios. Although these tissues are rarely of interest from a relaxometry perspective, our method may still offer a marginal improvement over an exponential fit.

We anticipate the utility of our proposed model to improve with static field strength. First, model accuracy improves with T_1/T_2 and this ratio increases with field strength. At 7.0 T cortical gray matter and WM have T_1 values of 2132 ms and 1220 ms, respectively [108]. Neglecting substantial T_2 shortening, ratios of at least 23 in gray matter and 17 in WM are expected at 7.0 T — nearly a 2-fold increase from 1.5 T. Second, the B_1 distribution broadens with field strength

[54, 143], necessitating some form of stimulated echo compensation.

The *in vivo* relaxation times reported in Table 3.2 are in excellent agreement with those recently published by Mitsumori et al. [46] using adiabatic refocusing on 54 individuals at 4.7 T. This further suggests the proposed fit is applicable to T_2 quantification at high field.

Echo editing techniques have been used successfully at field strengths up to 3.0 T [144]. Despite composite RF pulses, these approaches remain sensitive to B_0 heterogeneity and to B_1 variations exceeding $\sim$30% (see Fig 6a in [126]) whereby considerable signal exclusion occurs following each refocusing pulse. Correction schemes have been proposed [134], but additional information, such as a B_1 field map, is required and SNR is irreparably degraded. Extension to multislice mode is possible via time consuming 3D scans [145] or nontrivial T_2 preparation methods [146, 147]. Although our model contains several assumptions and may slightly misestimate T_2 (provided T_1 is short and refocusing pulses are $<90°$), it operates in multislice mode, is compatible with short echo spacings and long echo trains, compensates for B_1 variations, and does not require additional data input. As such, it presents a practical alternative to echo editing techniques.

The multiexponential analysis capabilities of the proposed fit have not been explored in this work. We anticipate compatibility with the non-negative least-square algorithm [120, 139, 148], although an additional optimization stage may be required to solve for $B_1^{+\,rel}$. As with all fitting models, incidental magnetization transfer during multislice acquisitions [109] will preclude quantification of tissues with multiple water compartments [78].

As presented, the proposed fit requires the RF profiles to compute the refocusing angle distribution across the excitation profile. The model can be simplified, and computationally accelerated, if very thick refocusing pulses or very high time-bandwidth pulses are used. If the refocusing angles are uniform across the excitation width, the integral in Eq 3.3 may be collapsed into a single echo train, eliminating the need for RF profile input and computation of echo trains at multiple profile locations.

In most cases, finite refocusing widths contribute to stimulated echo formation and pulse profiles should be considered. Bloch simulations provide faithful representations of the magnetization states following excitation and refocusing and can produce reliable decay curves; however, the EPG compensation approach, using the Fourier pulse profiles, provides exceptional fit accuracy. The Fourier slice profile assumption tends to overestimate T_2, in contrast to neglecting T_1 relaxation, which underestimates T_2. Simulation results in Figs 3.5a, 3.6a, and 3.7a indicate a maximum 4.1% overestimation due to the Fourier assumption, occurring only with equal excitation and refocusing pulse widths, very long T_1 values, and $B_1^{+\,rel}$ near unity.

Misestimation of the $B_1^{+\,rel}$ field is the largest consequence of using the Fourier slice profiles. The Fourier width of the refocusing pulses overestimates the actual magnetization width [140]. This inflates the fraction of stimulated echoes, which are then attributed to an artificially low $B_1^{+\,rel}$ field. This can be observed in Fig 3.8e where the $B_1^{+\,rel}$ field fails to reach unity, but relaxation times remain accurate. Ultimately, an estimate of the RF profiles — even a suboptimal, but rapid, Fourier approach — yields accurate transverse relaxometry.

The proposed fit is designed for data acquired with a multiecho spin echo sequence where complete images are formed at each echo time. For each voxel, fitting is performed on the full echo train; this is necessary for simultaneous $B_1^{+\,rel}$ and T_2 extraction. We believe accuracy could be improved with additional data input. An external T_1 estimate would lift the infinite T_1 assumption and improve accuracy with very thin refocusing widths in extreme B_1 environments. A B_1 map could improve accuracy and precision by removing one degree of freedom from the fitting; it could also permit accelerated data acquisition via echo sharing. Alternatively, spatial regularization of the $B_1^{+\,rel}$ field will constrain this parameter, improving fitting accuracy and precision.

Finally, we note that the proposed model does not dispute exponential decay of individual isochromats. Traditional exponential relaxation, via T_1 and T_2 processes, still occurs. The superposition of isochromats, each with unique T_1 and T_2 weighting, produces nonexponential signal decay [139].

3.1.6 Conclusion

We have described and validated a fit model for multiecho spin echo data that estimates the transmit field and incorporates stimulated echo contributions for accurate transverse relaxometry. The proposed model is compatible with the commonly available multiecho spin echo pulse sequence and requires no additional data input. We have shown, both numerically and experimentally, that this model exceeds 95% accuracy for a wide range of imaging environments and refocusing widths. The fit permits accurate transverse relaxometry in heterogeneous transmit fields and allows thin refocusing pulses.

Chapter 4

Multiecho Gradient Echo

Effective spin echo methods are extremely advantageous at high magnetic field strengths where magnetic susceptibility effects can produce signal voids near air/tissue boundaries in GRE sequences. Despite limitations, GRE methods are largely complementary to spin echoes. Image phase and enhanced venous contrast contribute additional information; low RF power enables efficient acquisitions. This chapter contains the description of an acquisition modification and data processing pipeline for susceptibility artifact correction and extraction of numerous data sets from 3D multiecho GRE data.

4.1 Field-Corrected 3D Multiecho Gradient Echo: Extraction of $T_2^\star$ Weighting, Quantitative $R_2^\star$, and Susceptibility Phase.[1]

4.1.1 Abstract

The proliferation of susceptibility weighted imaging (SWI) and the trend toward high magnetic field strengths have popularized GRE sequences for high resolution neurological studies. Presented is a method for optimizing 3D multiecho GRE acquisitions and image processing for the extraction of quantitative $R_2^\star$, composite $T_2^\star$ weighting, and susceptibility related datasets. A simple, but optional, pre-scan is proposed to pre-condition data and improve subsequent processing. A susceptibility correction method, for reduction of signal voids near air/tissue interfaces, is adapted from several previous works and applied to artifact suppression in three-dimensional composite $T_2^\star$ weighted images and quantitative $R_2^\star$ maps. Susceptibility phase im-

---

[1] A version of this section has been presented. Lebel RM, Wilman AH. Field-corrected 3D multiecho gradient echo: Simultaneous extraction of quantitative R2*, T2* weighting, SWI, and venography. In Proceedings of the Joint Annual Meeting of ISMRM-ESMRMB, Stockholm, Sweden, 2010. p. 5002.

ages are obtained at each echo using a novel adaptive filtering technique that modifies its cutoff frequency based on the residual phase offset and local phase deviation. This filter is shown to suppress background phase artifacts more uniformly than a filter with constant width. Filtered phase images at each echo time are combined into a single image, based on optimal CNR criteria. The utility of this acquisition and processing pipeline is demonstrated for high resolution neurological imaging.

4.1.2 Introduction

Modern high field MRI scanners offer improved SNR and some enhanced contrast mechanisms relative to lower field machines. GRE sequences are gaining popularity at high field due to low RF power deposition, the potential for quantitative $R_2^\star$ measures, and a unique sensitivity to susceptibility contrast.

SWI [21] exploits the image phase, which accrues during the echo time, to enhance image contrast. Data is typically collected with a flow-compensated spoiled GRE sequence. *TE* is selected for sufficient phase evolution, which scales linearly with *TE* and B_0, while maintaining acceptable acquisition efficiency and tolerable artifacts from background field heterogeneities. Echo times of ∼30 ms at 3 T and ∼15 ms at 7 T are common, although longer echo times improve phase contrast. These relatively long echo times present an opportunity for improved acquisition schemes: multiple echoes could be collected in a similar repetition time, providing additional contrast and processing options. Furthermore, traditional echo times are comparable to deep gray matter relaxation times (∼29 ms in the globus pallidus at 3 T [149]) and only a factor of two shorter than the longest gray matter $T_2^\star$ times (∼73 ms in frontal gray matter at 3 T [149]). Multiecho GRE with repetition times only slightly longer than traditional SWI could enable $R_2^\star$ relaxometry without a drastic reduction in acquisition efficiency.

GRE methods are sensitive to non-local field offsets. These arise from two general sources: erroneous measurement gradients and background field gradients. Measurement errors result from inadvertent application of linear encoding gradients. Eddy currents, pulse sequence timing inaccuracies, gradient amplifier non-linearity and ripple can all produce residual gradient areas. These effects typically produce a linear phase ramp in the readout direction and can hinder effective SWI processing; they have relatively little effect on magnitude images. Their deleterious effects are exacerbated in multiecho GRE since, small inaccuracies accrue with each echo, eventually producing substantial phase artifact.

Non-linear background field gradients, which result primarily from air/tissue interfaces, are inevitable but are slightly attenuated prior to acquisition with efficient shimming. In image space, they produce bulk phase shifts and intra-voxel phase dispersion. Bulk phase shifts corrupt the local phase variations exploited in SWI and are typically attenuated via high-pass filtering. Intra-voxel phase dispersion reduces signal intensity, resulting in artifactual hypointensity on magnitude images.

Numerous works have addressed these intra-voxel dephasing artifacts through gradient compensation, tailored RF pulses, or post-processing. In general, gradient compensation methods apply gradient lobes, typically in the thicker slice select direction, to null the gradient area imparted by background fields [150, 151, 152, 153, 154]. These methods invariably require some combination of long acquisition times, poor resolution, and/or limited slice coverage. Since intra-voxel dephasing scales with voxel dimensions, techniques which compromise resolution are intrinsically hindered. Simply reducing voxel dimensions has a considerable capacity for artifact suppression [155]. Like gradient methods, tailored RF pulses manipulate magnetization phase in the slice select direction to improve coherence at the echo time; unlike gradient methods, they are not restricted to linear phase modulations. Quadratic [156] or case specific [157] phases can reduce destructive interference at the echo time. Unfortunately, these methods either reduce the SNR or require prior information and multiple acquisitions to fill-in susceptibility voids making them inadequate for general imaging.

Post-processing techniques model the salient magnetization behaviour to account, or correct, for susceptibility induced signal loss. These methods rarely require multiple datasets or elaborate gradient schemes. As such, they enable high resolution acquisition and susceptibility artifacts can be intrinsically reduced relative to acquisition based methods. Remaining artifacts are modeled from the background field gradient and voxel dimensions. A linear gradient through a rectangular voxel produces a sinc modulated signal degradation [158], which occurs in addition to $T_2^\star$ relaxation:

$$S_{x,y,z}^{(\mathrm{sinc})} = \mathrm{sinc}\left(\frac{\gamma\ \mathit{BFG}_{x,y,z}\ \Delta x, y, z\ \mathit{TE}}{2}\right). \tag{4.1}$$

This sinc decay scales with the background field gradient ($\mathit{BFG}_{x,y,z}$), voxel dimension ($\Delta x, y,$ or z), and TE. Since the sinc function quenches the signal, post-processing techniques have a limited functional domain, which for argument sake is less than the first null point of the sinc function:

$$\gamma\ \mathit{BFG}_{x,y,z}\ \Delta x, y, z\ \mathit{TE} < 2\pi. \tag{4.2}$$

Provided this condition is satisfied, post-processing has proven extremely effective at mitigating background field gradients. Fernandez-Seara *et al.* included the background field gradient as a degree of freedom in a fitting routine for $R_2^\star$ using 2D multiecho data [158]. Volz *et al.* computed the background field gradient in the slice select direction using phase variations across adjacent slices of 2D multiecho data and successfully corrected the image signal intensity [159]. Furthermore, this work elegantly condensed all multiecho suceptibility-corrected images into a contrast-optimized composite T_2 weighted image. The same intensity correction method was later applied to $T_2^\star$ mapping [160]. To date there have been numerous effective post-processing techniques for suppression of background gradients, however none have been applied to simultaneous qualitative and quantitative imaging, nor to SWI.

Combined time-of-flight angiography and susceptibility weighted venography was recently presented using a 3D multiecho sequence [161]. This work successfully extracted multiple data sets, including susceptibility phase, from a multiecho acquisition. Acquisition parameters were optimized for angiography by suppressing signals from gray and white matter tissues, and thus its utility for general neurological imaging was not investigated. Additionally, no form of susceptibility correction was applied to magnitude images. The phase at multiple echo times has been recently employed for composite-echo SWI [162]. This work employed high-pass phase filters with progressively broadening cutoff frequencies to compensate for diverging background gradients with increasing *TE*. Adapting the filter width to match the echo time was shown to improve background gradient suppression relative to a constant filter. We hypothesize that an improved high-pass filter varies its frequency cutoff based on *TE and* spatial location.

In this work, we present an approach for combined quantitative and qualitative brain imaging with 3D multiecho GRE. High resolution $R_2^\star$ maps, SWI, and composite $T_2^\star$ weighted images are generated from a single scan. Scan time is invested to improve image resolution and sample a wide range of echo times. We employ a variety of optimized post-processing techniques to suppress background field gradient artifacts in magnitude images and present a novel adaptive filter for improved susceptibility phase imaging. We present a rapid and robust pre-scan method for readout gradient optimization to minimize residual and unbalanced encoding gradients, ultimately improving SWI processing of multiecho data.

4.1.3 Materials and Methods

All experimental data were acquired from a Varian Unity Inova 4.7 T whole-body imaging system with a maximum gradient strength of 60 mT/m and slew rate of 120 T/m/s. Human brain images were collected with a 27 cm birdcage coil operating in transmit only mode; a tight fitting 4-element array coil was used for signal reception.

We employ a 3D multiecho GRE imaging sequence where entire images are encoded at each echo time, Fig 4.1. Mono-polar readouts are used for consistent off-resonant artifacts. Flow compensation is discarded in favour of improved acquisition efficiency and shorter initial echo times. Slab selection is performed with linear-phase

SLR pulses [140]. The only pulse sequence modification is the pre-scan readout gradient optimization, described below. The reconstruction process is summarized in Fig 4.2 and described in more detail below.

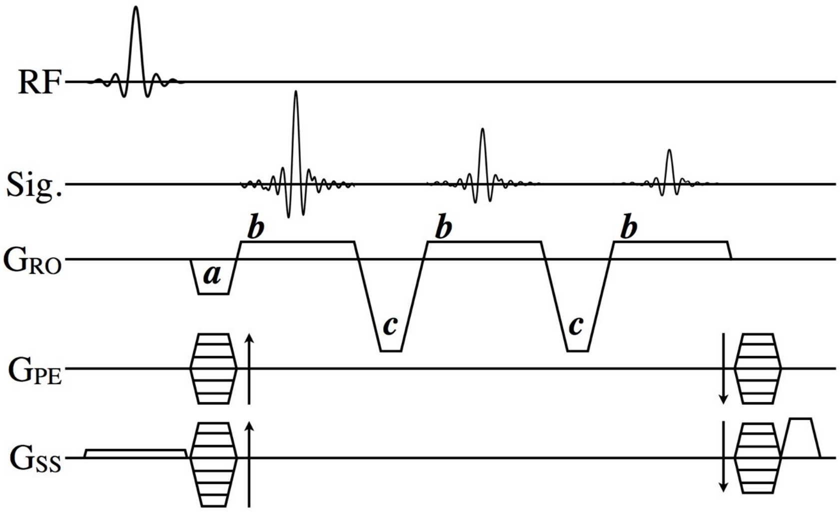

Figure 4.1: Pulse sequence diagram for 3D multiecho gradient echo. Three echoes are shown. Pre-phasing gradient a and re-phasing gradient c are scaled during the pre-scan to balance the area of the readout gradient b.

Images from two protocols are presented: a quick protocol to demonstrate efficacy of the pre-scan, and a high resolution, full-brain protocol to illustrate the proposed processing pipeline. The utility of the pre-scan is demonstrated by comparing raw and filtered phase images with optimized $\xi_{a,b}$ and with an intentional 2% mis-set. The FOV was $25.6 \times 16.0 \times 6.4$ cm^3 with a $512 \times 160 \times 16$ imaging matrix.

The high resolution protocol was acquired with a FOV of $25.6 \times 18.0 \times 18.0$ cm^3, matrix of $512 \times 240 \times 90$ (image resolution: $0.50 \times 0.75 \times 2.0$ mm^3), 7 echoes ranging from 3.8 ms to 39.1 ms, *TR* of 48.0 ms, bandwidth of 245 Hz/pixel. The tip angle was 8°— a slight SNR concession (Ernst angles between ~13° and ~16° for white and gray matter respectively) in exchange for minimal T_1 weighting. The total scan time was 17.3 minutes.

Pre-Scan Gradient Optimization

High-pass filtering of phase images is typically performed in SWI processing to suppress non-local phase variations. Unbalanced readout/re-phasing lobes produce residual phase ramps in image space; these errors accrue with each echo of a multi-echo sequence and should be minimized during acquisition. Scaling the amplitude of the pre- and re-phasing lobes (lobes labelled a and c in Fig 4.1, respectively) to balance the readout gradient areas (lobes labelled b) ensures no residual readout

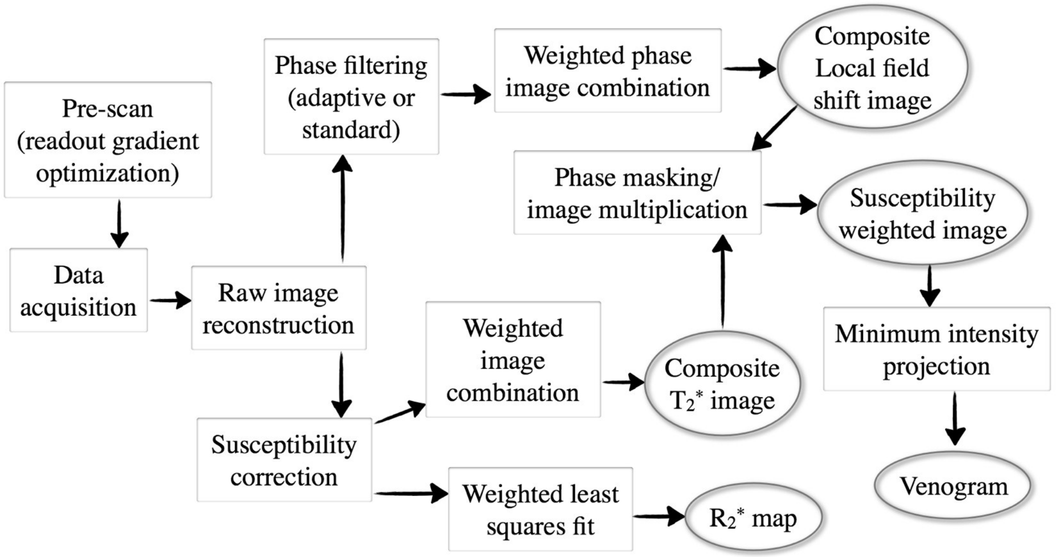

Figure 4.2: Reconstruction flowchart for multiecho GRE. Acquisition and processing stages are shown in boxes; final images in ovals. A total of five image sets are reconstructed from a single acquisition.

gradient remains at the center of the readout window.

The proposed pre-scan collects a small subset of both phase encode domains (we collect the central 8 × 8 lines). Phase encoding is employed to account for potential shifts in the k-space center in the phase encode directions. The scaling factor for lobes a and c is determined from the spacing between echoes in readout direction. To compute the scaling factor, modulus k-space data are averaged over all phase encodes. All echo times are concatenated and the resulting vector, which has periodic peaks (corresponding to the echoes), is spline interpolated by a factor of 10, Fig 4.3. We employ a peak-find algorithm to locate the peaks and compute the spacing between individual echoes, $\delta_j = P_{j+1} - P_j$. In our experience, the spacings between echoes are constant during the echo train (i.e., they do not diverge and thus do not require linear/non-linear regression). The scaling factor to adjust the amplitude of the pre- and all re-phasing gradient lobes is computed according to

$$\xi_{a,b} = 10\,\frac{N_{RO}}{\langle\delta\rangle}. \tag{4.3}$$

In the above expression, $\langle\delta\rangle$ is the average peak spacing and N_{RO} is the number of readout points.

In our experience, this single scale factor, applied to the pre- and all re-phasing lobes, is sufficient to eliminate the phase ramp in the readout direction. However, a unique scale factor for the pre-phasing lobe (gradient a in Fig 4.1) can be computed

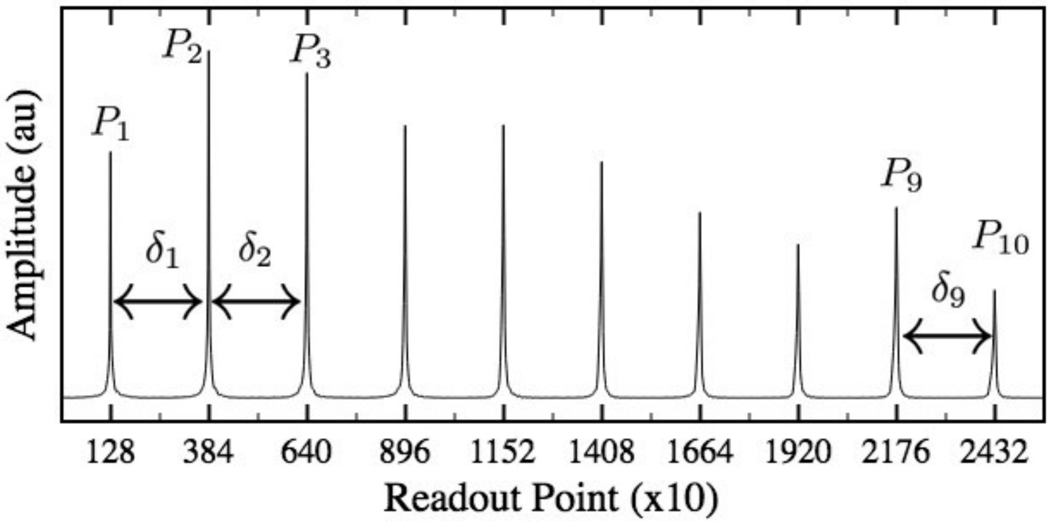

Figure 4.3: Pre-scan echo train with 10 echoes and 256 acquired readout points, interpolated to 2560 points per echo for improved resolution of the echo peak locations, P_j, and measurement of their spacing, δ_j.

from the location of the first echo peak (P_1) via

$$\xi_a = 10\,\frac{N_{RO}}{2P_1}. \tag{4.4}$$

Intensity based susceptibility correction

We employ a combination of promising post-processing techniques for removal of susceptibility induced signal voids. These techniques are applied to correct the signal intensity of magnitude images at each *TE*. Corrected images are condensed into a composite $T_2^\star$ weighted image and are employed for $R_2^\star$ fitting.

The three orthogonal background field gradients can be rapidly computed as described by Du *et al.* [161]. This method computes the phase difference between the first two echo times, then the spatial gradient. It is highly robust to phase wrapping since it employs complex exponentials and avoids directly computing angles (introduces phase wrap) until after all temporal and spatial differences are computed.

Using the background field gradients, susceptibility corrected images at each echo time are generated. Three intensity correction factor maps, corresponding to background gradients in the readout and both phase encode directions, are computed from the inverse of Eq 4.1 with the appropriate gradient, voxel dimension, and *TE*. For each *TE*, the three correction factor maps are multiplied into a single scale factor map. The correction factors are capped to avoid excessive noise amplification: correction factors exceeding 5.0 are zeroed — the resulting image may contain voids where dephasing prohibits reliable correction. This cap was selected empirically based on accuracy of the background field gradient estimation and the assumption of rectangular and homogeneous voxels required in defining Eq 4.1.

A composite $T_2^\star$ weighted image is created from the susceptibility corrected images following the methodology of Volz *et al.* [159]. Briefly, a single image volume is created from a weighted average of corrected images across all echo times. Weighting factors for this average are computed for each pixel and *TE* based on the desired contrast between two tissues with $T_2^\star$ values of 30 ms and 50 ms — roughly representing the range of values observed in gray and white matter at 4.7 T. Weighting factors are attenuated by susceptibility correction values to account for noise amplification. This weighting scheme optimizes contrast-to-noise by favouring later echoes, background field gradients permitting, or emphasizing earlier echoes if later echoes are degraded.

Quantitative $R_2^\star$ maps are obtained via mono-exponential fitting of the susceptibility corrected image intensity versus *TE*. This process is a modified version of that proposed by Baudrexel *et al.* [160]. Our implementation has several important differences, notably:

- We employ susceptibility intensity correction in all three spatial dimensions.
- During non-linear fitting, we weight the signal intensity at each echo by the inverse of its intensity scaling factor to account for noise amplification and thus increased uncertainty relative to other data points.
- Data points along an echo train were excluded if their intensity correction exceeded the cap, set at 5.0 in this work, as described above.

Adaptive Phase Filtering

High-pass filtering is required to suppress background phase shifts that corrupt the desired local phase offsets. This can be achieved by dividing a complex image by a low-pass filtered version of this image, Eq 1.33. The spatial-width of the filter determines the degree of phase attenuation: narrow filters (large cutoff frequency) suppress more phase than do wide filters (small cutoff frequencies). Selection of the filter width is a compromise between artifact removal and contrast preservation; unfortunately, no single filter width satisfies both criteria at all image locations. The fundamental similarity in characteristics of local and background phase preclude perfect isolation of these local effects with linear filtering; however, analysis of the residual phase following filtering provides insight into filtering performance and enables modification of filter parameters.

In the absence of background phase perturbation, tissue phase typically displays sharp edges between positive and negative phase; homogeneous regions may have a small but relatively uniform phase shift. The range of expected phase is also limited:

at 4.7 T we observe a deflection of approximately -40° in the globus pallidus and ±70° near venous vasculature at an echo time of 15 ms. Although phase is defined between ±180°, its standard deviation within a small area of tissue is typically highly constrained.

There are several characteristics suggestive of insufficient filtering. Phase wrap within a small region, evident from a large standard deviation within the region, is a strong indication of residual background phase. Additionally, a large net phase offset within a local neighbourhood may also indicate inadequate filtering.

As such, we propose an adaptive filter to improve suppression of background phase and enhance tissue contrast. The proposed method applies a 2D Gaussian filter that dynamically modifies its width to emphasize phase characteristics of local fields while suppressing qualities resembling residual background phases. The quality metric to minimize is

$$Q = \left|SD\left[\Phi_{loc}\right] - \beta \cdot TE\right| + \alpha_{penalty}\left\langle\Phi_{loc}\right\rangle^2. \tag{4.5}$$

In this expression, SD is the standard deviation operator and Φ_{loc} contains the post-filtered phase values in a local neighbourhood, defined as a block of voxels within a specified distance — we employ 5.0×5.0 mm^2 blocks for human brain imaging. The parameter β defines a target standard deviation that increases with echo time. we penalize large baseline phase offsets with the mean squared phase angle, $\langle\Phi_{loc}\rangle^2$. The scaling factor $\alpha_{penalty}$ weights the relative importance of achieving the target standard deviation versus maintaing a minimal phase offset. Additional constraints on the neighbouring field could be added to this expression.

Selection of tuning parameters β and $\alpha_{penalty}$ is performed empirically, and should be reassessed for other field strengths or anatomy. We found that $\beta = 10$ and $\alpha_{penalty} = 30$ provided reliable filtering for neurological imaging at 4.7 T, although a wide range of tuning parameters provided comparable image quality (data not shown). Although Eq 4.5 intrinsically constrains the filter width, we restrict the adaptive filter to widths between 0.25 mm and 10.0 mm. These bounds are not necessary to prevent divergent or singular filters — they simply improve computational efficiency.

The adaptive phase filter is applied to the 3D data sets on a slice-by-slice basis and at every TE. Images are compared to a those processed with a standard high-pass filter with a 5.0 mm filter width.

Multiecho Phase Combination

Phase images at multiple echo times can be combined into a composite phase image. This is performed by first converting phase angles into local field shifts (LFS), which are independent of TE and field strength. Image combination is performed via weighted average across all echo times:

$$LFS_{comp} = -10^9 \times \frac{1}{\sum_j w_j} \sum_j w_j \cdot \frac{\Phi_j}{\gamma\, B_0\, TE_j} \tag{4.6}$$

The local field shift is expressed in parts-per-billion (ppb). The negative sign accounts for the positive field shift in paramagnetic regions — it is neglected in this work to maintain a consistent visual appearance with phase images. It has been shown in the context of magnitude image combination, that weighting factors to maximize the final contrast-to-noise ratio (CNR) are determined from the CNR of each image [159]. Phase contrast evolves linearly with TE while phase noise is inversely proportional to the image intensity [21, 163]; as such, the optimal weights are given by:

$$w_j = TE_j \cdot S_j, \tag{4.7}$$

where S_j is the image intensity at the j^{th} echo. The utility of this phase combination technique is demonstrated with the same high resolution protocol described above.

Susceptibility weighted images and venograms

Susceptibility weighted images are created as described by Haacke *et al.* [21]. We employ the composite LFS image in lieu of phase images to create the negative "phase" mask. This mask is multiplied into the image four times. Venograms are created from minimum intensity projections through SWI images.

4.1.4 Results

The effects of unbalanced and balanced readout gradients on image phase are shown in Fig 4.4. An intentional 2% scaling of the readout pre- and re-phasing lobes produces a relatively benign phase ramp at the first echo, but this ramp diverges in subsequent echoes. The linear component of the image phase is removed following waveform optimization. As shown in Fig 4.4(c, f), linear phase ramps can impair high-pass phase filtering, and should be prevented — ideally during data acquisition. This gradient optimization has the added benefit of correcting for sub-optimal shims in the readout direction, over the slab volume. As such it varies with slab positioning and patient orientation. A 2% mis-set is exceptionally large and is used for demonstration purposes. Typical changes are less than ~1%, but phase errors compound sufficiently with long echo trains to obstruct local phase extraction.

$R_2^\star$ relaxometry benefits from susceptibility correction and from appropriate weighting of data points along each decay curve, Fig 4.5. The bias observed in regions of extreme background field gradients is reduced, by up to 50 s^{-1}, by fitting

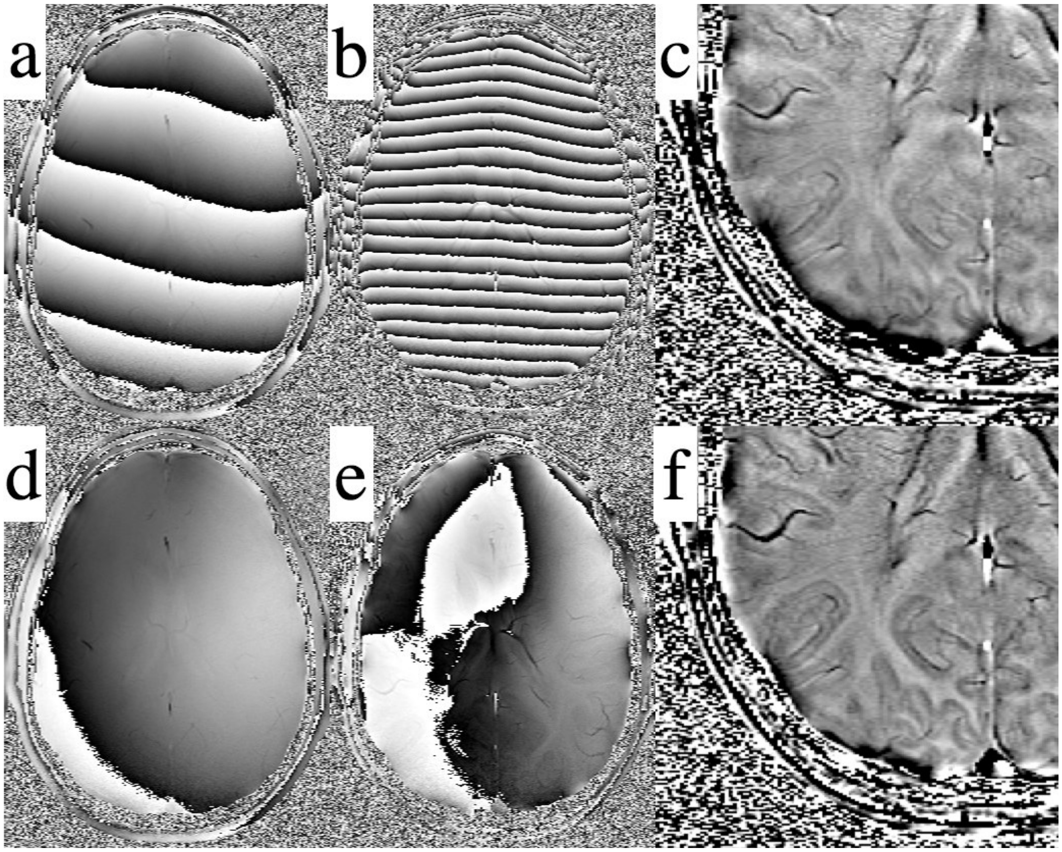

Figure 4.4: Phase images with an intentional 2% mis-set of the readout scaling factors at (a) the first and (b) the third echoes. Readout direction is anterior/posterior. Following the pre-scan, phase images at (d) the first and (e) the third echoes have no phase ramps in the readout direction. This reduces burden on the high-pass filter, enabling improved susceptibility phase detection (f) with the pre-scan than (c) without.

susceptibility corrected images, relative to fitting raw images. The difference map shows that fitting the raw and corrected images is equivalent in regions where the background field gradient is small, but that severe $R_2^\star$ overestimation occurs near the cortex and above the sinus cavities if raw images are employed for fitting.

In Fig 4.6, adaptive phase filtering is compared to conventional phase filtering of images with a 33 ms *TE* (the 6^{th} echo). The 5.0 mm Gaussian filter provides adequate suppression of background phase in regions far from air/tissue interfaces, but fails to fully attenuate phase offsets in regions such as the cortex or immediately above the sinus cavities. Phase wraps are evident in frontal regions of frame (a) and some cortical regions in frame (b). The adaptive filter provides reliable filtering in all brain regions: reduced phase wrap is evident in the frontal cortex relative to the constant-width filter. More reliable visualization of the cortical ribbon is also pos-

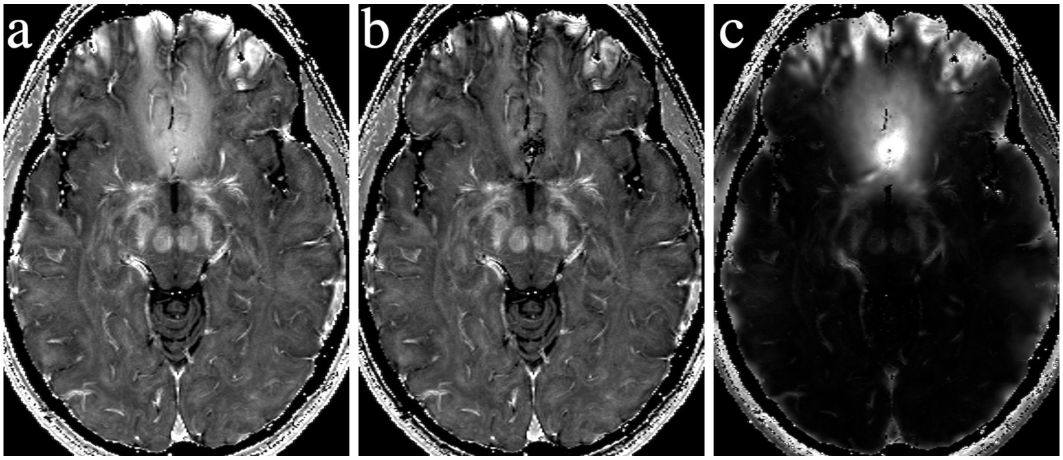

Figure 4.5: Quantitative $R_2^\star$ maps through a region with very strong susceptibility gradients, scaled from 0 to 100 s^{-1}. (a) Map without susceptibility correction and (b) with correction are shown. (c) The difference between the map without susceptibility correction and the map with correction, scaled from 0 to 50 s^{-1}.

sible with the adaptive filter than with the standard filter, as seen in Fig 4.6(f, g). The adaptive filter is successful in detecting traits suggestive of excessive or insufficient filtering, but has a limited ability to restore information corrupted by extreme phase variations. The frontal regions in Fig 4.6(b) require narrow filters, as shown in panel (c), to remove background phase; tissue contrast is irreversibly attenuated by this filter.

Composite LFS images are shown in Fig 4.7. Composite phase images display improved SNR and CNR relative to LFS images from a single *TE*. Artifact suppression is also enhanced in the composite image, as evidenced by improved image fidelity in the cortex compared to most individual echo time images. As expected from Fig 4.6, the adaptive filter produces cleaner composite LFS images than does the constant width filter. This additional artifact suppression comes at a price: contrast is lost in large venous structures. The sagittal sinus and neighbouring veins are clearly delineated with the standard filter, but are excessively smothered by the variable filter. Adjustment of tuning parameters (increased β, decreased $\alpha_{penalty}$) can restore this contrast (not shown).

A sample slice from the five image sets generated from the reconstruction pipeline (Fig 4.2) are shown in Fig 4.8. The composite, susceptibility corrected image displays strong $T_2^\star$ weighting and insensitivity to background field gradients. The composite LFS map is masked and multiplied (four times) into the composite $T_2^\star$ image to produce the SWI image. In this image, contrast between different brain tissues is vastly enhanced, due primarily to exaggerated venous contrast. Venograms reveal striking microvascular detail.

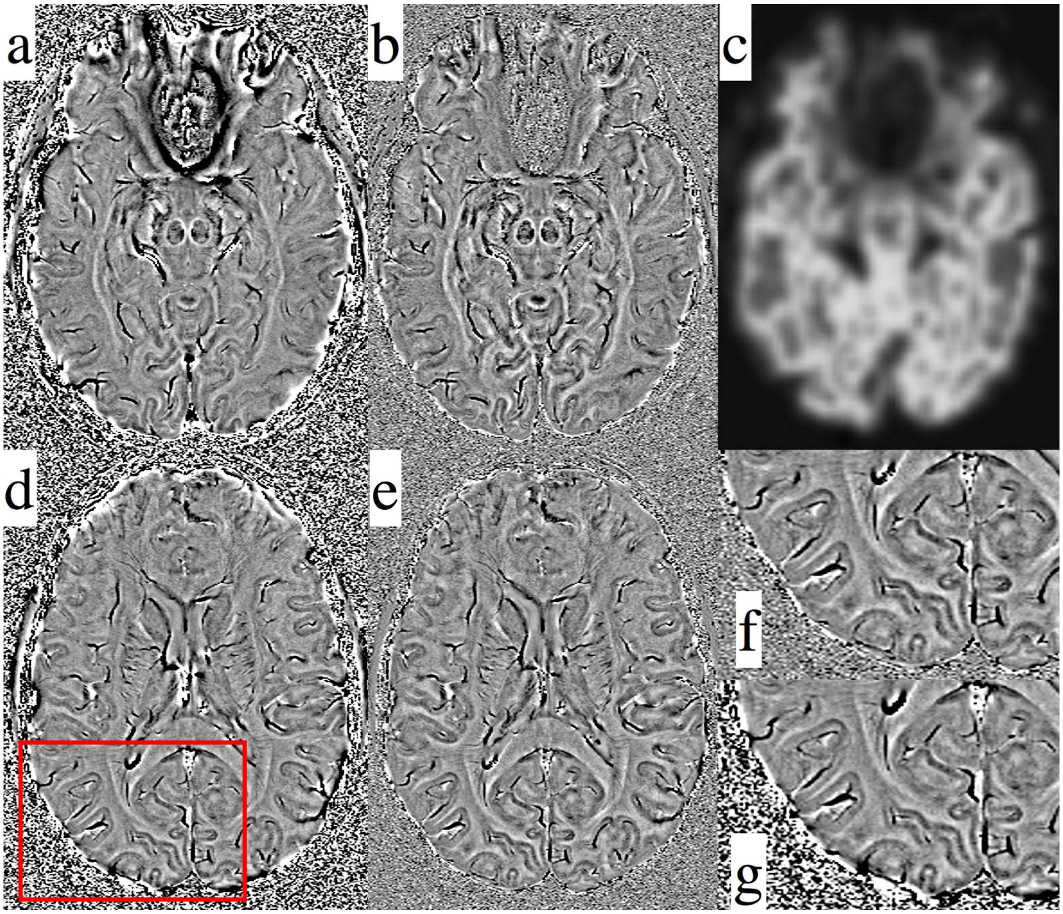

Figure 4.6: Phase image comparison between (a, d, g) constant-width and (b, e, f) adaptive-width high-pass filtering. (c) Map of the filter width used to produce image (b), scaled from 0.5 mm to 10.0 mm. (f, g) Enlarged portions of the adaptive-width and constant-width phase images. The echo time is 33 ms throughout.

4.1.5 Discussion

The gradient optimizing pre-scan is demonstrated to effectively eliminate linear phase ramps in the readout direction. The consequence of slightly unbalanced gradients is typically negligible for single echo GRE, but can seriously impede multiecho acquisitions. These imbalances can arise from suboptimal shimming, but usually result from hardware imperfections. Pre-phasing and fly-back gradients (lobes ‘a’ and ‘c’, Fig 4.1) are executed hastily, making them more prone to amplifier imperfections and residual eddy currents than are the readout lobes (lobes ‘b’, Fig 4.1). Small unbalanced areas rapidly accrue into large phase ramps in multiecho scans. Phase ramps can alternatively be corrected during post-processing. Shifting the k-space data to center the echo within the readout window will suppress the phase ramp, but data on one periphery will be excluded and the resulting void on the other

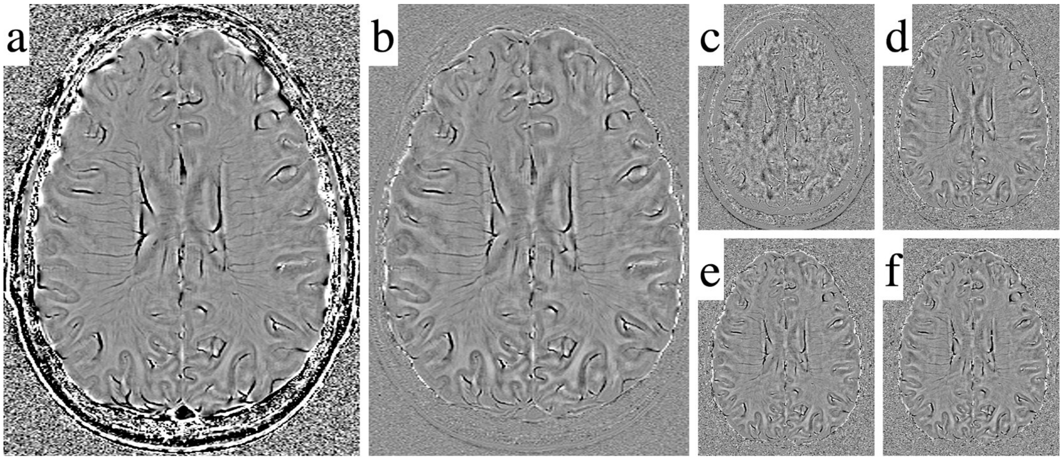

Figure 4.7: (a) Composite local field shift image with a nominal 5 mm filter, (b) composite image with the adaptive filter. Local field shift images from (c) the 1^{st} (3.8 ms), (d) the 3^{rd} (15.6 ms), (e) the 5^{th} (27.3 ms), and (f) the 7^{th} (39.1 ms) echoes, which are used (along with the even echoes) to create the composite image (b). All images are scaled between 20 ppb (black) and -20 ppb (white).

periphery requires filling. A simple correction during acquisition is preferred. Unbalanced gradient errors are particularly problematic with high resolution readouts: small fractional errors translate into sizeable residual gradients. This pre-scan is not an absolute pre-requisite for the processing pipeline presented here, it just helps pre-condition the data. Simplicity of the proposed solution to this problem warrants its use.

The adaptive filter provides more uniform appearing phase maps than does the constant filter, potentially improving its clinical and research value, but has some limitations that should be considered. This method updates the filter width to enhance traits suggestive of tissue contrast, while penalizing those indicative of residual gradients. Unfortunately, the fundamental similarity between tissue and background phase prevents perfect isolation of local phase. Overall, this approach reduces artifacts in the cortex and near the sinus cavities, yet maintains strong contrast in most other brain regions. These traits may improve visualization of many neurological conditions [164], including traumatic brain injury, stroke, and a range of neurodegenerative disorders. In detection and characterization of MS, susceptibility phase has been employed to visualize white matter lesions [80, 81], but robust detection of cortical lesions remain elusive. These lesions are seen at 8 T with standard gradient echo imaging [165], suggestive of a local magnetic field disturbance; the proposed filter may aid in their detection.

Since the filter width varies across an image, Fig 4.6(c), spatial variations in tissue contrast are likely to occur. The lack, or presence, of contrast may reflect this

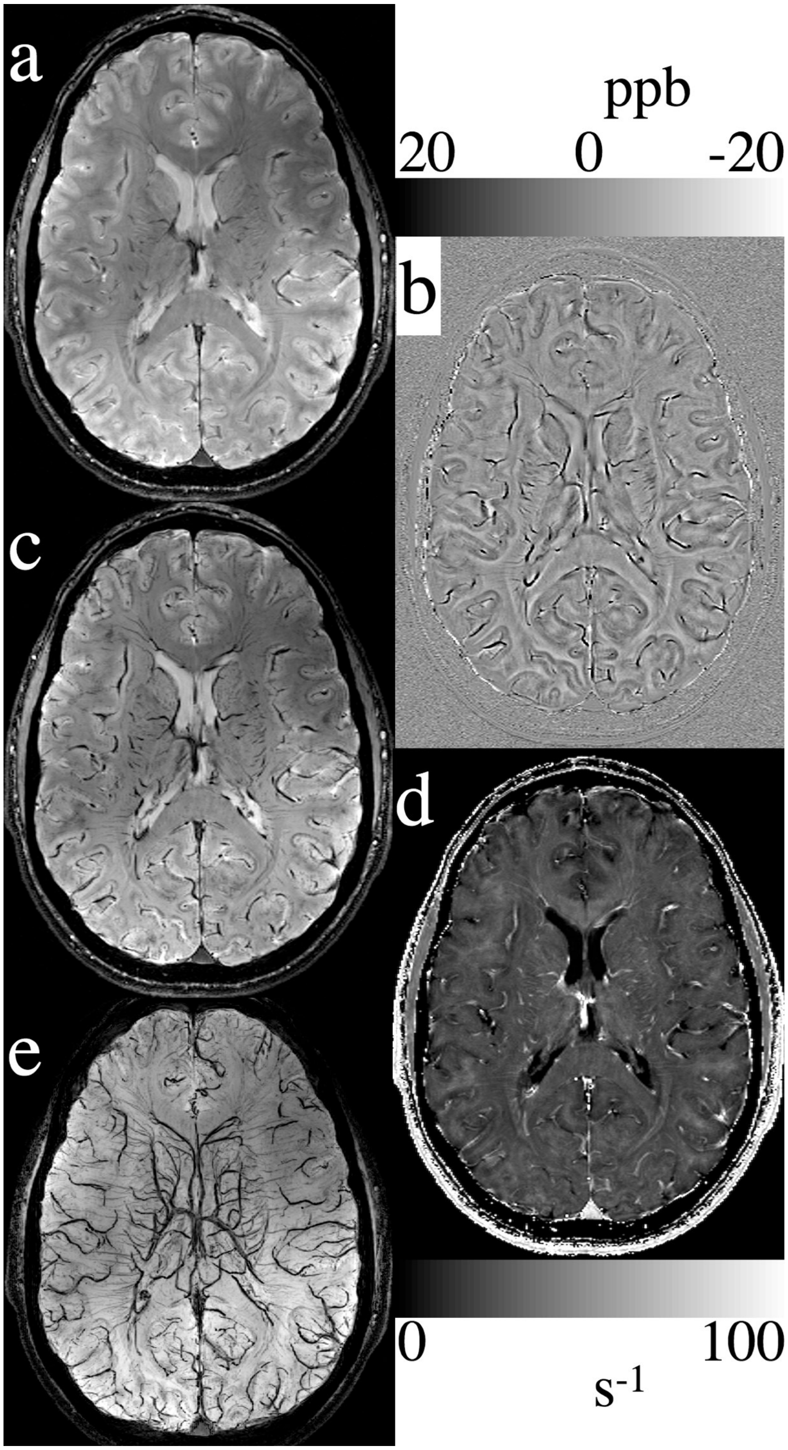

Figure 4.8: Summary of output images from the multiecho gradient echo reconstruction pipeline. (a) Composite $T_2^\star$, (b) local field shift (negated), (c) susceptibility weighted, (d) $R_2^\star$ map, and (e) a 1.6 cm minimum projection venogram. Image resolution is $0.50 \times 0.75 \times 2.0$ mm^3; full brain coverage was obtained in 17.3 minutes.

filter variation rather than anatomy. Quantitative comparisons between regional field shifts may be hindered by adaptive filtering. However, these measurements are challenging with conventional filtering since unsuppressed background phase can preclude phase comparisons within and between subjects.

There are potential enhancements to the adaptive filter that warrant further investigation. Currently, filtering occurs equally in all directions, guided only by the mean and standard deviation of the local neighbourhood. Additional directionally sensitive criteria could enable anisotropic filter design. This may further enhance visualization of elongated structures, such as the cortex and veins. Any additional constraints imposed on Eq 4.5 are likely to improve background phase suppression by reducing reliance on the current criteria. Currently, reliance on achieving a target standard deviation can over-suppress regions with high vascular density (sagittal sinus area, Fig 4.7) while potentially under-attenuating homogeneous regions. Additional constraints have vast potential for enhancing the sensitivity and specificity to local phase disruptions; more investigation is warranted.

In this work we employ a contrast maximizing combination of images spanning all echo times. Magnitude images were combined, as previously proposed [159], by weighting each echo by the predicted contrast for tissues roughly representing GM and WM, but reducing the weights in regions where susceptibility correction amplifies noise. We found this method efficiently corrected for most susceptibility voids; it only struggled in regions immediately bordering air/tissue interfaces. Phase image combination was achieved in a similar fashion: phase images were first scaled to a common basis (the local field shift), then added with appropriate weighting factors. These weighting factors are given by the phase CNR, which is proportional to TE and inversely proportional to noise. A recent report performed an unweighted average of high pass filtered phase images [162]. They demonstrated improved CNR in the combined phase image relative to single echo phase images; we expect improved results could be obtained with appropriate weighting.

For visualization of neurological tissues, we opted for a sub-Ernst angle excitation. This improved contrast between GM/WM/CSF relative to a tip angle closer to the SNR optimal angles for GM or WM. An estimated 20% signal loss is obtained with 8° pulses relative to 14°, but this was acceptable with a 3D acquisition at high field. Furthermore, combination of images at multiple echo times increased the SNR by up to 250%.

4.1.6 Conclusion

We have demonstrated a robust and versatile reconstruction pipeline for multiecho GRE imaging. This pulse sequence generates a tremendous quantity of data that must be distilled to efficiently visualize its information. We have adapted and combined several previously published methods for manipulating GRE data sets and demonstrated their mutual compatibility for processing 3D multiecho GRE data. We present a new phase filtering method that adapts the filter parameters based on the pattern of residual image phase. This filtering method enables improved visualization of cortical gray matter and aids in suppressing large background phase offsets. In all, we extract five image sets from a single acquisition: a composite $T_2^\star$ weighted image, an $R_2^\star$ map, a composite local field shift map (analogous to susceptibility phase), susceptibility weighted images, and venograms.

Chapter 5

Applications

The techniques for quantitative imaging at 4.7 T developed in this thesis (i.e., R_2, $R_2^\star$, and susceptibility phase) are all sensitive to tissue iron content. As such, these techniques hold considerable promise for investigation of numerous neurological disorders, some of which are associated with abnormal iron metabolism, storage, and transport [96, 166, 167, 168, 95]. Unfortunately, the exact sensitivity of these MRI parameters to tissue iron is unclear; changes in iron distribution or water diffusion can also alter relaxation rates and image phase. A brief preface to this chapter is warranted.

5.1 Foreword: Iron Sensitivity

The three MRI parameters quantified in this thesis, R_2, $R_2^\star$, and susceptibility phase, are all influenced — in a dissimilar manner (of course!) — by magnetization evolution as water molecules diffuse through iron induced micro-gradients. The enhancement observed with each method is highly dependent on two factors:

- Proton mobility, which is based on water content and barriers to diffusion.
- The magnetic field distribution, generated by the concentration and dispersal of iron.

In a review article, Schenck notes that "satisfactory models relating T_2-shortening to tissue iron content have so far been difficult to establish." Specifically, "this reflects lack of knowledge of the detailed magnetic properties of the iron oxide particles and their distribution in space" [83]. Changes in iron distribution or water diffusion alter how reversible and irreversible phase is accrued. Simply put: relaxation rates and bulk phase shifts are dependent on factors other than iron concentration. This is a crucial issue since accumulation of free iron is known to generate and maintain neurotoxic free-radicals while accrual of ferritin-bound iron may be harmless, even beneficial. Interpreting parameter changes in neurodegenerative disease is challenging and multiple quantitative measures offer a greater chance of detecting harmful iron compounds.

In Fig 5.1, the three quantitative parameters at 4.7 T are plotted versus tissue iron, the later is assessed by post-mortem histochemistry in a different group of subjects [85]. Despite interpretational challenges, all three quantitative methods (in healthy individuals) relate to published non-heme iron concentrations, Table 5.1. $R_2^\star$ displays the greatest sensitivity, largest R^2 value, and lowest p-value; R_2 displays much lower sensitivity, but a correlation nearly equivalent to $R_2^\star$. Curiously, the LFS does not show a statistically significant correlation with iron — this is a slightly artificial result as contrast is degraded in large structures by high pass filtering. All correlation coefficients are limited by accuracy in the tissue iron estimates (note the large horizontal error bars in Fig 5.1). As each measure is sensitive to different iron properties, the combination of measures may provide a useful assessment of regional changes in non-heme (and heme) iron.

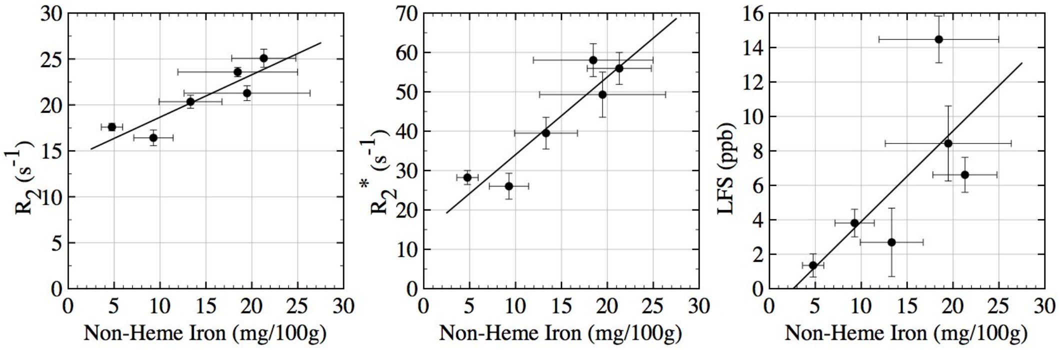

Figure 5.1: Quantitative MRI parameters in seven healthy volunteers (average age, 36.4±4.6 years; minimum age, 32 years) versus brain iron, measured histochemically *ex vivo* in a different subject group [85]. Left, R_2; middle, $R_2^\star$; right, LFS.

Table 5.1: Regression parameters for quantitative MRI measures (R_2 and $R_2^\star$ in s^{-1}; LFS in ppb) versus brain iron concentration (in mg/100 g), as plotted in Fig 5.1. Note the similar intercepts between R_2 and $R_2^\star$.

	R_2	$R_2^\star$	LFS
Slope	0.462	1.977	0.526
Intercept	14.05	14.31	-1.361
R^2	0.803	0.863	0.505
p	0.016	0.007	0.114

Presented in this chapter is a quantitative assessment of these MRI parameters in sub-cortical GM regions in a group of relapsing-remitting MS patients and matched controls. The susceptibility-phase measurement in this chapter is performed with a conventional 2D, flow-compensated SWI sequence and is processed with a constant-width high-pass filter rather than the multiecho phase method presented in Chapter 4.

5.2 Quantitative Evaluation of Sub-Cortical Gray Matter in Relapsing-Remitting Multiple Sclerosis[1]

5.2.1 Abstract

Objective

Multiple sclerosis may be associated with increased iron deposition in sub-cortical gray matter nuclei, typically visualized as hypointensity on T_2 weighted MRI. Very high field MRI is sensitive to iron accumulation, with relaxation rates R_2 and $R_2^\star$ and susceptibility phase, expressed as a local field shift, all correlated to tissue iron concentration. This study demonstrates the utility of a 4.7 T scanner to quantify imaging parameters in sub-cortical gray matter for detection of abnormalities in early stage relapsing-remitting MS patients.

Methods

Fourteen MS patients and 14 age- and gender-matched controls were imaged. The above parameters were quantified in most basal ganglia nuclei, the thalamus, and the red nuclei using manual ROI segmentation. Parameters were compared to controls and correlated with clinical scores.

Results

Significant increases in relaxation rates and/or LFS were observed in the basal ganglia and thalamus, particularly the pulvinar nucleus. These parameter enhancements are attributed to increased tissue iron. A significant correlation with EDSS was observed in the red nucleus; mildly significant correlations were observed in the caudate, putamen, and pulvinar. No significant correlations were observed with disease duration.

---

[1] A version of this section has been presented. Lebel RM, Eissa A, Emery DJ, Blevins G, Wilman AH. Iron-Sensitive Quantitative Methods for Multiple Sclerosis: Lesion Evolution and Deep Grey Matter Iron Deposition. In Proceedings of the Joint Annual Meeting of ISMRM-ESMRMB, Stockholm, Sweden, 2010. p. 4324.

Interpretation

These findings indicate that MRI at very high field strengths with multiple quantitative measures reveals changes in sub-cortical gray matter in early stage relapsing-remitting MS. Furthermore, disease processes likely commence prior to symptom onset and quantitative MRI may report disease severity.

5.2.2 Introduction

In addition to inflammatory and demyelinating processes, increased iron content has been observed in MS patients. Histological assessments suggest abnormal iron levels in neurons and GM near lesions [82], in macrophages and microglia [168], and in the putamen and thalamus [68]. MRI corroborates these findings: T_2 hypointensity has been observed in most deep GM nuclei [68, 69, 169] and quantitative measures of relaxation times/rates or susceptibility-induced field shifts strongly suggest increased iron in the basal ganglia. Interestingly, imaging metrics in deep GM correlate better with disability and cognitive function [170] than does T_2 lesion load [74].

Iron is capable of donating or stripping electrons, making it a crucial element in the electron transport chain and playing a role DNA synthesis; however, it must be carefully regulated via chelation to prevent unwanted reactions [171, 172]. Redox active iron, resulting from inadequate chelation or storage, can catalytically promote the formation of highly reactive hydroxyl radicals via the Fenton reaction [91]. Hydroxyl radicals are known to denature proteins, damage DNA, and oxidize lipid membranes [172]. Furthermore, chronic hypoxic conditions have been reported in demyelinated axons [173, 174]; this state is attributed to decreased mitochondrial output coupled with an increased energy demand from impaired impulse conduction. Iron is so intimately linked with the immune response that experimental autoimmune encephalomyelitis, an animal model of MS, could not be induced in iron deficient mice [175].

Whether iron accumulation is a primary [176] or secondary neurodegenerative factor in MS pathology, or is simply a benign by-product of the disease, it may serve as a biomarker of disease severity [83]. Furthermore, any characteristic iron accretion patterns could potentially be exploited as discrimination factors for exclusion of alternate pathology and facilitate diagnosis, which is presently biased toward white matter lesions [61]. Quantitative imaging methods that are particularly sensitive to non-heme iron are required to identify and exploit this potential biomarker.

Many MRI studies of MS have been performed at 1.5 T, and more recently, at 3.0 T. Sensitivity to non-heme (and heme) iron increases with field strength [44, 50] and a near-linear increase in signal-to-noise ratio enables detailed visualization of iron distribution. Very high field (VHF) systems, defined loosely as those exceeding

3.0 T, have been employed for improved lesion detection, visualization and vascular identification [177, 165, 178, 179, 180, 181, 182].

Quantitative methods at VHF are particularly desirable for measurement of iron overload. Currently, no absolute quantitative measure of iron is possible with MRI; however, numerous methods are highly sensitive to iron. Quantitative R_2 mapping suppresses background field gradients, including those from vasculature. Its iron relaxivity increases with field strength and may prove sufficiently sensitive and specific to become a reliable measure of non-heme iron at VHF. Quantitative $R_2^\star$ is very sensitive to iron but is obfuscated by field gradients surrounding air/tissue boundaries and veins. Both relaxation measures are confounded by changes in tissue water content. Susceptibility weighted imaging (SWI) [21] is a relatively new method, sensitive to field shifts caused by the magnetic susceptibility of tissues. Non-heme iron is paramagnetic and tends to strengthen the local field. Field shifts can be visualized and quantified on high pass filtered phase images from a gradient echo acquisition. SWI can be very sensitive to iron and has been used to visualize venous vasculature [21], characterize lesions [80, 81], and to quantify LFS in sub-cortical GM of relapsing-remitting MS patients [48].

Unfortunately, when implemented at VHF, all of these methods are limited by radiofrequency (RF) power deposition or by heterogeneous B_0 and RF fields. These effects preclude traditional methods for R_2 and $R_2^\star$ quantification. As a result, some VHF studies employ SWI, or related techniques, to probe the bulk phase shift within a voxel. This is rather limiting since susceptibility methods are complementary to transverse relaxometry techniques, which measure intra-voxel phase dispersion. Furthermore, current susceptibility phase analysis is only partially quantitative: tissue phase measurements can be performed, but results are corrupted by high-pass filtering and by residual background field shifts. Nonetheless, it remains a powerful tool in the very high field armamentarium, but is complementary, not equivalent, to transverse relaxometry.

We have recently developed independent methods for R_2 [183] and $R_2^\star$ [184] relaxometry in the presence of heterogeneous RF and B_0 fields respectively and validated their utility at 4.7 T. With these methods and susceptibility phase imaging, a multi-modality VHF study of iron accumulation in sub-cortical GM can be performed. This study evaluates the utility of quantitative imaging at VHF for detecting changes in sub-cortical GM of early stage relapsing-remitting MS patients.

5.2.3 Subjects and Methods

Fourteen patients with relapsing-remitting MS, diagnosed according to the McDonald criteria [61], were recruited based on evidence of recent lesion activity; they were paired with 14 age- and gender-matched controls. All subjects provided informed consent, in compliance with institutional regulations, prior to participation. Subject information is summarized in Table 5.2.

Table 5.2: Subject demographics

	Patients	Controls
Number	14	14
Gender, M/F	4/10	4/10
Age, Mean ± SD (years)	32.6 ± 7.4	31.4 ± 6.3
Disease duration, Mean ± S.D.(years)	3.5 ± 2.2	—
EDSS, Mean ± S.D.	2.5 ± 1.5	—

Imaging was performed on a Varian Inova whole-body 4.7 T MRI with a maximum gradient strength of 60 mT/m and slew rate of 120 T/m/sec. Images were collected with a 4-element receive array [103] paired with a TORO birdcage coil for transmit [102]. As summarized in Table 5.3, three quantitative imaging sequences were acquired in the axial plane: a 2D multislice multiecho spin echo for R_2, a 3D multiecho gradient echo for $R_2^\star$, and a 2D flow-compensated gradient echo for LFS.

Table 5.3: Acquisition parameters for quantitative imaging.

Parameter	R_2	$R_2^\star$	LFS
Voxel volume (mm^3)	5.00	1.00	0.75
In-plane resolution (mm^2)	1.00×1.25	1.00×1.00	0.50×0.75
Slice thickness (mm)	4.00	2.00	2.00
Number of slices	2	90	50
Repetition time (ms)	3000	44.0	1540
First echo time (ms)	10.0	2.93	15.0
Echo spacing (ms)	10.0	4.10	—
Echo train length	20	10	—
Tip angle (deg)	90x–180y–180y $\cdots$	10	65
Acquisition time (min)	4.50	9.39	6.57

The R_2 quantitation protocol was SAR limited to 2 slices; the low acquisition efficiency also limited the in-plane resolution. One slice was placed through the globus pallidus, caudate, putamen, internal capsule, and thalamus; the other, through the red nucleus and substantia nigra. The typical gap between slices was 8.0 mm, which also served to minimize cross-talk.

Quantitative R_2 maps were processed using the stimulated echo compensating fit [183]; $R_2^\star$ maps employed 3D susceptibility compensation [184], which was based on a previous 2D method [160]. Susceptibility phase images (Φ) were obtained by dividing the original complex image by a low pass filtered image created by using a 2D Gaussian frequency kernel that extended over $1/8^{th}$ of the k-space matrix, then measuring the resulting phase angle. Phase angles were converted to LFS [48], measured in parts-per-billion (ppb), via

$$\text{LFS} = -10^9 \times \frac{\Phi}{\gamma\, B_0\, TE} \tag{5.1}$$

to enable comparison between field strengths (B_0) and echo times (TE).

Using the coverage limiting R_2 images, bilateral regions-of-interest (ROIs) were drawn around the globus pallidus (GP), putamen (Put), head of the caudate nucleus (CN), substantia nigra (SN), and the red nucleus (RN). The thalamus was subdivided into the pulvinar nucleus (Pul) and the remainder of the thalamus (Th) due to reliable contrast in all subjects. The only white matter region analyzed was the internal capsule (IC). If required, ROIs were modified on $R_2^\star$ and LFS maps to compensate for inter-scan motion, to exclude vasculature, and to avoid excessive background field gradients. This slight ROI modification was required to capitalize on the strengths of each method while avoiding its weaknesses. LFS is not referenced to neighbouring tissue, such as a ventricle or normal appearing white matter. An example data set from a 34 year old female MS patient, with ROIs overlaid on the R_2 map, are shown in Fig 5.2.

Parameter values were averaged within the entire ROI and between hemispheres. The standard deviations of the local field shift (LFSSD) within ROIs were also measured. This provides a measure for susceptibility phase that is complementary to averaging and helps negate the deleterious effects of high pass filtering. Parameters were compared to those from healthy controls using Student's t-test. The percent change (PC) between the inter-patient and inter-control mean was calculated. The effect size (ES), defined as the difference of means divided by the average of standard deviations, is also reported. Pearson product-moment correlation coefficients were calculated between MRI parameters and both disease duration and EDSS [62]. Group differences and correlations at the $p < 0.05$ significance level are noted; differences satisfying $p < 0.006$ — a level obtained via stringent Bonferroni correction with 8 independent comparisons — were considered highly significant.

5.2.4 Results

Average MRI measures were higher in MS patients than in controls in all sub-cortical GM regions we investigated, Fig 5.3 and Table 5.4. In most regions, statistically significant ($p < 0.05$) changes in one, or more, MRI parameters were observed in patients. The globus pallidus and pulvinar were ubiquitously different, with increased R_2, $R_2^\star$, LFS, and LFSSD — often with very high significance ($p < 0.006$) — in

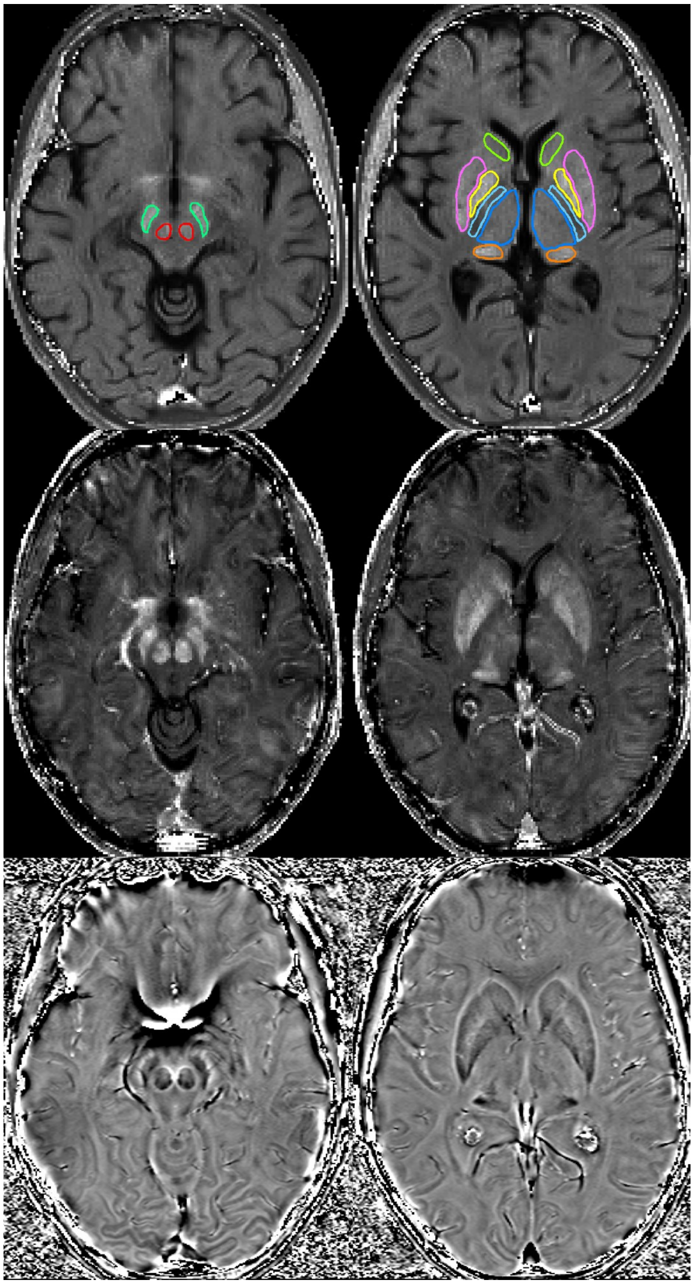

Figure 5.2: Quantitative images of a 34 year old MS patient. R_2 maps (top row) are scaled from 0 (black) to 50 s^{-1} (white), $R_2^\star$ maps (middle row) from 0 to 100 s^{-1}, susceptibility phase (bottom row) from -0.2π to 0.2π (equivalent to LFS from 35 to -35 ppb). ROIs covering the globus pallidus (yellow), putamen (pink), caudate (light green), thalamus (dark blue), pulvinar (orange), substantia nigra (dark green), red nucleus (red), and internal capsule (light blue) are shown on the R_2 maps. For this patient, ROIs required no modification when transferred to $R_2^\star$ and LFS maps.

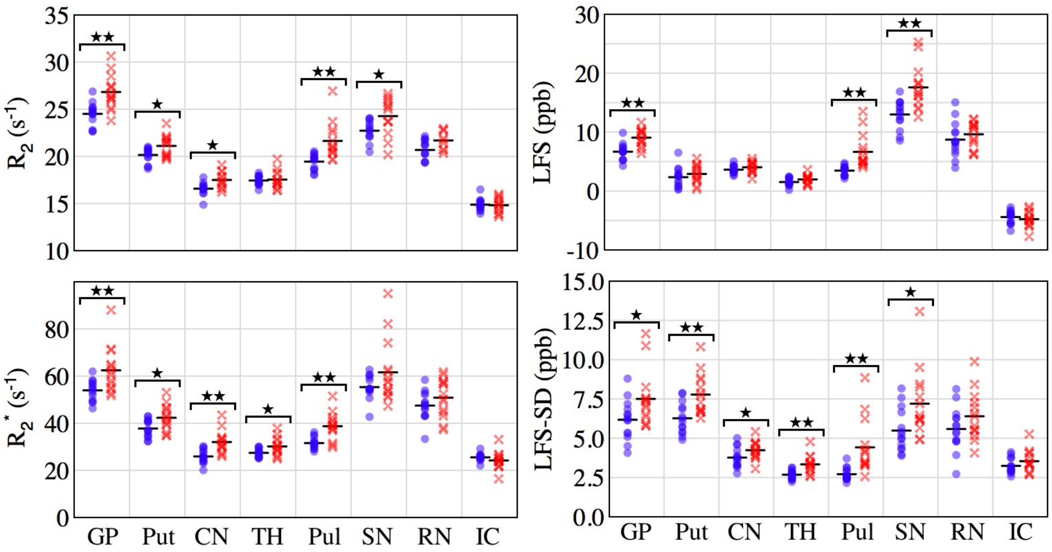

Figure 5.3: Quantitative MRI parameters in healthy controls (blue, circles) and in MS patients (red, crosses). Single starred comparisons indicate $p < 0.05$; double starred, $p < 0.006$. Every basal ganglia structure in MS patients shows highly significant differences from control subjects on one or more measures. The pulvinar nucleus shows highly significant changes with all measures; the remainder of the thalamus shows relatively little change.

MS patients. The putamen and caudate nucleus had higher relaxation rates, and abnormal LFSSD in MS patients. The substantia nigra showed enhanced R_2 and LFS, including both its average and standard deviation. The thalamus (excluding the posterior pulvinar nucleus), differed by less than 10% with $R_2^\star$, but had a substantial 24.5% change, with very high statistical significance, in LFSSD. The red nucleus and internal capsule showed no significant group differences, although the red nucleus trended higher in all metrics.

A total of six regions in the basal ganglia and thalamus showed highly significant differences; their identification required the use of all three quantitative measures. R_2 relaxometry revealed changes in two regions while $R_2^\star$ measurements indicate three abnormal regions. Susceptibility phase imaging allowed identification of five abnormalities, but required atypical processing (i.e., LFSSD) to identify these differences.

Of the three methods, LFS provided the largest change, Table 5.4. In the globus pallidus, its PC is more than double that of $R_2^\star$ and nearly quadruple that of R_2. In the pulvinar, this sensitivity of LFS is even more pronounced: it quadruples the PC of $R_2^\star$ and is more than eight-fold greater than R_2. Despite this high sensitivity, it does not provide drastically improved ES over either R_2 nor $R_2^\star$. This is particularly true of large structures, like the putamen, caudate nucleus, and thalamus, which

Table 5.4: Percent change and effect size for quantitative MRI parameters in MS patients relative to controls. Bold faced values are significant at the $p < 0.006$ level, as shown in Fig 5.3.

	R_2		$R_2^\star$		LFS		LFSSD	
Region	PC	ES	PC	ES	PC	ES	PC	ES
GP	**9.46**	**1.54**	**15.76**	**1.22**	**35.51**	**1.66**	21.45	0.88
Put	4.77	1.01	12.16	1.01	23.38	0.34	**24.11**	**1.32**
CN	5.59	1.20	**23.58**	**1.61**	11.13	0.51	12.47	0.78
TH	0.56	0.13	9.99	1.01	28.77	0.64	**24.50**	**1.55**
Pul	**11.31**	**1.55**	**22.61**	**1.76**	**92.03**	**1.71**	**63.11**	**1.60**
SN	6.83	1.01	11.33	0.68	**35.44**	**1.51**	31.29	0.98
RN	4.89	1.03	7.04	0.47	10.43	0.35	14.43	0.55
IC	-0.36	-0.08	-5.25	-0.51	8.20	-0.30	9.52	0.53

show greater ES with relaxometry. Heterogeneity within these structures — due to either high pass filtering or intrinsic contrast — provides a larger ES with LFSSD.

Three weakly significant correlations with EDSS were observed, Fig 5.4. R_2 correlated with EDSS in the caudate and putamen, while $R_2^\star$ correlated with EDSS in the pulvinar. Significance is lost following any form of multiple comparison correction. The red nucleus showed a strong and significant correlation between LFSSD and EDSS. This correlation remained highly significant even with the exclusion of the patient with an EDSS score of 6.5. No significant correlations between MRI measures and disease duration were observed in any region.

5.2.5 Discussion

Recent advances in imaging methodology enable numerous quantitative measures at very high field strengths, as shown in Fig 5.2. Correction for stimulated echoes resulting from heterogeneous RF fields permits R_2 mapping with multiecho spin echo; however, RF power deposition restricts imaging efficiency. Susceptibility correction, using magnetic field gradient information inherently contained in a 3D multiecho gradient echo sequence, enables accurate $R_2^\star$ mapping despite strong susceptibility gradients (note the accurate quantitation above the sinus cavity in Fig 5.2). Susceptibility phase can be extracted from a single high resolution image and benefits from the SNR and pronounced susceptibility contrast at very high field.

Each quantitative method has unique strengths and weaknesses; the combination of techniques is promising for evaluation of neurodegenerative disease. R_2 relaxometry is insensitive to background field gradients and blood vessels, the former due to RF refocusing and the latter due to dephasing from incomplete refocusing of flowing

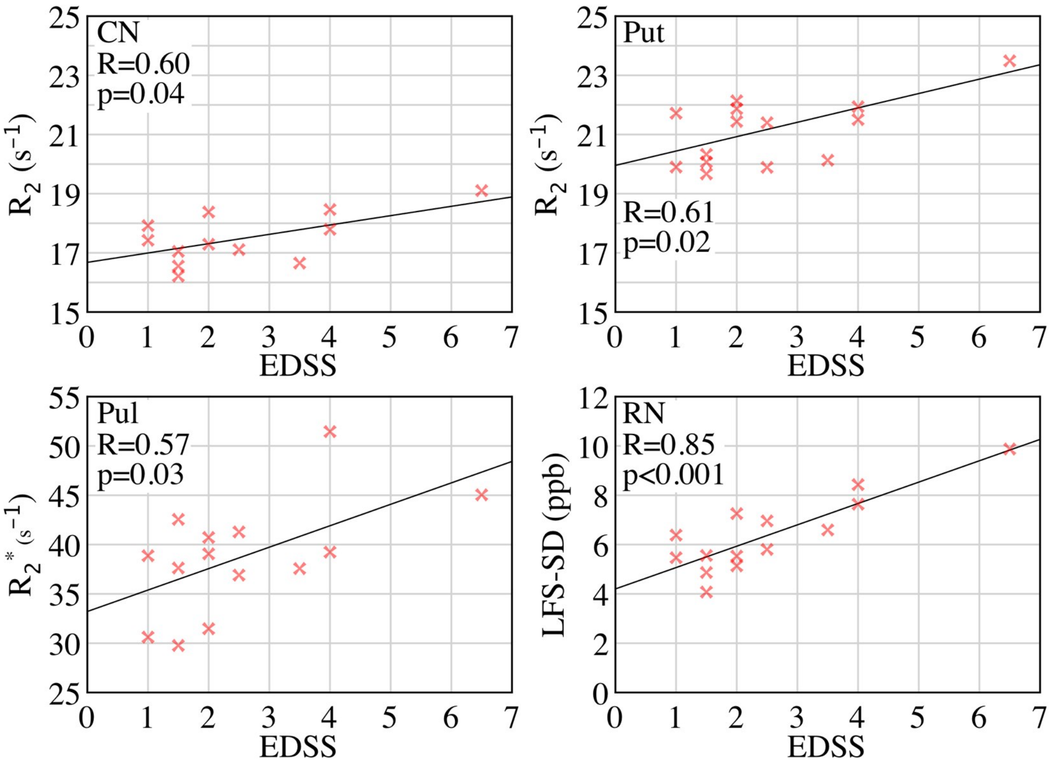

Figure 5.4: Correlations between quantitative MRI parameters EDSS. Possible correlations were observed in the striatum with R_2 and in the pulvinar with $R_2^\star$. Significance is lost following multiple comparison correction. The red nucleus showed a strong and significant correlation between LFSSD and EDSS.

spins. As such, it provides low artifact images, compensating for a relatively low relaxivity to produce a useful effect size, as listed in Table 5.4. Currently, it is limited by acquisition efficiency at high field. We employed 4 mm thick slices with R_2 (in contrast to 2 mm slices with the other methods) to improve targeting accuracy and used lower in-plane resolution to reduce acquisition time. These factors increase partial voluming effects and may artificially reduce the PC and the ES. Multiecho $R_2^\star$ mapping provides full brain coverage at relatively high resolution. High sensitivity to both heme and non-heme iron is evident in Fig 5.2. Without undersampling, such as parallel imaging, long scan times can be prohibitive and motion artifacts can degrade data quality.

Of the methods employed, susceptibility phase imaging produces the highest resolution images because it requires only a single echo. It also displays the largest PC in deep grey matter of MS patients relative to controls. However, it is severely hampered by background field gradients — and the processing used to suppress them. High pass filtering attenuates contrast, particularly in large structures, reducing the average LFS within a structure. We have employed an unconventional metric, the standard deviation of LFS within an ROI, to account for either natural or synthetic contrast variations. This measure is useful in two scenarios: First, regions with highly concentrated phase/LFS are often surrounded by opposing phase/LFS. This dilutes the regional average, but augments the standard deviation. Phase variations within the red nuclei in Fig 5.2 exemplify this effect (even neglecting the strong white border, substantial variation exists). Second, large homogeneous regions display central contrast attenuation due to high pass filtering; this effect is seen in the caudate and putamen in Fig 5.2. In this case, the average LFS is reduced but the standard deviation captures this variation. Essentially, LFSSD is an alternative to strategic, and possibly biased, ROI placement [185, 186]. Although mildly disconcerting, such empirically profitable processing methods are currently required to compensate for inadequate tissue phase extraction methods. Eventually, susceptibility mapping [187] may augment or supplant current phase processing and eliminate the need for such *ad hoc* measures.

Interpretation of changes in relaxation rates and local field shifts is challenging. In addition to iron concentration, relaxation rates depend on the form and distribution of iron. To compound matters, relaxation rates can be altered by the proton mobility, which is related to integrity and content of myelin and cell membranes, and by cellular water content, which may be altered by edema [79]. Evidence suggests that the mean diffusivity in the basal ganglia appears unchanged in relapsing-remitting or secondary-progressive MS [188], suggesting that the relaxation changes we observe in MS patients are likely due to abnormal iron content, not diffusion/water content confounds.

Using three quantitative measures, significant group differences were observed in all sub-cortical GM regions investigated, except the red nucleus, which trended higher. These differences are attributed to iron accumulation, which is reported to occur in the sub-cortical GM of MS patients [68, 189] and to which these quantitative measures are known to be sensitive [44, 21, 46]. The abnormal GM regions identified in this work are in agreement with other imaging reports. Susceptibility phase changes have been previously noted in the pulvinar thalamus [48, 80], but for the first time we have quantified and compared them to controls. We confirm a recent 7.0 T report of abnormal phase in the basal ganglia [48]; they observed more extensive phase differences using the average LFS than we currently report. This is likely due to a combination of factors: first, their patient population had a much longer average disease duration. Second, our studies employed different image resolutions, and third, there are possible differences in phase filtering between studies. Additionally, their LFS is referenced to the internal capsule, which we felt was at risk of coupling with the highly enhancing GP. The substantia nigra has appeared normal on T_2 weighted scans at 1.5 T [69]; we observe a potential increase with R_2 and a likely change with LFS, both attributed to high sensitivity to iron at VHF.

The widespread pattern of deep GM damage that we observe could potentially complement the current lesion based assessment of spatial disease dissemination. A recent evaluation of the McDonald criteria for MRI scans suggestive of MS showed good specificity (89%) when applied to patients diagnosed with an alternate neurological disorder [190]; however, improved specificity, and potentially sensitivity, could perhaps be achieved by incorporating deep GM abnormalities; further investigation is warranted.

A strong correlation with EDSS was observed in the red nucleus and possible correlations with EDSS were detected in the caudate, putamen, and pulvinar. All of these regions are associated with either movement or visual processing and the EDSS is biased toward these functional systems. The red nucleus has afferent connections with the motor cortex and cerebellum and efferent connections in the rubrospinal tract, which indirectly modulates flexor muscle tone. The striatum is intimately involved in planning and modulation of motor tasks. EDSS correlation in the pulvinar nucleus may reflect its role as a visual relay [191]. At 7.0 T, Hammond *et al.* did not observe any correlations between LFS and EDSS [48]. The correlation reported in the current work was only elicited via LFSSD; it would be telling if their data supported this finding.

Lack of correlation with disease duration is attributed to population homogeneity: the average disease duration was 3.5±2.2 years and ranged from 0.9 to 7.8 years. Lack of correlation between MRI parameters and disease duration implies that iron accumulation, and potentially neurodegenerative processes, commence considerably prior to symptom onset. Furthermore, it emphasizes inaccuracy in the term "disease duration", which is commonly used to represent time since initial symptom onset.

This study has several limitations. First it employs a small sample size. With increased patients, more highly significant group differences may be observed and more confident relationships might be established between MRI parameters and clinical scores. Second, limited slice coverage and resolution with R_2 mapping restricts its analysis and prevents perfect overlap with ROIs from other methods. Approaches with higher resolution and improved slice coverage may improve the sensitivity of R_2 as a measure of abnormal deep GM.

In conclusion, very high field MRI with multiple quantitative measures reveals widespread abnormalities in the deep GM of early stage relapsing-remitting MS patients. The combination of three quantitative protocols was necessary to discern all affected regions. A phase measurement in the red nucleus correlated with EDSS; possible correlations between EDSS and relaxometry measures in the caudate, putamen, and pulvinar were also observed. These correlations are possibly based on the bias toward motor and visual components of the EDSS, but demonstrate the potential for iron sensitive measures at VHF to detect and monitor disease severity. No correlations with disease duration, attributed to our homogeneous patient population, suggests abnormalities in sub-cortical GM may commence prior to symptom onset. Further very high field MRI investigations in early stage MS patients are warranted.

Chapter 6

Concluding Remarks and Future Directions

The objectives of this thesis were to implement, characterize, and apply conventional and/or promising imaging sequences at 4.7 T. The primary challenges were addressing the RF power requirements of FSE, compensating for heterogeneous RF fields for T_2 mapping, refining susceptibility correction schemes for multiecho gradient echo, and applying these techniques to study a cohort of MS patients.

The SAR limitations, precluding traditional FSE at 4.7 T, were overcome primarily via reduced refocusing angles. This approach, while valid at clinical field strengths, was previously untested at high field. It was demonstrated that reduced refocusing angles, in combination with appropriate RF and readout bandwidths, are ideal for SAR mitigation. Using reduced and variable refocusing angles, a wide assortment of T_2 weighted images can be obtained in a time-efficient manner. Image contrast is modified with low angles, a result of three factors: reduced incidental magnetization transfer, enhanced sensitivity to heterogeneous transmit fields, and slower apparent transverse relaxation.

Heterogenous transmit fields are catastrophic for transverse relaxometry, which relies on perfect 180° refocusing. Longer relaxation times are observed with non-180° pulses (shorter times if stimulated echoes are excluded). Sub-optimal conditions can result from transmit miscalibration, finite refocusing pulse width, and from non-uniform excitation fields. The latter cannot be avoided at high field. It was demonstrated that RF profiles and transmit fields could be incorporated into the relaxation model, accounting for stimulated and indirect echo pathways to more accurately extract the T_2 relaxation time. This method is not restricted to high field as it permits thinner refocusing widths than are typically employed, thus improving multislice imaging efficiency.

Gradient echo imaging at high field provides exceptional susceptibility contrast through changes in relaxation rates and bulk phase shifts. Unfortunately, images are corrupted by artifacts from background field shifts. A multiecho GRE sequence was shown to provide a plethora of information that can be used to correct for intra-voxel dephasing, thus providing accurate $R_2^\star$ mapping and producing high SNR magnitude images with composite $T_2^\star$ weighting. An adaptive phase filter was presented to more uniformly suppress background phase shifts and enable crisp visualization of susceptibility phase images. Phase images at multiple echo times were condensed into a CNR optimized LFS map, which was then used to generate SWI and venograms. Scan times are long, but often worthwhile.

The techniques developed in this thesis are all sensitive to iron compounds in the brain. The ability to assess brain iron is important since abnormal iron concentrations or compounds can produce free-radicals with neurotoxic properties. Although it is not clear (to me, anyway) *exactly* how iron concentration, form, or distribution relates to these quantitative MRI parameters, they likely provide insight into abnormal tissue metabolism and iron storage. An initial application involves quantification of R_2, $R_2^\star$, and LFS, within sub-cortical gray matter structures in a cohort of relapsing-remitting MS patients. Multiple regions were shown to differ from a control population. Most prominently, the globus pallidus and pulvinar nucleus showed differences with all three quantitative methods. Most other regions differed on one or two measures. No correlations with disease duration were observed, suggesting the disease processes commences well before symptom onset.

The methods presented in this thesis will likely be applicable at higher field strengths, such as 7.0 T. Depending on the actual RF power increase between 4.7 T and 7.0 T, an additional power attenuation factor between 1.5 (linear dependence) and 2.2 (quadratic dependence, Eq 1.39) is likely required. Standard imaging protocols at 4.7 T (e.g., Fig 2.8) employ refocusing angles of around 90° to mitigate SAR; at 7.0 T, angles between 60° and 75° would sufficiently reduce the RF power. An SNR reduction (from loss of echo coherence) of $\sim$20% would be observed, as shown in Fig 2.4, but this neglects potential averaging from prolonged signal decay at lower angles, and is also less than the 50% SNR gain available at 7.0 T. Additionally, approaches such at the Virtual 180, which recoup lost coherence, may be particularly beneficial at these very high field strengths.

At 7.0 T, transverse relaxometry using multiecho spin echo will be challenging due to SAR constraints, but the stimulated echo processing is likely very accurate due to the very long T_1 values in most brain tissues. This effect is discussed in Chapter 3, Page 96.

The proposed multiecho GRE method is anticipated to be extremely beneficial at 7.0 T. Susceptibility artifacts are exacerbated at 7.0 T relative to lower fields and will likely require a robust correction method. The proposed method has proven robust for the field variation observed at 4.7 T; it is expected to succeed at higher field. Additionally, this method is not SAR limited at 4.7 T, nor is it anticipated to be constrained at 7.0 T.

As demonstrated, modified FSE is compatible with high field strength and can produce exceptional images. This thesis also provides the first demonstration (to the best of my knowledge) of accurate transverse relaxometry in the human head at a field strength above 4.0 T without the use of adiabatic pulses[1]. Despite the promising advances, these methods have numerous limitations.

6.1 Limitations

High field strengths provide the SNR required for high resolution images, but physiology rarely obliges. In-plane resolutions of 0.43 mm were reported in Chapter 2 and even higher resolutions have been reported elsewhere [101], but images of this quality are hard to achieve and protocols yield unreliable results. Physiological motion, including bulk patient movement, blood flow, brain pulsation, and respiratory motion *seriously* degrade image quality. Patient compliance is no longer the limiting factor: considerable luck and perhaps planetary alignments are also required. In a recent collaborative study with Dr. Malykhin [192], two identical high resolution data sets were collected consecutively with the expectation that ~1/3 of image sets will have unacceptable physiological artifacts. Figure 6.1 contains a high resolution postmortem FSE image collected at 4.7 T and an *in vivo* image of above average quality acquired with a similar protocol. The effects of motion are appreciable: ghosting and ringing can be seen and an overall reduction in SNR is apparent relative to the postmortem scan — and this is a good image. For high resolution imaging, methods to reduce acquisition time and minimize sensitivity to a variety of motion artifacts are more important than increasing the field strength.

Current SWI image processing methodology is *seriously* lacking. The statistically insignificant correlation with tissue iron (see Fig 5.1 and Table 5.1) is likely due to suppression of contrast during processing. Extraction of phase images involves high pass filtering (see Section 1.3.3, Eq 1.33) to suppress slowly varying background field shifts. Unfortunately, linear filtering also attenuates contrast from local field shifts. This is especially noticeable in large structures such as the globus pallidus, whose field shift is likely homogeneous (see Fig 6.2) but appears diminished in the center on filtered phase images. The adaptive filtering method holds considerable promise for improved phase extraction but requires validation in various brain regions prior to widespread implementation. Additionally, the adaptive filter still inadvertently attenuates tissue contrast while suppressing background phase. Tech-

---

[1] Yikes, that's a lot of conditions!

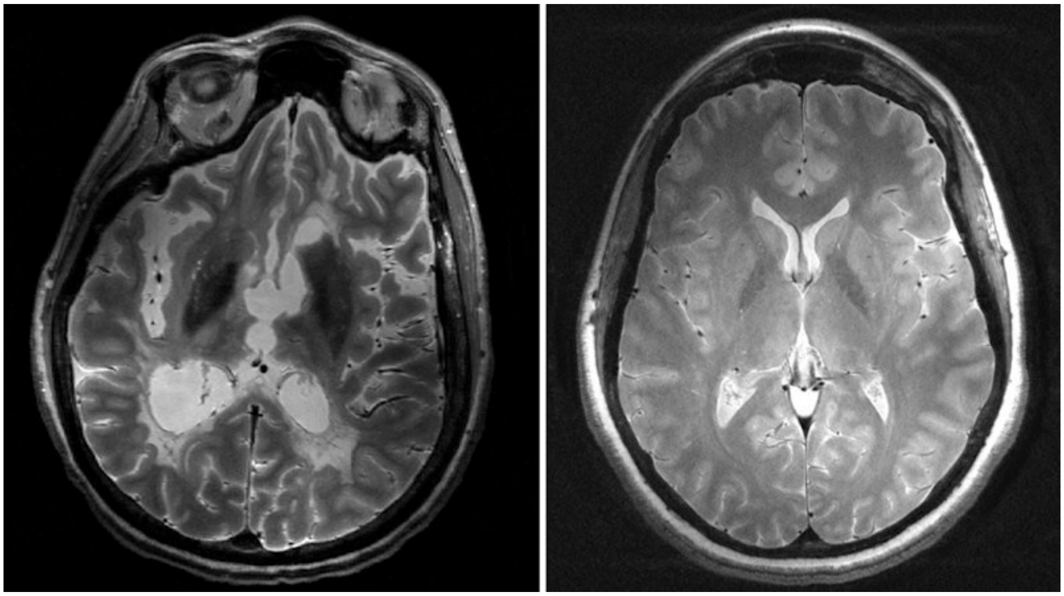

Figure 6.1: Image quality comparison between similar high resolution T_2 weighted FSE protocols of a postmortem MS patient (left) and a compliant relapsing remitting MS patient (right). Involuntary motion (i.e., brain pulsation, respiratory motion, swallowing, etc ...) yields a drastic increase in ghost and ringing artifacts and a concurrent SNR reduction.

niques to improve phase processing, such as preconditioning to suppress background fields prior to filtering [193], or improved filtering — perhaps wavelet methods or some form of dipole specific filter — could vastly enhance the accuracy and reliability of phase susceptibility imaging.

6.2 Future Directions

The sequences and techniques presented in this thesis are sensitive to non-heme iron. While “sensitive” is interesting — and in my opinion, degree worthy — it’s quite ineffective at revealing pathology or quantifying changes in iron concentration or form. Developing techniques that truly quantify iron concentrations, or reveal its chemical state, would be extremely rewarding. A method that varies the echo spacing [194] could be adapted and implemented at 4.7 T. In combination with the stimulated echo correction method presented here, this may permit more specific iron quantification. Alternatively, quantifying relaxation rates at lower refocusing angles may provide insight into iron concentration. Low refocusing angles contain a large fraction of stimulated and indirect echo pathways, which have a strong diffusion sensitivity — it’s analogous to varying the echo spacing. Other sequences may be worth investigating. Balanced steady-state free-precession, which mimics

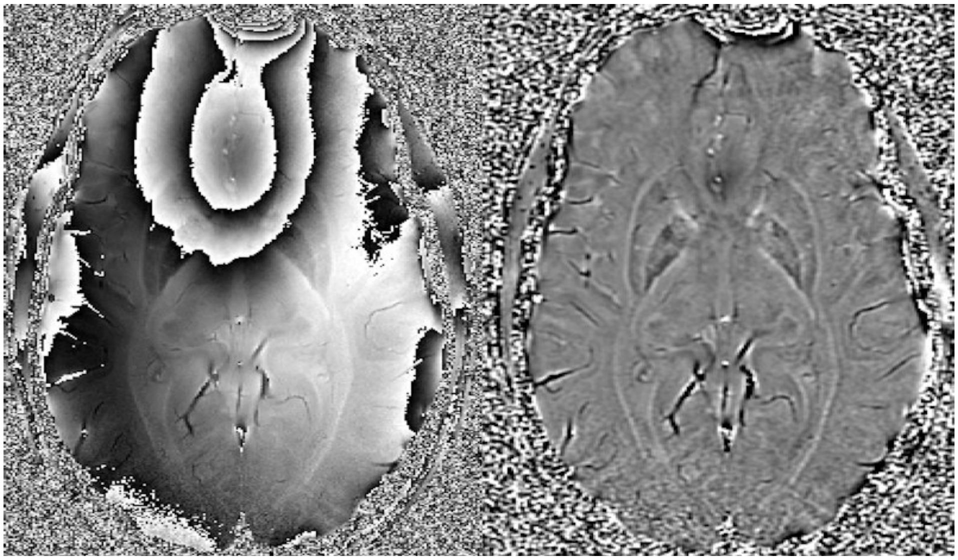

Figure 6.2: Phase images at the level of the globus pallidus and putamen before (left) and after (right) high-pass filtering (with a constant width filter). Prior to filtering, the contrast within these structures appears relatively uniform; after processing, contrast is heterogenous.

spin echo behaviour [195], has long coherence pathways and is known to be sensitive to non-heme iron [196].

The stimulated echo compensating fit presented in Chapter 3 was validated for mono-exponential fits. Complex tissue structures with multiple water compartments produce multi-exponential signal decay [78, 120]. The proposed fitting model is likely compatible with multi-exponential decay and with the non-negative least squares algorithm used to compute a pseudo-continuous distribution of relaxation times. In practice, extremely high SNR [197] is required for accurate fitting and residual errors should be small (less than ~0.5% [120, 144]). Since T_1 relaxation is neglected in the proposed model, it may struggle to fully account for the stimulated echo contribution and unacceptably high residuals may be observed. Additional work is required to verify the utility of this method for multi-exponential analysis.

Accelerating the stimulated echo compensating fit would vastly improve its utility at high field. The current implementation is SAR limited at ~2.5 minutes per slice. Rapid readout schemes, such as echo planar imaging (see Section A.1.4), could increase the number of phase encode lines collected after each refocusing pulse and vastly reduce total imaging time. Additionally, undersampling schemes could be implemented to reduce the required number of repetitions.

Additional investigation into the utility of the adaptive phase filter is warranted. This method may drastically improve quantification of phase abnormalities in the deep GM nuclei and cortex. A study that investigates the strengths and weaknesses of this method is warranted.

The methods developed in this thesis have been applied to a small group of MS patients. A larger cross-sectional study will likely reveal more/stronger correlations between MRI parameters and clinical scores. A longitudinal study may reveal changes in MRI parameters within individual patients as their disease progresses.

Bibliography

[1] Haacke EM, Brown RW, Thompson MR, Venkatesan R. Magnetic Resonance Imaging: Physical Principles and Sequence Design. Wiley-Liss, 1999.

[2] Bloch F. Nuclear Induction. Phys Rev 1946;70(7-8):460–474.

[3] Cowan B. Nuclear magnetic resonance and relaxation. Cambridge Univ Pr, 1997.

[4] Bloembergen N, Purcell EM, Pound RV. Relaxation Effects in Nuclear Magnetic Resonance Absorption. Phys Rev 1948;73(7):679–712.

[5] Bronskill M, Sprawls P (Editors). The Physics of MRI: 1992 AAPM Summer School Proceedings. The American Institute of Physics, 1993.

[6] Hoult D. The principle of reciprocity in signal strength calculations-a mathematical guide. Concepts in Magnetic Resonance 2000;12(4):173–187.

[7] Ratering D, Baltes C, Nordmeyer-Massner J, Marek D, Rudin M. Performance of a 200-MHz cryogenic RF probe designed for MRI and MRS of the murine brain. Magn Reson Med 2008;59(6):1440–7.

[8] Roemer PB, Edelstein WA, Hayes CE, Souza SP, Mueller OM. The NMR phased array. Magn Reson Med 1990;16(2):192–225.

[9] Hayes CE, Edelstein WA, Schenck JF, Mueller OM, Eash M. An efficient, highly homogeneous radiofrequency coil for whole-body NMR imaging at 1.5 T. Journal of Magnetic Resonance (1969) 1985;63(3):622 – 628. ISSN 0022-2364.

[10] Hoult DI, Chen CN, Sank VJ. Quadrature detection in the laboratory frame. Magn Reson Med 1984;1(3):339–53.

[11] Nishimura D. Principles of magnetic resonance imaging. 1996.

[12] Constantinides CD, Atalar E, McVeigh ER. Signal-to-noise measurements in magnitude images from NMR phased arrays. Magn Reson Med 1997; 38(5):852–7.

[13] Bydder M, Larkman DJ, Hajnal JV. Combination of signals from array coils using image-based estimation of coil sensitivity profiles. Magn Reson Med 2002;47(3):539–48.

[14] Noll DC, Nishimura DG, Macovski A. Homodyne detection in magnetic resonance imaging. IEEE Trans Med Imaging 1991;10(2):154–63.

[15] Pruessmann KP, Weiger M, Scheidegger MB, Boesiger P. SENSE: Sensitivity Dncoding for Fast MRI. Magn Reson Med 1999;42(5):952–62.

[16] Sodickson DK, Manning WJ. Simultaneous acquisition of spatial harmonics (SMASH): fast imaging with radiofrequency coil arrays. Magn Reson Med 1997;38(4):591–603.

[17] Griswold MA, Jakob PM, Heidemann RM, Nittka M, Jellus V, Wang J, Kiefer B, Haase A. Generalized autocalibrating partially parallel acquisitions (GRAPPA). Magn Reson Med 2002;47(6):1202–10.

[18] Lustig M, Donoho D, Pauly JM. Sparse MRI: The application of compressed sensing for rapid MR imaging. Magn Reson Med 2007;58(6):1182–95.

[19] Zur Y, Wood ML, Neuringer LJ. Spoiling of transverse magnetization in steady-state sequences. Magn Reson Med 1991;21(2):251–63.

[20] Yablonskiy DA, Haacke EM. Theory of NMR signal behavior in magnetically inhomogeneous tissues: the static dephasing regime. Magn Reson Med 1994; 32(6):749–63.

[21] Haacke EM, Xu Y, Cheng YCN, Reichenbach JR. Susceptibility weighted imaging (SWI). Magn Reson Med 2004;52(3):612–8.

[22] Hahn EL. Spin Echoes. Phys Rev 1950;80(4):580–594.

[23] Carr HY, Purcell EM. Effects of Diffusion on Free Precession in Nuclear Magnetic Resonance Experiments. Phys Rev 1954;94(3):630–638.

[24] Meiboom S, Gill D. Modified Spin-Echo Method for Measuring Nuclear Relaxation Times. Review of Scientific Instruments 1958;29(8):688–691.

[25] Hennig J, Nauerth A, Friedburg H. RARE imaging: a fast imaging method for clinical MR. Magn Reson Med 1986;3(6):823–833.

[26] Hennig J. Multiecho Imaging Sequences With Low Refocusing Flip Angles. Journal of Magnetic Resonance 1988;78(3):397–407.

[27] Vlaardingerbroek MT, den Boer JA. Magnetic Resonance Imaging: Theory and Practice. Springer-Verlag Berlin Heidelberg New York, 3rd edition, 2003.

[28] Hennig J. Echoes - how to generate, recognize, use or avoid them in MR-imaging sequences. Part II: Echoes in imaging sequences. Concepts in Magnetic Resonance 1991;3(4):179–192.

[29] Hennig J. Echoes - how to generate, recognize, use or avoid them in MR-imaging sequences. Part I: Fundamental and not so fundamental properties of spin echoes. Concepts in Magnetic Resonance 1991;3(3):125–143.

[30] Hennig J, Scheffler K. Easy improvement of signal-to-noise in RARE-sequences with low refocusing flip angles. Rapid acquisition with relaxation enhancement. Magn Reson Med 2000;44(6):983–985.

[31] Hennig J, Scheffler K. Hyperechoes. Magn Reson Med 2001;46(1):6–12.

[32] Hennig J, Weigel M, Scheffler K. Calculation of flip angles for echo trains with predefined amplitudes with the extended phase graph (EPG)-algorithm: principles and applications to hyperecho and TRAPS sequences. Magn Reson Med 2004;51(1):68–80.

[33] Weigel M, Hennig J. Development and optimization of T2 weighted methods with reduced RF power deposition (Hyperecho-TSE) for magnetic resonance imaging. Z Med Phys 2008;18(3):151–61.

[34] Alsop D. The sensitivity of low flip angle RARE imaging. Magn Reson Med 1997;37(2):176–184.

[35] Le Roux P, Hinks RS. Stabilization of echo amplitudes in FSE sequences. Magn Reson Med 1993;30(2):183–90.

[36] Hennig J, Weigel M, Scheffler K. Multiecho sequences with variable refocusing flip angles: optimization of signal behavior using smooth transitions between pseudo steady states (TRAPS). Magn Reson Med 2003;49(3):527–535.

[37] Busse R. Reduced RF power without blurring: correcting for modulation of refocusing flip angle in FSE sequences. Magn Reson Med 2004;51(5):1031–1037.

[38] Busse R, Hariharan H, Vu A, Brittain J. Fast spin echo sequences with very long echo trains: design of variable refocusing flip angle schedules and generation of clinical T2 contrast. Magn Reson Med 2006;55(5):1030–1037.

[39] Weigel M, Hennig J. Contrast behavior and relaxation effects of conventional and hyperecho-turbo spin echo sequences at 1.5 and 3 T. Magn Reson Med 2006;55(4):826–35.

[40] Woessner D. Effects of diffusion in nuclear magnetic resonance spin-echo experiments. The Journal of Chemical Physics 1961;34:2057.

[41] Vedrine P, Aubert G, Beaudet F, Belorgey J, Beltramelli J, Berriaud C, Bredy P, Chesny P, Donati A, Gilgrass G, Grunblatt G, Juster F, Molinie F, Meuris C, Nunio F, Payn A, Quettier L, Rey J, Schild T, Sinanna A. The Whole Body 11.7 T MRI Magnet for Iseult/INUMAC Project. Applied Superconductivity, IEEE Transactions on 2008;18(2):868 –873. ISSN 1051-8223.

[42] Kim YC, Narayanan SS, Nayak KS. Accelerated three-dimensional upper airway MRI using compressed sensing. Magn Reson Med 2009;61(6):1434–40.

[43] Gati JS, Menon RS, Ugurbil K, Rutt BK. Experimental determination of the BOLD field strength dependence in vessels and tissue. Magn Reson Med 1997;38(2):296–302.

[44] Gelman N, Gorell JM, Barker PB, Savage RM, Spickler EM, Windham JP, Knight RA. MR imaging of human brain at 3.0 T: preliminary report on transverse relaxation rates and relation to estimated iron content. Radiology 1999;210(3):759–67.

[45] Gelman N, Ewing JR, Gorell JM, Spickler EM, Solomon EG. Interregional variation of longitudinal relaxation rates in human brain at 3.0 T: relation to estimated iron and water contents. Magn Reson Med 2001;45(1):71–9.

[46] Mitsumori F, Watanabe H, Takaya N. Estimation of brain iron concentration in vivo using a linear relationship between regional iron and apparent transverse relaxation rate of the tissue water at 4.7T. Magn Reson Med 2009; 62(5):1326–30.

[47] Haacke EM, Cheng NYC, House MJ, Liu Q, Neelavalli J, Ogg RJ, Khan A, Ayaz M, Kirsch W, Obenaus A. Imaging iron stores in the brain using magnetic resonance imaging. Magn Reson Imaging 2005;23(1):1–25.

[48] Hammond KE, Metcalf M, Carvajal L, Okuda DT, Srinivasan R, Vigneron D, Nelson SJ, Pelletier D. Quantitative in vivo magnetic resonance imaging of multiple sclerosis at 7 Tesla with sensitivity to iron. Ann Neurol 2008; 64(6):707–13.

[49] Tong KA, Ashwal S, Obenaus A, Nickerson JP, Kido D, Haacke EM. Susceptibility-weighted MR imaging: a review of clinical applications in children. AJNR Am J Neuroradiol 2008;29(1):9–17.

[50] Yao B, Li TQ, Gelderen Pv, Shmueli K, de Zwart JA, Duyn JH. Susceptibility contrast in high field MRI of human brain as a function of tissue iron content. Neuroimage 2009;44(4):1259–66.

[51] Hoult DI, Chen CN, Sank VJ. The field dependence of NMR imaging. II. Arguments concerning an optimal field strength. Magn Reson Med 1986; 3(5):730–46.

[52] Collins C, Smith M. Signal-to-noise ratio and absorbed power as functions of main magnetic field strength, and definition of "90 degrees " RF pulse for the head in the birdcage coil. Magn Reson Med 2001;45(4):684–691.

[53] Ibrahim T. A numerical analysis of radio-frequency power requirements in magnetic resonance imaging experiment. Microwave Theory and Techniques, IEEE Transactions on 2004;52(8):1999 – 2003. ISSN 0018-9480.

[54] Vaughan J, Garwood M, Collins C, Liu W, DelaBarre L, Adriany G, Andersen P, Merkle H, Goebel R, Smith M, Ugurbil K. 7T vs. 4T: RF power, homogeneity, and signal-to-noise comparison in head images. Magn Reson Med 2001; 46(1):24–30.

[55] Collins CM, Liu W, Schreiber W, Yang QX, Smith MB. Central brightening due to constructive interference with, without, and despite dielectric resonance. J Magn Reson Imaging 2005;21(2):192–6.

[56] Rubin M, Safdieh J. Netter's concise neuroanatomy. Saunders Elsevier, 2007.

[57] Cottrell DA, Kremenchutzky M, Rice GP, Koopman WJ, Hader W, Baskerville J, Ebers GC. The natural history of multiple sclerosis: a geographically based study. 5. The clinical features and natural history of primary progressive multiple sclerosis. Brain 1999;122 (Pt 4):625–39.

[58] Kurtzke JF. Multiple sclerosis in time and space–geographic clues to cause. J Neurovirol 2000;6 Suppl 2:S134–40.

[59] Beck CA, Metz LM, Svenson LW, Patten SB. Regional variation of multiple sclerosis prevalence in Canada. Mult Scler 2005;11(5):516–9.

[60] Charil A, Yousry TA, Rovaris M, Barkhof F, De Stefano N, Fazekas F, Miller DH, Montalban X, Simon JH, Polman C, Filippi M. MRI and the diagnosis of multiple sclerosis: expanding the concept of "no better explanation". Lancet Neurol 2006;5(10):841–52.

[61] McDonald WI, Compston A, Edan G, Goodkin D, Hartung HP, Lublin FD, McFarland HF, Paty DW, Polman CH, Reingold SC, Sandberg-Wollheim M, Sibley W, Thompson A, van den Noort S, Weinshenker BY, Wolinsky JS. Recommended diagnostic criteria for multiple sclerosis: guidelines from the International Panel on the diagnosis of multiple sclerosis. Ann Neurol 2001; 50(1):121–7.

[62] Kurtzke JF. Rating neurologic impairment in multiple sclerosis: an expanded disability status scale (EDSS). Neurology 1983;33(11):1444–52.

[63] Lassmann H, Brück W, Lucchinetti CF. The immunopathology of multiple sclerosis: an overview. Brain Pathol 2007;17(2):210–8.

[64] Fransson ME, Liljenfeldt LSE, Fagius J, Tötterman TH, Loskog ASI. The T-cell pool is anergized in patients with multiple sclerosis in remission. Immunology 2009;126(1):92–101.

[65] Benveniste EN. Role of macrophages/microglia in multiple sclerosis and experimental allergic encephalomyelitis. J Mol Med 1997;75(3):165–73.

[66] Kirov II, Patil V, Babb JS, Rusinek H, Herbert J, Gonen O. MR spectroscopy indicates diffuse multiple sclerosis activity during remission. J Neurol Neurosurg Psychiatry 2009;80(12):1330–6.

[67] Vercellino M, Masera S, Lorenzatti M, Condello C, Merola A, Mattioda A, Tribolo A, Capello E, Mancardi GL, Mutani R, Giordana MT, Cavalla P. Demyelination, inflammation, and neurodegeneration in multiple sclerosis deep gray matter. J Neuropathol Exp Neurol 2009;68(5):489–502.

[68] Drayer B, Burger P, Hurwitz B, Dawson D, Cain J. Reduced signal intensity on MR images of thalamus and putamen in multiple sclerosis: increased iron content? AJR Am J Roentgenol 1987;149(2):357–63.

[69] Bakshi R, Benedict RHB, Bermel RA, Caruthers SD, Puli SR, Tjoa CW, Fabiano AJ, Jacobs L. T2 hypointensity in the deep gray matter of patients with multiple sclerosis: a quantitative magnetic resonance imaging study. Arch Neurol 2002;59(1):62–8.

[70] Ge Y, Jensen JH, Lu H, Helpern JA, Miles L, Inglese M, Babb JS, Herbert J, Grossman RI. Quantitative assessment of iron accumulation in the deep gray matter of multiple sclerosis by magnetic field correlation imaging. AJNR Am J Neuroradiol 2007;28(9):1639–44.

[71] Ormerod IE, Bronstein A, Rudge P, Johnson G, Macmanus D, Halliday AM, Barratt H, Du Boulay EP, Kendal BE, Moseley IF. Magnetic resonance imaging in clinically isolated lesions of the brain stem. J Neurol Neurosurg Psychiatry 1986;49(7):737–43.

[72] Guttmann CR, Ahn SS, Hsu L, Kikinis R, Jolesz FA. The evolution of multiple sclerosis lesions on serial MR. AJNR Am J Neuroradiol 1995;16(7):1481–91.

[73] van Walderveen MA, Barkhof F, Hommes OR, Polman CH, Tobi H, Frequin ST, Valk J. Correlating MRI and clinical disease activity in multiple sclerosis: relevance of hypointense lesions on short-TR/short-TE (T1-weighted) spin-echo images. Neurology 1995;45(9):1684–90.

[74] Miki Y, Grossman RI, Udupa JK, Wei L, Polansky M, Mannon LJ, Kolson DL. Relapsing-remitting multiple sclerosis: longitudinal analysis of MR images–lack of correlation between changes in T2 lesion volume and clinical findings. Radiology 1999;213(2):395–9.

[75] MacKay AL, Vavasour IM, Rauscher A, Kolind SH, Mädler B, Moore GRW, Traboulsee AL, Li DKB, Laule C. MR relaxation in multiple sclerosis. Neuroimaging Clin N Am 2009;19(1):1–26.

[76] Henkelman RM, Stanisz GJ, Graham SJ. Magnetization transfer in MRI: a review. NMR Biomed 2001;14(2):57–64.

[77] Schmierer K, Wheeler-Kingshott CAM, Tozer DJ, Boulby PA, Parkes HG, Yousry TA, Scaravilli F, Barker GJ, Tofts PS, Miller DH. Quantitative magnetic resonance of postmortem multiple sclerosis brain before and after fixation. Magn Reson Med 2008;59(2):268–77.

[78] MacKay A, Whittall K, Adler J, Li D, Paty D, Graeb D. In vivo visualization of myelin water in brain by magnetic resonance. Magn Reson Med 1994; 31(6):673–7.

[79] Laule C, Vavasour IM, Moore GRW, Oger J, Li DKB, Paty DW, MacKay AL. Water content and myelin water fraction in multiple sclerosis. A T2 relaxation study. J Neurol 2004;251(3):284–93.

[80] Haacke EM, Makki M, Ge Y, Maheshwari M, Sehgal V, Hu J, Selvan M, Wu Z, Latif Z, Xuan Y, Khan O, Garbern J, Grossman RI. Characterizing iron deposition in multiple sclerosis lesions using susceptibility weighted imaging. J Magn Reson Imaging 2009;29(3):537–44.

[81] Eissa A, Lebel RM, Korzan JR, Zavodni AE, Warren KG, Catz I, Emery DJ, Wilman AH. Detecting lesions in multiple sclerosis at 4.7 tesla using phase susceptibility-weighting and T2-weighting. J Magn Reson Imaging 2009; 30(4):737–42.

[82] Craelius W, Migdal MW, Luessenhop CP, Sugar A, Mihalakis I. Iron deposits surrounding multiple sclerosis plaques. Arch Pathol Lab Med 1982;106(8):397–9.

[83] Schenck JF, Zimmerman EA. High-field magnetic resonance imaging of brain iron: birth of a biomarker? NMR Biomed 2004;17(7):433–45.

[84] Connor JR, Pavlick G, Karli D, Menzies SL, Palmer C. A histochemical study of iron-positive cells in the developing rat brain. J Comp Neurol 1995; 355(1):111–23.

[85] Hallgren B, Sourander P. The effect of age on the non-haemin iron in the human brain. J Neurochem 1958;3(1):41–51.

[86] Brooks RA, Vymazal J, Goldfarb RB, Bulte JW, Aisen P. Relaxometry and magnetometry of ferritin. Magn Reson Med 1998;40(2):227–35.

[87] Andrews SC, Harrison PM, Yewdall SJ, Arosio P, Levi S, Bottke W, von Darl M, Briat JF, Laulhère JP, Lobreaux S. Structure, function, and evolution of ferritins. Journal of Inorganic Biochemistry 1992;47(1):161 – 174. ISSN 0162-0134.

[88] Makhlouf SA, Parker FT, Berkowitz AE. Magnetic hysteresis anomalies in ferritin. Phys Rev B 1997;55(22):R14717–R14720.

[89] Cowley JM, Janney DE, Gerkin RC, Buseck PR. The Structure of Ferritin Cores Determined by Electron Nanodiffraction. Journal of Structural Biology 2000;131(3):210 – 216. ISSN 1047-8477.

[90] Andrews SC, Treffry A, Harrison PM. Siderosomal ferritin. The missing link between ferritin and haemosiderin? Biochem J 1987;245(2):439–46.

[91] Koppenol WH. The Haber-Weiss cycle–70 years later. Redox Rep 2001; 6(4):229–34.

[92] Morris CM, Candy JM, Omar S, Bloxham CA, Edwardson JA. Transferrin receptors in the parkinsonian midbrain. Neuropathol Appl Neurobiol 1994; 20(5):468–72.

[93] Sofic E, Riederer P, Heinsen H, Beckmann H, Reynolds GP, Hebenstreit G, Youdim MB. Increased iron (III) and total iron content in post mortem substantia nigra of parkinsonian brain. J Neural Transm 1988;74(3):199–205.

[94] Dexter DT, Wells FR, Lees AJ, Agid F, Agid Y, Jenner P, Marsden CD. Increased nigral iron content and alterations in other metal ions occurring in brain in Parkinson's disease. J Neurochem 1989;52(6):1830–6.

[95] Dexter DT, Carayon A, Javoy-Agid F, Agid Y, Wells FR, Daniel SE, Lees AJ, Jenner P, Marsden CD. Alterations in the levels of iron, ferritin and other trace metals in Parkinson's disease and other neurodegenerative diseases affecting the basal ganglia. Brain 1991;114 (Pt 4):1953–75.

[96] Martin W, Wieler M, Gee M. Midbrain iron content in early Parkinson disease: a potential biomarker of disease status. Neurology 2008;70(16 Part 2):1411.

[97] Norris D. High field human imaging. J Magn Reson Imaging 2003;18(5):519–529.

[98] De Vita E, Thomas DL, Roberts S, Parkes HG, Turner R, Kinchesh P, Shmueli K, Yousry TA, Ordidge RJ. High resolution MRI of the brain at 4.7 Tesla using fast spin echo imaging. Br J Radiol 2003;76(909):631–7.

[99] Thomas DL, De Vita E, Roberts S, Turner R, Yousry TA, Ordidge RJ. High-resolution fast spin echo imaging of the human brain at 4.7 T: implementation and sequence characteristics. Magn Reson Med 2004;51(6):1254–64.

[100] Speck O, Weigel M. Optimization of HyperTSE at 7T for Efficient T2-Weighted Imaging. Proceedings 16th Scientific Meeting, International Society for Magnetic Resonance in Medicine 2008;1333.

[101] Theysohn JM, Kraff O, Maderwald S, Schlamann MU, de Greiff A, Forsting M, Ladd SC, Ladd ME, Gizewski ER. The human hippocampus at 7 T–in vivo MRI. Hippocampus 2009;19(1):1–7.

[102] Barberi E, Gati J, Rutt B, Menon R. A transmit-only/receive-only (TORO) RF system for high-field MRI/MRS applications. Magn Reson Med 2000; 43(2):284–289.

[103] Carmichael DW, Thomas DL, De Vita E, Fernández-Seara MA, Chhina N, Cooper M, Sunderland C, Randell C, Turner R, Ordidge RJ. Improving whole brain structural MRI at 4.7 Tesla using 4 irregularly shaped receiver coils. Neuroimage 2006;32(3):1176–84.

[104] Bowen CV, Gati JS, Menon RS. Robust prescan calibration for multiple spin-echo sequences: application to FSE and b-SSFP. Magn Reson Imaging 2006; 24(7):857–67.

[105] Insko E, Bolinger L. Mapping of the Radiofrequency Field. Journal of Magnetic Resonance, Series A 1993;103(1):82–85.

[106] Mitsumori F, Watanabe H, Takaya N, Garwood M. Apparent transverse relaxation rate in human brain varies linearly with tissue iron concentration at 4.7 T. Magn Reson Med 2007;58(5):1054–60.

[107] Jezzard P, Duewell S, Balaban R. MR relaxation times in human brain: measurement at 4 T. Radiology 1996;199(3):773–779.

[108] Rooney WD, Johnson G, Li X, Cohen ER, Kim SG, Ugurbil K, Springer CS Jr. Magnetic field and tissue dependencies of human brain longitudinal 1H2O relaxation in vivo. Magn Reson Med 2007;57(2):308–18.

[109] Melki PS, Mulkern RV. Magnetization transfer effects in multislice RARE sequences. Magn Reson Med 1992;24(1):189–95.

[110] Weigel M, Helms G, Hennig J. Investigation and modeling of magnetization transfer effects in two-dimensional multislice turbo spin echo sequences with low constant or variable flip angles at 3 T. Magn Reson Med 2009;63(1):230–234.

[111] Lebel R, Wilman A. Intuitive design guidelines for fast spin echo imaging with variable flip angle echo trains. Magn Reson Med 2007;57(5):972–975.

[112] Busse RF, Brau ACS, Vu A, Michelich CR, Bayram E, Kijowski R, Reeder SB, Rowley HA. Effects of refocusing flip angle modulation and view ordering in 3D fast spin echo. Magn Reson Med 2008;60(3):640–9.

[113] Mugler JI, Wald L, Brookeman J. T2-Weighted 3D Spin-Echo Train Imaging of the Brain at 3 Tesla: Reduced Power Deposition Using Low Flip-Angle Refocusing RF Pulses. In Proceedings of the 9th Annual Meeting of ISMRM 2001;438.

[114] Ullmann P, Junge S, Wick M, Seifert F, Ruhm W, Hennig J. Experimental analysis of parallel excitation using dedicated coil setups and simultaneous RF transmission on multiple channels. Magn Reson Med 2005;54(4):994–1001.

[115] Meara SJP, Barker GJ. Impact of incidental magnetization transfer effects on inversion-recovery sequences that use a fast spin-echo readout. Magn Reson Med 2007;58(4):825–9.

[116] Turner R, Oros-Peusquens AM, Romanzetti S, Zilles K, Shah NJ. Optimised in vivo visualisation of cortical structures in the human brain at 3 T using IR-TSE. Magn Reson Imaging 2008;26(7):935–42.

[117] Lebel RM, Wilman AH. Time-efficient fast spin echo imaging at 4.7 T with low refocusing angles. Magn Reson Med 2009;62(1):96–105.

[118] Lebel RM, Wilman AH. Intuitive design guidelines for fast spin echo imaging with variable flip angle echo trains. Magn Reson Med 2007;57(5):972–5.

[119] Jackson GD, Connelly A, Duncan JS, Grünewald RA, Gadian DG. Detection of hippocampal pathology in intractable partial epilepsy: increased sensitivity with quantitative magnetic resonance T2 relaxometry. Neurology 1993; 43(9):1793–9.

[120] Whittall KP, MacKay AL, Graeb DA, Nugent RA, Li DK, Paty DW. In vivo measurement of T2 distributions and water contents in normal human brain. Magn Reson Med 1997;37(1):34–43.

[121] MacKay A, Laule C, Vavasour I, Bjarnason T, Kolind S, Mädler B. Insights into brain microstructure from the T2 distribution. Magn Reson Imaging 2006; 24(4):515–25.

[122] Dardzinski BJ, Mosher TJ, Li S, Van Slyke MA, Smith MB. Spatial variation of T2 in human articular cartilage. Radiology 1997;205(2):546–50.

[123] St Pierre TG, Clark PR, Chua-anusorn W, Fleming AJ, Jeffrey GP, Olynyk JK, Pootrakul P, Robins E, Lindeman R. Noninvasive measurement and imaging of liver iron concentrations using proton magnetic resonance. Blood 2005; 105(2):855–61.

[124] Perry J, Haughton V, Anderson PA, Wu Y, Fine J, Mistretta C. The value of T2 relaxation times to characterize lumbar intervertebral disks: preliminary results. AJNR Am J Neuroradiol 2006;27(2):337–42.

[125] Hosch W, Bock M, Libicher M, Ley S, Hegenbart U, Dengler TJ, Katus HA, Kauczor HU, Kauffmann GW, Kristen AV. MR-relaxometry of myocardial tissue: significant elevation of T1 and T2 relaxation times in cardiac amyloidosis. Invest Radiol 2007;42(9):636–42.

[126] Poon CS, Henkelman RM. Practical T2 quantitation for clinical applications. J Magn Reson Imaging 1992;2(5):541–53.

[127] Majumdar S, Orphanoudakis SC, Gmitro A, O'Donnell M, Gore JC. Errors in the measurements of T2 using multiple-echo MRI techniques. I. Effects of radiofrequency pulse imperfections. Magn Reson Med 1986;3(3):397–417.

[128] Crawley AP, Henkelman RM. Errors in T2 estimation using multislice multiple-echo imaging. Magn Reson Med 1987;4(1):34–47.

[129] Does MD, Snyder RE. Multiecho imaging with suboptimal spoiler gradients. J Magn Reson 1998;131(1):25–31.

[130] Pell GS, Briellmann RS, Waites AB, Abbott DF, Lewis DP, Jackson GD. Optimized clinical T2 relaxometry with a standard CPMG sequence. J Magn Reson Imaging 2006;23(2):248–52.

[131] Smith HE, Mosher TJ, Dardzinski BJ, Collins BG, Collins CM, Yang QX, Schmithorst VJ, Smith MB. Spatial variation in cartilage T2 of the knee. J Magn Reson Imaging 2001;14(1):50–5.

[132] Maier CF, Tan SG, Hariharan H, Potter HG. T2 quantitation of articular cartilage at 1.5 T. J Magn Reson Imaging 2003;17(3):358–64.

[133] Majumdar S, Gmitro A, Orphanoudakis SC, Reddy D, Gore JC. An estimation and correction scheme for system imperfections in multiple-echo magnetic resonance imaging. Magn Reson Med 1987;4(3):203–20.

[134] Sled JG, Pike GB. Correction for B(1) and B(0) variations in quantitative T(2) measurements using MRI. Magn Reson Med 2000;43(4):589–93.

[135] Schmitt P, Griswold MA, Jakob PM, Kotas M, Gulani V, Flentje M, Haase A. Inversion recovery TrueFISP: quantification of T(1), T(2), and spin density. Magn Reson Med 2004;51(4):661–7.

[136] Deoni SCL, Rutt BK, Peters TM. Rapid combined T1 and T2 mapping using gradient recalled acquisition in the steady state. Magn Reson Med 2003; 49(3):515–26.

[137] Deoni SCL. High-resolution T1 mapping of the brain at 3T with driven equilibrium single pulse observation of T1 with high-speed incorporation of RF field inhomogeneities (DESPOT1-HIFI). J Magn Reson Imaging 2007;26(4):1106–11.

[138] Deoni SCL, Ward HA, Peters TM, Rutt BK. Rapid T2 estimation with phase-cycled variable nutation steady-state free precession. Magn Reson Med 2004; 52(2):435–9.

[139] Jones C, Xiang Q, Whittall K, MacKay A. Calculating T2 and B1 from Decay Curves Collected with non-180 ° Refocusing Pulses. Proceedings 11th Scientific Meeting, International Society for Magnetic Resonance in Medicine 2003;1018.

[140] Pauly J, Le Roux P, Nishimura D, Macovski A. Parameter relations for the Shinnar-Le Roux selective excitation pulse design algorithm [NMR imaging]. IEEE Trans Med Imaging 1991;10(1):53–65.

[141] Breger RK, Rimm AA, Fischer ME, Papke RA, Haughton VM. T1 and T2 measurements on a 1.5-T commercial MR imager. Radiology 1989;171(1):273–6.

[142] Gold GE, Han E, Stainsby J, Wright G, Brittain J, Beaulieu C. Musculoskeletal MRI at 3.0 T: relaxation times and image contrast. AJR Am J Roentgenol 2004;183(2):343–51.

[143] Collins CM, Li S, Smith MB. SAR and B1 field distributions in a heterogeneous human head model within a birdcage coil. Specific energy absorption rate. Magn Reson Med 1998;40(6):847–856. ISSN 0740-3194 (Print); 0740-3194 (Linking).

[144] Kolind SH, Mädler B, Fischer S, Li DKB, MacKay AL. Myelin water imaging: Implementation and development at 3.0T and comparison to 1.5T measurements. Magn Reson Med 2009;62(1):106–15.

[145] Mädler B, MacKay A. In-vivo 3D Multi-component T2-Relaxation Measurements for Quantitative Myelin Imaging at 3T. Proceedings 14th Scientific Meeting, International Society for Magnetic Resonance in Medicine 2006;2112. Seattle.

[146] Foltz WD, Al-Kwifi O, Sussman MS, Stainsby JA, Wright GA. Optimized spiral imaging for measurement of myocardial T2 relaxation. Magn Reson Med 2003;49(6):1089–97.

[147] Oh J, Han ET, Pelletier D, Nelson SJ. Measurement of in vivo multi-component T2 relaxation times for brain tissue using multi-slice T2 prep at 1.5 and 3 T. Magn Reson Imaging 2006;24(1):33–43.

[148] Lawson CL, Hanson RJ. Solving Least Squares Problems. Society for Industrial Mathematics, 1987.

[149] Péran P, Hagberg G, Luccichenti G, Cherubini A, Brainovich V, Celsis P, Caltagirone C, Sabatini U. Voxel-based analysis of R2* maps in the healthy human brain. J Magn Reson Imaging 2007;26(6):1413–20.

[150] Frahm J, Merboldt KD, Hänicke W. Direct FLASH MR imaging of magnetic field inhomogeneities by gradient compensation. Magn Reson Med 1988; 6(4):474–80.

[151] Yang QX, Dardzinski BJ, Li S, Eslinger PJ, Smith MB. Multi-gradient echo with susceptibility inhomogeneity compensation (MGESIC): demonstration of fMRI in the olfactory cortex at 3.0 T. Magn Reson Med 1997;37(3):331–5.

[152] Yang QX, Williams GD, Demeure RJ, Mosher TJ, Smith MB. Removal of local field gradient artifacts in T2*-weighted images at high fields by gradient-echo slice excitation profile imaging. Magn Reson Med 1998;39(3):402–9.

[153] Glover GH. 3D z-shim method for reduction of susceptibility effects in BOLD fMRI. Magn Reson Med 1999;42(2):290–9.

[154] Wild JM, Martin WRW, Allen PS. Multiple gradient echo sequence optimized for rapid, single-scan mapping of R(2)(*) at high B0. Magn Reson Med 2002; 48(5):867–76.

[155] Young IR, Cox IJ, Bryant DJ, Bydder GM. The benefits of increasing spatial resolution as a means of reducing artifacts due to field inhomogeneities. Magn Reson Imaging 1988;6(5):585–90.

[156] Cho ZH, Ro YM. Reduction of susceptibility artifact in gradient-echo imaging. Magn Reson Med 1992;23(1):193–200.

[157] Chen Nk, Wyrwicz AM. Removal of intravoxel dephasing artifact in gradient-echo images using a field-map based RF refocusing technique. Magn Reson Med 1999;42(4):807–12.

[158] Fernández-Seara MA, Wehrli FW. Postprocessing technique to correct for background gradients in image-based R*(2) measurements. Magn Reson Med 2000;44(3):358–66.

[159] Volz S, Hattingen E, Preibisch C, Gasser T, Deichmann R. Reduction of susceptibility-induced signal losses in multi-gradient-echo images: application to improved visualization of the subthalamic nucleus. Neuroimage 2009; 45(4):1135–43.

[160] Baudrexel S, Volz S, Preibisch C, Klein JC, Steinmetz H, Hilker R, Deichmann R. Rapid single-scan T2*-mapping using exponential excitation pulses and image-based correction for linear background gradients. Magn Reson Med 2009;62(1):263–8.

[161] Du YP, Jin Z, Hu Y, Tanabe J. Multi-echo acquisition of MR angiography and venography of the brain at 3 Tesla. J Magn Reson Imaging 2009;30(2):449–54.

[162] Denk C, Rauscher A. Susceptibility weighted imaging with multiple echoes. J Magn Reson Imaging 2010;31(1):185–91.

[163] Duyn JH, van Gelderen P, Li TQ, de Zwart JA, Koretsky AP, Fukunaga M. High-field MRI of brain cortical substructure based on signal phase. Proc Natl Acad Sci U S A 2007;104(28):11796–801.

[164] Mittal S, Wu Z, Neelavalli J, Haacke EM. Susceptibility-weighted imaging: technical aspects and clinical applications, part 2. AJNR Am J Neuroradiol 2009;30(2):232–52.

[165] Kangarlu A, Bourekas EC, Ray-Chaudhury A, Rammohan KW. Cerebral cortical lesions in multiple sclerosis detected by MR imaging at 8 Tesla. AJNR Am J Neuroradiol 2007;28(2):262–6.

[166] Ye F, Allen P, Martin W. Basal ganglia iron content in Parkinson's disease measured with magnetic resonance. Movement Disorders 2004;11(3):243–249.

[167] Connor J, Juneau P, Snyder B, Kanaley L, DeMaggio A, Nguyen H, Brickman C, LeWitt P. Transferrin and iron in normal, Alzheimer's disease, and Parkinson's disease brain regions. Journal of neurochemistry 2002;65(2):710–716.

[168] LeVine SM. Iron deposits in multiple sclerosis and Alzheimer's disease brains. Brain Res 1997;760(1-2):298–303.

[169] Ceccarelli A, Rocca MA, Neema M, Martinelli V, Arora A, Tauhid S, Ghezzi A, Comi G, Bakshi R, Filippi M. Deep gray matter T2 hypointensity is present in patients with clinically isolated syndromes suggestive of multiple sclerosis. Mult Scler 2010;16(1):39–44.

[170] Neema M, Arora A, Healy BC, Guss ZD, Brass SD, Duan Y, Buckle GJ, Glanz BI, Stazzone L, Khoury SJ, Weiner HL, Guttmann CRG, Bakshi R. Deep gray matter involvement on brain MRI scans is associated with clinical progression in multiple sclerosis. J Neuroimaging 2009;19(1):3–8.

[171] Galaris D, Pantopoulos K. Oxidative stress and iron homeostasis: mechanistic and health aspects. Crit Rev Clin Lab Sci 2008;45(1):1–23.

[172] Kell DB. Iron behaving badly: inappropriate iron chelation as a major contributor to the aetiology of vascular and other progressive inflammatory and degenerative diseases. BMC Med Genomics 2009;2:2.

[173] Aboul-Enein F, Rauschka H, Kornek B, Stadelmann C, Stefferl A, Brück W, Lucchinetti C, Schmidbauer M, Jellinger K, Lassmann H. Preferential loss of myelin-associated glycoprotein reflects hypoxia-like white matter damage in stroke and inflammatory brain diseases. J Neuropathol Exp Neurol 2003; 62(1):25–33.

[174] Trapp BD, Stys PK. Virtual hypoxia and chronic necrosis of demyelinated axons in multiple sclerosis. Lancet Neurol 2009;8(3):280–91.

[175] Grant SM, Wiesinger JA, Beard JL, Cantorna MT. Iron-deficient mice fail to develop autoimmune encephalomyelitis. J Nutr 2003;133(8):2635–8.

[176] Qian ZM, Shen X. Brain iron transport and neurodegeneration. Trends Mol Med 2001;7(3):103–8.

[177] Bourekas EC, Christoforidis GA, Abduljalil AM, Kangarlu A, Chakeres DW, Spigos DG, Robitaille PM. High resolution MRI of the deep gray nuclei at 8 Tesla. J Comput Assist Tomogr 1999;23(6):867–74.

[178] Ge Y, Zohrabian VM, Grossman RI. Seven-Tesla magnetic resonance imaging: new vision of microvascular abnormalities in multiple sclerosis. Arch Neurol 2008;65(6):812–6.

[179] Kollia K, Maderwald S, Putzki N, Schlamann M, Theysohn JM, Kraff O, Ladd ME, Forsting M, Wanke I. First clinical study on ultra-high-field MR imaging in patients with multiple sclerosis: comparison of 1.5T and 7T. AJNR Am J Neuroradiol 2009;30(4):699–702.

[180] Mainero C, Benner T, Radding A, van der Kouwe A, Jensen R, Rosen BR, Kinkel RP. In vivo imaging of cortical pathology in multiple sclerosis using ultra-high field MRI. Neurology 2009;73(12):941–8.

[181] Tallantyre EC, Morgan PS, Dixon JE, Al-Radaideh A, Brookes MJ, Evangelou N, Morris PG. A comparison of 3T and 7T in the detection of small parenchymal veins within MS lesions. Invest Radiol 2009;44(9):491–4.

[182] Metcalf M, Xu D, Okuda DT, Carvajal L, Srinivasan R, Kelley DAC, Mukherjee P, Nelson SJ, Vigneron DB, Pelletier D. High-resolution phased-array MRI of the human brain at 7 tesla: initial experience in multiple sclerosis patients. J Neuroimaging 2010;20(2):141–7.

[183] Lebel RM, Wilman AH. Transverse relaxometry with stimulated echo compensation. Magnetic Resonance in Medicine 2010;9999(9999):NA.

[184] Lebel RM, Wilman AH. Field-corrected 3D multiecho gradient echo: Simultaneous extraction of quantitative R2*, T2* weighting, SWI, and venography. Joint Annual Meeting ISMRM-ESMRMB, 5002. Stockholm, Sweden, 2010; .

[185] Ogg RJ, Langston JW, Haacke EM, Steen RG, Taylor JS. The correlation between phase shifts in gradient-echo MR images and regional brain iron concentration. Magn Reson Imaging 1999;17(8):1141–8.

[186] Haacke EM, Ayaz M, Khan A, Manova ES, Krishnamurthy B, Gollapalli L, Ciulla C, Kim I, Petersen F, Kirsch W. Establishing a baseline phase behavior in magnetic resonance imaging to determine normal vs. abnormal iron content in the brain. J Magn Reson Imaging 2007;26(2):256–64.

[187] Shmueli K, de Zwart JA, van Gelderen P, Li TQ, Dodd SJ, Duyn JH. Magnetic susceptibility mapping of brain tissue in vivo using MRI phase data. Magn Reson Med 2009;62(6):1510–22.

[188] Filippi M, Bozzali M, Comi G. Magnetization transfer and diffusion tensor MR imaging of basal ganglia from patients with multiple sclerosis. J Neurol Sci 2001;183(1):69–72.

[189] Khalil M, Enzinger C, Langkammer C, Tscherner M, Wallner-Blazek M, Jehna M, Ropele S, Fuchs S, Fazekas F. Quantitative assessment of brain iron by

R(2)* relaxometry in patients with clinically isolated syndrome and relapsing-remitting multiple sclerosis. Mult Scler 2009;15(9):1048–54.

[190] Nielsen JM, Korteweg T, Barkhof F, Uitdehaag BMJ, Polman CH. Overdiagnosis of multiple sclerosis and magnetic resonance imaging criteria. Ann Neurol 2005;58(5):781–3.

[191] Leh SE, Chakravarty MM, Ptito A. The connectivity of the human pulvinar: a diffusion tensor imaging tractography study. Int J Biomed Imaging 2008; 2008:789539.

[192] Malykhin NV, Lebel RM, Coupland NJ, Wilman AH, Carter R. In vivo quantification of hippocampal subfields using 4.7 T fast spin echo imaging. Neuroimage 2010;49(2):1224–30.

[193] Neelavalli J, Cheng YCN, Jiang J, Haacke EM. Removing background phase variations in susceptibility-weighted imaging using a fast, forward-field calculation. J Magn Reson Imaging 2009;29(4):937–48.

[194] Ye FQ, Martin WR, Allen PS. Estimation of brain iron in vivo by means of the interecho time dependence of image contrast. Magn Reson Med 1996; 36(1):153–8.

[195] Scheffler K, Hennig J. Is TrueFISP a gradient-echo or a spin-echo sequence? Magn Reson Med 2003;49(2):395–7.

[196] Lebel R, Menon R, Bowen C. Relaxometry model of strong dipolar perturbers for balanced-SSFP: Application to quantification of SPIO loaded cells. Magn Reson Med 2006;55(3):583–591.

[197] Graham S, Stanchev P, Bronskill M. Criteria for analysis of multicomponent tissue T2 relaxation data. Magnetic resonance in medicine: official journal of the Society of Magnetic Resonance in Medicine/Society of Magnetic Resonance in Medicine 1996;35(3):370.

[198] Chow K, Paterson I, Thompson R. Radiofrequency (B1) Field Mapping In the Heart and Lungs Using a HASTE Double Angle Method. Proceedings 16th Scientific Meeting, International Society for Magnetic Resonance in Medicine 2008;1244. ISSN 1545-4428. Toronto.

Appendix A

System Resources

Completion of this thesis required substantial technological development for a comparatively minute quantity of actual research. The Peter S. Allen MR Research Center is a major beneficiary of this development. The 4.7 T MRI system is now equipped with several new or improved pulse sequences, and calibration techniques to facilitate and enable numerous and diverse research studies. This appendix provides a brief summary of these residual tools.

A.1 Imaging Capabilities

The Varian spectrometer software at the time of writing, VnmrJ 1.1D (Unity Inova console), ships with a wide assortment of mildly-defective imaging sequences. Simple sequences — those requiring minimal tuning or post-processing (i.e., incoherent gradient echo, single spin echo) — are reasonably well developed and suitable for basic imaging; *useful* sequences are inefficient or nonexistent. Detailed here are four sequences developed to conduct the research contained in this thesis or to assist collaborators with their research objectives.

A.1.1 Fast Spin Echo

The majority of this thesis describes high field modifications to the routine FSE sequence. A base sequence was kindly provided by Dr. Chris Bowen at the National Research Council for Biodiagnostics (Atlantic). The crucial component of this sequence was its incorporation of a pre-scan calibration technique to satisfy the CPMG condition, where multiple echo pathways are coherently aligned [104]. This sequence was heavily modified to incorporate:

- Rapid pre-scan calibration with receiver gain adjustment (standard version was *very* slow)
- Improved looping structure for arbitrary data size and rapid data transfer
- Variable angle echo trains
- Partial Fourier acquisitions
- Interleaved inversion recovery (including dual inversion recovery)

- Single shot acquisitions
- Relaxometry acquisitions

Usage

Many parameters are user selectable and careful consideration is required when selecting parameter sets — not all combinations will produce acceptable images. A graphical user interface allows access to all necessary parameters. The user defines the number of slices, slice thickness and spacing, field-of-view, matrix size, bandwidth, echo train length, effective echo, echo spacing, and repetition time. Preparation macros (invoked automatically prior to acquisition, or manually with the "Prep" button, or via the generic "prep" command) compute gradient amplitudes, requisite RF powers, and ensure requested timing parameters are possible. Partial Fourier under-sampling is available; the number of phase encode steps used for homodyne detection [14] is specified. The user can also select various contrast enhancements including single or double inversion, fat saturation, or blood saturation.

Angles of the refocusing train can be adjusted to drastically reduce the RF power or modify the image contrast. This train can be reduced in several ways: (1) full manual adjustment, (2) constant angle, (3) constant angle but with the first pulse set to $90 + \alpha/2$, (4) smooth transition to a low angle, or (5) a modulated train for tailored signal levels. The fifth option yields echo trains that can compensate for relaxation blurring and includes an optional Gaussian windowing argument to boost signal near the contrast dominant echo, serving as an acquisition filter to improve SNR.

Image processing is performed in MATLAB. The Varian data file is first reshaped with "fse2fid2E.m". Images can then be loaded into MATLAB with "ImageReshape.m"; alternatively, automatic processing and DICOM export is invoked with "fseprocE.m". Relaxation data is pre-processed with "fse2fid2E.m" then fit with "fseR2procE.m".

Calibration

Prior to acquisition, the gradient tweak procedure described by Bowen *et al.* [104] must be run. This ensures gradient areas are balanced (including possible eddy currents) and the phase of the RF pulses satisfy the CPMG condition. This procedure also optimizes the receiver gain. Once calibrated, a protocol can be created and re-run without tweaking. This tweak procedure is required if parameters affecting gradient amplitude or timing are modified. Calibration is started by pressing the "Autotweak" button on the user interface.

Limitations

The FSE sequence has been under continuous and steady development. The majority of known software bugs have been patched but several glitches remain. Recently, updates have not been issued for minor issues to ensure compatibility with existing clinical protocols.

The macro invoked to compute and write the phase encode table for standard, fully phase encoded, imaging is incompatible with an *odd* number of shots. Ensure that the number of segments, given by the ratio of phase encode steps to echo train length (Varian parameters “nv” and “etl” respectively), is even.

Online reconstruction is possible, but typically discouraged since computation time is often prohibitive and the console is unavailable during this time.

Several computationally intense components are written in MATLAB and require compilation to interface with VnmrJ. These include phase encode table generation for partial Fourier, online reconstruction, and automated calculation of refocusing angles for predefined echo amplitudes. They are compiled in MATLAB with the command “mcc -m -R foo.m”; runtime libraries are required for execution as described in the MATLAB documentation.

Example Images

This thesis contains a plethora of images acquired with this sequence. They are scattered abundantly throughout Chapters 2 and 3. The FSE sequence is capable of generating a very diverse array of image sets including single shot images, extremely high resolution T_2-weighted images, T_1-weighted images using magnetization preparation, and quantitative transverse relaxation maps. Figure A.1 contains a diverse sample from image sets not presented elsewhere in this work.

A.1.2 Magnetization Prepared Rapid Gradient Echo

Magnetization prepared rapid gradient echo (MPRAGE) is the *de facto* standard for volumetric neuroimaging. It provides exceptional and consistent contrast between GM, WM, and CSF and can acquire full brain data sets with isotropic resolution in clinically acceptable scan times.

There are two implementations available: “mp_flash3d” and “mprage”. The former was kindly provided by Dr. Chris Bowen at the National Research Council for Biodiagnostics (Atlantic); the latter is a U of A sequence designed to eventually replace the more cumbersome mp_flash3d. While mp_flash3d can be employed, it utilizes a sub-optimal gradient scheme and must be pre-processed on the console via “dft3d -f” prior to processing with “mprageproc2E.m” in MATLAB.

The newer (and preferred) MPRAGE implementation is a three dimensional, slab selective sequence with linear in-plane phase encoding during the transient signal recovery. In-plane phase-encode segmentation is available to minimize blurring. High time-bandwidth (∼16) minimum phase SLR pulses [140] are employed for optimal excitation slice profiles, minimal echo times, and minimal flow artifacts. Additionally, short echo times reduce $T_2^\star$ weighting, which reduces GM/WM contrast and causes signal voids near steep background gradients. Optional partial Fourier in the readout direction can further minimize the echo time; both zero-padding and homodyne reconstruction options are available in this case. Adiabatic RF pulses are used for complete inversion in the non-uniform transmit field.

Usage

The field-of-view, matrix size, in-plane phase encode segments, inversion time, delay time, and bandwidth are adjusted through the user interface. The echo time is automatically minimized and the repetition time is constrained by the other parameters. The readout fraction for partial Fourier appears next to the readout matrix size —

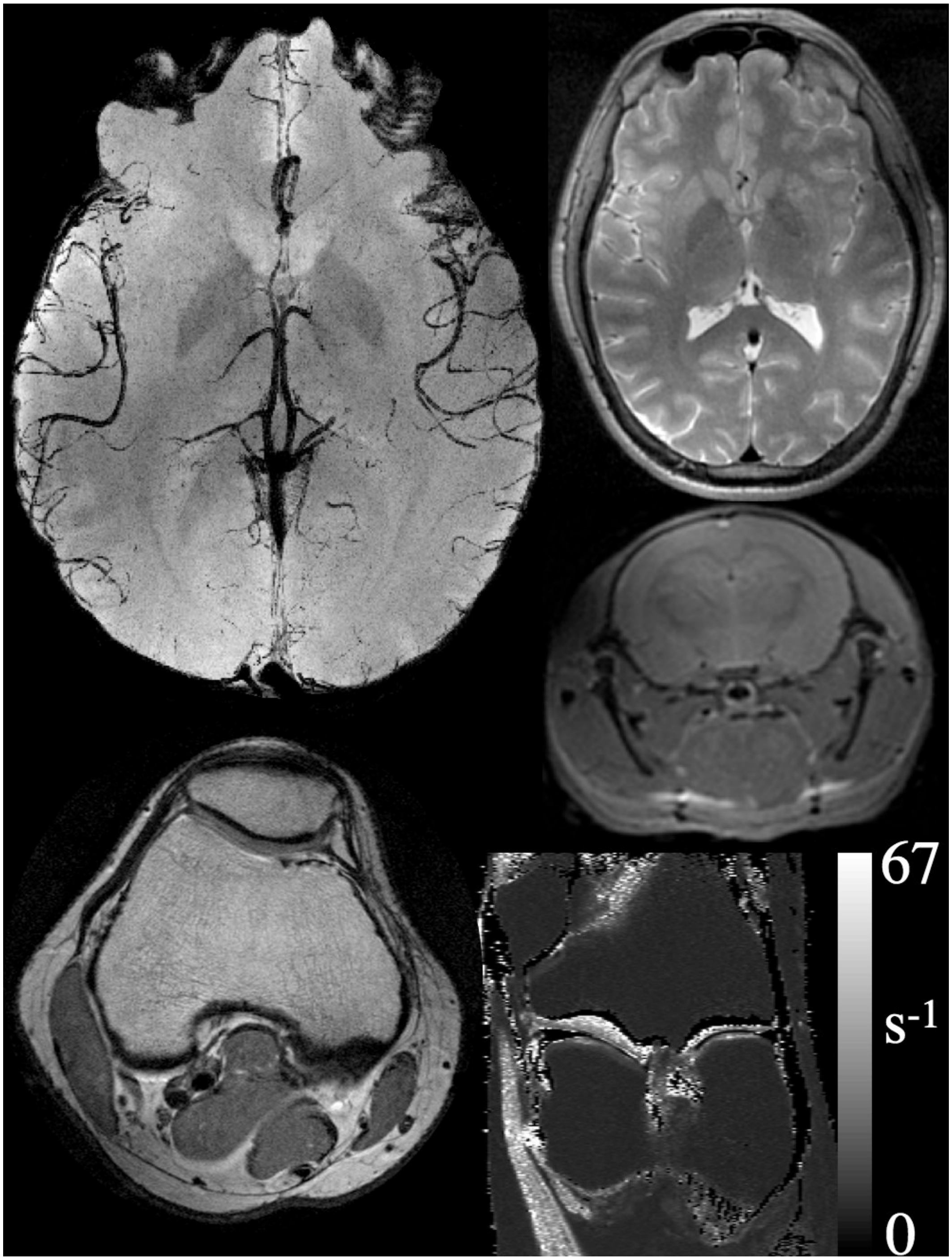

Figure A.1: Montage of fast spin echo images obtained from the 4.7 T imaging system. Clockwise from upper left: a minimum intensity projection over a 3 cm volume to emphasize vasculature; a T_2-weighted image from a full brain data set acquired in ∼60 s at a clinical equivalent resolution; an axial slice from a sacrificed rat pup (Courtesy of Alireza Karimipour, Dr. Jerome Yager, and Dr. Chris Hanstock); articular cartilage R_2 map; high resolution knee image.

a value of 1.0 implies full sampling; a value of 0.75 accelerates echo formation and collects 3/4 of the readout data.

Reconstruction is performed in MATLAB and is not available for on-line reconstruction through VnmrJ. No pre-processing is required to modify the fid file, raw images are loaded into the workspace using "MPRAGErec.m" for viewing while an automated reconstruction producing DICOM files is invoked with "MPRAGE-proc.m".

Calibration

A rapid pre-scan, initiated by pressing "Tweak", ensures the gradient echoes occur in the appropriate portion of the readout window and sets the receiver gain. This process is optional and takes ∼10 s.

Limitations

The number of in-plane phase encode steps must be divisible by the number of segments. The result of this operation must be an even number for proper phase encode generation.

Extreme magnetic field shifts directly above the sinuses can shift the resonant frequency outside the adiabatic inversion bandwidth. Inversion pulse duration should be minimized, subject to RF amplifier and SAR constraints.

Example Images

Example MPRAGE images are shown in Fig A.2.

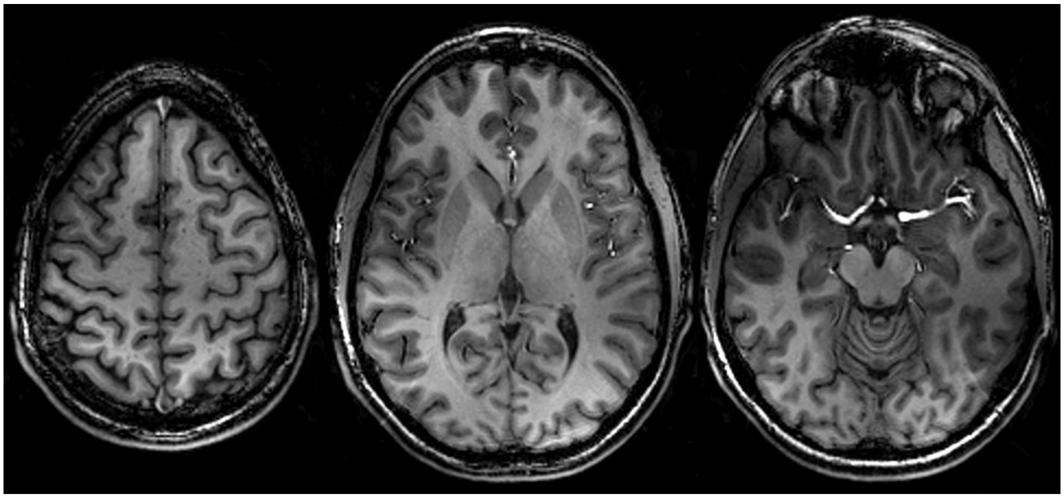

Figure A.2: Transverse MPRAGE images at 4.7 T with 300 ms inversion and post-acquisition delay times. Resolution is $1.0 \times 1.0 \times 2.0$ mm^3, acquired with 80 slices in 4.2 minutes.

A.1.3 Multiecho Gradient Echo

Spoiled gradient echo imaging has many uses at high magnetic field strength due to acceptable RF power deposition, high acquisition duty cycles and SNR efficiency, and enhanced susceptibility contrast relative to lower field strengths. Traditional single echo sequences use either short echo times to maintain acquisition efficiency or longer echo times to elicit stronger $T_2^\star$ or susceptibility contrast. Regardless, either acquisition efficiency or tissue contrast must be sacrificed.

A multiecho acquisition enables high data collection efficiency and long echo times. Our implementation encodes entire images at each echo time enabling numerous post-processing options. Images from each echo time may be processed into separate magnitude, phase, and susceptibility-weighted data sets; alternatively, images from all echo times may be combined into a composite image for improved SNR and CNR. Furthermore, quantitative $R_2^\star$ maps can be obtained by exponential fitting of the temporal signal decay.

Usage

Both 3D and multislice 2D versions of this sequence exist; the 3D sequence has undergone more extensive testing and has more advanced processing options. Basic sequence parameters are selected through the graphical user interface. The user selects the field-of-view, the matrix size, and the acquisition bandwidth. The minimum echo time and spacing are automatically set from these parameters. The number of echoes and the repetition time can be adjusted. Although no direct echo spacing adjustment exists, the slew-rate and bandwidth can be intentionally modified to shift the echoes. Excitation angle and pulse duration can be selected.

Reconstruction is performed in MATLAB with no on-line reconstruction. The core reconstructions are performed with “gemsmerec.m” and “gemsme3drec.m” for 2D and 3D acquisitions respectively. A complete reconstruction tool, including quantitative $R_2^\star$ maps and SWI images, for the 3D approach is invoked with “gemsmeproc.m”.

Calibration

These sequences employ a gradient balancing pre-scan to align echoes and readout windows. The receiver gain is also optimized. This procedure compensates for shim inadequacy in the readout direction and improves image post-processing, particularly for susceptibility weighted imaging. This procedure is suggested, but optional, and takes approximately 30 s.

Limitations

These sequences are written for linear phase RF pulses; the slice refocusing lobe does not accommodate minimum phase excitations. These pulses would be advantageous for 3D imaging.

Images are fully encoded at each echo necessitating long scan times. Echo sharing, as done in fast spin echo, may accelerate imaging by sacrificing full image sets at each echo.

Theoretically, accurate field mapping is possible with this approach by linear regression of the phase evolution. It is sensitive to both large and small frequency shifts, based on the echo spacing and maximum echo time respectively; however, eddy currents and the optional pre-scan impose artificial frequency variations on the sample, limiting this method's ability to quantify natural frequency shifts. Despite this inaccuracy, it may be sufficient for rapid field mapping in native space, as required for unwarping echo planar images.

Example Images

Chapter 4 contains an assortment of multiecho GRE images.

A.1.4 Echo Planar Imaging

Two dimensional echo planar imaging (EPI) is the standard imaging technique for functional MRI. It samples multiple — often all — phase encode lines per excitation pulse. Entire low-resolution images can be collected in ∼50 ms and volumes in several seconds.

Our implementation employs a sinusoidal readout gradient with blipped phase encodes. Continuous sampling (at a constant rate) occurs for the duration of the readout. This approach minimizes gradient waveform and acquisition timing delays which plague approaches with segmented acquisition windows and/or variable rate sampling. This is achieved at the expense of additional reconstruction complexity involving data gridding and an optimization routine to align data sampling and gradient waveforms. We employ a unique, empirically validated, phase correction scheme, detailed below.

Usage

The user selects common sequence parameters including the field-of-view, data matrix, and echo time. Partial Fourier is available by neglecting samples either before or after the gradient echo. This enables shorter echo times or improved slice density respectively. Partial Fourier is enabled indirectly: the total number phase encodes is selected and represents the number of pixels in the image; the number of phase encode lines to actually collect (must be less than or equal to, while remaining greater than half, of the total number of lines) is then selected. The sign on this number (i.e., positive or negative) dictates where phase encode lines should be dropped: a negative number neglects lines *prior* to the center of k-space; a positive number neglects lines *after* the center. Missing data points are zero-filled during reconstruction. The maximum slew-rate (occurring only at the sinusoid zero crossings) and the maximum gradient amplitude (coinciding with the center of each readout line) are user adjustable. Typically, most EPI parameter sets are intrinsically slew rate limited; the prescribed slew-rate shouldn't exceed ∼150 T/m/s to avoid peripheral nerve stimulation.

This sequence employs shaped gradient waveforms exclusively and does not require the integrated Varian slew rate filter to limit gradient rise times. Furthermore, since data acquisition occurs during time varying gradients, short time constant eddy currents can distort the waveforms; appropriate eddy current correction is required. A special gradient coil setting has been created for this sequence that disables the

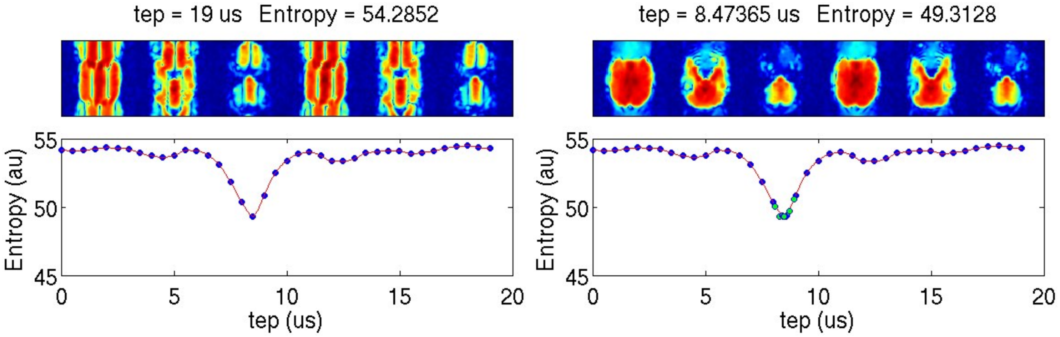

Figure A.3: Automatic alignment optimization of the gradient waveform and the acquisition window during EPI reconstruction. A subset of images are reconstructed with varying delays ("tep" in the above images) between waveform start and acquisition. Image entropy minimization concentrates energy in the primary image and reduces N/2 ghosts. Despite sampling with a 3.0 μs dwell time, shifts as small as 0.25 μs produce visible changes in image ghosting!

slew-rate filter and enables short time constant eddy current correction. This setting is selected by executing "setgcoil('SPIRAL')"; the setting must be returned to the default 120 T/m/s slew-rate, via "setgcoil('SR120')", prior to standard imaging sequences to avoid tripping the gradient amplifier.

Several scan options are available. Spectrally selective fat saturation pulses can be enabled prior to each excitation pulse. A spin echo refocusing pulse can be toggled to rephase off-resonance. Multi-shot capabilities are available to segment the acquisition for distortion reduction. An option to acquire reference data for phase correction should typically be enabled. This collects an entire volume without phase encodes and is used during reconstruction to reduce ghosting, as described below.

Multiple image volumes can be acquired for functional studies by changing the "Images" entry on the graphical interface. This collects the specified number of images, in addition to reference data.

Gradient waveform generation is performed by complied MATLAB code. This whole process is computationally inefficient, thus its execution is minimized. It needs to be performed, by pressing "Prep", after any parameter is changed that will alter the readout waveform. Waveforms are automatically generated prior to starting the scan. This process is required to compute the minimum echo and repetition times.

Trigger signals are sent to "SPARE 4" (a BNC port on the Breakout panel of the left console cabinet) prior to the first slice of each repetition time. The trigger is active immediately prior to the fat saturation pulse and is disabled prior to readout. Total active time is ∼10 ms and can be used for controlling functional tasks. Currently, input triggers are not implemented.

Reconstruction is performed in MATLAB; online reconstruction is not available. Images are reconstructed with "sinepirec.m" and its associated functions, which together automatically align the acquisition windows and the gradient waveforms (shown in Fig A.3), convolve the data onto cartesian grids, and perform phase corrections.

Assuming the optional non-phase encoded reference data was collected, there

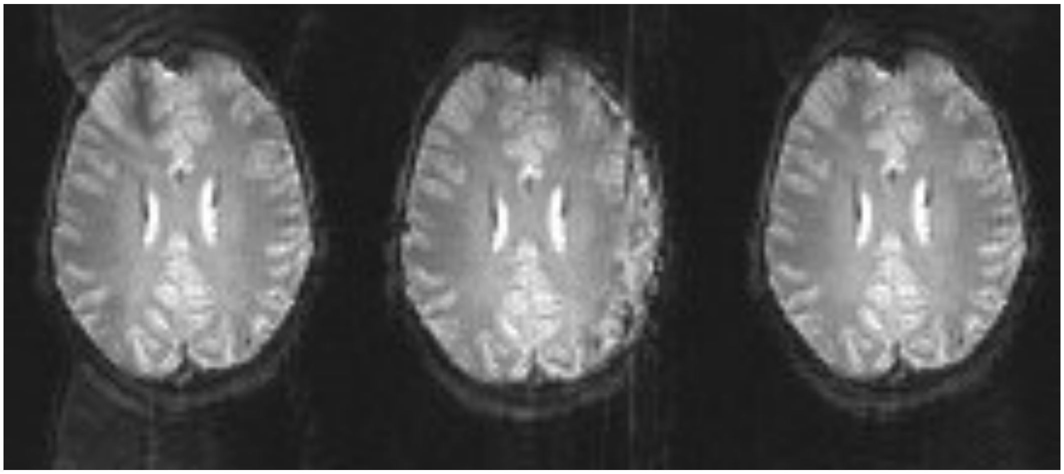

Figure A.4: Performance of the three phase correction options available during EPI reconstruction. From left to right, no phase correction, non-linear phase correction, and our permutative correction. Images are gamma adjusted to emphasize ghosting.

Table A.1: Signal-to-ghost ratio of the three EPI phase correction options and their reconstruction times on a 2.66 GHz processor for an image set of size $96 \times 96 \times 40 \times 2$.

	No Correction	Non-Linear	Permutative Correction
Signal-to-ghost ratio	8.527	21.73	19.55
Reconstruction time (s)	13.87	14.07	126.9

are three phase correction options available during reconstruction: first, no phase correction can be applied. This is the fastest reconstruction option but ghosting will be visible. Second, conventional non-linear phase correction is available. This option is also very fast and provides the best N/2 ghost suppression at the expense of streaking in regions of high off-resonant shifts and produces additional distortion. Third, an unconventional and unpublished — yet empirically excellent — approach is available. This method separates reference lines into pairs of even and odd lines, replicates these lines into full reference sets then reconstructs entire images for each pair of reference lines. These images are combined, on a pixel-by-pixel basis, via a weighted median operation; weighting factors are determined by image entropy — an indirect measure of ghosting (see Fig A.3). This method has the advantage of ghost suppression without the streaking and distortion of non-linear correction, but requires considerable processing time. Example images reconstructed with the three phase correction options are shown in Fig A.4; their signal-to-ghost ratios and reconstruction times are presented in Table A.1.

Calibration

An optional automatic gain calibration can be invoked by pressing “Tweak”.

Limitations

The minimum acquisition bandwidth is defined by the maximum sinusoidal gradient amplitude; a sampling rate greater than or equal to the Nyquist rate must be employed. The waveform generation stage ensures this criteria is satisfied, however a limitation exists: in this sequence, the “sw” parameter controls both gradient and data sampling rates and must be selected carefully to ensure gradient waveform execution and data acquisition are synchronized. Acquisition dwell times are restricted to multiples of 12.5 ηs (minimum acquisition dwell time is 2.0 μs) while gradient waveforms operate on a 50 ηs time base (minimum gradient dwell time is $\sim$1.0 μs). The bandwidth *must* be selected to satisfy the longer gradient time base.

The waveform generation code requires that the number of phase encodes to reconstruct and the number to collect (these can differ when using partial Fourier) be even numbers. Furthermore, the number of phase encodes collected per shot must also be even.

The sequence is not gated to an accurate time base. This results in very small timing inaccuracies; actual echo and repetition times may differ by $\sim$1% from their prescribed values. This is rarely an issue for standard imaging; however, this can be catastrophic for event related fMRI since these errors accrue when multiple volumes are acquired and can total several seconds after a 5 minute scan. Gating the functional task to the scanner is recommended.

Example Images

This protocol is capable of generating rapid image volumes; the primary application is mapping functional activation. Example single and dual shot image volumes are shown in Fig A.5; functional maps comparing activation during a finger tapping task in a healthy volunteer and a patient with amyotrophic lateral sclerosis are shown in Fig A.6.

A.2 Field Mapping

Every imaging study commences with a basic calibration routine. Often automated and transparent to the user, this typically involves a permutation of:

- Setting the global (i.e., averaged over the entire imaging volume) resonant frequency
- Applying a global shim
- Globally calibrating the transmit coil(s)
- Collecting low-resolution localizer images

Imaging at high field strength and/or with multiple receiver coils (as on the 4.7 T system) necessitates several modifications to the calibration procedure. The transmit field (B_1^+) is typically heterogenous across the sample (see Chapter 2) precluding a global calibration value from accurately representing the majority of the sample or a specific region-of-interest. Strong susceptibility induced field shifts near air/ tissue boundaries often necessitates high order shims; efficient calibration requires

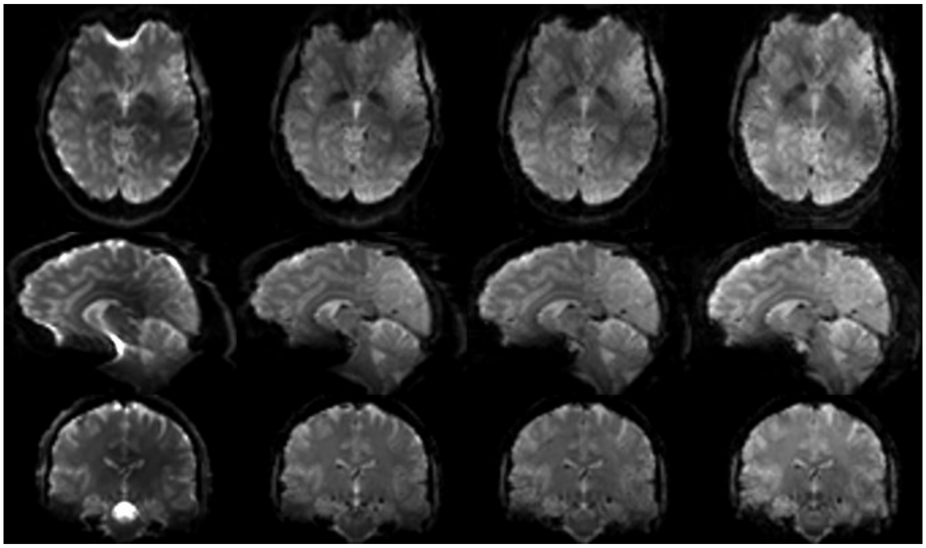

Figure A.5: Example EPI images with $2.5 \times 2.5 \times 2.5$ mm^3 resolution. Sixty axial slices with no gap were acquired (phase encoding is anterior/posterior); sagittal and coronal reslices are also shown. Left column: single shot spin echo, $TE = 45$ ms. Middle left column: single shot GRE. Middle right column: two shot GRE. Right column: four shot GRE. GRE images have $TE = 19$ ms.

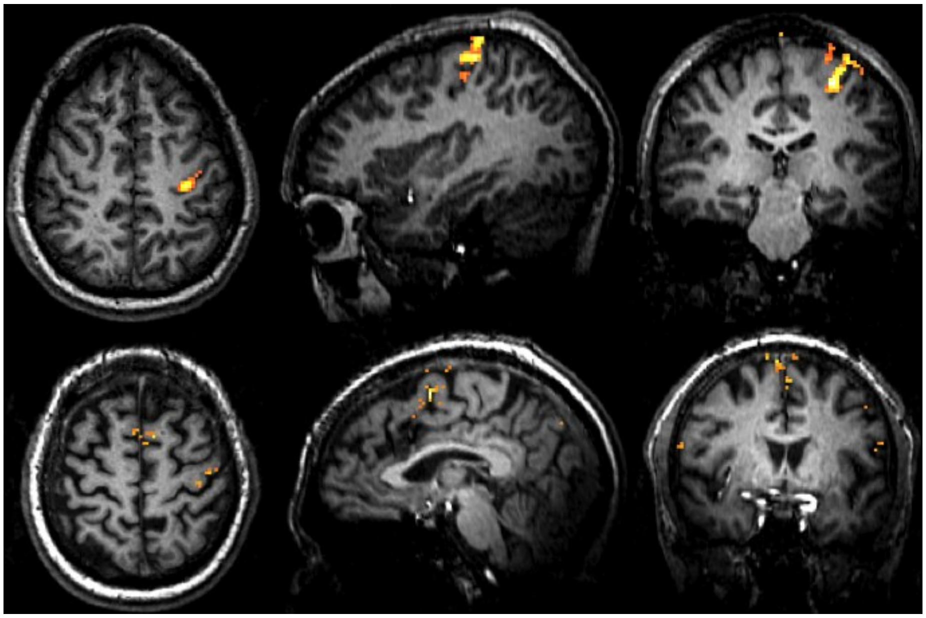

Figure A.6: Functional activation maps overlaid on T_1-weighted anatomic scans. A visually-cued right finger tapping task elicits activation in the left motor cortex (specifically, within the "hand bulb") of a healthy volunteer (top row). In a patient with amyotrophic lateral sclerosis, primary motor cortex activation is reassigned to the supplementary motor area and other cortical regions (bottom row).

deterministic data. Furthermore, spatially varying reception sensitivity (typically enhanced at the center with a volume coil or enhanced at the edges with array coils) introduces undesirable weighting into simple pulse-acquire methods often used for B_0 and B_1^+ calibrations. This can bias the global average settings by weighting them heavily on a subset of the sample. Required are field calibration methods that are:

- Insensitive to reception sensitivity
- Spatially localized
- Accurate and precise
- Time-efficient

Presented below are rapid methods for calibrating the B_1^+ and B_0 fields that satisfy the above criteria and have been implemented, and are in regular use, on the 4.7 T imaging system.

A.2.1 Calibrating the B_1^+ field

Implemented is a rapid image based calibration procedure employing the double-angle method initially proposed by Insko *et al.* [105]. This approach collects two image sets using excitation angles of α and 2α. In the long *TR* limit, image intensities are proportional to $\sin(\alpha)$ and $\sin(2\alpha)$ respectively; a tip angle map is readily derived from their ratio:

$$\alpha = \arccos\left(\frac{I_{2\alpha}}{2I_\alpha}\right). \tag{A.1}$$

This method was combined with a HASTE readout as demonstrated by Chow *et al.* in the context of lung/cardiac imaging [198]. We employ an extremely low and variable angle refocusing train, typically ramped below 40°, as described in Chapter 2 (specifically, Fig 2.7) to vastly reduce RF power deposition, thus ensuring compatibility at 4.7 T.

Usage

On the 4.7 T console, this method can be invoked automatically with the macro “fseb1(‘trans’)”[1], which retrieves a 9-slice HASTE protocol with a 9.0 s *TR* (stored in /vnmr/parlib/b1map_trans.par), arrays the excitation angle at 100° and 50°, and acquires both image sets. Data processing is automatically invoked; a calibration window, similar to that shown in Fig A.7, is opened. The user can optionally toggle the colour scale and contour lines, scroll though slices and adjust windowing on the field map. The intensity scale represents a relative tip angle; unity implies ideal calibration. The histogram provides information regarding the center and range of values. The user can select specific brain regions by first clicking “Get Values”, then adding points to the $B_1^{+\,rel}$ map. Pressing “enter” or “return” computes the average power adjustment for the selected points. An RF coil name can be entered (defaults to “Head”); the calibration procedure is completed by clicking “Accept

---

[1] Optional arguments are ‘trans’ for transverse slices, ‘sag’ for sagittal slices, or ‘cor’ for coronal slices.

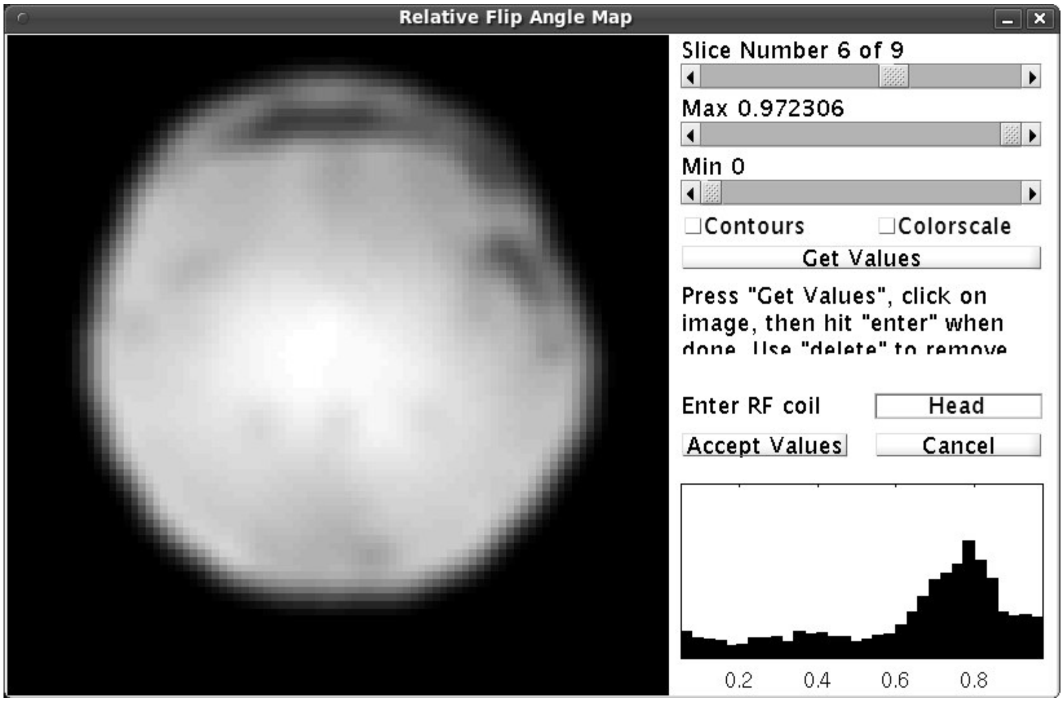

Slice Number 6 of 9

Max 0.972306

Min 0

Press "Get Values", click on image, then hit "enter" when done. Use "delete" to remove

Enter RF coil: Head

Figure A.7: Example B_1^+ calibration interface. A relative tip angle map (i.e., $B_1^{+\,rel}$) is displayed on the left. This interface allows the user to scroll through slices, select the calibration location, and update the RF coil settings.

Values", which creates or modifies an entry in the user's pulsecal file ($vnmruser/ pulsecal). Alternatively, the procedure is terminated, without modification to the user's pulsecal file, by clicking "Cancel".

Initial Calibration

The "fseb1" macro searches for a parameter set named "b1map_trans.par". This parameter set is based on the "fsemsuf" pulse sequence and is created and calibrated as described in Section A.1.1. A long repetition time is required for adequate T_1 recovery. A low resolution single shot protocol is recommended. Minimum echo spacings are not suggested since the probability of image artifacts is increased, which can produce significant errors in the tip angle map. A short echo time — while abiding by partial Fourier constraints — to reduce T_2-weighting and maintain high signal levels is typically desirable.

Limitations

There are multiple phenomena affecting the accuracy of this method. First, considerable noise amplification occurs in the linear regime of the sinusoid (small B_1^+) where both image SNR and parameter estimability are poor. Empirical observation suggests this method is ineffective at $B_1^{+\,rel}$ values below ~1/3. It is suggested that the RF coil be roughly calibrated, ideally to within a factor of ~2, before employing this method. Second, non-rectangular slice profiles and the non-linear magnetiza-

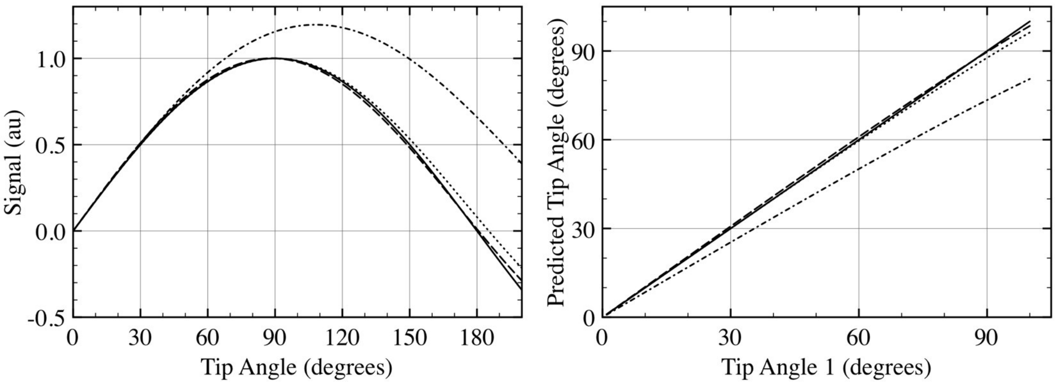

Figure A.8: Left, simulated relationship between signal and prescribed tip angle for three RF pulse shapes and the sinusoidal relation assumed in the double angle method. Signal from a Gaussian pulse (dash-dot) and two SLR pulses designed for 90° excitation angles with time-bandwidth products of 6.0 (dashed) and 4.0 (dotted) are plotted along with a sinusoidal curve (solid). Right, estimated tip angle from the double angle method using these pulses as functions of the actual tip angle.

tion response to high tip angles distort the assumed sinusoidal relation between signal and tip angle; this effect is shown in Fig A.8. Tailored RF pulses, such as those designed with the Shinnar-LeRoux (SLR) transform [140], are required for accurate results. Finally, additional complications including finite *TR* and amplifier non-linearity may also degrade calibration accuracy.

A.2.2 Shimming the B_0 field

Magnetic field distortions surrounding susceptibility interfaces, notably the air/tissue boundaries in the sinus regions, warp the magnetic field. The magnitude and extent of these distortions is proportional to the static magnetic field strength. At 4.7 T susceptibility effects are the primary source of image artifact in gradient echo imaging sequences and severely degrade or prevent reliable spectroscopy in the orbitofrontal cortex and surrounding regions. Imaging systems are equipped with multiple shim coils designed to counteract these distortions; the limited number and remote nature of the shim channels provides an imperfect polynomial approximation to the field warping but can drastically improve image quality. Assessment of the magnetic field within the sample followed by an optimal shim calculation is required to efficiently smooth the magnetic field.

The current software revision installed on the 4.7 T system, VnmrJ 1.1D, provides an automatic routine for mapping the magnetic field and computing shim currents. It is available through the “ge3dshim” sequence. This approach collects three image sets with adjustable echo time delays. The magnetic field is mapped from the phase evolution during these delays and optimal shim values are computed. Some documentation on the use and calibration of this technique can be found on pages 31-33, 51-52, and 82-91 of the “VnmrJ Imaging User Guide” (Pub. No. 01-999236-00, Rev. B0704). Additional usage and calibration notes garnered through numerous trials and tribulations are presented below.

Usage

A calibrated parameter set can be copied from /home/marc/vnmrsys/parlib/ ge3shim_01.par. The shim protocol collects low-resolution 3D volumes with a very large field-of-view, as defined during the calibration stage. The user selects the echo delay, typically starting at ∼2 ms and perhaps iterating to ∼4 ms, the shim region (global, slab, or voxel — described below), the shim orders to calibrate, and a threshold value for image masking. After processing, the field map should be viewed, by displaying the B0.f image, to ensure adequate thresholding and no frequency aliasing. The change in shim values should be scrutinized: changes greater than ∼10 000 digital units are likely erroneous.

Localized shimming can be achieved by first planning a 3D slab or a large spectroscopy voxel spanning the region-of-interest. The macro "gs_slice" saves the current slab for shimming. This must be done prior to loading the shim protocol.

Several iterations are recommended to optimize the shims. Empirically, a coarse manual shim (linear and z^2) followed by two gradient shim iterations converge on a physiologically limited shim set. Manually setting the resonance frequency, using a global pulse acquire or a spectroscopy voxel, is highly recommended after shimming. For spectroscopy, a final manual polish of the linear shims reduces spectral linewidth.

Calibration

Very accurate calibration is necessary for rapid shim convergence. Calibration stores the field change per digital current unit in each voxel for each shim coil. As such, a calibration file is associated with a specific field-of-view and resolution and cannot be interpolated or extrapolated for arbitrary shim protocols. In practice, a single generic calibration file can be used for most imaging samples. This protocol must span a large field-of-view and can be sampled at the minimum resolution necessary to define the spatial shim variations. The existing calibration uses a $330 \times 300 \times 300$ mm^3 field-of-view sampled with $64 \times 32 \times 32$ points. It was calibrated with a large (270 mm diameter, 300 mm length) cylindrical phantom containing mono-resonant silicone oil. This phantom ensures calibration data exists at all spatial locations within the available RF coils.

The calibration procedure is finicky and time-consuming, often requiring multiple restarts (and coffee runs) for optimal calibration. The basic procedure involves mapping the non-shimmed magnetic field, applying a known shim current then remapping the field — the field change is attributed to the applied shim. Once started, this process is repeated automatically for each shim channel. To start, the user selects the shim step percentage to apply during calibration. Separate percentages are available for linear and higher order shims; their values are selected by trial and error in combination with the delay time to obtain maps providing sufficient field change across the sample but *without* phase aliasing. This is exceptionally challenging — impossible perhaps — since certain shim channels are *far* more sensitive than others; a single current percentage is inadequate for all higher order shims. A solution involves iteratively modifying the macro "gs_acqshimmap" (/vnmr/maclib/ maclib.imaging/gs_acqshimmap) to apply unique current values to each shim channel. The entire calibration procedure be performed once acceptable current steps are determined for each channel. Dedicate an entire weekend to this process.

Calibration data is stored in $vnmruser/gshimdir. A pre-calibrated directory can be copied from /home/marc/vnmrsys/gshimdir.

Limitations

The gradient shim routine has several limitations that must be considered for consistent shimming. First, the repetition time may be adjusted for a given protocol (field-of-view and resolution *cannot* be modified). The *TR* should be sufficiently short to rapidly map the field, but long enough that the prescribed delay time does not drastically alter the sequence structure; a 12 ms repetition time is a reasonable compromise for delays less than $\sim$4 ms.

The gradient shim cannot process multiple receiver coil data. A single element must be selected prior to shimming.

The generic shim protocol is very low resolution ($5.2 \times 9.3 \times 9.3$ mm^3). This is adequate for global or slab localized shimming, but is sub-optimal for voxel shimming since the field pattern within the voxel is not resolved. In the latter case, the shim computation is underdetermined and produces unstable results. Reasonably accurate voxel shimming can be obtained by planning a very large voxel specifically for shimming. Alternatively, a higher resolution protocol could be configured.

Appendix B

Flip Book

Fun for readers of all ages. The instructions are simple:

1. Print page (or tear directly from thesis)
2. Cut along dotted lines
3. Sort in ascending order with images facing upward
4. Staple left side (a bulldog clip is acceptable)
5. For smooth animation, trim the right edge diagonally to stagger alignment
6. Flip repeatedly until paper is worn out

Beware of paper cuts.

B.1 Fast Spin Echo

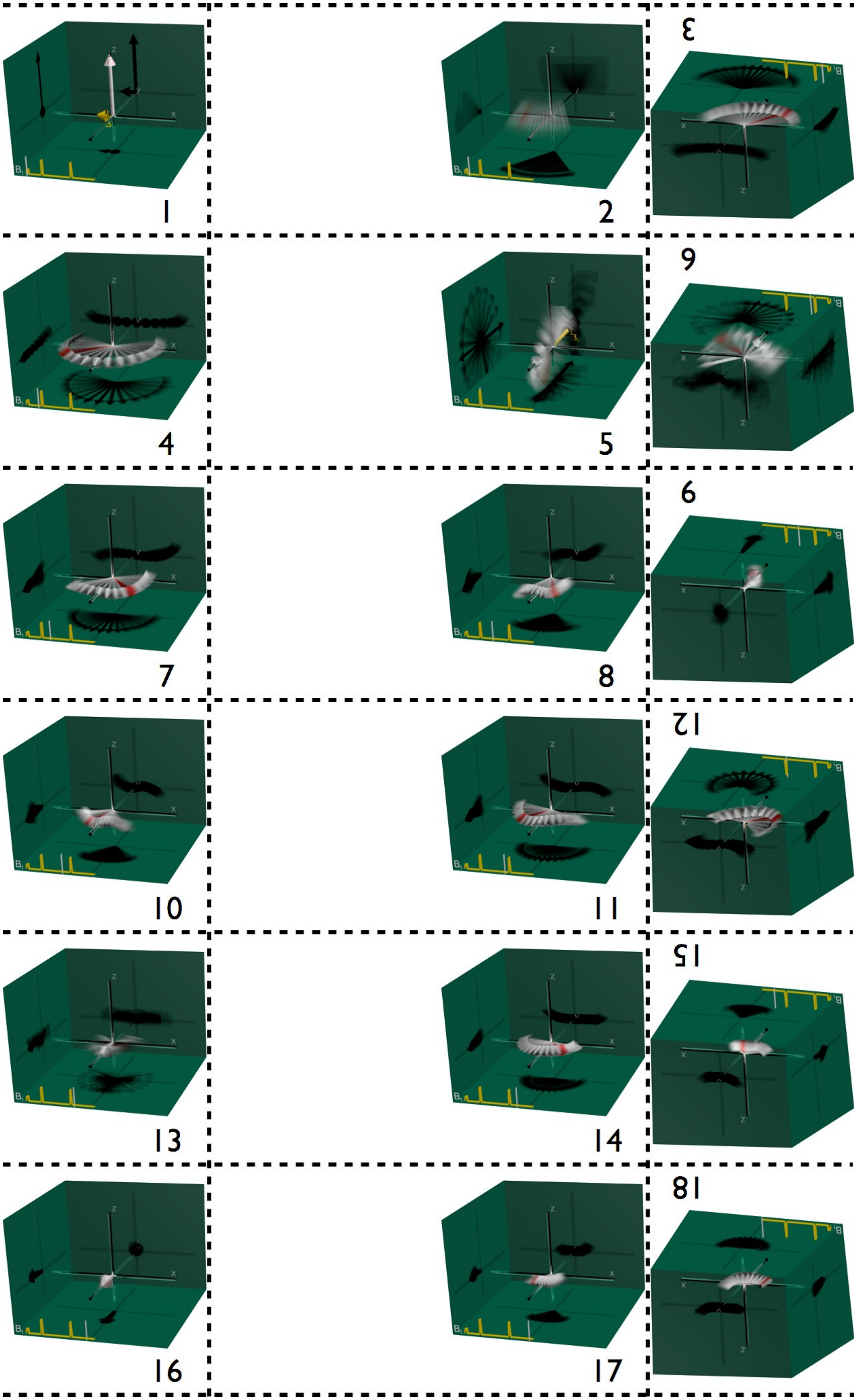

Figure B.1: Do-it-yourself rendering: fast spin echo.